

# **Photoactivatable Kinase and Tubulin Inhibitors**

**Dissertation**

zur Erlangung des Doktorgrades

der Mathematisch-Naturwissenschaftlichen Fakultät

der Christian-Albrechts-Universität zu Kiel

vorgelegt von

**Alexander Döbber**

Kiel 2018



# **Photoactivatable Kinase and Tubulin Inhibitors**

**Dissertation**

zur Erlangung des Doktorgrades

der Mathematisch-Naturwissenschaftlichen Fakultät

der Christian-Albrechts-Universität zu Kiel

vorgelegt von

**Alexander Döbber**

Kiel 2018

Dekan: Prof. Dr. Frank Kempken

Erster Gutachter: Prof. Dr. Christian Peifer

Zweiter Gutachter: Prof. Dr. Maaz Zuhayra

Tag der mündlichen Prüfung: 13. Juli 2018

Zum Druck genehmigt: 13. Juli 2018

*Meiner Familie*



## Abstract

The idea of regulating complex biological processes by the use of light has been appealing for the scientific community for a long time. At the same time, soon after the impressive arriving of kinase inhibitors in clinic, the occurrence of adverse effects and rapid resistances lowered the expectations *e.g.* for anticancer approaches and called for more innovational therapy strategies. As combination, using light to control biological activity of highly potent drugs like kinase inhibitors or microtubule-targeting agents both temporal and spatial became a promising strategy.

This study reports on the development of both a photoactivatable small-molecule microtubule-targeting agent (smMTA) as well as a photoactivatable cyclin-dependent kinase inhibitor. Therefore, in a caging approach the 4,5-dimethoxy-2-nitrobenzyl photoremovable protecting group (DMNB PPG) was attached to crucial pharmacophoric functionalities of both active drugs in order to biologically inactivate them. Upon irradiation with near UV light, the PPG was rapidly cleaved and the active drugs released. The subsequent biological evaluation of the photoactivatable prodrugs addressed two major objectives: biological inactivity of the caged prodrugs as well as the restoration of biological activity upon irradiation with UV light *in vitro*. Attachment of the PPG to the active drugs led in both projects to a significant loss of biological function. As an important proof of concept, biological activity was completely restored upon irradiation with near UV light within a time of irradiation which did not affect cell viability. Thus, both the photoactivatable smMTA as well as the photoactivatable CDK inhibitor represent highly valuable tool compounds for studying biological processes. Despite this important proof of concept, the limited penetration depth of UV light into biological tissues remains. In order to address this issue and enhance translational value for medical applicability, two promising strategies to overcome this limitation were investigated. First of all, a BODIPY caged CDK inhibitor, which could be photoactivated upon irradiation with deeper penetrating green light, was developed and its utility for biological applications could be demonstrated. Secondly, the possibility to use Cherenkov radiation induced by beta emitting radionuclides to photocleave the DMNB caged prodrugs was evaluated. As an important result, evidence for photoactivation of the DMNB caged CDK inhibitor upon incubation with an acid solution of the beta emitter <sup>68</sup>Gallium was demonstrated.

In conclusion, the first photoactivatable smMTA and a photoactivatable CDK inhibitor with high biological utility have been developed. Furthermore, two strategies to overcome the limited penetration depth of UV light were evaluated. Utilization of Cherenkov radiation induced by radionuclides represents an exciting strategy and could lead to a novel therapeutic approach combining caged prodrugs with existing radiotherapeutic applications.





## Kurzzusammenfassung

Die Idee, komplexe biologische Prozesse mit Licht zu steuern, beschäftigt Wissenschaftler seit einiger Zeit. Gleichzeitig, kurz nach dem beeindruckenden Einzug der Kinase Inhibitoren in die Klinik, senkten das Auftreten von schweren Nebenwirkungen und erworbenen Resistenzen die klinischen Erwartungen an Kinaseinhibitoren und der Ruf nach innovativen Therapiekonzepten wurde laut. Licht als Trigger für die Steuerung der Wirkung hochpotenter Arzneistoffen stellt möglicherweise eine vielversprechende Strategie dar. Diese Arbeit berichtet über die Entwicklung eines photoaktivierbaren „caged“ niedermolekularen Tubulininhibitors als auch eines photoaktivierbaren CDK Inhibitors. Dabei wurden die aktiven Wirkstoffe jeweils durch Einführung der 4,5-Dimethoxy-2-nitrobenzyl Schutzgruppe (DMNB) an die Pharmakophore geschützt. Durch Bestrahlung mit nahem UV Licht konnten die Schutzgruppen abgespalten und die aktiven Wirkstoffe wieder freigesetzt werden. Die nachfolgende biologische Testung zielte darauf ab, zwei wichtige Ziele des Proof-of-concept zu adressieren: die biologische Inaktivität der geschützten Prodrugs genauso wie die anschließende Wiederherstellung der biologischen Wirkung durch Bestrahlung mit nahem UV Licht. In beiden Fällen führte das Einführen der photoabspaltbaren Schutzgruppe zu einem signifikanten Verlust an biologischer Aktivität. Die biologische Aktivität konnte anschließend durch Bestrahlung mit UV Licht einer Dosis, die die Viabilität der Zellen nicht beeinträchtigt, vollständig wiederhergestellt werden. Zusammenfassend stellen beide photoaktivierbaren Prodrugs wertvolle Werkzeuge für die biochemische Kinase- und Tubulinforschung dar. Trotz dieser großen Nützlichkeit limitiert die geringe Eindringtiefe von UV Licht in biologisches Gewebe Studien mit beiden photoaktivierbaren Substanzen auf oberflächliches Gewebe. Um diese Limitierung zu überwinden, wurden zwei vielversprechende Strategien untersucht. Zum einen konnte die photoaktivierbare Schutzgruppe BODIPY an das Pharmakophor des CDK inhibitors gekoppelt, dann mit grünem tiefer eindringendem Licht abgespalten und die Nutzbarkeit für biologische Anwendungen demonstriert werden. Zum anderen wurde untersucht, ob die durch radioaktive Betastrahler im Medium induzierte Cherenkov Strahlung zur Aktivierung von DMNB geschützten „caged“ Prodrugs genutzt werden kann. Dabei wurde die Aktivierung des DMNB geschützten CDK Inhibitors durch Inkubation mit <sup>68</sup>Gallium in Lösung gezeigt. Zusammenfassend wurde der erste photoaktivierbare niedermolekulare Tubulininhibitor als auch der erste photoaktivierbare CDK Inhibitor entwickelt und charakterisiert. Weiterhin konnten zwei Strategien zur Überwindung der limitierenden Eindringtiefe des UV Licht entwickelt werden. Dabei erscheint vor allem die Ausnutzung von radioaktiv induzierter Cherenkov Strahlung von hohem Wert und würde ein neuen innovativen Therapieansatz darstellen, der photoaktivierbare Prodrugs mit bereits genutzten radiotherapeutischen Ansätzen kombiniert.



## Table of contents

---

<b>1</b>	<b>Introduction .....</b>	<b>1</b>
1.1	Activation by light.....	2
1.2	Caging concept .....	3
1.3	Photoremovable protecting groups .....	4
1.4	Strategies to overcome the limiting penetration depth of light into biological tissues .....	6
1.4.1	Visible light absorbing PPGs .....	8
1.4.2	Cherenkov radiation .....	9
1.5	Protein kinases and kinase inhibitors.....	12
1.6	Microtubule-targeting agents (MTAs).....	15
<b>2</b>	<b>Aims and Objectives.....</b>	<b>18</b>
2.1	Photoactivatable cyclin-dependent kinase inhibitor.....	19
2.2	Photoactivatable small-molecule microtubule-targeting agent .....	22
<b>3</b>	<b>Results and Discussion .....</b>	<b>23</b>
3.1	Photoactivatable small-molecule microtubule-targeting agent .....	23
3.1.1	Selection of inhibitor and PPG.....	23
3.1.2	Stability upon irradiation.....	24
3.1.3	Synthesis.....	25
3.1.4	Photochemical characterization.....	28
3.1.5	Biological evaluation .....	29
3.2	Photoactivatable cyclin-dependent kinase inhibitor.....	38
3.2.1	Selection of inhibitor and PPG.....	38
3.2.2	Stability upon irradiation.....	39
3.2.3	Molecular modeling .....	40
3.2.4	Synthesis.....	43
3.2.5	Photochemical characterization.....	46
3.2.6	Biological evaluation .....	49
3.2.7	Scaffold project.....	56
3.3	Visible light absorbing PPG.....	67
3.3.1	Stability upon irradiation.....	68
3.3.2	Synthesis.....	69

3.3.3	Photochemical characterization.....	73
3.3.4	Biological evaluation .....	78
3.4	Activation by Cherenkov radiation .....	80
3.4.1	Activation utilizing beta emitting radionuclides.....	81
3.4.2	Activation utilizing external radiation beams.....	85
<b>4</b>	<b>Conclusion .....</b>	<b>87</b>
4.1	Photoactivatable small-molecule microtubule-targeting agent .....	88
4.2	Photoactivatable CDK inhibitor .....	90
<b>5</b>	<b>Experimental .....</b>	<b>94</b>
5.1	Molecular modeling .....	94
5.2	Photoexperiments .....	95
5.2.1	Inhibitor stability upon irradiation .....	95
5.2.2	UV/Vis absorptions spectra .....	95
5.2.3	Photoactivation .....	95
5.3	Chemical Synthesis and Characterization .....	97
5.3.1	Reagents and solvents.....	97
5.3.2	TLC .....	97
5.3.3	Flash Chromatography .....	97
5.3.4	HPLC.....	97
5.3.5	NMR.....	98
5.3.6	LC-MS.....	98
5.3.7	HRMS .....	98
5.3.8	X-ray Crystallography .....	99
5.3.9	Synthetic procedures.....	100
5.4	Biological evaluation .....	135
5.4.1	Kinase assay.....	135
5.4.1	Tubulin polymerization assay .....	135
5.4.2	Immunofluorescence imaging .....	135
5.4.3	Apoptosis assay .....	136
5.4.4	Cell culture.....	136
5.4.5	Cell viability assay.....	137
5.4.6	Cell proliferation assay .....	137
5.4.7	Compound stability for biological evaluation.....	138
5.5	Cherenkov radiation experiments.....	139

5.5.1	Reagents .....	140
5.5.2	Linear Particle Accelerator .....	140
5.5.3	HPLC.....	140
<b>6</b>	<b>References.....</b>	<b>141</b>
<b>7</b>	<b>Appendix .....</b>	<b>154</b>
	<b>List of Abbreviations.....</b>	<b>156</b>
	<b>Table of Compounds.....</b>	<b>160</b>
	<b>Curriculum Vitae .....</b>	<b>164</b>
	<b>Erklärung .....</b>	<b>166</b>
	<b>Danksagung .....</b>	<b>168</b>



# 1 Introduction

---

The idea of regulating complex biological processes by the use of light has been appealing for the scientific community for a long time. The orthogonality towards biological tissues, the precisely controllable intensity and spatial resolution of light highlights an ideal external trigger for remote control. Although the idea is not new, a major interest in improved photopharmacological technologies and applications have emerged in recent years. At the same time, soon after the impressive arriving of kinase inhibitors in clinic, the occurrence of adverse effects and rapid resistances lowered the expectations and called for more innovational therapy strategies.<sup>1,2</sup> Using light to control biological activity of highly potent drugs like kinase inhibitors in both temporal and spatial manner became a promising strategy.

## 1.1 Activation by light

Light exhibits some unique characteristics, attractive for photochemistry. Adjustable intensity and wavelength, non-invasiveness and orthogonality towards most biological systems enables a precise photopharmacological control over time and place with modern light sources such as lasers and LEDs.<sup>3-5</sup>

There are four major approaches to implement light as a trigger for a remote control of biological activity. First of all, the “caging concept” utilizes photoremovable protecting groups (PPGs) for an irreversible photoactivation. Secondly, photoswitches enable a reversible activation and deactivation upon irradiation.<sup>6,7</sup> A third technique utilizes encoded light-responsive elements called optogenetics aiming for dynamic control over biological events in living cells such as neurons.<sup>8-10</sup> Finally, photodynamic therapy (PDT) bases on photosensitizers, which are molecules that generate cell toxic reactive oxygen species (ROS) upon irradiation with light.<sup>11-13</sup> As a milestone in the field of photopharmacology, the photosensitizer Padeliporfin (Tookad®) was approved for the treatment of low-risk prostate cancer by the EMA in 2017.<sup>14</sup> Thereby, Padeliporfin is given as an injection and subsequently locally activated by laser light using optical fibers placed in the prostate.<sup>15,16</sup> However, the present work aims to bring the caging concept for photocontrol over biological activity of potent drugs into focus.



## 1.2 Caging concept

The idea of the caging concept is straightforward: A photoremovable protecting group is covalently attached to a biologically active compound. The so called “caged” compound is not capable of binding to its target or receptor anymore, hence biologically inactive. By irradiation with light, the “cage” is removed and the original biological activity is restored (Figure 1). This results in a rapid concentration jump upon irradiation, thus became a powerful tool for studying biological processes and regulation of biological activity.<sup>4</sup> The introduction of large PPGs severely changes the molecules structure typically resulting in complete loss of biological activity. Furthermore, there is no steady state in the reaction of photoactivation. This combines to an excellent active/inactive ratio, which happens to be particularly useful for biological and medicinal applications.<sup>17</sup> Several examples of caged compounds have proven the utility in biological research. Kaplan *et al.* introduced the first caged compound by caging ATP to study the  $\text{Na}^+/\text{K}^+$  pump in 1978.<sup>18</sup> Since then extensive research was carried out to improve the characteristics of PPGs and many examples followed like caged neurotransmitters<sup>19</sup>, nucleotides<sup>20</sup>, mRNA<sup>21</sup>, peptides<sup>22</sup> or kinase inhibitors<sup>23,24</sup>.

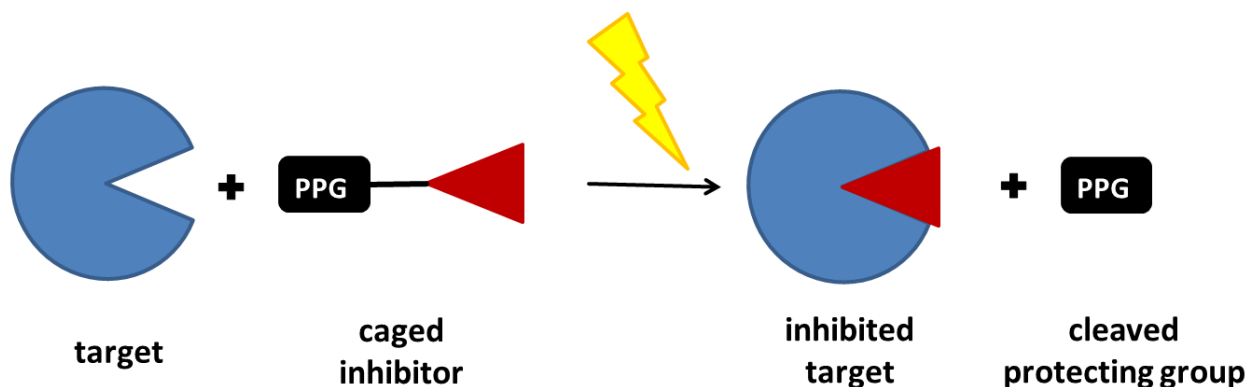


**Figure 1: Schematic representation of the caging concept.**<sup>25</sup> The photoremovable protecting group is covalently attached to the active inhibitor. The caged inhibitor is not capable of binding to its target. After irradiation with light, the photoremovable protecting group is cleaved and the inhibitor is able to bind to its target. The biological activity is restored.

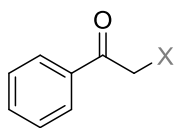
Due to their biological inactivity, the caged compounds ideally prevent systemic side effects. Upon irradiation of the treatment site only, the active compound is spatiotemporally released in high concentrations. This might not only reduce systemic side effects, but also allow higher local drug doses compared to systemic administration. Additionally, since the release of the active drug is temporally controllable it might offer the opportunity of a potent intermittent therapy which could be favorable in prevention of resistances.<sup>26,27</sup>

Besides the irreversibility of the activation, the caging concept exhibits another drawback. The activation upon irradiation is always accompanied by the formation of a byproduct – the cleaved protecting group. This byproduct might not only be toxic, but interfere with the photoreaction by absorbing light of the respective wavelength. However, the issue of toxicity is controvertible. For the purpose of medicinal applications *e.g.* caged kinase inhibitors for cancer treatment, toxicity of the photoactivation byproduct might be beneficial in terms of a synergistic effect together with the active drug, since a photoactivation upon irradiation ideally occurs exclusively at the treatment site. Caged compounds for medicinal use are termed as photoactivatable prodrugs.

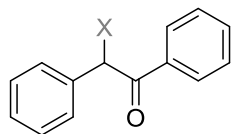
### 1.3 Photoremovable protecting groups

The selection of an adequate PPG is vital to benefit from the particular advantages of the caging concept. The requirements for a suitable PPG in medicinal chemistry approaches are manifold. The synthetic introduction has to be simple and should not impair pharmacokinetic parameters such as solubility. The caged compound should be stable in solution as well as under physiological conditions and low toxicity of the cleaved protecting group is favored. Additionally, high light absorption at the irradiation wavelength is essential for an efficient photoactivation.<sup>8,28</sup>

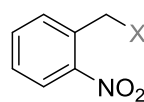
This photoactivation does not only depend on excitation, but rather on the percentage of the excited molecules that actually undergo photocleavage.<sup>8</sup> The *quantum yield*  $\Phi_{\text{rel}}$  describes the ratio between the effectively cleaved compound and the photons absorbed, as an important measure for the efficacy of a PPG.<sup>28</sup> A remarkable research effort has been devoted to the development and applications of UV-light-absorbing PPGs, such as *o*-nitrobenzyl<sup>29</sup>, benzoinyl (desyl)<sup>30</sup> and coumarinyl moieties (Figure 2).<sup>31</sup> *o*-Nitrobenzyl derivatives were introduced among the first PPGs and are still most widely used due to their robust and well understood photochemistry.<sup>32</sup> The most prominent member of this group of PPGs is the 4,5-dimethoxy-2-nitrobenzyl protecting group (DMNB, **4**) with an excitation wavelength of 365 nm for photocleavage.<sup>28</sup> For most parts of the present work the DMNB protecting group was utilized.

**Arylcarbonylmethyl groups**

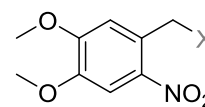
**1**  
phenacyl



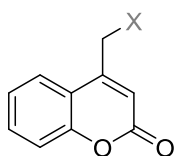
**2**  
benzoin

**Nitroaryl groups**

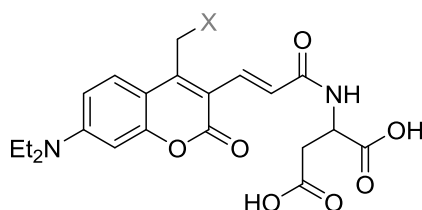
**3**  
o-nitrobenzyl



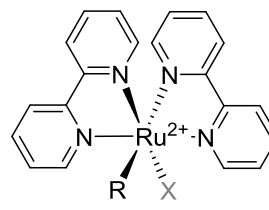
**4**  
4,5-dimethoxy-2-nitrobenzyl  
= DMNB

**Coumarin-4-ylmethyl groups**

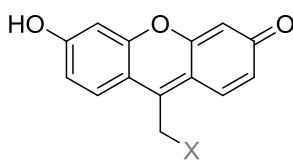
**5**  
coumarin-4-ylmethyl



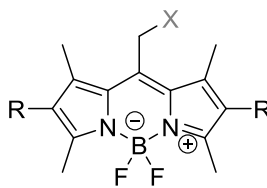
**6**  
diethylaminocoumarin analogues  
= DEAC

**Metal-containing groups**

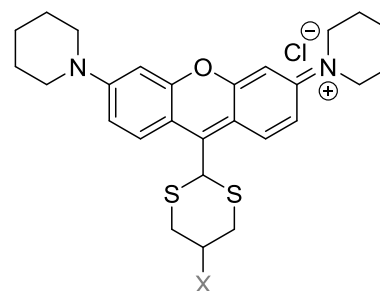
**7**  
organometallic ruthenium complex

**Miscellaneous groups**

**8**  
xanthene analogues



**9**  
*meso*-methyl boron-dipyrromethene analogues  
= BODIPY



**10**  
pyronin analogues

**Figure 2: Overview of different PPG classes.**<sup>17,28,33-36</sup> "X" represents the compound released upon irradiation.

The mechanism of photoactivation of *o*-nitrobenzyl caged compounds has been studied intensively.<sup>28</sup> It includes the formation of an *aci*-nitro derivative (**12**), followed by an irreversible cyclization (**13**) and rate-determining ring-opening (**14**). In the final step the leaving group is released as an anion leaving the cleaved protecting group as *o*-nitroso aldehyde (**15**, Figure 3).<sup>28</sup> Early reports show, that the efficacy of this photoactivation is depended on the solvent, pH and substitution of the *o*-nitrobenzyl ring. Recent studies gave guidance that the leaving group X is of similar importance.<sup>37</sup> In the context of photoactivatable prodrugs, the selection of the leaving group, in this study an inhibitor, might be essential for success.

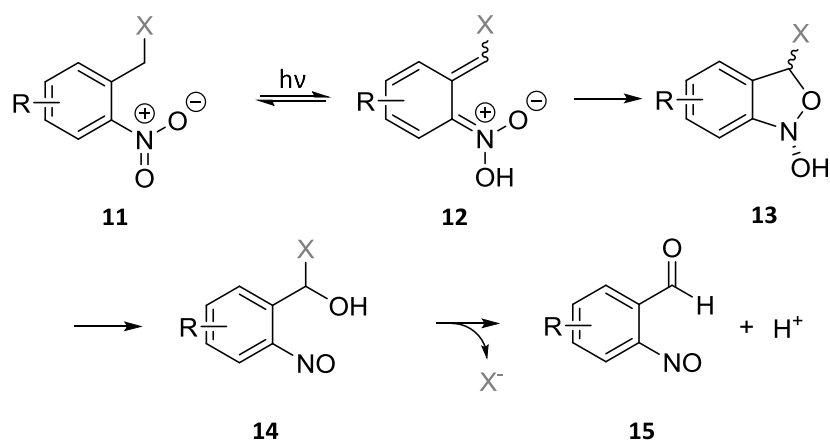


Figure 3: Mechanism of photoreaction of *o*-nitrobenzyl caged compounds.<sup>28</sup>

## 1.4 Strategies to overcome the limiting penetration depth of light into biological tissues

As a matter of course, a photoactivation can only occur if enough light of the respective wavelength reaches the photosensitive target molecule, in this case the photoremovable protecting group of the caged inhibitor. Hence, to utilize the caging concept for translational medicinal applications in particular, the most crucial selection criterion is the wavelength required for photoactivation. Most treatment sites of highly potent drugs (e.g. tumors) lie in deeper, vascularised tissues. The penetration depth of light into these tissues is strongly dependent on the wavelength (Figure 4). Below 600 nm the penetration depth is only a few millimeters deep, below 500 nm even less than a millimeter. The key players for light absorption in biological tissues are melanin, hemoglobin and water. Between 650 and 900 nm the light

absorption of hemoglobin and water is low, which results in decent tissue penetration. Biological tissues are considered optically transparent within this range which is referred to as the bio-optical window.<sup>38,39</sup> Limited penetration into tissue, restricts studies utilizing UV light to superficial tissues *in vivo* as well as *in vitro*.<sup>40</sup> Furthermore, UV-light with wavelength shorter than 300 nm can cause unwanted tissue damage.<sup>28,41</sup>

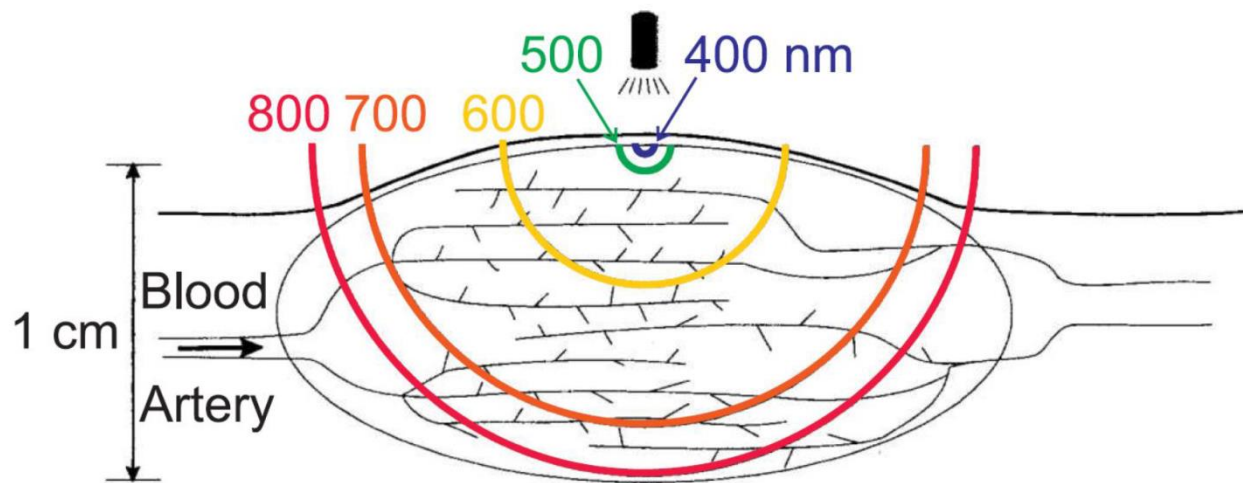


Figure 4: The penetration depth of light into biological tissues.<sup>39,42,43</sup>

Since it is not possible to change the penetration depth of light, scientist developed different strategies to overcome this restriction. Significant progress has been made in the field of light sources and fiber optics together with microendoscopic technology. Laser light of any wavelength can be focused into thin optical fibers with high intensity for light delivery into difficult to access treatment sites such as pancreatic, head or neck tumors.<sup>44</sup> However, the necessity of surgical intervention to facilitate optical fibers goes hand in hand with tissue damage.<sup>45</sup> Another exciting strategy to overcome the limiting tissue penetration of light is the two-photon excitation. Simultaneous absorption of two photons of approximately twice the wavelength (half the energy) by the same molecule results in excitation. Two-photon excitation is a true nonlinear optical effect, which only happens at high light intensities with poor efficacy.<sup>8</sup> The advantage of doubling the irradiation wavelength is offset by following key limitation: PPGs suitable for a two-photon uncaging are generally very large and inefficient, which renders them inappropriate for medicinal applications so far.<sup>46</sup>

By reason of an inefficient two photon excitation, PPGs absorbing light within the bio-optical window are highly desired for biological and medicinal applications.<sup>17</sup>

### 1.4.1 Visible light absorbing PPGs

Visible light absorbing PPGs have been reported only recently.<sup>17</sup> In 2007 the first introduced PPG activated by visible light was based on a ruthenium complex absorbing blue light around 447 nm.<sup>35</sup> In 2012 the groups of Klan and Wirz managed a green shift by reporting of PPGs incorporating xanthene and pyronin chromophores with absorption maxima around 550 nm.<sup>33,34</sup> At the same time the workgroup of Ellis-Davies evolved a PPG (DEAC, **6**) with a strong absorption at 450 nm from the coumarin-4-ylmethyl moiety (**5**).<sup>36</sup> But in the recent years another potential candidate came into spotlight: the hemi-porphyrin like BODIPY core (**9**).

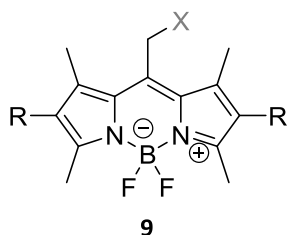


Figure 5: Chemical structure of the *meso*-BODIPY core.

BODIPY derivatives are widely used as probes<sup>47</sup>, laser dyes<sup>48,49</sup>, photosensitizers<sup>50</sup> and fluorescent tags<sup>51</sup>. This popularity results from their superior properties, such as stability in various media, sharp absorption peaks, low toxicity and high quantum yields.<sup>52</sup> In 2015 Winter *et al.* introduced the idea of utilizing BODIPYs as photoremovable protecting group.<sup>40</sup> Thereupon great interest has been aroused and different groups proved the applicability. The BODIPY core is easily accessible by organic synthesis. By substitution of the ring system, residue R particularly (Figure 5), the absorption maximum and the quantum yield can be altered dramatically.<sup>17</sup> Even near-infrared BODIPY dyes are available through ring substitution.<sup>53</sup> To further improve the efficacy of the photocleavage and the synthesis, the Feringa group showed that it is feasible to implement a carbamate linker in the *meso* position between the BODIPY core and the leaving group.<sup>52</sup> However, all these studies could not yet demonstrate the *in vivo* applicability. The full potential of BODIPY based PPGs might not be exploited so far.

## 1.4.2 Cherenkov radiation

Besides visible light absorbing PPGs, the idea of using Cherenkov radiation to approach photoactivatable prodrugs is more than exciting. If the required light for photoactivation is not able to penetrate to the place of destination, it might be an option to generate the irradiation in place.

In modern tumor therapy both radiopharmaceuticals and external beam radiotherapy play a vital role. Radiopharmaceuticals are radiolabeled molecules designed to deliver therapeutic doses of ionizing radiation to specific therapy sites in the body. In combination with sophisticated tumor targeting vectors (e.g. immuno-derived molecules or receptor-avid tracers) radiation is specifically delivered to tumor sites *in vivo*. Radionuclides that decay by  $\beta$ -particle emission are most extensively used.<sup>54</sup>  $\beta$ -decay comes along with emission of high energy electrons or positrons from the nucleus. These high energy particles interact with tissue and matter to consequently kill tumor cells. Energy of the emitted electrons or positrons by  $\beta$ -decay is not quantized, but a continuum of energies up to a maximum value.<sup>54</sup> Beyond a certain level of energy charged particles like electrons or positrons induce a secondary effect known as Cherenkov radiation. The phenomenon is commonly known as the blue luminescence in the cooling pool of a nuclear reactor (Figure 6).

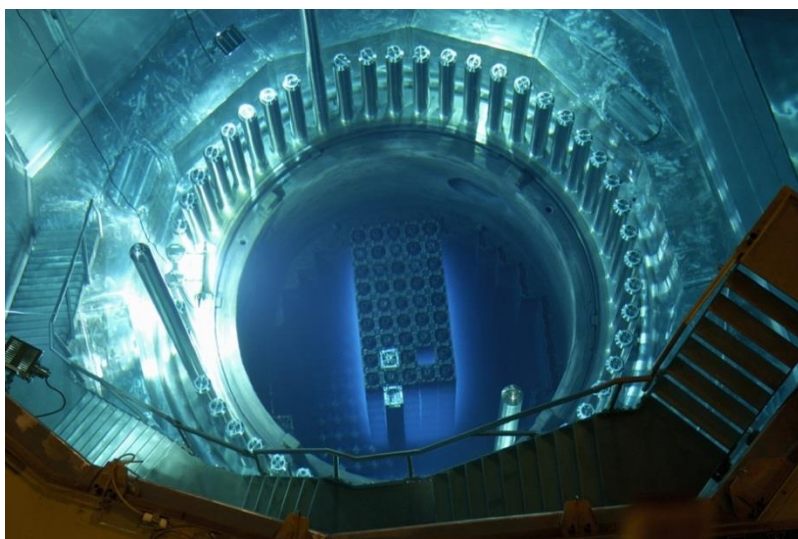
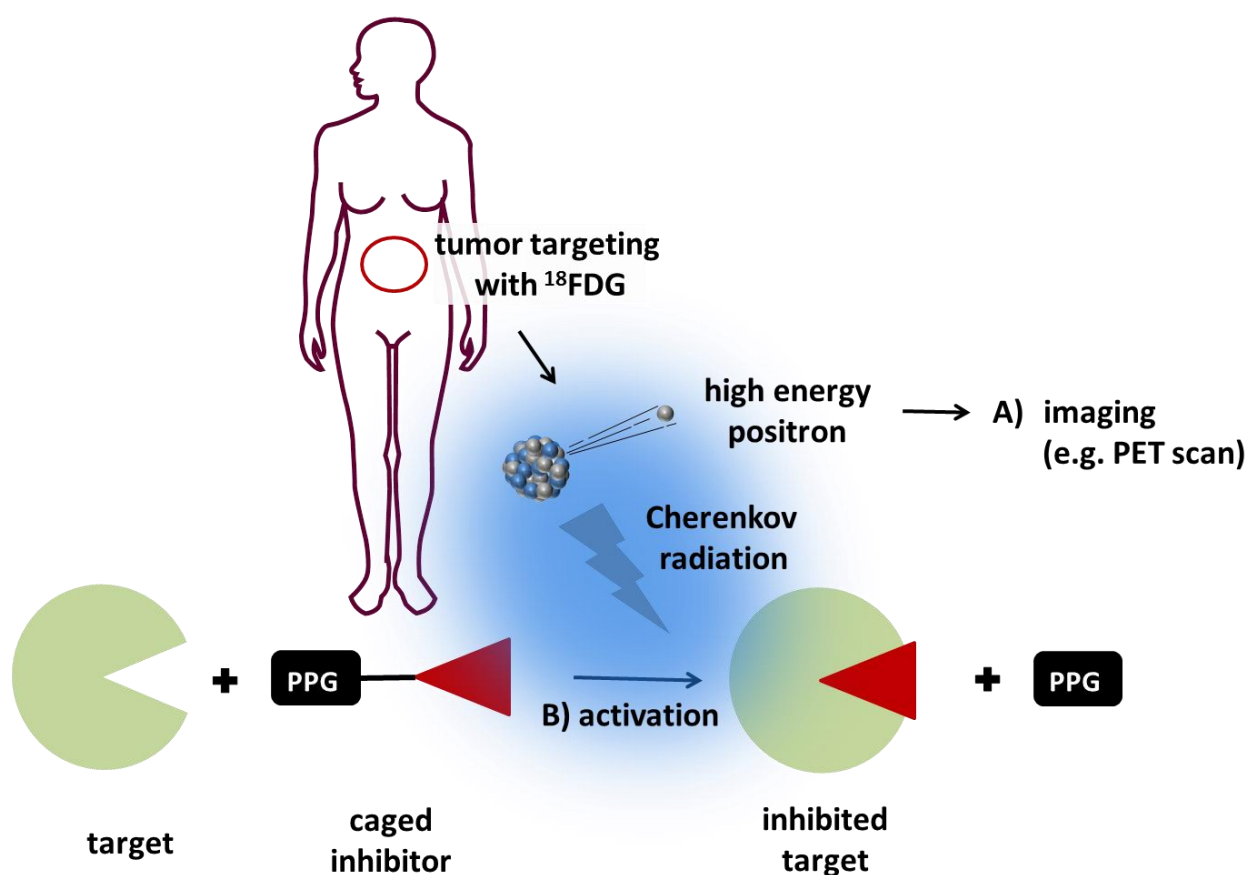


Figure 6: Cherenkov radiation in a cooling pool of a nuclear reactor core.<sup>55</sup>

Cherenkov radiation is induced when a charged particle moves faster than the speed of light in a dielectric medium (e.g. water).<sup>56</sup> The charged particle locally polarizes the medium and thereby excites the medium molecules. During return to the ground state, the energy is emitted as radiation.<sup>57</sup> The threshold condition for induction of Cherenkov radiation is not only dependent on the energy of the charged particles but also on the refractive index of the medium.<sup>57</sup> Cherenkov radiation is emitted as a continuous spectrum ranging from ultraviolet to visible light with its maximum intensity in the UV range, thus outside the bio-optical window.<sup>58</sup> Since its first observation by Pavel Cherenkov in 1937, Cherenkov radiation was mainly of academic interest to physicists for particle identification<sup>59</sup> or detection of high-energy gamma-rays.<sup>60,61</sup> However, a few years ago Cherenkov radiation became more and more important for optical *in vivo* imaging and as a readout method in biochemical assays.<sup>62–66</sup> Taking into account that most of the Cherenkov radiation is emitted as ultraviolet light, the idea of utilizing it for the activation of *o*-nitrobenzyl caged prodrugs is obvious.



**Figure 7: Schematic representation of utilizing Cherenkov radiation for activation of caged compounds.** Clinically used radiopharmaceuticals such as <sup>18</sup>Fluorodeoxyglucose (<sup>18</sup>FDG), a positron emitter, accumulates in the tumor (red circle) due to the high metabolic rates of tumor cells. The emitted positron is not only detected during a PET scan (A) but also induces blue Cherenkov radiation in the tumor cells. Subsequent, the Cherenkov radiation cleaves the PPG and activates the caged inhibitor (B). The inhibitor is able to bind to its target.



In 2012 Ran et al. gave evidence that Cherenkov radiation induced uncaging is feasible. Herein in a proof-of-concept study a caged derivative of luciferin was uncaged by  $^{18}\text{F}$ Fluorodeoxyglucose in a mouse breast cancer model.<sup>67</sup> However, up to date there are no photoactivatable prodrugs using Cherenkov radiation for photoactivation. The concept would offer some unparalleled advantages. Multiple radiopharmaceuticals are already approved for clinical use. Together with tumor targeting vectors a specific activation only in tumor sites could be achieved detached from the limited penetration depth of UV light. Unfortunately, the intensity of Cherenkov radiation is relatively weak.<sup>58</sup> The question if the intensity is sufficient to induce photoactivation of caged prodrugs remains to be answered. Since the intensity is dependent on the energy of the charged particle the intensity might be increased dramatically by the use of linear particle accelerators.<sup>56,57</sup> Linear particle accelerators are already used for external beam radiotherapy in clinic.<sup>54</sup> Earlier studies showed that accelerated high energy electrons can induce Cherenkov emission.<sup>56</sup> Importantly, particle beams from linear particle accelerators are able to reach deep tissues with high local resolution.<sup>68</sup>

Utilizing Cherenkov radiation either induced by therapeutic radiopharmaceuticals or external beam radiotherapy offers a great possibility to combine radiotherapy with targeted pharmacotherapy (e.g. kinase inhibitors or microtubule-targeting agents). A novel synergistic therapy strategy is conceivable.

## 1.5 Protein kinases and kinase inhibitors

Protein kinases are enzymes that catalyze specific protein phosphorylation. Thereby, a phosphate group from a phosphate donor, usually adenosine triphosphate (ATP), is transferred onto a substrate protein subsequently modulating its activity.<sup>69</sup> Modulating activity of proteins by phosphorylation is one of the major tools of signal transduction within a cell. Protein kinases play key regulatory roles in nearly every aspect of cell biology. Apoptosis, cell cycle progression, cytoskeletal rearrangement, differentiation, development and transcription are just some examples of transduction cascades regulated by kinases. Due to their physiological relevance, aberrant kinase function caused by mutation, chromosomal rearrangements or gene amplification is closely linked to a variety of pathophysiological events and diseases.<sup>70–72</sup> Especially cancer is highly related to kinase dysfunction. As a consequence protein kinases became one of the most important targets for drug development in the last two decades.<sup>73</sup>

The architecture of protein kinases consists of two subdomains: a N-terminal lobe with mainly  $\beta$ -sheets and a C-terminal lobe with  $\alpha$ -helices. The two lobes are connected by a cleft called hinge region (Figure 8). The hinge region represents the binding site of the essential phosphate donor ATP, which is targeted by the majority of small-molecule kinase inhibitors (smKI).<sup>69,71</sup>

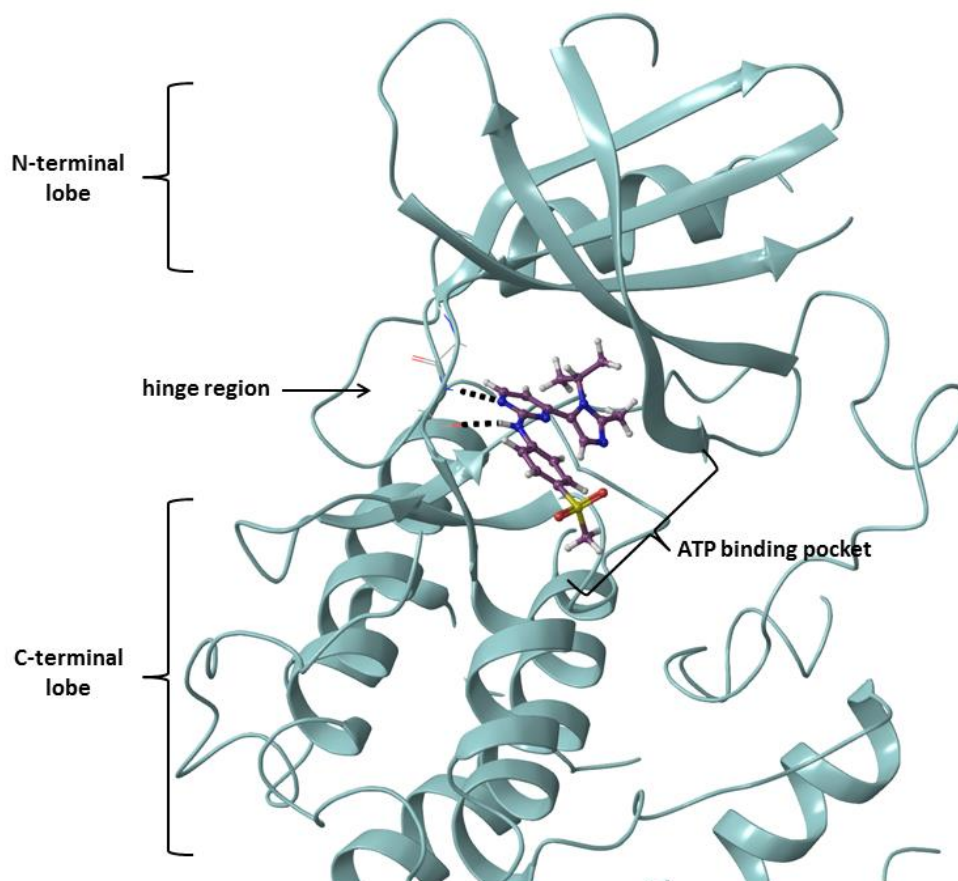


**Figure 8: General architecture of kinases.**<sup>74</sup> Exemplified on the structure of CDK2 (pdb 4FKO). The ATP binding pocket is occupied by AZD5438 (16).

Since the approval of the first small-molecule kinase inhibitor Imatinib (Gleevec®) in 2001, great effort in development of new smKIs for so called “targeted therapy” has been expended. Conventional chemotherapeutics affect all rapidly proliferating cells likewise. In contrast, kinase inhibitors target specific cellular transduction pathways. As of 2017 39 small-molecule kinase inhibitors have been approved for clinical use by the FDA mainly for oncological indications.<sup>75</sup> Despite this success some major restrictions have emerged. Due to the highly conserved ATP binding pocket selectivity towards a particular kinase remains difficult to achieve. Although therapy with kinase inhibitors is generally less toxic than conventional chemotherapy, kinase inhibitor can cause severe side effects. Non-selectivity with subsequent off-target effects might be one reason.<sup>71</sup> Another major drawback of kinase inhibitors are rapidly emerging resistances, limiting therapy prospects.<sup>76</sup>

The human genome encodes for 518 protein kinases, but only a small subset has been studied.<sup>77</sup> Thus, there is a need to develop tools and selective probes to uncover functions of the unknown kinases. Promising results are emerging for the inhibition of cyclin-dependent kinases (CDKs).<sup>78</sup> CDKs are enzymes whose activity depends on a regulatory subunit – a cyclin. Human cells exhibit not less than 20 different CDKs together with 29 cyclins.<sup>79</sup> Regarding their function within a cell, CDKs can be subdivided into two groups. The first group is involved in gene transcription. But more importantly the second group of CDKs are enzymes that drive the cell through every transition of cell cycle in mitosis and are therefore responsible for functional cell division.<sup>80</sup> Since cell cycle regulation is a highly sensitive process, aberrations of CDK activity is a common characteristic of cancer cells.<sup>81,82</sup> CDKs have been in focus for drug developers since the 1990s.<sup>83</sup> It took until 2015 before the first CDK inhibitor, Palbociclib, got approval for clinical use by the FDA. Up to date there are already three clinically approved CDK inhibitors available in the United States (Figure 9).<sup>84–86</sup>

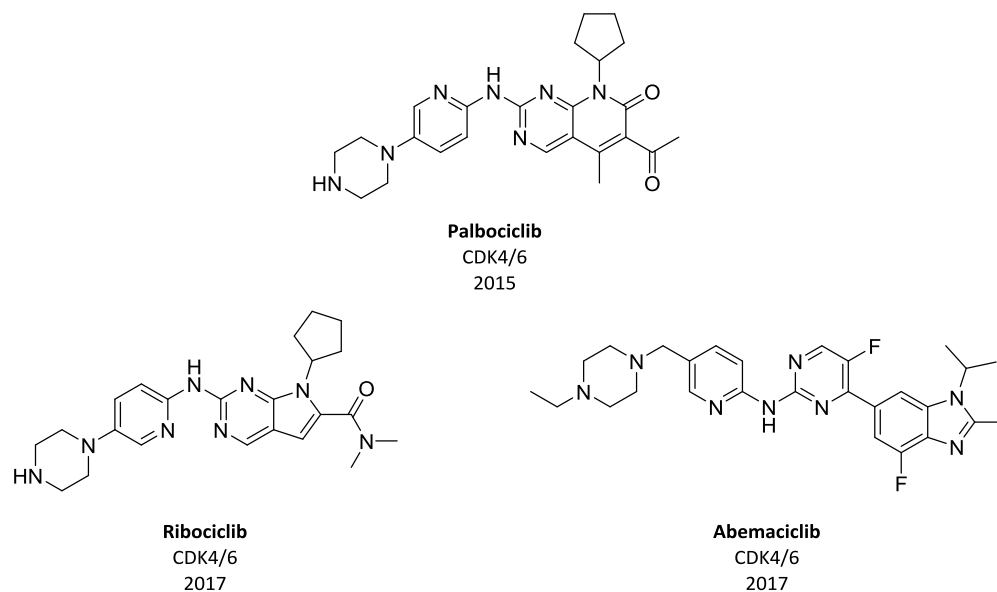


**Figure 9: FDA-approved CDK inhibitors until 2018.**<sup>84–86</sup> Both Palbociclib and Ribociclib got clinical approval by the European Medicines Agency (EMA) as well. Clinical approval of Abemaciclib by the EMA is still pending.<sup>87,88</sup>

However, a tremendous number of CDK inhibiting candidates entered clinical trials but failed mostly due to high toxicity. It appeared that there is a lack of therapeutic window.<sup>80</sup> This might be due to the fact that correct function of certain CDKs are critical for survival of healthy cells. So far most of the CDK inhibitors showed intrinsic inability to discriminate between cancerous and healthy tissues.<sup>80</sup>

To achieve this discrimination between therapy site and healthy tissue, innovational therapy strategies like activation by light, at therapy sites only, might be helpful. To examine this hypothesis we chose AZD5438 (**16**) as a model compound for potent CDK inhibition, but low tolerability in clinical studies.<sup>89,90</sup>

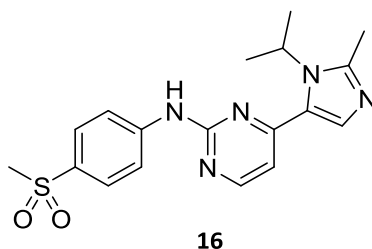


**Figure 10: Chemical structure of AZD5438.** AZD5438 as oral inhibitor of CDK 1,2 and 9 showed potent antitumor effects in human tumor xenografts. Due to a lack of tolerability the clinical development program was stopped.<sup>89</sup>

## 1.6 Microtubule-targeting agents (MTAs)

Microtubules are hollow tubes composed of polymerized  $\alpha$ - and  $\beta$ -tubulin. Microtubules represent one major component of the cytoskeleton of eukaryotic cells. They are critical in various cell processes, such as cell movement, intracellular transport and cell division.<sup>91</sup> The polymerization and depolymerization of  $\alpha$ - and  $\beta$ -tubulin is a highly dynamic process.<sup>92</sup> By rapid addition or removal of tubulin subunits at the end of microtubules, human cells are able to precisely regulate growth and shrinking of microtubules.<sup>93</sup> During mitosis microtubules are required to separate the chromosomes and partition them to each daughter cell.<sup>94</sup> To ensure flawless cell division, tightly regulated microtubule dynamics are crucial.

Compounds that interfere with microtubule dynamics disrupt the progression of the cell cycle during mitosis and subsequently provoke apoptosis. Therefore, microtubule-targeting agents are highly effective in killing rapidly dividing cells. Importantly, functioning microtubules are of vital significance also for non-mitotic cells.<sup>95</sup> This has made microtubules an attractive target for development of anticancer drugs.<sup>96</sup>

Microtubule-targeting agents (MTAs) disrupt microtubule dynamics and can broadly be classified into microtubule-stabilizing (such as Taxanes *e.g.* Paclitaxel) and microtubule-destabilizing (such as *Vinca* alkaloids *e.g.* Vincristine and Colchicine) agents.<sup>91</sup> As the vast majority are natural products isolated from bacteria, plants and marine sponges, MTAs are very often structurally diverse and complex molecules (Figure 11).<sup>97</sup>

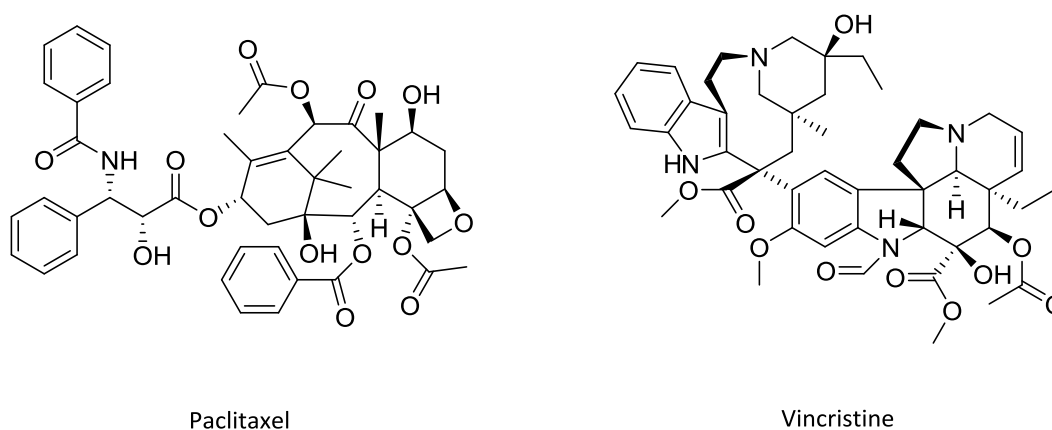


**Figure 11: Chemical structures of chosen MTAs.**

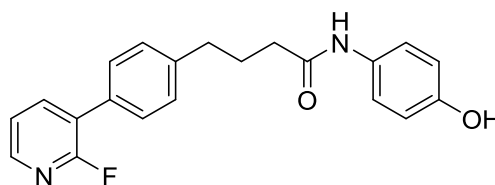
Left: Paclitaxel (Taxol<sup>®</sup>) stabilizes microtubules, protects it from disassembly and subsequently blocks the progression of mitosis. *Taxanes* are isolated from the Pacific yew *Taxus brevifolia*.<sup>98</sup>

Right: Vincristine (Oncovin<sup>®</sup>) as a microtubule-destabilizing agent inhibits the formation of the spindle apparatus during mitosis. *Vinca* alkaloids are isolated from the Madagascar periwinkle *Catharanthus roseus*.<sup>99</sup>

The binding modes of MTAs are diverse and complex. There are three major binding domains on microtubules identified: the taxane-binding domain on the inside surface of the microtubule tube, the colchicine-binding domain, where colchicine-tubulin complexes copolymerize into the microtubule lattice and finally the *Vinca*-binding domain at the very end of the microtubules. Furthermore *Vinca*-domain binders rapidly bind to soluble tubulin dimers, the building blocks for microtubule tubes, as well. Occupying any of these binding sites results in a disruption of microtubule dynamics.<sup>96,97</sup> Although the exact binding modes of most classical MTAs such as Paclitaxel is fully understood<sup>100</sup>, the binding mechanisms of some MTAs particularly novel small-molecule MTAs (smMTAs) remain unclear.

With the long history of clinical efficacy, MTAs remain to date the most classical yet reliable chemotherapeutics which are often integrated in combination chemotherapy regimens.<sup>97,101</sup> Microtubule-targeting *Vinca* alkaloids and *Taxanes* are frontline treatments for several tumors such as

breast, ovarian and non-small cell lung cancer as well as non-Hodgkin's lymphoma.<sup>102-106</sup> Despite this broad applicability, clinically approved MTAs are ineffective for treatment of brain tumors as their large molecular weight (> 800 g/mol) renders them unable to cross the blood-brain barrier.<sup>107</sup> Hence, there has been increasing research interest towards the development of effective MTA delivery methods and small-molecule microtubule-targeting agents able to cross the blood-brain barrier.<sup>108-110</sup> In 2015 the group of L. Munoz discovered compound **17** as a small-molecule inhibitor of tubulin polymerization and demonstrated its anticancer efficacy in patient-derived glioblastoma cells.<sup>101,104,111</sup>



**17**

**Figure 12: Small-molecule tubulin inhibitor as an attractive lead for development of potential chemotherapeutics for brain tumors.**

Cancer therapy with established MTAs has two major drawbacks. Unfortunately, resistance acquired during treatment is a common event and has plagued the overall success.<sup>112</sup> Since classical chemotherapeutics like MTAs attack all rapidly proliferating cells, regardless of whether being tumor or healthy cells, severe side effects such as neuropathy further restrict therapy.<sup>113,114</sup> Combination of a small-molecule microtubule targeting agent together with the advantages of the caging concept could not only make MTAs available for brain tumor therapy while also limit systemic side effects and resistances. At the same time, since knowledge about binding modes and the structure-activity relationships of small-molecule MTAs is little, photoactivatable small-molecule MTAs could serve as valuable tools to study their binding mechanisms and kinetics.

## 2 Aims and Objectives

---

The general aim of this work was the development of a photoactivatable CDK inhibitor as well as a photoactivatable small-molecule microtubule-targeting agent (MTA). By implementation of the caging concept, its unique features might be used to address two major issues both of smKIs and MTAs: systemic side effects and acquired resistances.<sup>115–120</sup> Based on an excellent active/inactive ratio, a rapid concentration jump of the active drug upon irradiation of only the cancer-afflicted tissues is possible.<sup>121</sup> As a consequence, cancer cells have to face abruptly high drug concentrations, compared to a slow increase of the drug concentration with oral administration. The intrinsic inability of smKIs and MTAs to discriminate between tumor and healthy cells, can be overcome by an external discrimination using light as a remote trigger to regulate the biological activity of the drugs. Systemic side effects might be minimized, which would enable higher local drug doses if required. Additionally to this novel therapeutic approach, photoactivatable inhibitors could serve as valuable tools to study biological processes *e.g.* kinetics and binding mechanisms.<sup>122–127</sup>

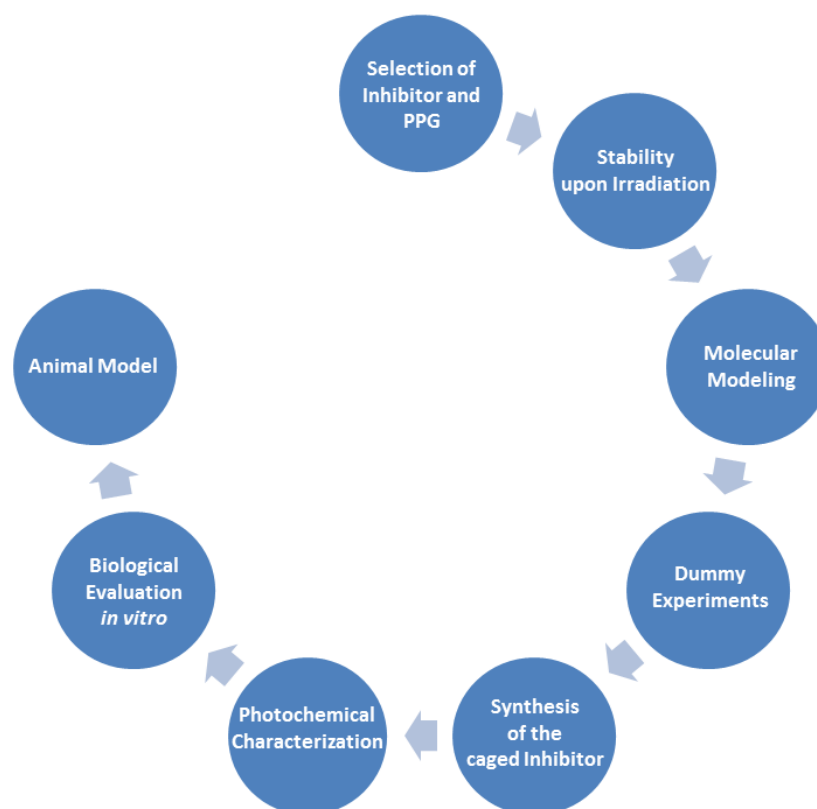


Figure 13: General workflow for the development of photoactivatable prodrugs.



## 2.1 Photoactivatable cyclin-dependent kinase inhibitor

The objective of this project included the design, synthesis, photochemical characterization and biological evaluation of a photoactivatable prodrug of a CDK inhibitor. The workflow (Figure 13) for the development of photoactivatable prodrugs was followed.

Starting point was the selection of the particular inhibitor on which the caging concept should be applied. AZD5438 (**16**) was the CDK inhibitor of choice and all further experiments within this project were dedicated to it (see chapter 1.5). Additionally, selection of the photoremovable protecting group was of similar importance (see chapter 1.3). To exploit the features of the caging concept, inhibitor stability upon irradiation with light of the respective wavelength needed for photoactivation is indispensable to preclude inhibitor degradation right after photoactivation. Subsequently, molecular modeling studies were to be performed to reveal the binding mode together with key interactions between the active inhibitor and the kinase. Regarding a high active/inactive ratio it was considered to be essential to block these key interactions by attachment of the PPG to the pharmacophore. In order to save some valuable inhibitor material prior to the actual usage of AZD5438 (**16**), dummy experiments were to be carried out. Therefore, the pharmacophore of the inhibitor had to be synthesized (Figure 14) and subsequently caged with the PPG by the intension of optimizing reaction conditions.

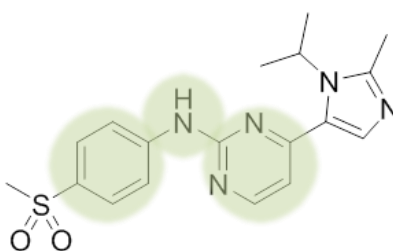


**Figure 14:** Chemical structure of AZD5438 (**16**). The pharmacophore is highlighted in grey.

By the time an efficient way to cage the pharmacophore with the chosen PPG was found, synthesis of the actual caged inhibitor had to be performed. Having the caged inhibitor in hand, the photochemical characterization should be one of the central parts of this work. It should include the identification of the ideal irradiation wavelength for photoactivation with subsequent studies of the efficacy of the photoactivation. In order to function as a valuable probe for biological applications, a quick and efficient

photoactivation *in vitro* is desperately needed, since cell viability should not be impaired by the irradiation. Therefore, photoactivation experiments had to be designed as close to the *in vitro* conditions as possible.

The following biological evaluation had to address two major objectives. First of all, it had to be shown whether the biological activity could have been diminished by attachment of the PPG. In order to tackle the problems of side effects and resistances or to serve as a tool compound, biological inactivity of the caged prodrug is crucial for success. Secondly, the local and temporal restoration of biological activity upon irradiation had to be demonstrated *in vitro*. Biological inactivity of the prodrug as well as its restoration upon irradiation are of major significance for the proof of concept. Both kinase assays and cell viability assays were to be utilized to examine the biological activity of the prodrug as well as the subsequent photoactivation. Furthermore, the impact of the applied light on cell viability had to be evaluated. Since the photoactivation is accompanied by the formation of a byproduct a possible cell toxicity of the cleaved protecting group had to be investigated.

To determine whether a photoactivatable compound is valuable for biological applications or as a tool compound, the reaction rate of the photoactivation is a critical attribute. Obviously the PPG plays the key role, but recent reports show that the leaving group, in this study the inhibitor, effects the rate of photoactivation as well.<sup>37</sup> To elucidate this issue, several analogues of the pharmacophoric scaffold with different substituents in position R (Figure 15) had to be synthesized and caged with the PPG following the objective of studying the influence of the electronic and mesomeric effects of the substituent R on the rate of photoactivation.

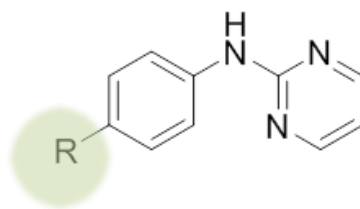


**Figure 15: Chemical structure of the pharmacophoric scaffold of AZD5438 (16).**

Residue R (highlighted in grey) was to be modified to study the influence of the electronic and mesomeric effects of R on the reaction rate of the photoactivation.

Although extensive effort has been devoted to the development of visible light absorbing PPGs and a couple of promising candidates were introduced, the vast majority of the photoactivatable prodrugs for biological applications known today utilize near UV light absorbing PPGs.<sup>125</sup> In the course of this project two promising strategies to overcome the limited penetration depth of UV light were to be further investigated. On the one hand, the applicability of a visible light absorbing PPG, namely BODIPY (**9**), towards the chosen CDK inhibitor was to be examined. Therefore, a strategy to synthesize the PPG as a precursor which can serve as a universal coupling reactant together with the actual synthetic attachment of the PPG to the inhibitor had to be found. Again, dummy experiments utilizing the pharmacophore of the inhibitor seemed to be useful prior synthesis of the BODIPY caged prodrug of inhibitor **16**. Subsequent photochemical characterization should examine whether a fast and clean photoactivation with visible light is feasible. To be useful for biological applications a quantitative photoactivation by irradiation has to occur within a short period in which the cell viability is not impaired. Hence, impact of irradiation of the respective wavelength on the cell viability had to be investigated, further referred to as light titration experiments. Photoactivation experiments together with light titration experiments should answer the question of the BODIPY group's utility for biological applications.

On the other hand, the possibility of utilizing beta radiation respectively thereupon induced Cherenkov radiation for a photoactivation was to be investigated. Two strategies had to be followed. Firstly, the ability of  $\beta$ -emitting radionuclides to activate a photoactivatable prodrug in solution should be determined. In a second setup, particle beams of a linear particle accelerator were to be used to induce Cherenkov radiation in solution in the interest of investigating a potential subsequent photoactivation. For both reasons a cooperation with the clinic for nuclear medicine and radio pharmacy at the university hospital (UKSH) in Kiel, Germany, has been established.

## 2.2 Photoactivatable small-molecule microtubule-targeting agent

The objectives of this project compromised the design, synthesis, photochemical and biological evaluation of a photoactivatable small-molecule MTA. The general workflow (Figure 13) had to be followed with few exceptions. The binding modes of MTAs are complex since there is no tight and distinct binding pocket compared to the ATP binding pocket of kinases.<sup>96,97</sup> Also, the microtubule polymerization and depolymerization is a highly dynamic process thus molecular modeling studies struggle to predict a reliable binding mode for small-molecule MTAs. Since the pharmacophore of the chosen small-molecule MTA is unknown, structure activity data had to be used to reveal a favorable position to attach the PPG. Nonetheless, whether the biological activity could had been significantly diminished by introduction of the PPG had to be examined. Therefore, cell viability assays, tubulin polymerization assays, colchicine binding assays, immunofluorescence imaging and apoptosis assays had to be performed to not only demonstrate a potential inactivation due to the caging, but also the restoration of biological activity upon irradiation *in vitro*. A cooperation with the workgroup of Lenka Munoz from the school of medical science, University of Sydney has been established to perform all experiments of the biological evaluation at the University of Sydney.

## 3 Results and Discussion

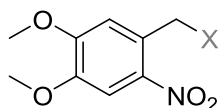
---

### 3.1 Photoactivatable small-molecule microtubule-targeting agent

#### 3.1.1 Selection of inhibitor and PPG

In 2015 the workgroup of L. Munoz discovered compound **17** as a potent inhibitor of microtubule polymerization (Figure 12). Consequently, effective antimitotic and apoptotic activity was demonstrated *in vitro* on established glioblastoma cell lines as well as on patient-derived primary glioblastoma cells.<sup>104,111</sup> Cytotoxic activity together with its low molecular weight (349 g/mol) renders **17** an attractive lead for the development of potential agents against brain tumors. Hence, we chose compound **17** for the development of a photoactivatable small-molecule MTA (smMTA) – a novel concept in the field of smMTAs.

Due to its well understood photochemistry, a rapid photocleavage upon irradiation with UV light and the simple chemical accessibility, the 4,5-dimethoxy-2-nitrobenzyl protecting group (DMNB, Figure 16) was the PPG of choice for this proof of concept study.<sup>28</sup>



**4**

4,5-dimethoxy-2-nitrobenzyl  
= DMNB

**Figure 16: Chemical structure of the DMNB protecting group.** X represents the leaving group.

### 3.1.2 Stability upon irradiation

Inhibitor stability upon irradiation of light with the wavelength required for photoactivation is an essential prerequisite of the caging concept. Otherwise, the active inhibitor might degrade during or right after the photoactivation. Therefore, UV stability of **17** was examined by irradiation of a 1 mM compound solution in DMSO with UV light of 365 nm. The content determination was carried out by HPLC analysis. Under this conditions the compound appeared to be stable for up to 20 min of irradiation.

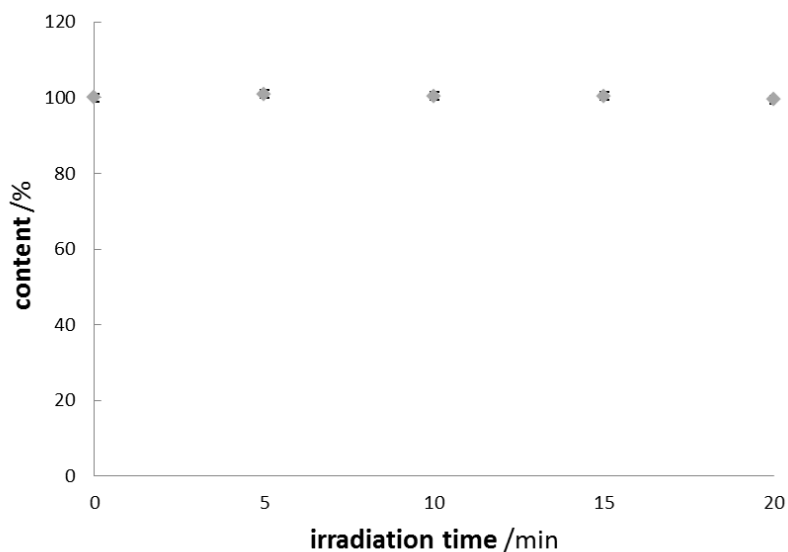


**Figure 17: UV stability of smMTA 17.** The compound solution (1mM) in DMSO was irradiated at 365 nm (5.4 W) and subsequently analyzed by HPLC. Each value is a mean  $\pm$  SD of two independent experiments.

### 3.1.3 Synthesis

Since chosen smMTA **17** is commercially not available, it had to be synthesized. Hence, the four step synthesis route discovered by the Munoz group was followed (Figure 18).<sup>104</sup> Starting from bromobenzene, the first step represents a Friedel-Crafts acylation with succinic anhydride to yield a 4-oxo-4-phenylbutanoic acid derivative. The resulting ketone function of the oxobutanoic acid derivative was subsequently reduced in terms of a Clemmensen reduction by the use of amalgamated zinc. Next, the carboxylic acid was converted to an amide by peptide coupling with 4-aminophenol utilizing PyBOP as the coupling reagent. In the last step a Suzuki coupling with an aryl boronic acid using microwave-assisted organic synthesis was carried out to substitute the bromine by a fluoropyridine to gain the desired inhibitor **17** in decent yields.

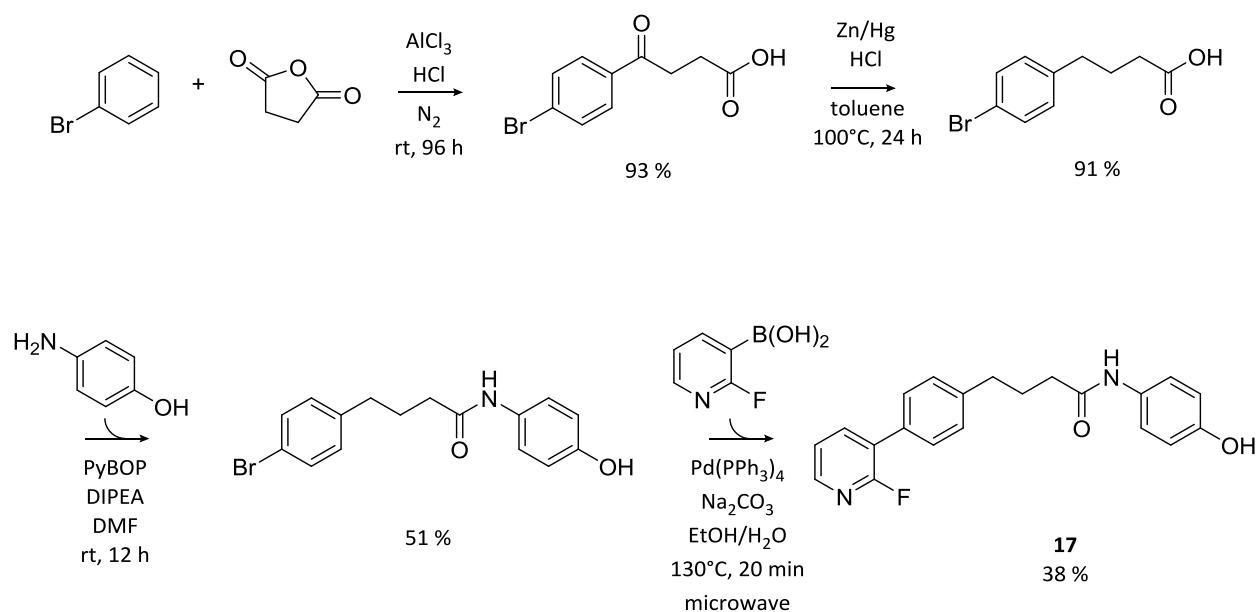


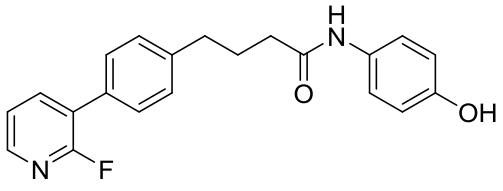
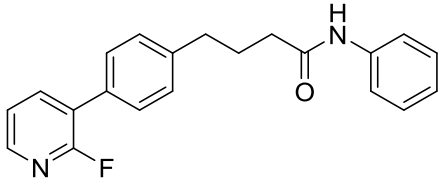
Figure 18: Synthesis of smMTA **17** according to literature<sup>104</sup>.

Having the inhibitor in hand, the decision where to attach the PPG had to be made. Since molecular modeling studies appeared to be unfavorable to identify the pharmacophore, information from former structure-activity relationship studies had to be used. Data from cell viability assays using the U87 and U251 glioblastoma cell lines indicate the phenolic moiety as important for biological activity. By removal of the phenolic moiety the  $\text{EC}_{50}$  values increase by factor 16 respectively 12 (Table 1).<sup>104,111</sup> Furthermore

the phenolic moiety appeared to be easily chemical accessible for caging due to its terminal position in the molecule as well as the decent phenolic reactivity. By this reasons the phenolic moiety was considered to be most appropriate for caging.

**Table 1: Cellular efficacy on the glioblastoma cells U87 and U251 of smMTA **17** and its dehydroxylated derivate **18**.**

Cellular efficacy ( $EC_{50}$ ) was determined after 72 h of drug treatment. Data represents mean  $\pm$  SEM from three independent experiments performed in triplicate.<sup>104</sup>

Compound	Chemical Structure	U87 ( $EC_{50}$ , $\mu$ M)	U251 ( $EC_{50}$ , $\mu$ M)
<b>17</b>		$0.4 \pm 0.1$	$0.4 \pm 0.1$
<b>18</b>		$6.6 \pm 0.9$	$4.6 \pm 0.4$

The caging of inhibitor **17** was accomplished by the use of DMNB-Br (**19**). In terms of a nucleophilic substitution the benzylic bromine of **19** was replaced by the inhibitor using potassium carbonate as a base with a yield of 60% (Figure 19). The main reason for a decreased yield was an elaborate purification. In order to eliminate residual educt **17** thoroughly from the product, two sequential flash chromatography columns were necessary. Since the caged prodrug **20** is photoactivatable by UV light, avoidance of extensive light exposure during all steps of synthesis and purification was of great importance. Minor impurities with the active inhibitor might result in remnant biological activity. This issue is particularly relevant for the handling of the caged prodrug during *in vitro* testing as a full avoidance of light exposure is hardly manageable. In order to detect whether an unwanted photoactivation during *in vitro* testing is relevant, derivative **21** was synthesized. Due to the lack of the *o*-nitro group compound **21** is not photoactivatable (Supplementary Figure 1) but should exhibit similar biological activity since interactions of the phenolic moiety with the target is disrupted in similar manners as by the caged prodrug **20**.



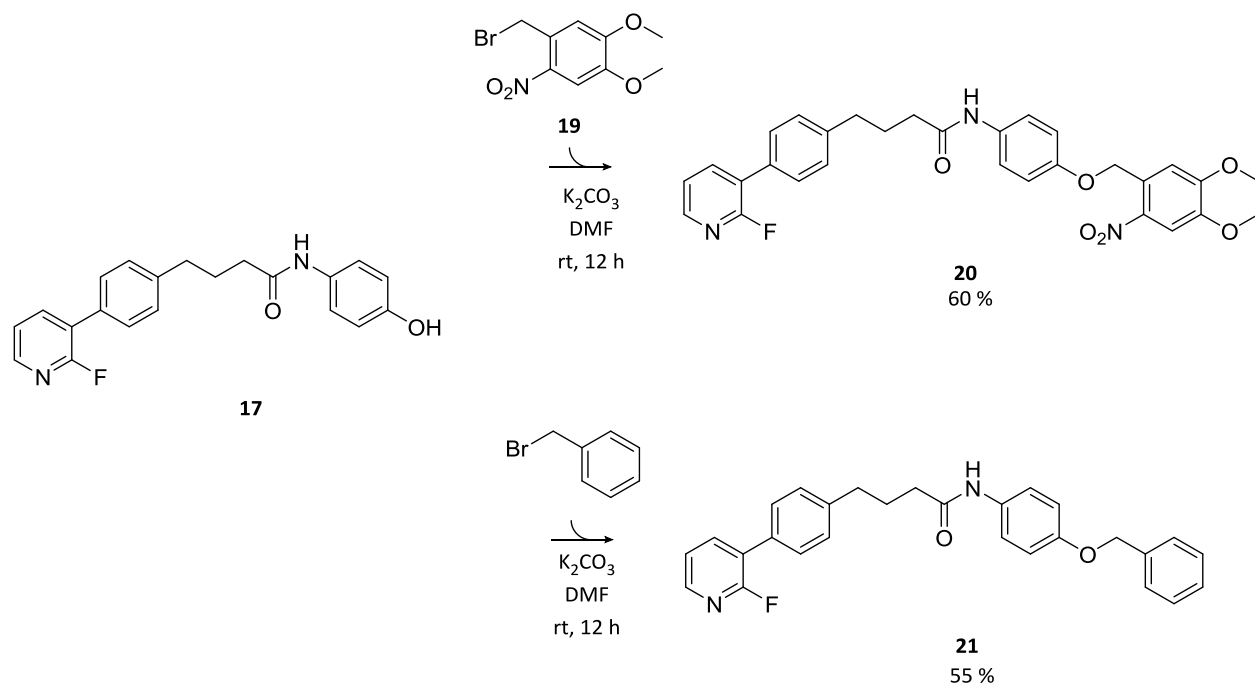


**Figure 19: Synthesis of the caged prodrug 20 from smMTA 17 (top).** Derivative **21** was synthesized under the same reaction conditions from smMTA **17** using (bromomethyl)benzene (bottom).

### 3.1.4 Photochemical characterization

In order to evaluate the photochemical characteristics of the caged prodrug **20**, UV/Vis absorption spectra of the unprotected inhibitor as well as the caged prodrug were recorded. The optimal irradiation wavelength is characterized by a high light absorption of the caged prodrug while the uncaged inhibitor should not absorb light of the respective wavelength at all by the reason of inhibitor stability as well as non-interference with the photoreaction. The unprotected smMTA **17** shows no light absorption above 320 nm whereas the caged prodrug exhibits a broad absorption band around 360 nm (Figure 20). This result is in good agreement with the generally described wavelength for photocleavage of the DMNB protecting group.<sup>28</sup> By the intention of utilizing the caged prodrug for biological applications, tissue damage of shortwave UV irradiation below 300 nm has to be minded. Hence, a wavelength of 365 nm was considered to be optimal. Due to the high intensity and easy handling of LEDs, custom made LED lamps with a emission wavelength of 365 nm were utilized for all further photochemical characterization as well as for the biological evaluation.

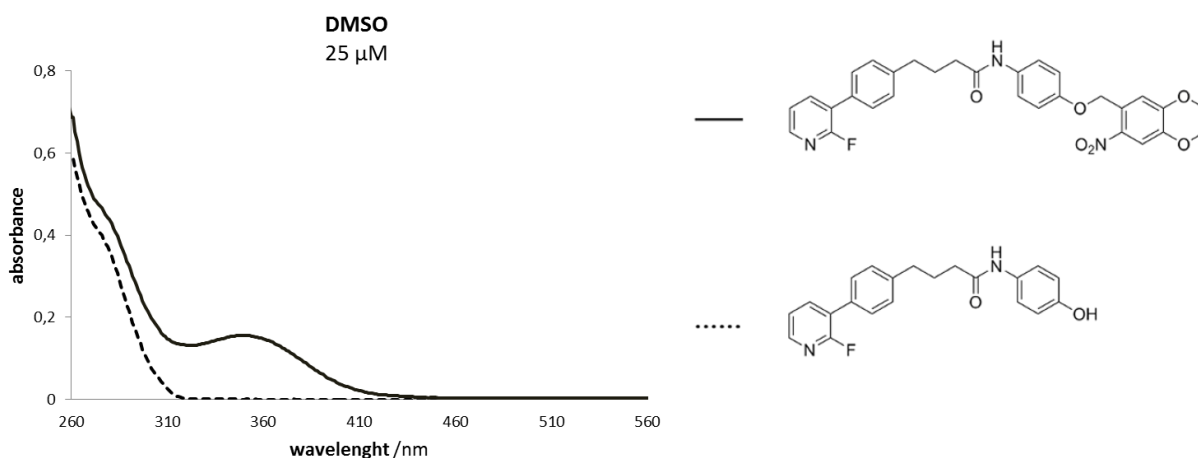


**Figure 20:** UV/Vis absorption spectra of smMTA **17** and its DMNB caged prodrug **20**. UV/Vis absorption spectra of caged prodrug (solid line) in comparison with the unprotected inhibitor (dashed line) in DMSO at a concentration of 25  $\mu$ M.

Having identified the optimal wavelength for irradiation, the next step represents the photoactivation experiment in order to investigate whether it is possible to cleave the PPG upon irradiation thus reactivating the prodrug **20**. Specifically, the kinetics of the photoactivation reaction were quantified. A compound solution of 1 mM in DMSO was irradiated by a LED reactor with an emission maximum at 365 nm (5.4 W) for 10 min (Figure 21). Samples were taken at indicated time points and quantified by HPLC analysis. Within less than 1 min half of the photoactivatable prodrug could have been cleaved under these conditions. After 2 min of irradiation, 100% of the photoactivatable prodrug has been converted, resulting in a full release of the active smMTA. In conclusion the phenolic moiety of smMTA **17** proved to be suitable for caging with a subsequent rapid and quantitative photoactivation.

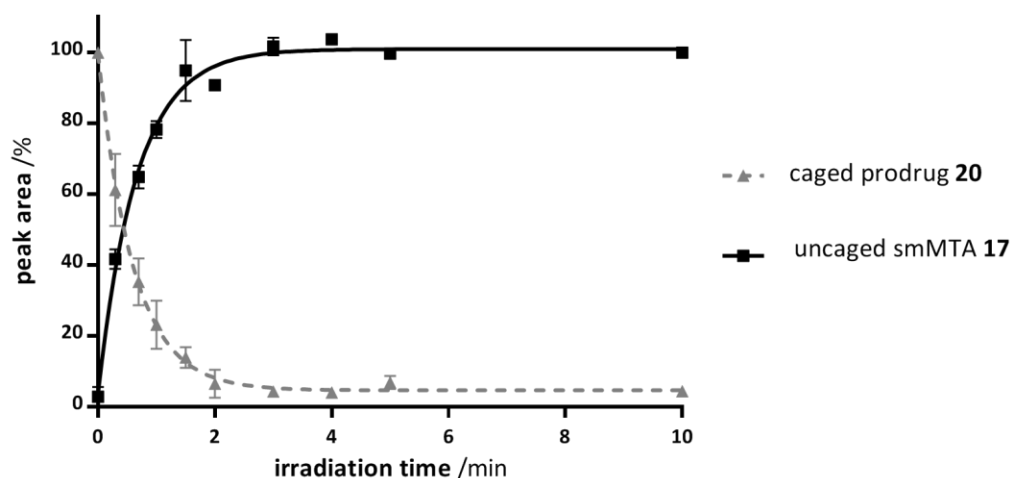


**Figure 21: Photoactivation of the photoactivatable prodrug **20** at a concentration of 1 mM in DMSO.** The compound solution was irradiated at 365 nm with 5.4 W for 10 min. After indicated time points samples were taken and analyzed by HPLC ( $n = 2$ ). The amount of the caged prodrug **20** (squares) is plotted against the released inhibitor **17** (triangles). Each value is a mean  $\pm$  SD of two independent experiments.

### 3.1.5 Biological evaluation

Having demonstrated a rapid and quantitative photoactivation under experimental conditions, the question of utility in biological systems remains to be answered. In order to evaluate whether photoactivation occurs under biological conditions too, biological activity was measured with and without irradiation utilizing several biological assays. All of these should address two major issues: biological inactivity of the caged prodrug **20** as well as the restoration of biological activity upon UV irradiation.

### Tubulin polymerization assay

First of all, the ability of **20** to inhibit the assembly of  $\beta$ -tubulin to microtubules was evaluated by performance of a tubulin polymerization assay (Figure 22). Within this assay Paclitaxel as the most prominent member of microtubule-stabilizing agents, Vinblastine a microtubule-destabilizing agent as well as DMSO were used as controls to ensure correct assay function. In agreement with their generally valid mechanism of action, Paclitaxel increased tubulin polymerization compared to the DMSO control whereas Vinblastine inhibited tubulin polymerization. Incubation with the caged prodrug **20** showed a negligible effect on tubulin polymerization. Upon irradiation, the cleaved prodrug decreases tubulin polymerization to a similar effect as smMTA **17**. Since inhibition of tubulin polymerization of smMTA **17** and its caged prodrug **20** irradiated with UV light was indistinguishable, the photoactivation within this assay worked perfectly. Furthermore, biological efficacy to inhibit tubulin polymerization could be significantly diminished by the caging with the PPG.

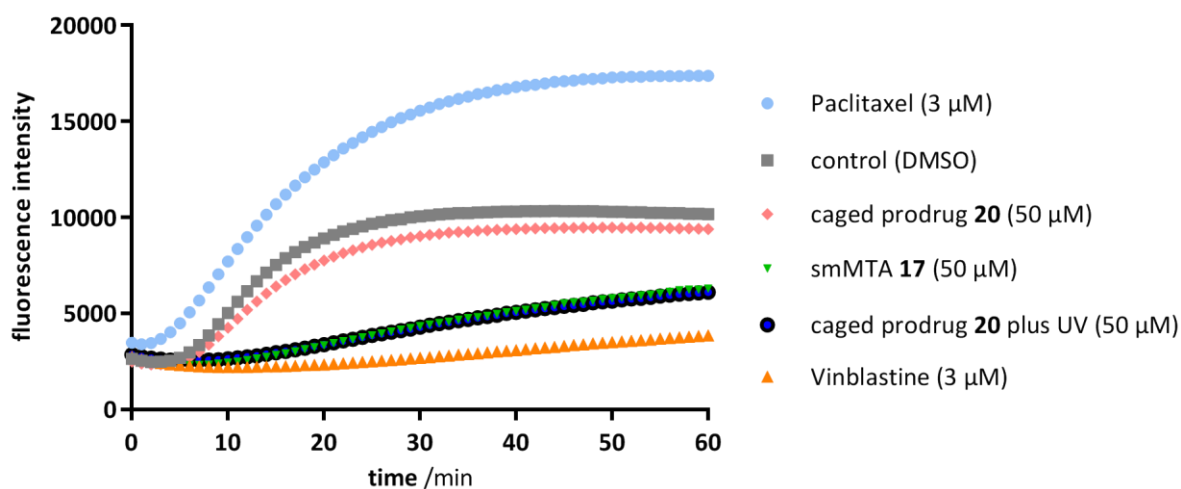


**Figure 22: Tubulin polymerization assay.** Purified porcine brain tubulin was incubated with paclitaxel, vinblastine, DMSO, smMTA **17** and caged prodrug **20**  $\pm$  UV irradiation (365 nm, 1.8 W, 5 min). The assembly of microtubules was monitored by an increase in fluorescence. The data represents the mean from three independent experiments. Each data point was performed in triplicate.

## Cell viability assays

In order to further validate the observed effects, cell viability assays with U251 and patient-derived RN1 glioblastoma cells were performed. Impairment of the irradiation on cell viability is a knock-out criterion in order to utilize caged prodrugs for biological applications. Hence, U251 and RN1 cells were treated with UV light (365 nm, 1.8 W) solely in order to determine tolerable levels of UV light exposure. U251 cells tolerated up to 60 s of irradiation without any implication (Supplementary Figure 2). In contrast, patient-derived RN1 cells tolerated only 30 s of irradiation which might be due to the characteristics of primary cancer cells. Primary cancer cells, such as patient-derived RN1 glioblastoma cells, are cultured as stem cells under specifically defined, *in vivo* simulating conditions in order to maintain both phenotype and genotype of the primary resected tumor.<sup>101,128</sup> Viability of primary tumor cells is strongly related to these defined conditions making them presumably less resistant to external impacts such as irradiation by light.<sup>128-132</sup>

Subsequently, cell viability was assessed by treatment of both cell lines with smMTA **17** and its caged prodrug **20** for 48 h respectively 72 h for RN1 cells (Figure 23). Without UV irradiation smMTA **17** showed an EC<sub>50</sub> of 1.3 μM on U251 cells respectively 0.2 μM on RN1 cells, which corresponds with previously published data.<sup>104,111</sup> Addition of the bulky PPG decreased cytotoxicity dramatically. Caged prodrug **20** exhibited no significant cytotoxicity up to high micromolar concentrations, resulting in an increase of the EC<sub>50</sub> by factor 55 respectively factor 185 (EC<sub>50</sub> = 72 μM, EC<sub>50</sub> = 37 μM for U251 and RN1 cells, respectively). The marginal residual cytotoxic activity of the caged prodrug could be due to several reasons. Minor impurities of the active smMTA originating from synthesis could have stayed undetected by the test of purity prior biological testing due to detection limits of the HPLC analysis. Off-target effects of the caged prodrug could furthermore contribute to cellular toxicity. More importantly, the binding mode of smMTA **17** is unknown. Although structure-activity relationship studies identified the terminal phenolic moiety as relevant for biological activity, the question whether a DMNB caged prodrug is still able to bind to its binding site remains uncertain, especially since microtubule binding sites lie on the surface of the protein. Hence, it is conceivable that the DMNB caged prodrug **20** still possesses a certain binding affinity to microtubules resulting in marginal residual biological activity.

Since remaining biological activity of the caged prodrug **20** was assessed, photoactivation *in vitro* had to be investigated next. Additionally to compound treatment, U251 and RN1 cells were irradiated for 60 s respectively 30 s with UV light (365 nm, 1.8 W). As an important result, cytotoxic efficacy of the caged prodrug **20** can be restored upon UV irradiation, while cytotoxic efficacy of smMTA **17** remains unchanged (Figure 23). Using RN1 cells, the slightly reduced cytotoxic activity of **20** irradiated with UV

light might be explained by the shortened time of irradiation. However, the dose-response curves of smMTA **17** and its caged prodrug **20** both irradiated with UV light coincide clearly to further provide evidence for an efficient photoactivation *in vitro*.

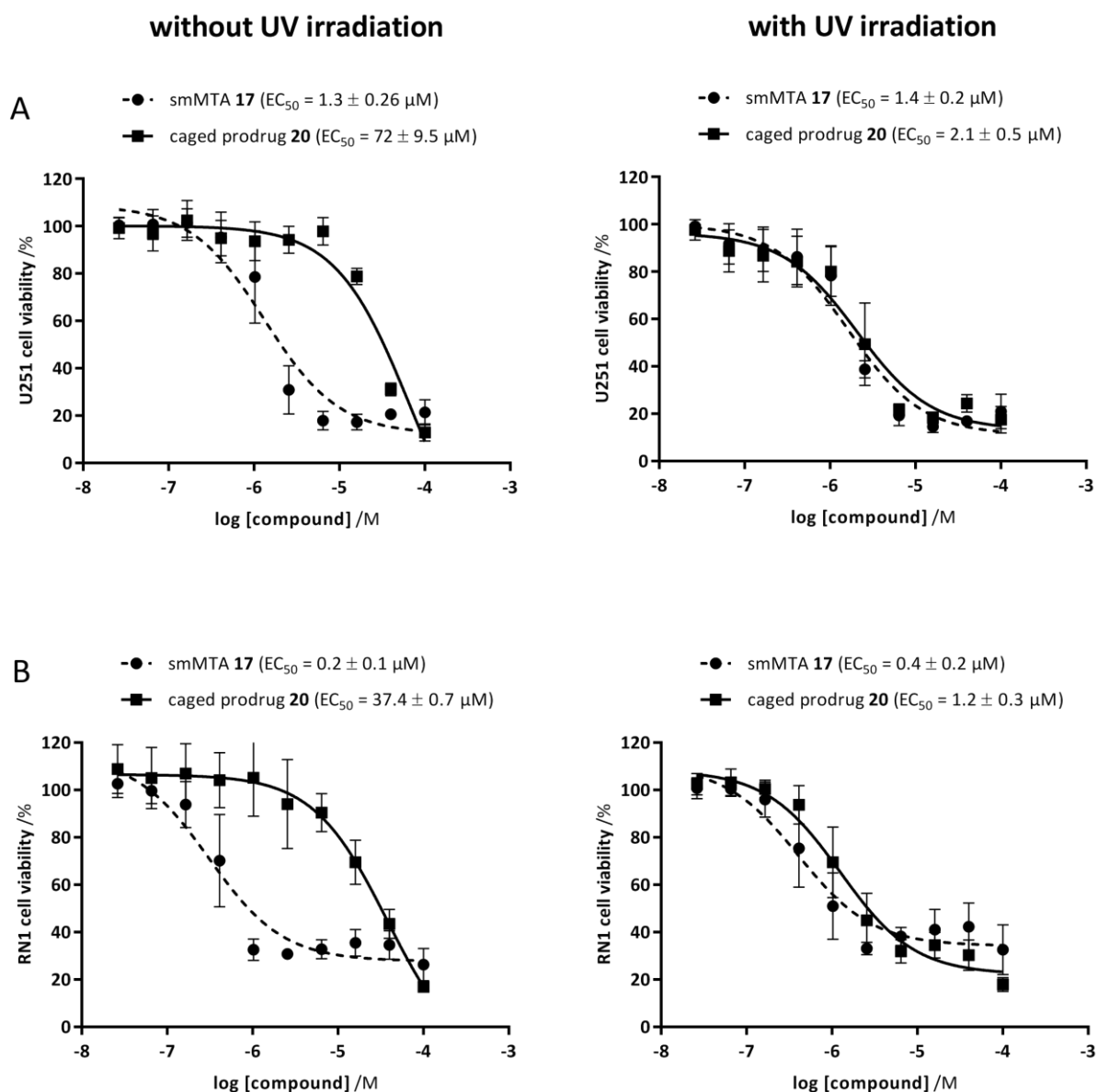


**Figure 23: Photoactivation of the caged prodrug in cell viability assays.** The restoration of biological activity of caged prodrug **20** upon irradiation with UV light was demonstrated *in vitro* using glioblastoma cell lines. A) U251 and B) patient-derived RN1 glioblastoma cells were treated with smMTA **17** and its caged prodrug **20** without UV irradiation (left). In a second setup, U251 and RN1 cells were irradiated with UV light (365 nm, 1.8 W) after treatment with smMTA **17** and caged prodrug **20**. U251 cells were irradiated for 1 min and RN1 cells for 30 s. Cell viability was determined after 48 h of drug treatment respectively 72 h for RN1 cells. Data represents mean  $\pm$  SEM from three independent experiments performed in triplicate.

Despite permanent dimming of compound solutions, unwanted photoactivation by ambient light is a common problem while working with photoactivatable compounds during all steps of an experiment *e.g.* handling, dilution or cell treatment. In order to quantify this effect, benzyl protected analogue **21** was synthesized (Figure 19). Due to similar spatial extension of the benzyl and DMNB moiety, biological activity of **20** and **21** is presumed to be equal. However, the absence of the *o*-nitro group in **21** prevents photocleavage of the benzyl moiety (Supplementary Figure 1). Using U251 cells, **21** affected cell viability only at concentrations higher than 40  $\mu\text{M}$ , which is in good agreement with cytotoxic efficacy of caged prodrug **20** (Figure 24 A). Unwanted photoactivation of the caged prodrug **20** during performance of the cell viability assays did not seem to occur.

Having demonstrated the prove of concept *in vitro*, the question of toxicity of the cleaved protecting group had to be addressed. Due to the intrinsic cytotoxicity of smMTA **17**, its caged prodrug **20** is unsuitable to address this issue. In 2015 Horbert *et al.* showed that both *tert*-butyloxycarbonyl (boc) protected alanine as well as its DMNB caged derivative **22** had no effect on the cell viability of SKMel13 cells.<sup>25</sup> Hence, DMNB caged boc-protected alanine **22** was utilized to investigate the impact of the cleaved protecting group on cell viability, since a photoactivation upon UV irradiation should release the biologically inactive boc-protected alanine, and more importantly the cleaved protecting group. Thus, U251 cells were treated with compound **22** and subsequently irradiated with UV light for 60 s (365 nm, 1.8 W). The cleaved protecting group had no impact on the cell viability up to the highest concentration of 100  $\mu\text{M}$  (Figure 24 A). This data indicates that cytotoxic efficacy after UV irradiation results from uncaging of **20**, but not from the cleaved protecting group.

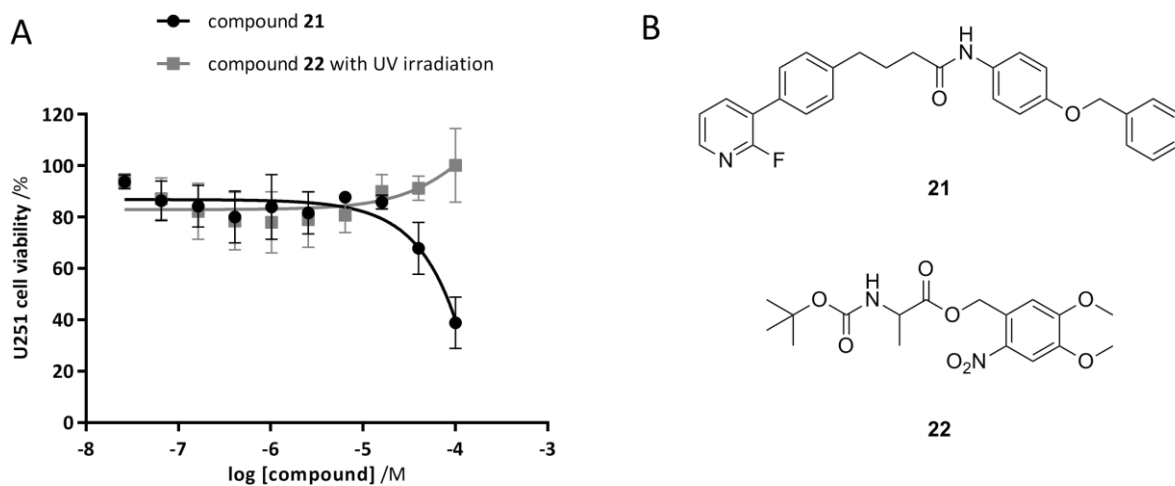


**Figure 24: Effects of negative controls 21 and 22 on U251 cell viability.** A) U251 cells were treated with compound **21** as well as compound **22** plus UV irradiation (365 nm, 1.8 W, 1 min). Data represents mean  $\pm$  SEM from three independent experiments performed in triplicate. B) Chemical structures of compound **21**, a benzyl protected analogue of smMTA **17** and compound **22**, DMNB protected boc-L-alanine.



### Immunofluorescence imaging

An essential requirement to utilize photoactivatable prodrugs for biological applications is leaving healthy tissues unaffected. Since a correct microtubule network is crucial for healthy cell function, investigation whether the caged prodrug **20** interferes with the microtubule network of U251 cells was conducted by immunofluorescence imaging. Thereby, U251 cells were treated with smMTA **17** and its caged prodrug **20**. By the addition of DAPI, the DNA of the cell nuclei became visible. The microtubule network of the cells was subsequently visualized by  $\beta$ -tubulin staining. Healthy U251 cells are characterized by a spindle shaped body and neuron-like morphology.<sup>133,134</sup> Treatment with smMTA **17** led to a pronounced disassembly of microtubule network as well as a distinct alteration of cell morphology in the form of a spherical shape and shrinkage (Figure 25). In contrast, caged prodrug **20** had no effect on both the microtubule network and cell morphology. Importantly, upon irradiation with UV light of **20**, the microtubule network lost their organization and cells rounded up, indicating a release of a microtubule-targeting agent upon irradiation.

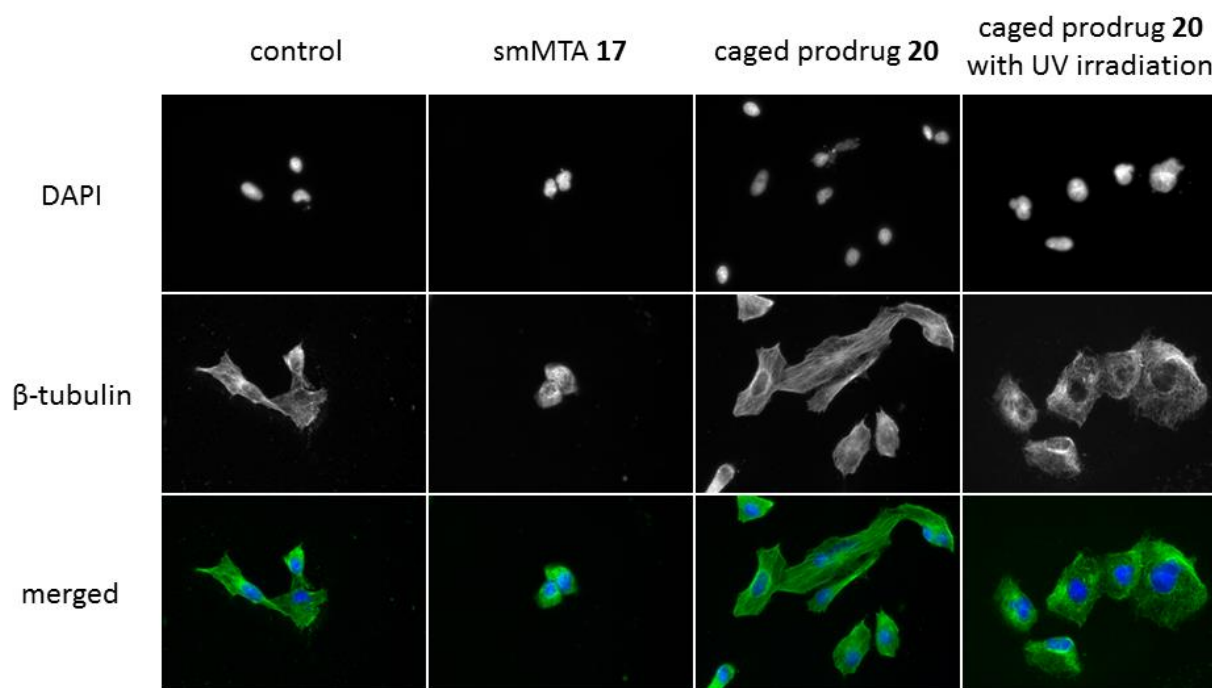


**Figure 25: Immunofluorescence imaging of treated U251 cells.** U251 cells were treated with smMTA **17**, the caged prodrug **20** and the caged prodrug **20** in combination with UV irradiation (365 nm, 5 min, 1.8 W). Cells were exposed to 5  $\mu$ M of smMTA **17** and caged prodrug **20** respectively for 24 hours. Cells were fixed with and stained with Alexa488-labeled anti- $\beta$ -tubulin antibody (green) or DAPI (blue). Representative images of three independent experiments are shown.

### Apoptosis assay

In addition to the disrupting of the tubulin filaments, microtubule-targeting agents are characterized by the induction of apoptosis through the intrinsic (mitochondrial) apoptotic pathway.<sup>101,135</sup> In order to determine whether this mechanism contributes to the cytotoxic activity of photoactivated **20**, Annexin V staining experiments have been performed. Early stage apoptosis is characterized by a translocation of phosphatidylserine (PS) to the outer surface of the cell membrane where they are exposed to Annexin V. Annexin V represents a  $\text{Ca}^{2+}$ -dependent phospholipid-binding protein with a high affinity to PS, hence being a sensitive probe for apoptosis.<sup>136</sup> RN1 cells have been treated with UV light solely, smMTA **17** and the caged prodrug **20** with and without UV irradiation. Apoptosis has subsequently been determined by quantification of Annexin V positive cells using flow cytometry. In agreement with data from cell viability assays, 30 s of UV irradiation (365 nm, 1.8 W) did not increase the basal level of apoptosis (Figure 26). In contrast, treatment with **17** results in a significant increase of apoptotic cells, whereas the caged prodrug **20** had no effect. However, upon UV irradiation of **20** the amount of apoptotic cells is comparable to treatment with **17**, suggesting that decreased cell viability is due to cells undergoing apoptosis.

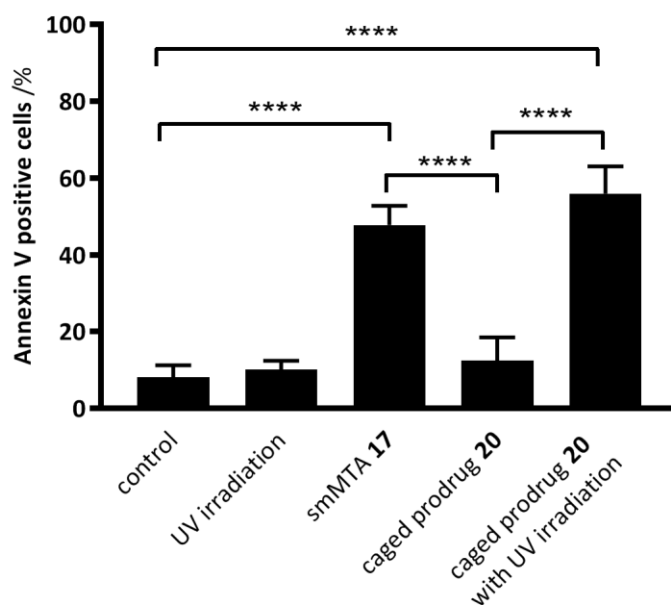


**Figure 26: Quantification of apoptosis by Annexin V staining.** RN1 cells were treated with smMTA **17**, the caged prodrug **20**, the caged prodrug **20** in combination with UV irradiation (365 nm, 30 s, 1.8 W) at a concentration of 5  $\mu\text{M}$  for 48 hours. Control cells received an equivalent amount of DMSO or UV irradiation (365 nm, 30 s, 1.8 W). Cells were stained with Annexin V and analyzed by using the MUSE Cell Analyzer. Data represents mean  $\pm$  SEM from three independent experiments (\*\*\*\* $P < 0.0001$ , one-way ANOVA followed by Tukey's multiple comparison test).

In summary, extensive biological evaluation of the DMNB caged prodrug **20** provided a notable proof of concept. All biological assays were successfully adapted for the specific issue. Only marginal biological activity of the caged prodrug could be detected examining tubulin polymerization, cell viability, microtubule interference and apoptosis. Additionally, the restoration of biological activity upon irradiation with UV light worked perfectly *in vitro* even with a significantly reduced irradiation time of 30 s working with the primary cancer cells RN1. Importantly, the required irradiation dose for a rapid and quantitative recovery of biological activity does not affect cell viability of the glioblastoma cells U251 and RN1, rendering the DMNB caged prodrug **20** valuable for biological applications.

## 3.2 Photoactivatable cyclin-dependent kinase inhibitor

### 3.2.1 Selection of inhibitor and PPG

The idea of regulating biological activity of cytotoxic compounds by using light under spatial and temporal control mainly aims to diminish systemic side effects as well as resistances, while executing biological activity in the targeted tissues. Hence, a spatial controlled prodrug concept is considered as highly beneficial to biological potent but low tolerable compounds. In order to satisfy these requirements, CDK inhibitor **16** was chosen for this project. Cyclin-dependent kinases (CDKs) are involved in the cell cycle transition in many ways. Since cell division is a highly sensitive process, CDK inhibition presumably goes hand in hand with cell toxicity (see chapter 1.5). As the photoremovable protecting group (PPG) for the caging of the inhibitor, the DMNB group was chosen to start this project with, due to its well understood and efficient photochemistry.

### 3.2.2 Stability upon irradiation

Stability of the inhibitor upon irradiation at the wavelength required for photoactivation represents a crucial criterion which had to be proved before the beginning of the project. Since the DMNB group shall be utilized for this project, UV stability of the inhibitor at a relevant wavelength has to be determined. By the intension of developing a caged prodrug of inhibitor **16** for biological applications, the experiments were designed as close to the *in vitro* conditions as possible. As a consequence the compound solution was not only prepared in DMSO (1 mM), but also in PBS buffer with 10% DMSO (25  $\mu$ M). The addition of DMSO is necessary in order to prevent precipitation of the inhibitor. Subsequently, 100  $\mu$ L of each solution were irradiated in a well of a commonly used 96-well plate for different durations up to a maximum of 10 min at 365 nm (360 mW). A custom made LED lamp particularly designed for irradiating 96-well plates was used for all photoexperiments within this project. The content determination was carried out by HPLC analysis. Both in high concentrations in DMSO as well as in low concentrations in PBS buffer, inhibitor **16** withstands UV irradiation for up to 10 min utterly (Figure 27).

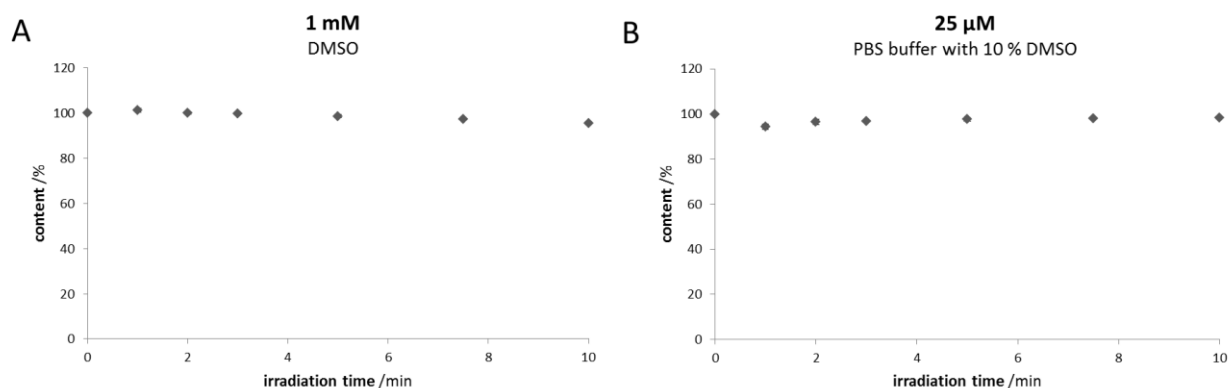


**Figure 27: UV stability of inhibitor 16.** A) A 1 mM compound solution in DMSO was irradiated at 365 nm (360 mW) in a 96-well plate for up to 10 min. B) A 25  $\mu$ M compound solution in PBS buffer with 10 % DMSO was irradiated at 365 nm (75 mW) in a 96-well plate for up to 10 min. Subsequently, samples of both A) and B) were analyzed by HPLC. Each value is a mean  $\pm$  SD of two independent experiments.

### 3.2.3 Molecular modeling

On the bases of molecular modeling studies the decision where to attach the PPG to the inhibitor had to be made. Inhibitor **16** exhibits different moieties available for the attachment of a PPG. However, with the objective of biologically inactivating the inhibitor by attachment of the PPG, the pharmacophore together with its key interactions with the target kinase had to be identified. Blocking these key interactions by the PPG was assumed to result in a loss of biological activity.

The binding mode of inhibitor **16** in the ATP binding pocket of CDK2 is shown in Figure 28 A and B (pdb 4FKO). Figure 29 shows the simplified corresponding two-dimensional (2D) ligand-interaction diagram. The *N*-phenylpyrimidine-2-amine moiety forms two H-bonds towards leucine 83 of the hinge region of the kinase rendering it as the critical core for binding to the target kinase. Furthermore the methylsulfonyl moiety is exposed to the solvent, whereas the 1-isopropyl-2-methyl-1*H*-imidazole moiety lies deeper in the ATP binding pocket of the kinase. The *N*-phenylpyrimidine-2-amine moiety was identified as the pharmacophore of inhibitor **16**. Both the NH as well as the pyrimidine nitrogen seem to be suitable for caging. Since attachment of the PPG to the pyrimidine nitrogen would entail a quaternary nitrogen with a permanent positive charge, the NH moiety was supposed to be most suitable for caging.

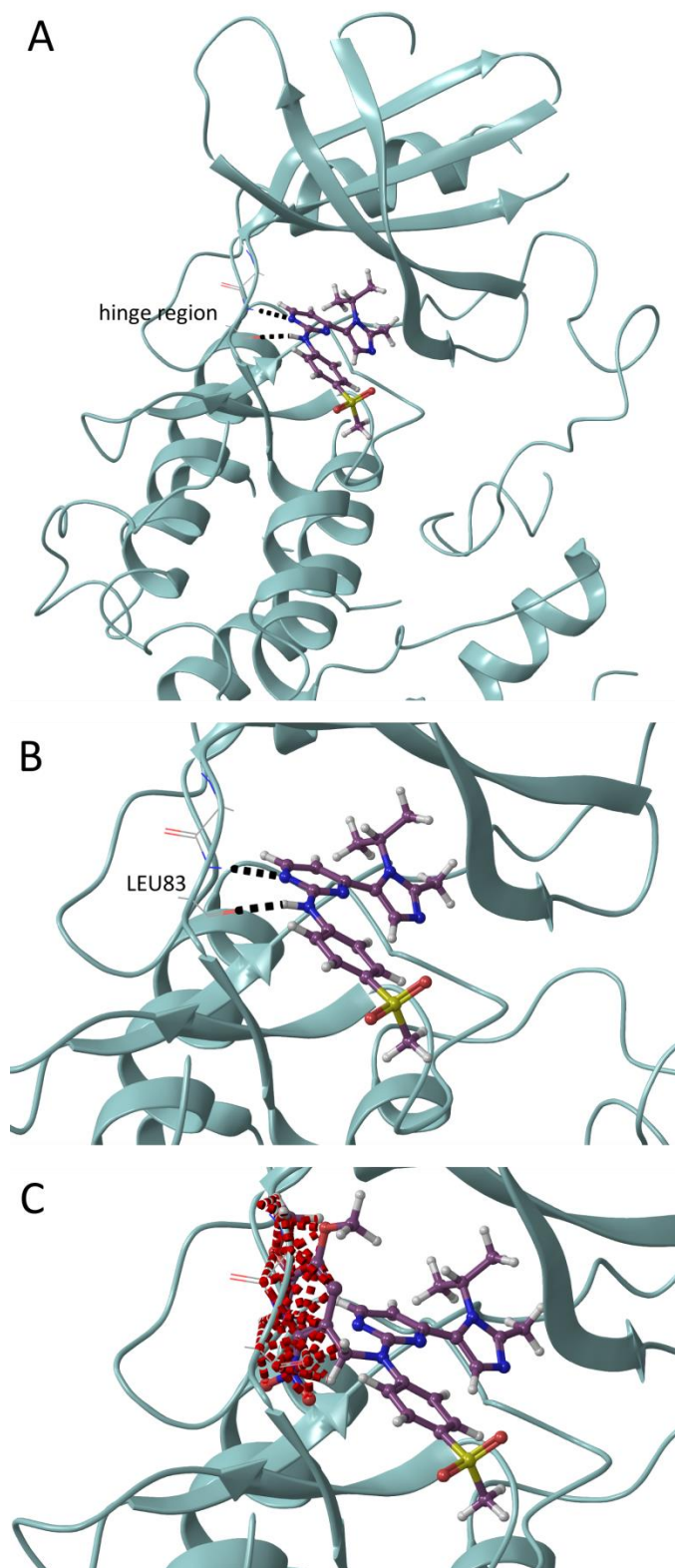


**Figure 28: 3D binding mode of inhibitor 16 in the ATP binding pocket of CDK2 predicted by molecular modeling studies (pdb 4FKO).** H-bonds formed between the ligand and the protein backbone are indicated by black dotted lines. B) Enlarged view of the binding mode. C) Superimposed DMNB caged derivative **23** in the ATP binding pocket. Red dashed lines represent sterical clashes between the PPG and the CDK2.

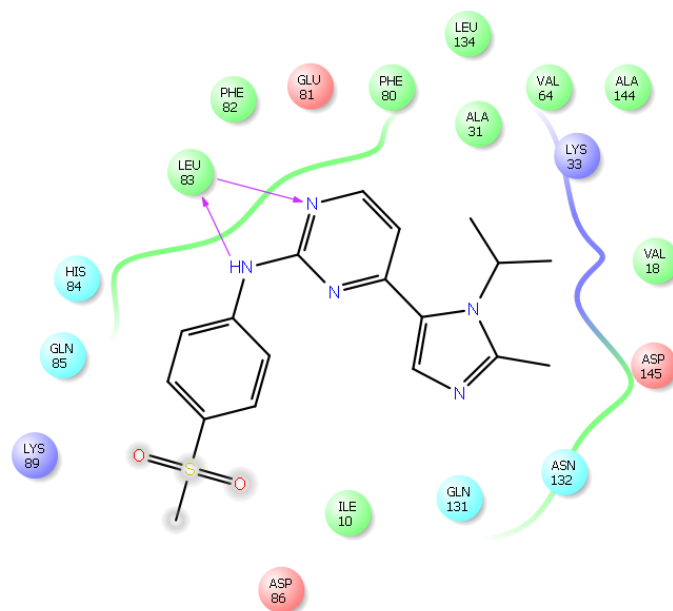
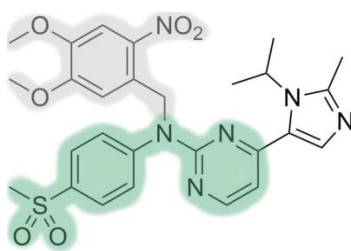


**Figure 29: 2D ligand-interaction diagram of inhibitor 16 in CDK2 (pdb 4FKO).** H-bond interactions of the ligand towards the protein backbone are shown in purple. Solvent exposure is highlighted in grey.

The assumption is supported by the simulated superposition of the NH caged prodrug **23** (Figure 30) in the ATP binding pocket of the target kinase CDK2 (Figure 28 C). Attachment of the DMNB group to the NH of the pharmacophore results in significant sterical clashes with the protein, while a plausible binding mode could not be calculated. Furthermore, the PPG presumably prevents formation of both H-bonds between the ligand and the kinase thus suggesting a loss of biological activity. Motivated by this hypothesis, the objective of synthesizing the NH caged prodrug **23** was subsequently pursued.



**23**

**Figure 30: Chemical structure of the caged prodrug of inhibitor 16.** The DMNB PPG is highlighted in grey. The pharmacophoric scaffold is highlighted in green.



### 3.2.4 Synthesis

Synthesis of the caged inhibitor **23** was approached by a one-step reaction between the inhibitor and a reactive precursor of the DMNB protecting group, since inhibitor **16** is commercially available (Figure 31). Considering the NH as the most nucleophilic moiety of inhibitor **16**, an one-step reaction appeared to be promising.

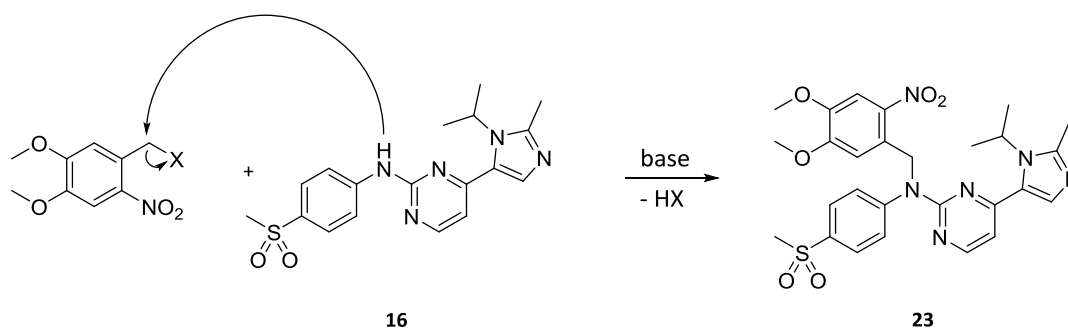


**Figure 31: Strategy for caging of inhibitor 16 with the DMNB PPG.** Caging was approached by a nucleophilic substitution reaction. Inhibitor **16** acts as the nucleophile. X represents a suitable leaving group of the DMNB precursor.

In the interest of saving valuable material of the inhibitor **16**, dummy experiments have initially been performed with the intention of optimizing the reaction conditions first. Hence, the key pharmacophoric scaffold **24** of the inhibitor, identified by molecular modeling studies, was prepared. In the sense of a nucleophilic aromatic substitution ( $S_NAr$ ) 4-(methylsulfonyl)aniline and 2-chloropyrimidine were refluxed in isopropyl alcohol with a few drops of hydrochloric acid to yield scaffold **24** (Figure 32).<sup>137</sup>

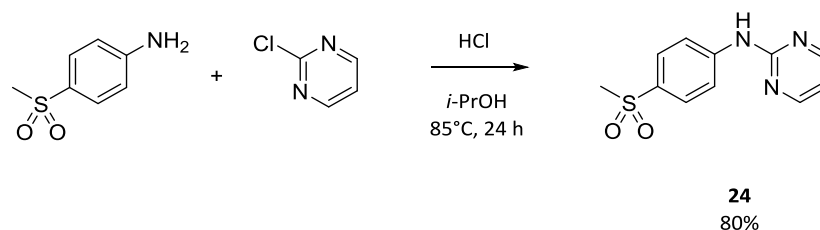


**Figure 32: Synthesis of the pharmacophoric scaffold of inhibitor 16.** Synthesis was adapted from <sup>137</sup>. The already electron deficient 2-chloropyrimidine is activated for a  $S_NAr$  by protonation. Consequently, the aniline attacks the pyrimidine C2 and substitutes the chlorine.

In a next step efficient reaction conditions for the attachment of the DMNB PPG to scaffold **24** were investigated. Since bromine at the benzylic position represents a good leaving group, 4,5-dimethoxy-2-nitrobenzyl bromide **19** was used as the reactant. Earlier works revealed reaction conditions utilizing potassium carbonate in dimethylformamide (DMF) at room temperature as superior for the caging of amines with **19**.<sup>23,101</sup> Unfortunately, in the present case conversion could not be observed under these reaction conditions (Figure 33). Assuming that the nucleophilicity of the NH moiety was not sufficient, a stronger base should be beneficial. After screening different bases, sodium hydride (NaH) turned out to be advantageous. Additionally to the higher basicity of hydride, the sodium counterion appeared to be favorable. The sodium cation might have the appropriate size to stabilize the resulting scaffold anion by complexing both the amine and one pyrimidine nitrogen. In order to enhance yields and prevent decomposing of **19** by sodium hydride, the reaction had to be performed at  $-30\text{ }^{\circ}\text{C}$  to gain the caged scaffold **25** in decent yields. Importantly, the reaction was carried out darkened to avoid unwanted photoactivation of the product by ambient light conditions.

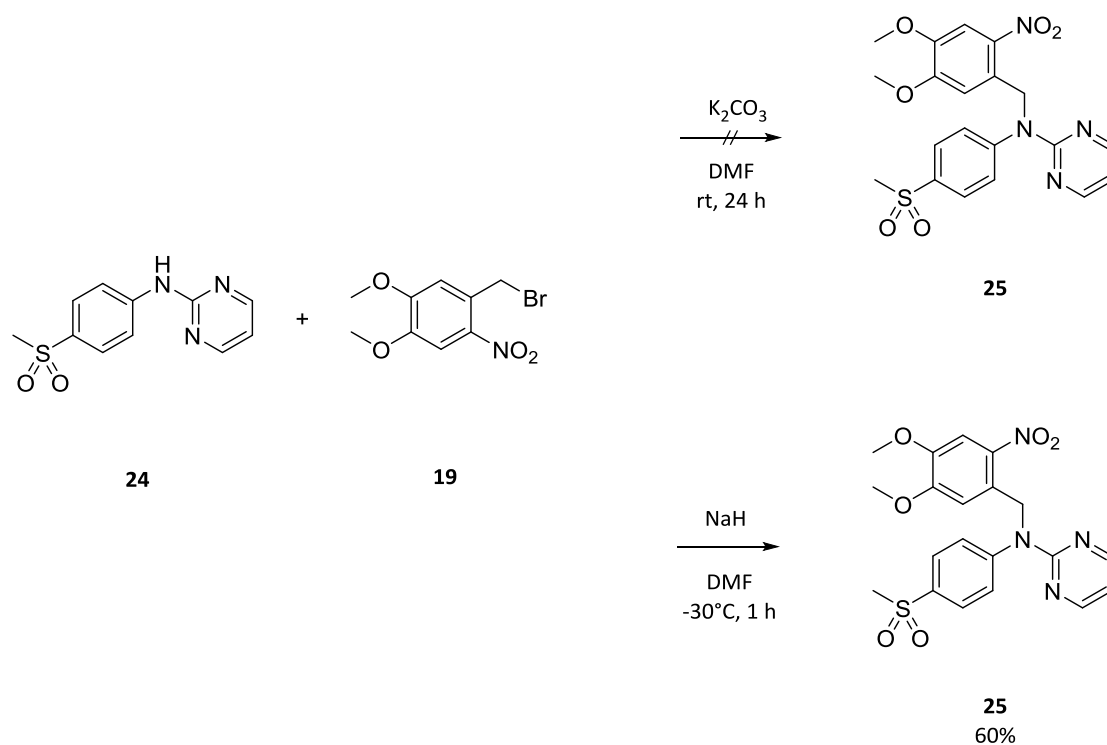


**Figure 33: Caging of the scaffold 24.** Top) Standard protocol to cage amines with the DMNB PPG from earlier works did not yield the desired product. Bottom) Adapted protocol utilizing sodium hydride as a stronger base while reducing the temperature significantly.

Having identified an efficient way to cage the NH moiety with the DMNB PPG as well as having proved a fast and clean photoactivation of the caged scaffold **25** (see chapter 3.2.5), the optimized reaction conditions were applied on the actual inhibitor **16**. Fortunately, caging of inhibitor **16** proceeded accordingly, yielding the desired caged inhibitor **23** (Figure 34). However, subsequent purification turned out to be tedious. Remaining educt, especially inhibitor **16**, had to be removed thoroughly from the product in order to prevent interference of residual biologically active inhibitor with biological testing. Two sequential flash chromatographies were necessary to gain the product at the required purity. Also the high light-sensitivity of photoactivatable compounds results in an elaborate purification since light exposure has to be diminished as much as possible. Particularly, handling solutions of photoactivatable compounds renders them endangered. This elaborate purification decreased the overall yield to 50%. Again a benzyl protected analogue **26** without the *o*-nitro group and thus lacking photocleavable properties was prepared (Figure 34) in order to detect unplanned photoactivation by ambient light during biological testing (see 3.1.5 cell viability assays).

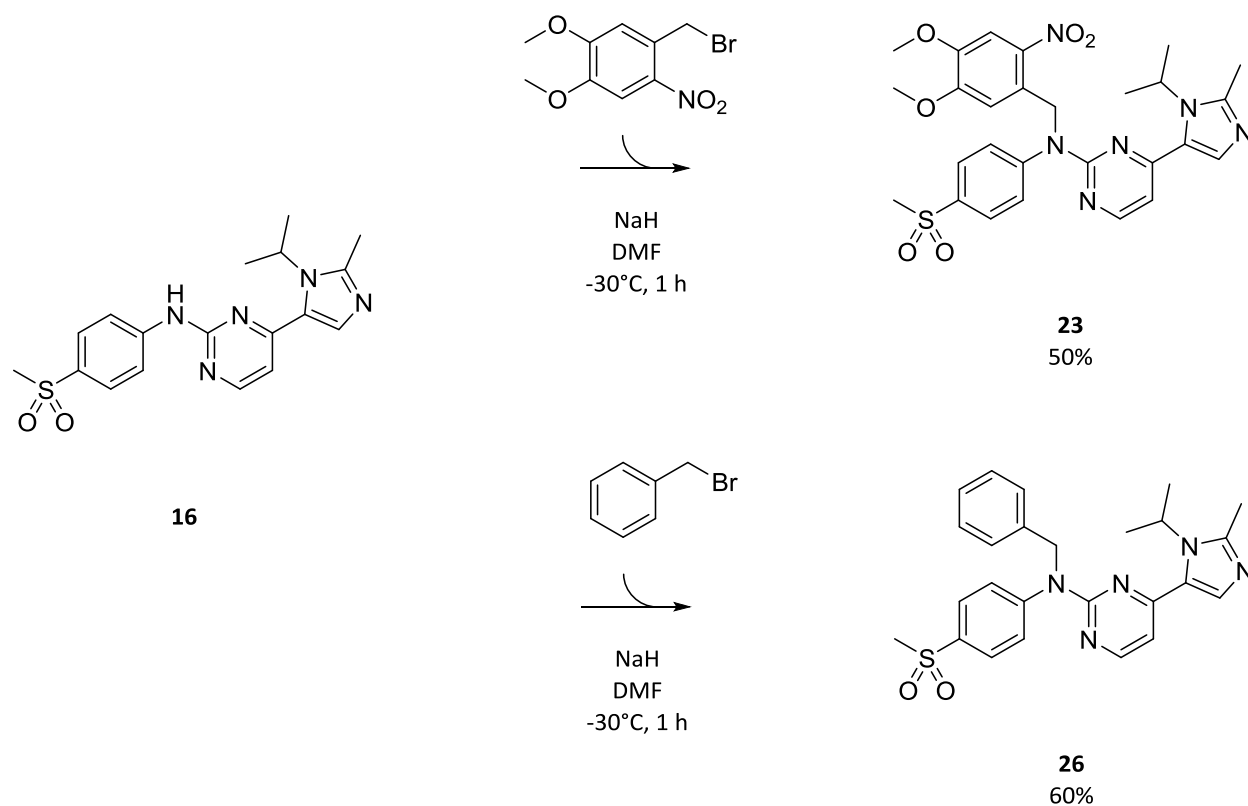


**Figure 34: Caging of inhibitor **16** with the DMNB protecting group.** Top) Preparation of the caged inhibitor **23** according to optimized reaction conditions. Bottom) Preparation of benzyl caged analogue **26** as a non-photoactivatable reference compound for biological testing.

### 3.2.5 Photochemical characterization

The subsequent photochemical characterization was composed of two steps. Firstly, the optimal irradiation wavelength for a rapid and clean photoactivation had to be identified. The efficacy of that photoactivation had to be determined in a second step. As discussed in chapter 3.1.4 high light absorption of the caged prodrug is mandatory for a rapid photoactivation, whereas the inhibitor itself should not show any absorption at the respective wavelength to ensure inhibitor stability on behalf of a rapid and clean photoactivation. Obviously, light absorption at the wavelength needed for photoactivation by the inhibitor could furthermore quench the photoactivation.

Identification of the optimal irradiation wavelength was accomplished by analysis of UV/Vis absorption spectra. The pharmacophoric scaffold **24** absorbed light up to 320 nm in DMSO (Figure 35). By attachment of the DMNB protecting group, a broad absorption band with a maximum around 365 nm emerged, which corresponds with the established wavelength for photocleavage of the DMNB PPG. However, inhibitor **16** absorbs light up to 360 nm in DMSO, making the compound potentially unstable towards irradiation with 365 nm (Figure 35). Since potential inhibitor instability towards irradiation with 365 nm represents an exclusion criterion for the use of the DMNB protecting group, UV stability of inhibitor **16** was proven for up to 10 min of irradiation at the very beginning of the project (chapter 3.2.2). UV/Vis spectra recorded in PBS buffer with 10% DMSO showed similar results. Again, attachment of the DMNB protecting group caused a broad absorption band in the near UV range. Consequently, a wavelength of 365 nm was considered optimal for an efficient photoactivation.

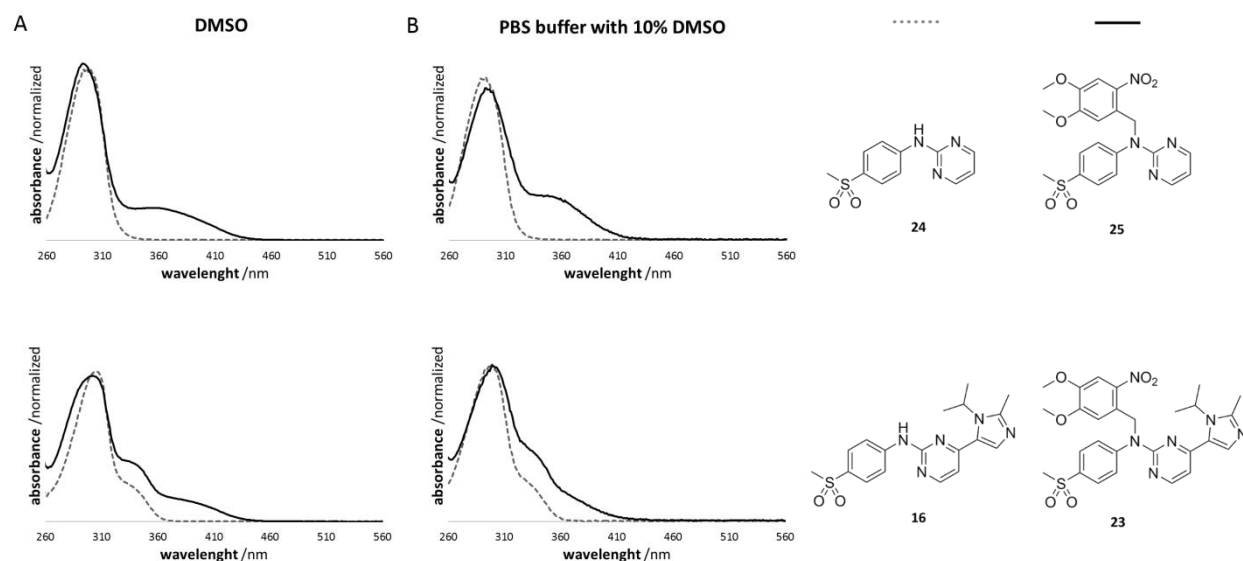


**Figure 35: UV/Vis absorption spectra.** UV spectra of both the pharmacophoric scaffold **24** and the actual inhibitor **16** (dotted lines) as well as their DMNB caged prodrugs (black lines) were recorded in A) DMSO and B) PBS buffer with 10% DMSO.

The quantification of efficacy of the photoactivation was one of the central parts of this work. The hypothesis of a rapid and clean photoactivation of the caged prodrug **23** still remained in question. The mechanism and efficacy of the photocleavage of *o*-nitrobenzyl PPGs is mainly examined for the caging of oxygens, presumably due to the fact that nitrogens represent poor leaving groups in terms of a photoactivation.<sup>28,37,138,139</sup> However, in order to utilize the caged prodrug for biological applications as well as a tool compound a rapid photoactivation is crucial, since assays or cell viability should not be disturbed by the irradiation.

The conditions for the investigation of the photoactivation were designed as close to eventual biological evaluations as possible. Therefore, all photoactivation experiments were performed in an opaque 96-well plate commonly used in biochemical assays using a custom made LED lamp for focused irradiation. Additionally to DMSO, commonly used to perform photoexperiments, the photoactivation was also examined by using PBS buffer with 10% DMSO in order to mimic biological conditions such as aqueous medium, pH and electrolyte concentration. Furthermore, photoactivation involves a bond cleavage between the PPG and the leaving group, in this study the inhibitor. On the supposition that this bond cleavage requires energy, provided by light, the concentration of the photoactivatable compound will be a relevant parameter for rate determination of the photoactivation. In line with this notion, less energy might be required for a quantitative photoactivation at lower concentrations typically present in biochemical assays. Regarding this assumption, investigation of the photoactivation in PBS buffer with 10% DMSO was performed at significant lower concentrations compared to the experiments in DMSO to

mimic the biochemical assay situation. Unfortunately, due to the limit of quantification set by HPLC analysis, low micromolar or even nanomolar concentrations as used in biological assays remained unfeasible in our lab.

In a first step the photoactivation of the caged scaffold **25** was investigated. Both in DMSO (1 mM) and in PBS buffer with 10% DMSO (25  $\mu$ M), the caged scaffold was entirely activated within 120 s of irradiation at 365 nm by using 37.5 mW (Figure 36, top). Since 37.5 mW is a considerably low power regarding UV light, the rate of photoactivation was considered to be more than sufficient. Motivated by these results, the caged prodrug **23** was prepared. The photochemical characterization delivered comparable results. Again, a full photoactivation occurred within a period of 120 s of irradiation (365 nm, 37.5 mW, Figure 36, bottom). Furthermore, no byproduct except the cleaved protecting group could be detected at significant concentrations, rendering the caged compound **23** a promising tool for further biological applications.

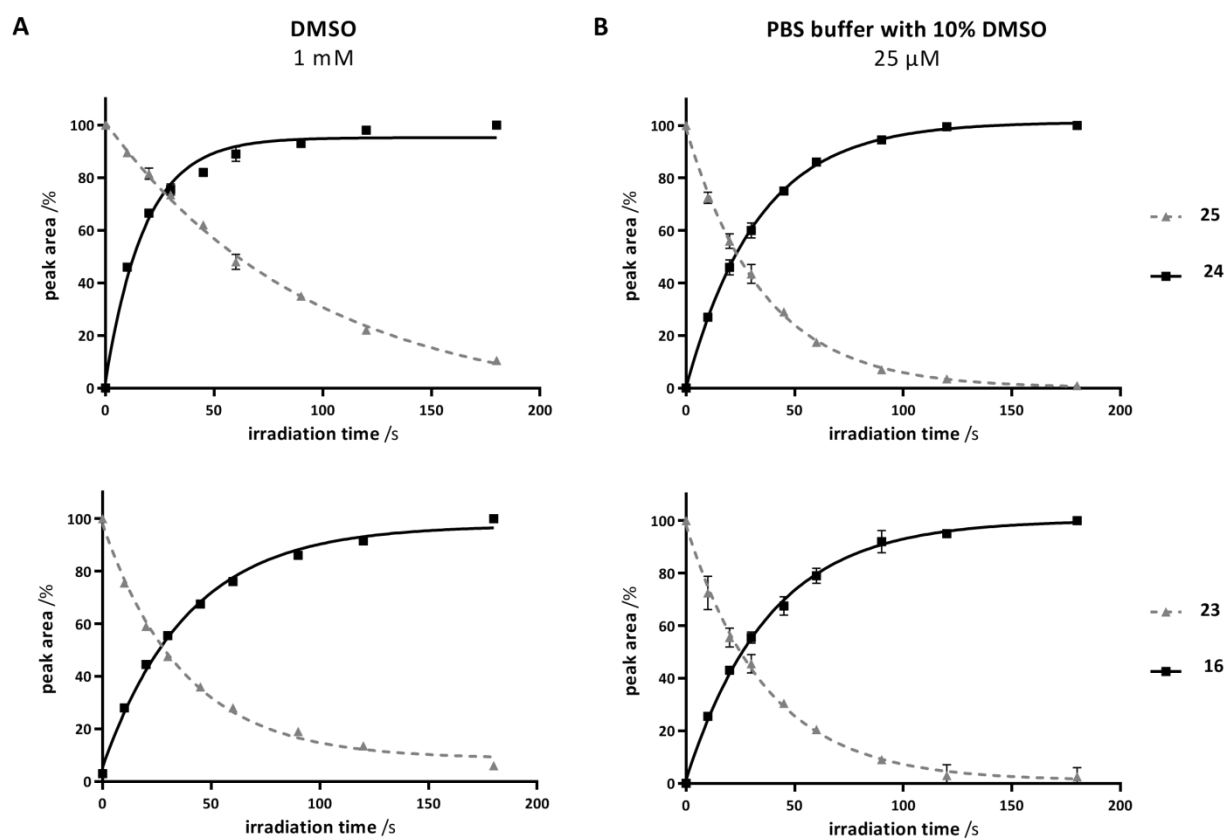


**Figure 36: Photoactivation of the caged scaffold **25** (top) and the caged prodrug **23** (bottom).** 100  $\mu$ L of each compound solution in A) DMSO (1 mM) and B) PBS buffer with 10% DMSO (25  $\mu$ M) were irradiated in wells of a 96-well plate for the indicated time at 365 nm (37.5 mW) and analyzed by HPLC ( $n = 2$ ). The amount of the caged compound (diamonds) is plotted against the released scaffold **24** (top, squares) respectively inhibitor **16** (bottom, squares). Each data point is a mean  $\pm$  SD of two independent experiments.

### 3.2.6 Biological evaluation

The photochemical characterization demonstrated a rapid and clean activation of the DMNB caged prodrug **23** upon irradiation with UV light under experimental conditions. Although photoactivation experiments were designed as close to biological conditions as possible, the photoactivation *in vitro* had to be assessed in order to determine utility for biological applications. Furthermore biological inactivity of the caged prodrug represents another central prerequisite. Molecular modeling studies exposed the NH caged prodrug **23** as incapable of binding to its target kinase (chapter 3.2.3). However, biological evaluation aimed to prove biological inactivity of the DMNB caged prodrug **23**. Both kinase and cell viability assays were performed with the intention of investigating remaining biological activity of **23** as well as its photoactivation *in vitro*.

Since photochemical characterization exhibited **23** as highly light sensitive, stability in solution was examined prior to biological evaluation. Regarding conditions during a cell viability assay, the DMNB caged prodrug **23** as well as its benzyl caged analogue **26** were incubated in PBS buffer with 20% DMSO for up to 48 h at 37°C in the incubator of the cell culture, reducing light exposure to a minimum. A second sample was stored in the lab being exposed to ambient light and room temperature. As an important result, storing a solution of the DMNB caged prodrug **23** at ambient light results in a significant activation whereas no activation was observed under dark conditions, indicating that all experiments of the biological evaluation had to be performed under light exclusion in order to avoid artefacts (Figure 37). Larger error bars obtained storing the sample at ambient light are due to natural differences of the light conditions. As expected, the benzyl caged analogue **26** was stable under both conditions.

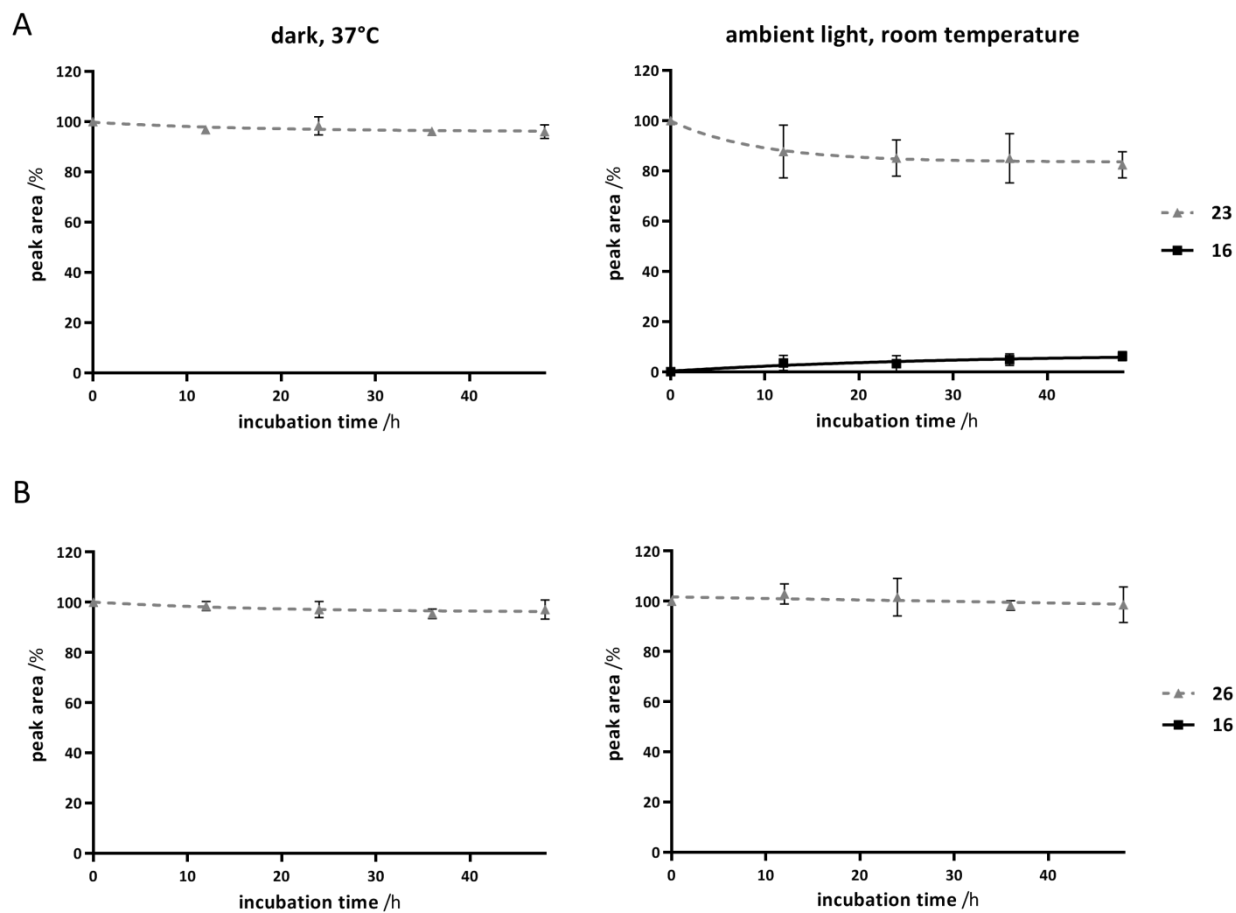


**Figure 37: Stability of the DMNB caged prodrug 23 and its benzyl caged analogue 26 in solution.** A) A compound solution of the DMNB caged prodrug 23 (100  $\mu$ M) in PBS buffer with 20% DMSO was incubated either in a cell culture incubator in the dark at 37°C (left) or in the lab exposed to ambient light at room temperature (right). After indicated time points peak area determination was performed using HPLC analysis. Contents of the caged species is plotted against the uncaged species. B) The experiment was repeated analogously with the benzyl caged analogue 26 (50  $\mu$ M). Each value is a mean  $\pm$  SD of two independent experiments.



## Kinase assay

In a next step, the inhibitory efficacy of the DMNB caged prodrug **23** with and without UV irradiation was determined using the target kinase, cyclin-dependent kinase 2 (CDK2), in an ADP-Glo™ Kinase Assay. Due to **23**'s light sensitivity, the kinase assay was performed using only red light for room illumination, since it does not show any light absorption above 450 nm (Figure 35). CDK inhibitor **16** exhibited an  $IC_{50}$  of 2.86 nM, which was in good agreement with published data.<sup>89</sup> Attachment of the DMNB protecting group to the inhibitor resulted in an extensive loss of inhibitory efficacy, rendering the DMNB caged prodrug **23** inactive up to micromolar concentrations ( $IC_{50} \approx 4798$  nM). Importantly, upon irradiation with UV light (365 nm, 600 mW, 120 s) the inhibitory efficacy was completely recovered ( $IC_{50} = 5.64$  nM).

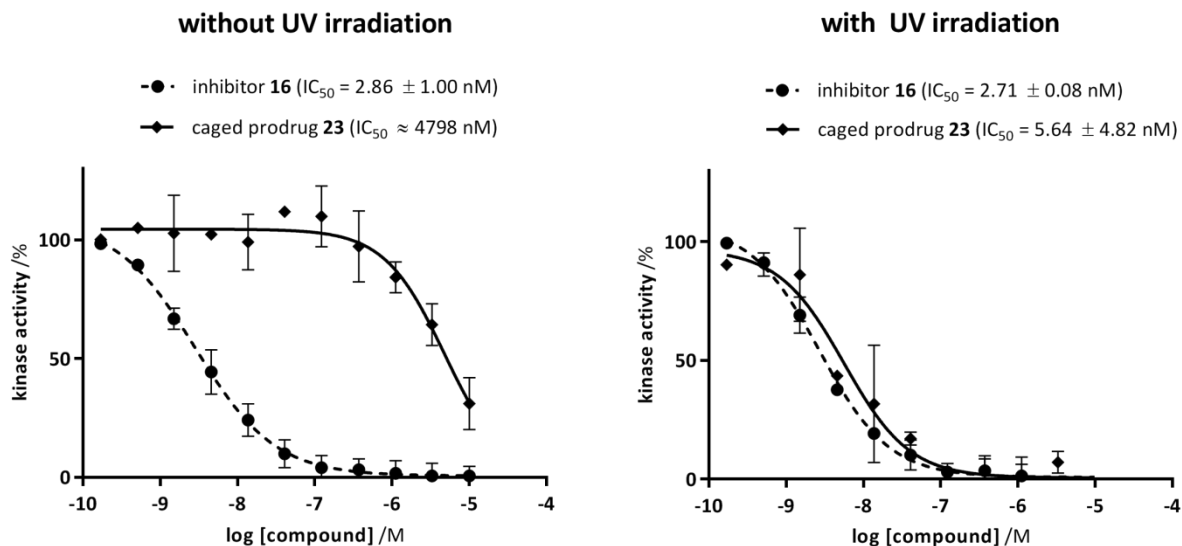


**Figure 38: Kinase assays of inhibitor 16 and its caged prodrug 23 using the target kinase CDK2/cyclin E1 with and without UV irradiation.** CDK2 in complex with cyclin E1 was incubated with inhibitor **16** as well as its caged prodrug **23** to determine kinase activity (left). In a second setup, 10 minutes after compound addition both **16** and **23** were irradiated with UV light for 2 minutes (365 nm, 37.5 mW). Data represents mean  $\pm$  SD from two independent experiments performed in triplicate.

### Cell proliferation assays

Having impressively demonstrated both inactivity of the DMNB caged prodrug **23** as well as its quantitative photoactivation in kinase assays, cell proliferation assays were performed using the pancreas carcinoma cell line Panc89 to further validate the observed effects. A pancreatic cancer cell line was chosen since CDK inhibition represents a promising strategy to effectively kill pancreatic tumor cells.<sup>140–142</sup> In a first step, the resistance of Panc89 cells towards UV irradiation was to be investigated in a UV titration experiment. Panc89 cells were therefore treated with UV light solely for a maximum of 5 minutes (365 nm, 37.5 mW). Cell viability was respectively determined for the indicated irradiation times. Importantly, up to 5 minutes of irradiation the cell proliferation was not impaired (Figure 39). In relation, not more than 2 minutes of irradiation (365 nm, 37.5 mW) are sufficient to completely activate the DMNB caged prodrug **23**. Thus, a quantitative photoactivation should be feasible without affecting cell proliferation.

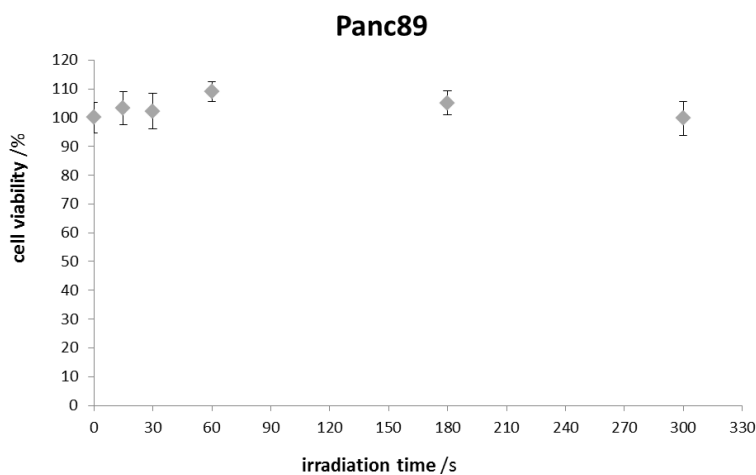


**Figure 39: UV titration using Panc89 cells.** Panc89 cells were irradiated with UV light (365 nm, 37.5 mW) for up to 5 min. Cell viability was determined after 48 h of drug treatment using Resazurin. Each value is a mean  $\pm$  SD of two independent experiments.

Consequently, cell proliferation assays using Panc89 cells with the uncaged inhibitor **16** and its caged prodrug **23** with and without UV irradiation were performed. Regarding results from stability experiments, cell proliferation assays were carried out under red light illumination. CDK inhibitor **16** exhibited an  $EC_{50}$  of  $0.70 \mu\text{M}$  without irradiation (Figure 40). As seen in kinase assays, attachment of the DMNB protecting group significantly diminished biological activity, hence increasing the  $EC_{50}$  to high micromolar concentrations ( $\approx 17.3 \mu\text{M}$ ). Noteworthy, the caged prodrug exhibited a poor water solubility resulting in compound precipitation at the highest concentration. Hence, cell proliferation at a compound concentration of  $100 \mu\text{M}$  was not measured, complicating a relevant  $EC_{50}$  calculation. However, the results show clearly that **23** does not affect cell proliferation up to high micromolar concentrations. Since the DMNB caged prodrug **23** was inactive utilizing CDK2 kinase assays, off-target effects might contribute to residual cytotoxic efficacy. As an important prove of concept, the biological efficacy of the DMNB caged prodrug can be completely recovered upon irradiation with UV light, producing an  $EC_{50}$  of  $0.80 \mu\text{M}$ , which is perfectly comparable to the  $EC_{50}$  of inhibitor **16** ( $EC_{50} = 0.85 \mu\text{M}$ ).

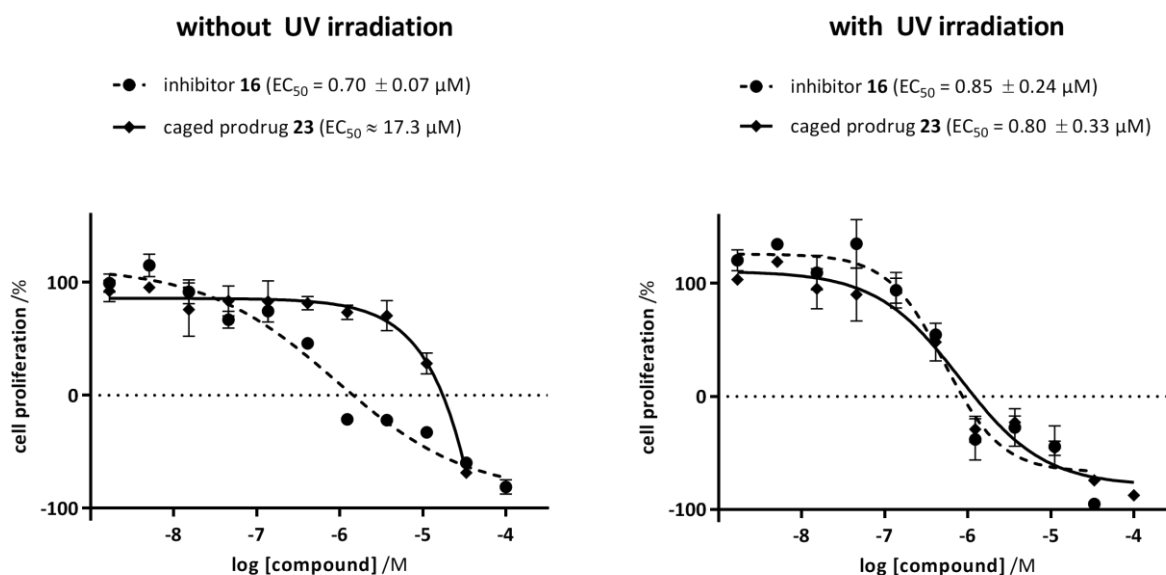


**Figure 40: Cell proliferation assays of the inhibitor **16** and its DMNB caged prodrug with and without UV irradiation using Panc89 cells.** Panc89 cells were treated with inhibitor **16** and its DMNB caged prodrug **23** without UV irradiation (left). In a second setup, Panc89 were irradiated for 2 minutes with UV light (365 nm, 37.5 mW) after treatment with **16** and **23**. Cell proliferation was determined after 48 h of drug treatment. Data represents mean  $\pm$  SEM from three independent experiments performed in quadruplicates.

Although red light was exclusively used for room illumination, inadvertent photoactivation during both preparation of the compounds solutions as well as performance of the assays might additionally contribute to remaining biological activity of the caged prodrug. In order to address this issue, the benzyl caged analogue **26** was synthesized and consequently tested as a non-photoactivatable control (Figure 41). Due to the removal of the *o*-nitrogroup a cleavage upon irradiation cannot proceed (Supplementary Figure 3). Yet, both analogues **23** and **26** presumably exhibit comparable biological activity due to similar spatial extension of the benzyl and DMNB moiety. Cell proliferation assays showed that both EC<sub>50</sub> curves overlap, suggesting that these compounds might affect other targets than CDKs at higher concentrations.

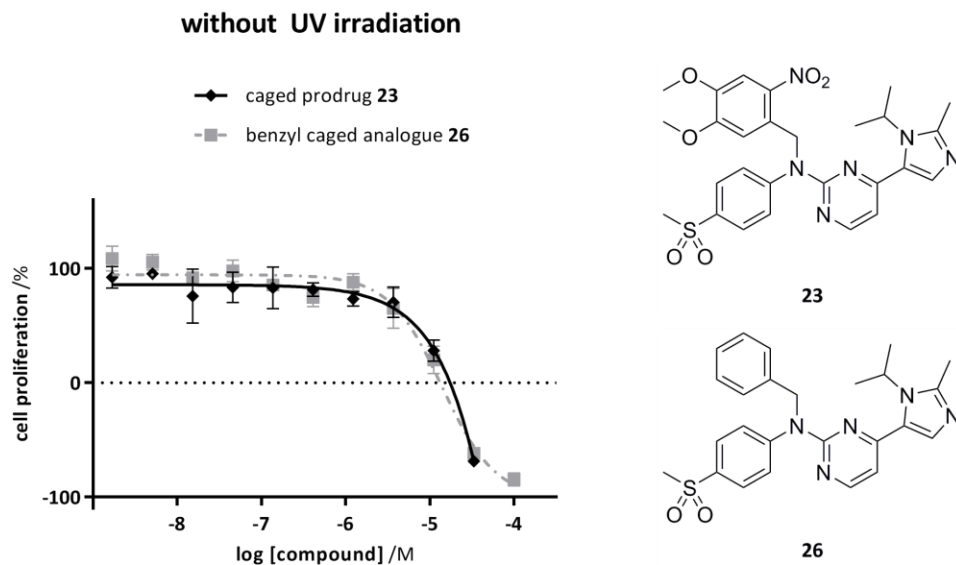


**Figure 41: Cell proliferation assays of the benzyl caged analogue 26.** Panc89 cells were treated with the DMNB caged prodrug **23** and its benzyl caged analogue **26** without UV irradiation. Cell proliferation was determined after 48 h of drug treatment. Data represents mean  $\pm$  SEM from three independent experiments performed in quadruplicates.

In a last experiment, potential cellular toxicity of the photocleaved DMNB protecting group was assessed by the use of two tool compounds: Boc-protected L-alanine **22a** and its DMNB caged analogue **22**. The Boc-protected L-alanine **22a** did not affect cell proliferation of Panc89 cells up to the highest concentration of 100  $\mu\text{M}$  and was thus accepted as biologically inert. Upon UV irradiation of the DMNB caged analogue **22** the biologically inert Boc-protected L-alanine **22a** as well as the cleaved protecting group showing a nitrosobenzaldehyd moiety was formed.<sup>23,25</sup> The UV irradiated DMNB caged analogue **22** exhibits moderate cytotoxic effects only at concentrations above 50  $\mu\text{M}$  (Figure 42). Nevertheless, potent kinase inhibitors exhibit cytotoxic effects at significantly lower concentrations rendering the observed cytotoxic effect of the cleaved DMNB protecting group as negligible suggesting a wide therapeutic window of a potential DMNB caged prodrug.

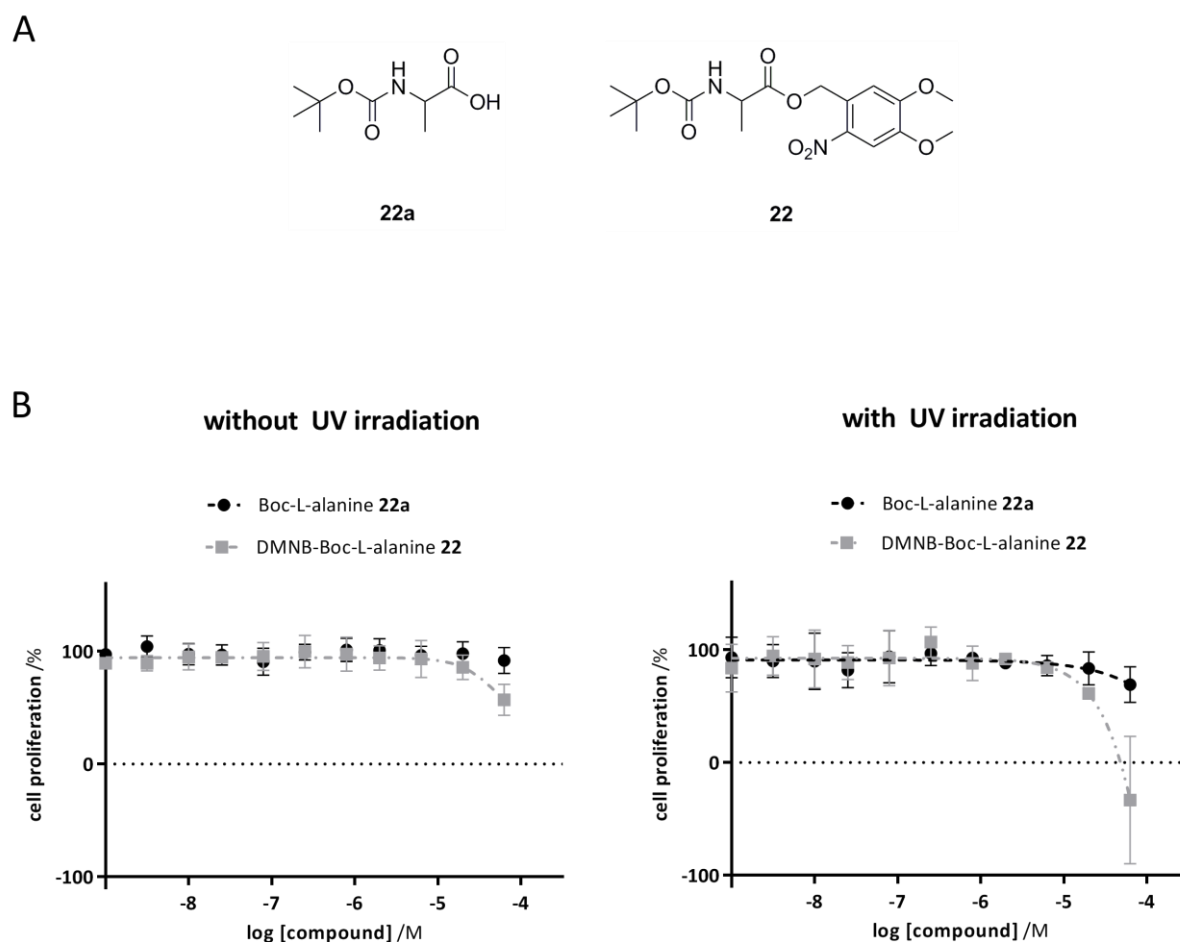


**Figure 42: Effect of the cleaved DMNB protecting group on cell proliferation.** A) Chemical structure of the utilized tool compounds: Boc-L-alanine **22a** and its DMNB caged derivative **22**. B) Panc89 cells were treated with **22a** and **22** without UV irradiation (left). In a second setup, Panc89 were irradiated for 2 minutes with UV light (365 nm, 37.5 mW) after treatment with **22a** and **22**. Cell proliferation was determined after 48 h of drug treatment. Data represents mean  $\pm$  SEM from two independent experiments performed in triplicates.

### 3.2.7 Scaffold project

Regarding applicability of photoactivatable compounds in biological setups, timing and rate of photoactivation are the most critical parameters. Regardless of whether photoactivatable compounds shall be used to study biological processes or for medicinal approaches, a fast and clean photoactivation is indispensable. Obviously the utilized PPG represents the decisive factor, but recent studies showed that the leaving group affects the rate of photoactivation as well.<sup>25,37,143</sup> The photoactivation mechanism of the most commonly used DMNB protecting group has been studied intensively yet the leaving groups feature responsible for affecting the photoactivation remains unclear.<sup>144</sup> Regarding this issue, a solely computational study was performed by Il'ichev *et. al* in 2003.<sup>145</sup> Their calculated results suggest that electron-donating substituents in the benzylic position hence electron-donating leaving groups improve the photocleavage. Furthermore, in 2011 Solomek *et. al* argued that radical stabilizing features of the leaving group enhance the photoreaction.<sup>37</sup> Radical stabilizing characters of different leaving groups have thereby been calculated by computational studies, actually making experimental data on the influence of the leaving group rarely available. Unfortunately, this experimental data would be markedly valuable in terms of developing photoactivatable prodrugs, since the uncaged biological active compounds themselves represent the leaving groups. These biological active compounds possess a specific pharmacophore which typically cannot be structurally modified without affecting important properties such as biological activity or pharmacokinetic parameters. Hence, some pharmacophores might be more suitable for the caging concept than others.

In order to address this issue, we aimed for a systematic investigation of substituents towards the *N*-phenylpyrimidine-2-amine scaffold regarding the photoactivation. The *N*-phenylpyrimidine-2-amine scaffold appeared to be highly suitable for this study since it is present in many kinase inhibitors and additionally gives more than 24000 hits upon inhibitor substructure search including biological studies using SciFinder® (Figure 43). Furthermore, the *N*-phenylpyrimidine-2-amine scaffold was identified as one of the most promising scaffolds for the development of CDK inhibitors.<sup>146–148</sup> Not surprisingly, all three clinically approved CDK inhibitors possess a closely related *N*-pyridinepyrimidine-2-amine scaffold as part of their hinge binding motif (Figure 43). The understanding of the influence of the substitution of the *N*-phenylpyrimidine-2-amine scaffold on the photoactivation would be of great value for the development of future photoactivatable CDK or further photoactivatable inhibitors.

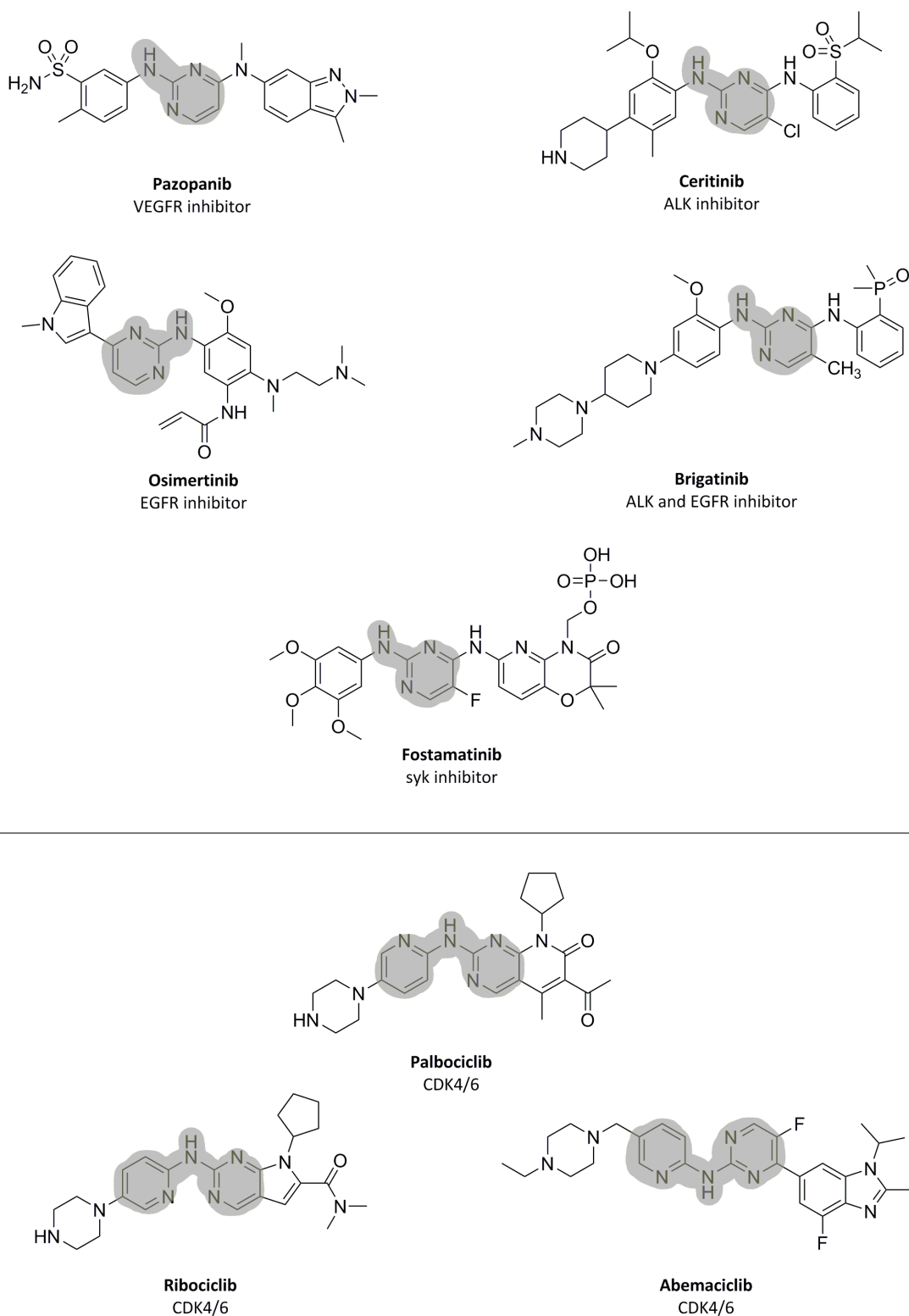
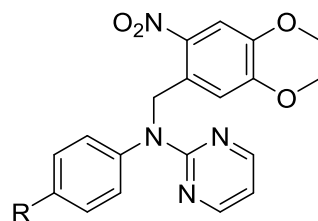


**Figure 43:** Examples of FDA-approved kinase inhibitors exhibiting the *N*-phenylpyrimidine-2-amine scaffold as their hinge binding motif (top) and FDA-approved CDK inhibitors exhibiting the *N*-pyridinepyrimidine-2-amine scaffold as part of their hinge binding motif (bottom). The hinge binder forming the H-bonds towards the target kinase is highlighted in grey. The C2-NH as well as the pyrimidine N1 is particularly important for binding to the target kinase. The respective target kinase is shown beneath the drug name.<sup>78,149–151</sup>

Importantly, the PPG is attached to the exocyclic NH, so both aromatic systems will influence the uncaging. In this study, exclusively the substitution in the para-position of the phenyl system is systematically investigated while maintaining the pyrimidine. In particular, electronic and mesomeric effects of different  $\pm M/I$ -substituents on the photoactivation rate were to be investigated. Therefore, eight analogues of the caged scaffold **25** have been synthesized (Table 2). The amino group in the 2-position of the pyrimidine has been chosen for effective caging, since it was identified as critical for binding to the target kinase in all examples (Figure 43). In order to quantify the electronic and mesomeric effects of these substituents, their Hammett constants were used, respectively. In 1936 Hammett studied the correlation between the electronic character of substituents and the rate and equilibrium of organic chemical reactions, quantified as the Hammett constants  $\sigma$  ( $\sigma_{\text{para}}$  or  $\sigma_{\text{meta}}$ ).<sup>152</sup> Taft *et. al* extended the concept by applying the same principles on steric as well as inductive and resonance effects.<sup>153</sup> Till this day, revised Hammett constants are generally utilized to quantify electronic and mesomeric effects of different substituents. More positive  $\sigma$ -values are associated with a more electron-withdrawing character of a substituent, whereas more negative  $\sigma$ -values represent more electron-donating characters (Table 2).<sup>154</sup>



**Table 2: Overview of the examined caged *N*-phenylpyrimidine-2-amine scaffolds with their respective Hammett constants.**<sup>155</sup> Substituents R in the para-position of the phenyl systems were altered in terms of designing a set of substituents aiming towards a valid hypothesis regarding a correlation between electronic parameters and the rate of photoactivation.



#	substituent (R =)	Hammett constant ( $\sigma_p$ ) <sup>155</sup>
35	-N(CH <sub>3</sub> ) <sub>2</sub>	-0.83
36	-OCH <sub>3</sub>	-0.27
37	-CH <sub>3</sub>	-0.17
38	-H	0
39	-Br	0.23
40	-COOEt	0.45
41	-CF <sub>3</sub>	0.54
42	-CN	0.66
25	-SO <sub>2</sub> CH <sub>3</sub>	0.72

## Synthesis

The synthesis of the differently substituted scaffolds was approached in two ways (Figure 44). Analogously to the preparation of the original pharmacophoric scaffold **24**, scaffolds **27-30** were synthesized by a nucleophilic aromatic substitution: the respective *p*-aniline derivatives were refluxed together with 2-chloropyrimidine in *tert*-butyl alcohol to gain the desired scaffolds in good yields.<sup>137</sup> In order to enhance the reactions rates, a few drops of concentrated HCl were added. In contrast, synthesis of the scaffolds **31-34** was achieved by a palladium catalyzed Buchwald-Hartwig amination utilizing either *S*-BINAP or Xantphos as ligand for the palladium catalyst. Dioxane has been used as the solvent, whereas potassium *tert*-butoxide was the base of choice. All Buchwald-Hartwig aminations were carried out in a microwave reactor to reduce reaction times.<sup>156-159</sup> Having all *N*-phenylpyrimidine-2-amine scaffolds in hand, the NH-protection with the DMNB group was carried out following the earlier

evaluated protocol. Accordingly to this method, the scaffolds were stirred with sodium hydride in DMF at 0°C. After cooling to -30°C, DMNB-Br was added carefully and the reaction was left stirring for an hour. After quenching by the addition of water, the crude product was purified by flash chromatography. Importantly, light exposure was avoided as much as possible during both synthesis and purification of the caged scaffolds due to their potential light sensitivity.

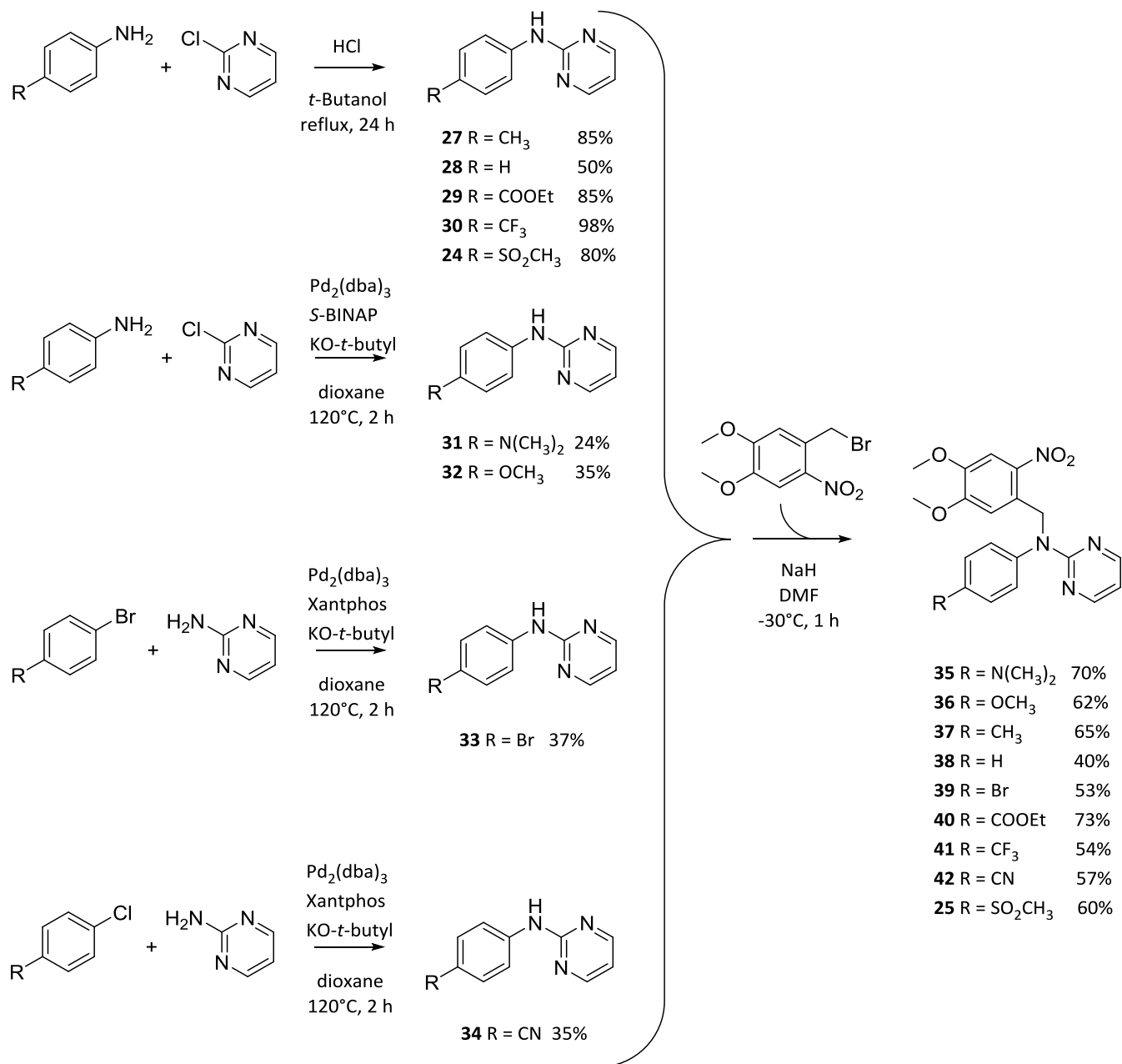


**Figure 44: Synthesis of the caged *N*-phenylpyrimidine-2-amine scaffolds.** Left: synthesis of the differently substituted scaffolds according to procedures<sup>156-159</sup>. Right: caging of the respective scaffolds with the DMNB protecting group.

### Photochemical characterization

Having the designed set of compounds in hand, the photochemical characterization aimed to determine and compare the photoactivation reaction rates of all scaffolds **25,35-42**. With the intention of developing photoactivatable prodrugs for biological applications, determination of the reaction rate appeared superior to quantum yield determinations, since it allows the performance of photoexperiments utilizing the custom-made UV LED lamp for the irradiation of commonly used 96-well assay plates. In contrast a quantum yield determination would demand a specific experimental setup not meeting biological assay conditions. However, in order to evaluate utility for biological applications the reaction rate of the photoactivation of photoactivatable prodrugs is highly valuable.

In a first step, light absorbance at the respective wavelength required for photoactivation was assessed. Higher light absorption at the respective wavelength required for photoactivation might enhance the rate of the photoactivation thus falsify results. However, all caged scaffolds showed comparable light absorption at 365 nm, with the exception of a slightly higher light absorption of the carboxyethyl substituted scaffold **40** (Table 3, Supplementary Figure 4).

Next, the photoactivation of each scaffold was examined using a UV LED with an emission maximum at 365 nm. The photoactivation experiments were carried out in a 96-well plate in order to maintain the relatedness to future biological applications. Furthermore, the experiments were not only performed in DMSO at a high 500  $\mu$ M concentration, but also in PBS buffer with 20% DMSO at a considerably lower concentration of 25  $\mu$ M. The concentration was not be further decreased in order to meet quantifications limits of the HPLC analysis. All scaffolds were irradiated for up to 2 min at a power of 7.5 mW in order to examine the photoactivation reaction. This resulted in a zero-order like curve shape within the first 45 s of irradiation, when plotting the amount of the caged species against the irradiation time. The decrease of the caged species as a result of a photoactivation was considered a reliable determinant for the rate of photoactivation due to a considerably low error-proneness, a procedure according to a similar study by Solomek et. al.<sup>37</sup> However, the photoactivation rate slows down after 45 s resulting in a flattening of the curve (Figure 45).

This is due to the fact that the number of photocleavage events per time is directly proportional to the number of photons absorbed. If the absorption of the irradiated solution is large ( $A > 2$ ), the number of photons absorbed per time is constant and independent from the concentration resulting in a zero order like curve shape. However, during photoactivation the concentration of the photoactivatable compound and consequently the absorption at the irradiation wavelength decreases. Thus, if the absorption is little ( $A \ll 1$ ) the number of photons absorbed per time is dependent on the concentration of the

photoactivatable compound resulting in a first order like curve shape. Noteworthy, describing of photochemical reactions by standard kinetic concepts remains arguable.<sup>160–165</sup>

In order to determine reaction rates, the range between 0 and 45 seconds was considered and processed by a zero-order fitting. The reaction rates were subsequently calculated from the slopes of the zero-order fits.

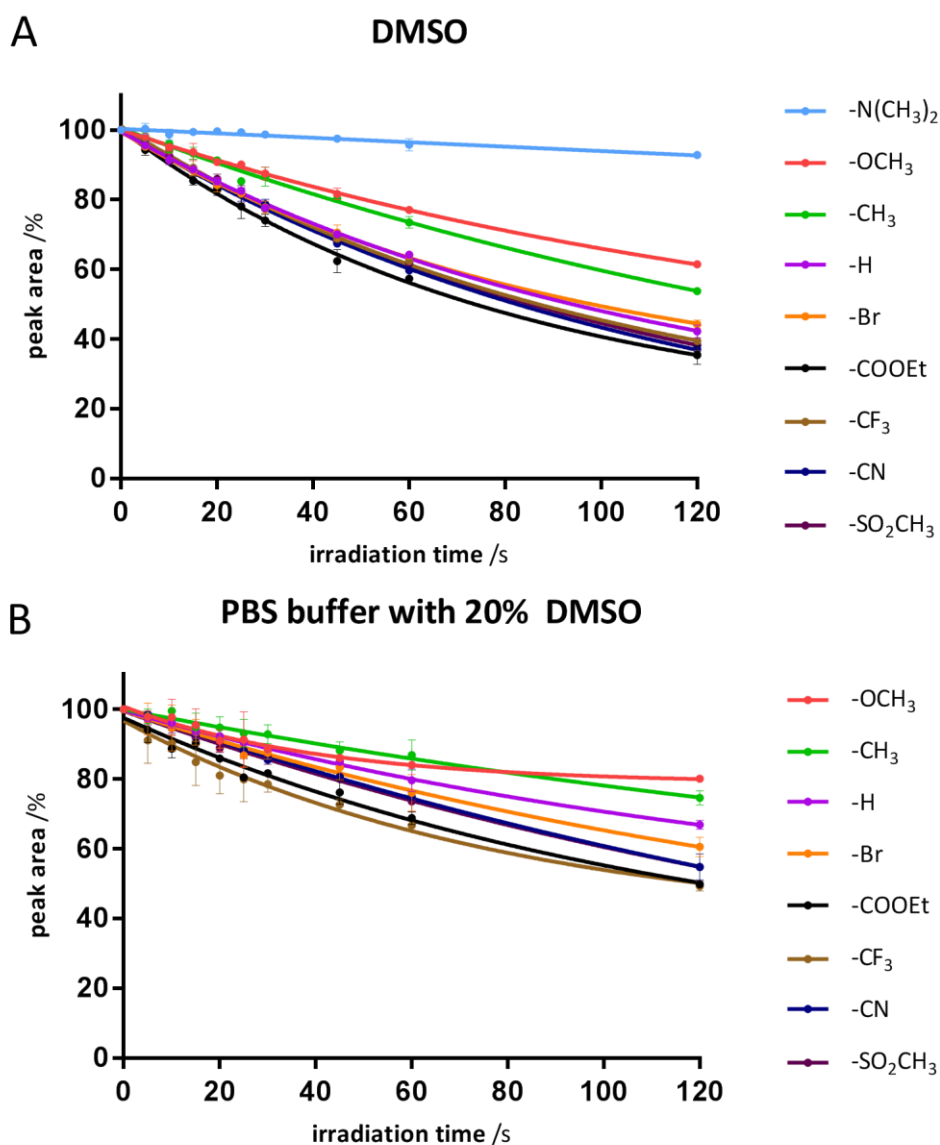


**Figure 45: Photoactivation of scaffolds 25,35-42.** 100 μl of each compound solution A) DMSO (500 μM) and B) PBS buffer with 20% DMSO (25 μM) were irradiated in a typical biochemical assay setup at 365 nm (7.5 mW) for up to 120 s. Peak areas were determined by HPLC analysis. Each value is a mean ± SD of two independent experiments.

As an important result, scaffolds **35-37**, substituted with the electron-donating substituents dimethylamine (+M), methoxy (+M) and methyl (+I), showed a significantly slower photoactivation in DMSO compared to the unsubstituted scaffold **38** (Figure 45, Table 3). In particular, the dimethylamine substituted scaffold **35** barely showed any photoactivation at all. However, scaffolds with electron-withdrawing (-I/-M) substituents such as bromo, trifluoromethyl, nitrile or sulfonylmethyl (scaffolds **39**, **41**, **42** and **25**) did not result in a significant faster photoactivation compared to the unsubstituted scaffold **38**. Hence, these substituents could not be further differentiated under the applied assay conditions. Only a trend in terms of a minor enhancement could be observed for the carboxyethyl ester substituent **40** (Table 3).

Also the sulfonylmethyl substituent of scaffold **25**, derived from the CDK inhibitor **16**, does only slightly enhance the rate of photoactivation compared to **38**. Performing the experiments in PBS with 20% DMSO (25  $\mu$ M), comparable results have been obtained, with the exception that the dimethylamine substituted scaffold **35** could not be measured due to precipitation despite the addition of 20% DMSO. Data from experiments in DMSO were therefore used for further analysis.

**Table 3: Overview of results from photochemical characterization experiments in DMSO.**

#	substituent	Hammett $\sigma_p^{155}$	absorbance (at 365 nm)	% photoactivated (after 45 s of irradiation)	Reaction rates / $\mu$ M*s <sup>-1</sup>
<b>35</b>	-N(CH <sub>3</sub> ) <sub>2</sub>	-0.83	0.123 $\pm$ 0.001	2.5 $\pm$ 0.6	0.316 $\pm$ 0.007
<b>36</b>	-OCH <sub>3</sub>	-0.27	0.118 $\pm$ 0.004	18.4 $\pm$ 1.6	2.02 $\pm$ 0.15
<b>37</b>	-CH <sub>3</sub>	-0.17	0.122 $\pm$ 0.002	19.7 $\pm$ 0.3	2.31 $\pm$ 0.13
<b>38</b>	-H	0	0.123 $\pm$ 0.010	29.9 $\pm$ 0.6	3.31 $\pm$ 0.03
<b>39</b>	-Br	0.23	0.121 $\pm$ 0.003	29.5 $\pm$ 2.2	3.27 $\pm$ 0.06
<b>40</b>	-COOEt	0.45	0.143 $\pm$ 0.000	37.6 $\pm$ 3.3	4.12 $\pm$ 0.33
<b>41</b>	-CF <sub>3</sub>	0.54	0.125 $\pm$ 0.007	31.3 $\pm$ 0.4	3.64 $\pm$ 0.17
<b>42</b>	-CN	0.66	0.123 $\pm$ 0.005	32.6 $\pm$ 0.6	3.51 $\pm$ 0.09
<b>25</b>	-SO <sub>2</sub> CH <sub>3</sub>	0.72	0.115 $\pm$ 0.000	32.0 $\pm$ 0.9	3.60 $\pm$ 0.26

Concerning an interpretation of the obtained results, the reaction rate of the unsubstituted *N*-phenylpyrimidine-2-amine scaffold **38** was taken as the reference value. Compared to that value, the reaction rates clearly decrease by attachment of a substituent with a more negative Hammett constant, implying that electron-donating substituents significantly decrease the rate of photoactivation. In contrast, by introduction of an electron-withdrawing substituent the reaction rate increases only minimally (Table 3). Plotting the Hammett constants  $\sigma_p$  vs. the determined reaction rates, a distinct correlation resulted, although a leveling of more positive  $\sigma_p$  occurs (Figure 46).

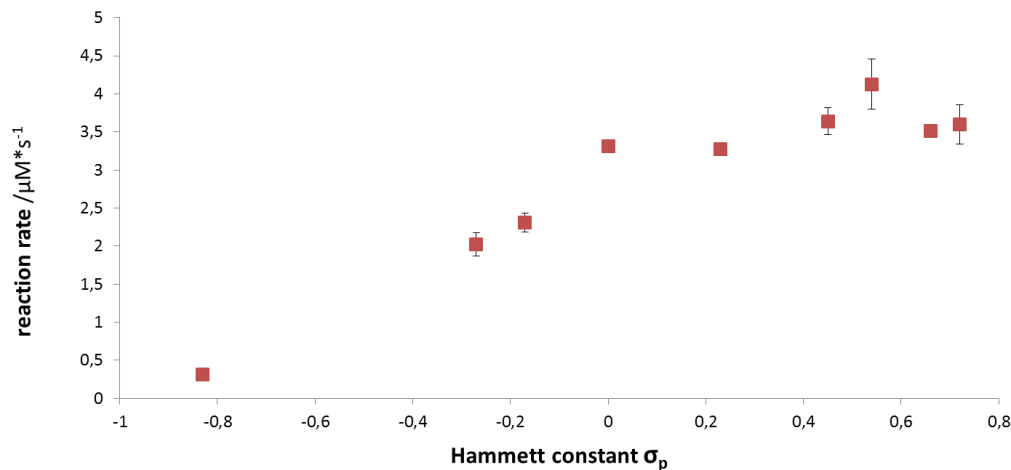


**Figure 46: Correlation between the Hammett constant  $\sigma_p$  of the respective substituent and the experimental determined reaction rates.** Squares represent means  $\pm$  SD of two independent experiments.

In order to discuss these findings, the mechanism of photocleavage of the DMNB caged scaffolds is of major interest (Figure 47). Three critical steps have been identified by studying the chemical mechanism of cleavage. In a first step (a), a photoinduced H-atom transfer from the benzylic carbon to the oxygen atom of the nitro group occurs, leading to *aci*-nitro intermediate **44**. This photoinduced H-atom transfer involves an excitation of the molecule. From the excited state of compound **44** two ground state reactions are possible, which compete with each other: reverse H-atom transfer to reform **43** (reaction b) or ground stage cyclization to form isoxazol derivative **45** (reaction c). Importantly, the cyclization (reaction c) is irreversible, ultimately leading to photocleavage. Having taken the path of photoactivation, the irreversible cyclization is followed by a ring opening (reaction d) coming to the final release of the scaffold (reaction e) and *o*-nitrosobenzaldehyde as the by-product. Since both reaction paths, photocleavage or relaxation, are possible from intermediate **44**, steps a-c were considered to be determining for the reaction rates of the photoreaction. During all steps a-c the benzylic carbon directly bound to the leaving group is in the center of action. A strong electronic effect is exerted on the benzylic carbon by the adjacent nitrogen of the leaving group due to its free ion pair. This free ion pair is further affected by both the pyrimidine ring as well as the phenyl ring with the substituents in the para-position. An electron-donating substituent is considered to increase the electron density at the nitrogen considerably. This consequently results in an enlarged electron density of the benzylic carbon, increasing its nucleophilicity. Due to this fact, the nucleophilic attack of the oxygen (reaction c) to form isoxazol derivative **45** will be diminished, potentially resulting in a shift towards the reverse H-atom transfer (reaction b). This circumstance might explain the significantly decreased reaction rates of the caged scaffolds **35-37** substituted with electron-donating substituents. Bringing the electron density of the benzylic carbon in the center of attention, electron-withdrawing substituents in the para-position should consequently enhance the photocleavage. Interestingly, the reaction rates of the caged scaffolds **39-42,25** possessing electron-withdrawing substituents are not significantly increased compared to the unsubstituted caged scaffold **38** although a relevant trend is discernible. The electron-withdrawing character of the electron deficient pyrimidine ring system might be the reason. Without an electron-donating substituent, the free ion pair of the nitrogen is already delocalized resulting in a decreased electron density at both the nitrogen atom and the benzylic carbon. By the addition of a further electron-withdrawing substituent, the electron withdrawing effect might be leveled by the pyrimidine ring resulting in similar reaction rates. In contrast to Solomek *et. al* radical stabilizing features of the residue R have not been quantified since relevant computational studies were not accessible in our lab.<sup>37</sup>

Relating to the original hypothesis, biological active compounds possessing the *N*-phenylpyrimidine-2-amine scaffold substituted with electron-donating substituents in the para-position of the phenyl system are unfavorable in terms of caging utilizing the DMNB protecting group. Contemplating the given examples of clinically approved kinase inhibitors exhibiting the considered scaffold, merely Pazopanib appears to be a potentially appropriate candidate (Figure 43). All others possess one or several electron-donating substituents at the phenyl ring rendering them potentially unsuitable for a NH caging due to a supposedly decreased rate of photoactivation utilizing the DMNB protecting group. Importantly, in order to ultimately assess suitability for the caging concept the whole molecule has to be considered.

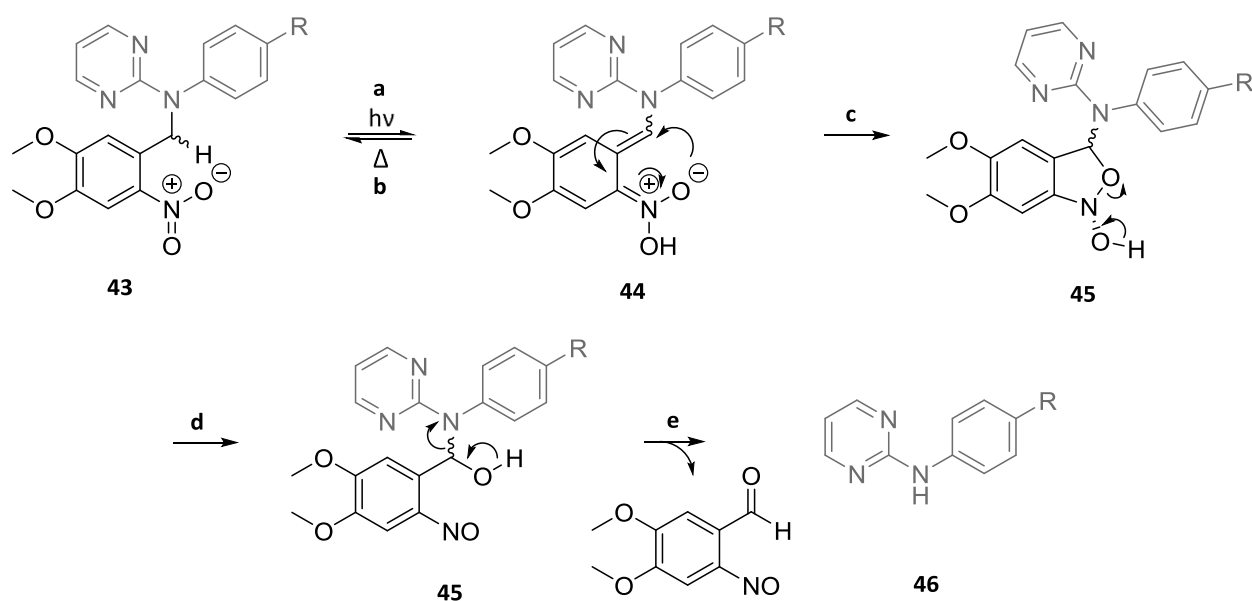


**Figure 47: Specific reaction mechanism of photocleavage of the DMNB caged scaffolds.** The leaving group and the uncaged scaffold, respectively are highlighted in grey. The relevant proton of the benzylic carbon for the H-atom transfer is particularly depicted in **43**. For clarification mechanism arrows are shown in black.



### 3.3 Visible light absorbing PPG

Despite the successful *in vitro* proof of concept, limited penetration depth of UV light into biological tissues remains, restricting the utility of the photoactivatable prodrug **23** to superficial tissues or thin cell layers (Figure 4). As a consequence, a PPG absorbing light within the bio-optical window might be highly beneficial towards biological applications in deeper tissues. In order to meet this requirement, the photosensitive *meso*-BODIPY protecting group has been chosen. The chemical structure of the *meso*-BODIPY core **8** is shown in Figure 48. The four methyl groups at the positions 1,3,5 and 7 are important for stability of the ring system, although further substitution of the methyl groups in order to modify photochemical characteristics such as the absorption and emission spectra is possible while retaining stability.<sup>166</sup> Furthermore, the 2,6-positions are particularly accessible for an electrophilic substitution.<sup>167</sup> By the introduction of different residues R at the 2,6-positions as well as substituting the methyl groups the absorption and emission spectra of the *meso*-BODIPY derivatives can be significantly altered, making blue light absorbing to even near-IR absorbing BODIPY derivatives possible.<sup>17,40,52,53,166,168,169</sup> As an example, the 1,3,5,7-methyl-substituted BODIPY core structure exhibits a light absorption maximum around 520 nm. Besides modifying the photochemical characteristics, substitution of the BODIPY core might additionally enable an improvement of pharmacokinetic parameters *e.g.* solubility, particularly relevant for potential biological applications. Importantly, the benzyl-analogous methylene group at the C8 position is essential for functioning as a PPG.<sup>17,40,170</sup> "LG" represents the leaving group thus the inhibitor to which the PPG should be applied. Hence, this methylene group, linking the leaving group with the BODIPY core has to be maintained during synthesis of a BODIPY-caged inhibitor. Although workgroups of Weinstain and Szymanski introduced a carbamate linker between the BODIPY PPG and the leaving group in order to enhance the photoactivation as well as chemical accessibility, the essential methylene group had to be maintained.<sup>52,170</sup>

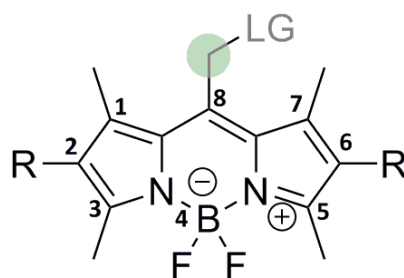


**Figure 48: Chemical structure of the *meso*-BODIPY core.** Numbering of the carbons is shown in black. The essential methylene group at the C8 position for functioning as a PPG is highlighted in grey.

### 3.3.1 Stability upon irradiation

In correspondence with the general workflow for the development of photoactivatable prodrugs inhibitor stability upon irradiation with light of the wavelength required for the prospective photoactivation has to be verified at the very beginning of the project (Figure 13). Therefore, a compound solution of CDK inhibitor **16** to which the BODIPY protecting group should be applied was irradiated with green light (530 nm, 4.6 W) for up to 25 min. Since utility of the BODIPY protecting group for biological applications was to be examined, irradiation was performed in a commonly used white opaque 96-well plate using PBS buffer with 20% DMSO as a solvent. Under this conditions the CDK inhibitor **16** appeared to be stable.

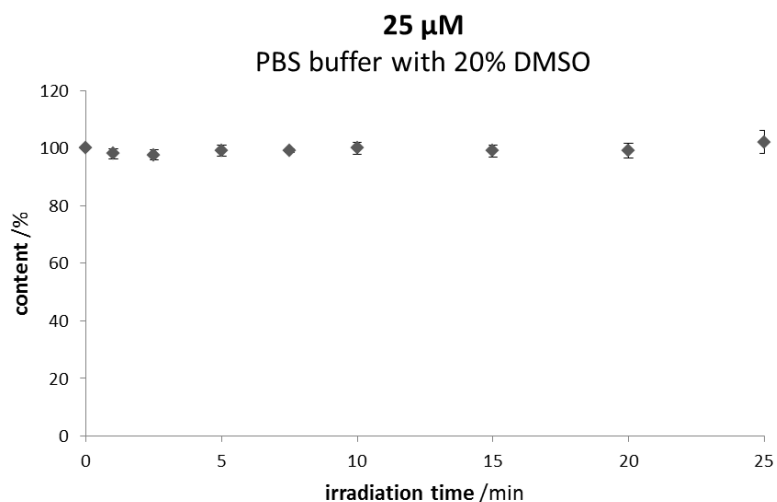


**Figure 49: Stability of CDK inhibitor 16 upon light irradiation with a wavelength of 530 nm.** A 25  $\mu$ M compound solution in PBS buffer with 20 % DMSO was irradiated at 530 nm (4.6 W) in a 96-well plate for up to 25 min. Subsequently samples were analyzed by HPLC. Each value is a mean  $\pm$  SD of two independent experiments.

### 3.3.2 Synthesis

In accordance with the synthesis of the DMNB caged prodrug **23**, direct attachment of the BODIPY protecting group to the CDK inhibitor was aimed for. Identifying an efficient strategy to introduce the BODIPY protecting group to a compound in a one-step  $S_N$  reaction might prove to be useful for caging of further biologically active compounds. Therefore, a BODIPY precursor exhibiting a suitable leaving group in terms of a nucleophilic substitution at the LG position is highly desired (Figure 48). In a first approach the 8-chloromethyl derivative **47** was synthesized as a potential precursor adapted from literature<sup>171,172</sup> (Figure 50). Importantly, the 2,6-positions remained unsubstituted. Thus, the *meso*-BODIPY core was built from 2,4-dimethylpyrrol and chloroacetyl chloride. The resulting uncomplexed intermediate was not isolated, but treated with triethylamine and boron trifluoride diethyletherate to gain the desired BODIPY precursor **47** in terms of a two-step synthesis representing a commonly used way for the preparation of *meso*-BODIPY derivatives.<sup>51</sup> The reaction was accompanied by the formation of several byproducts. The dehalogenated derivative **48** represented the major byproduct. Surprisingly, the chromatographic behavior of both the 8-chloromethyl BODIPY precursor **47** and its dehalogenated byproduct **48** were similar, making the purification by flash chromatography highly elaborate. Due to the dirty reaction as well as the elaborate purification the yield of **47** was only 16%. In a next step the attachment of the 8-chloromethyl BODIPY precursor **47** to the pharmacophoric scaffold **24** was investigated applying the formerly optimized reaction conditions from the photoactivatable CDK inhibitor project. The desired BODIPY-caged scaffold **49** could be achieved, but with a low 3% yield considerably due to the poor leaving group properties of chlorine in a nucleophilic substitution reaction.

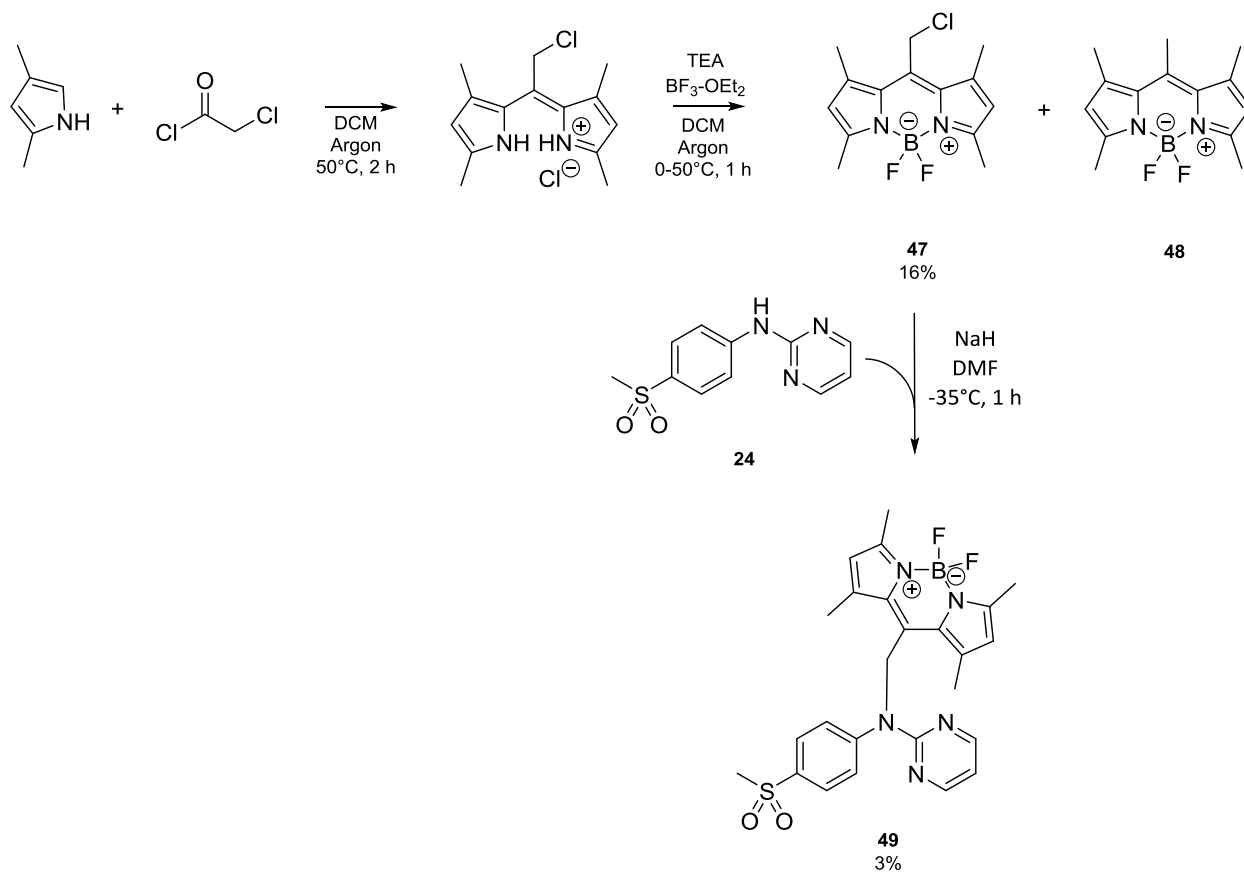


**Figure 50: Synthesis of the 8-chloromethyl precursor **47** with subsequent attachment to the pharmacophoric scaffold **24**.** Synthesis of BODIPY precursor **47** was adapted from literature<sup>171,172</sup>.

Having the BODIPY-caged scaffold **49** in hand and photochemically characterized (see chapter 3.3.3), a modified BODIPY protecting group was to be employed. In order to achieve a bathochromic shift of the light absorption spectra, the 2,6-positions of the BODIPY core were to be altered. Thus, ethyl moieties were introduced by starting from 3-ethyl-2,4-dimethylpyrrol for synthesis of the BODIPY core. In order to improve the attachment of the BODIPY precursor to the scaffold **24**, the 8-bromomethyl derivative **50** was approached starting from 3-ethyl-2,4-dimethylpyrrol and bromoacetyl chloride, but due to its instability it could not be isolated in a sufficient purity (Figure 51). Hence, a different strategy was pursued. Regarding its synthetic availability, the 8-chloromethyl derivative **51** was prepared and afterwards converted to its 8-iodomethyl derivative **52** in terms of a Finkelstein reaction with the intention of exploiting the iodine's superior properties as a leaving group.<sup>173,174</sup> The substitution of the chlorine by an iodine worked in sufficient yields, although formation of the dehalogenated byproduct could not be prevented. Again, due to comparable chromatographic behavior an entire removal of the

byproduct appeared to be unfeasible without diminishing the yield. Since 8-iodomethyl derivative **52** was further utilized as a reactant and the impurity was characterized, purity of 90% was accepted. Subsequent attachment of the BODIPY protecting group to the pharmacophoric scaffold **24** utilizing the 8-iodomethyl precursor **52** yielded the BODIPY-caged scaffold **53**. Compared to the reaction with the 8-chloromethyl BODIPY precursor **47**, the yield was moderately increased to 12%.

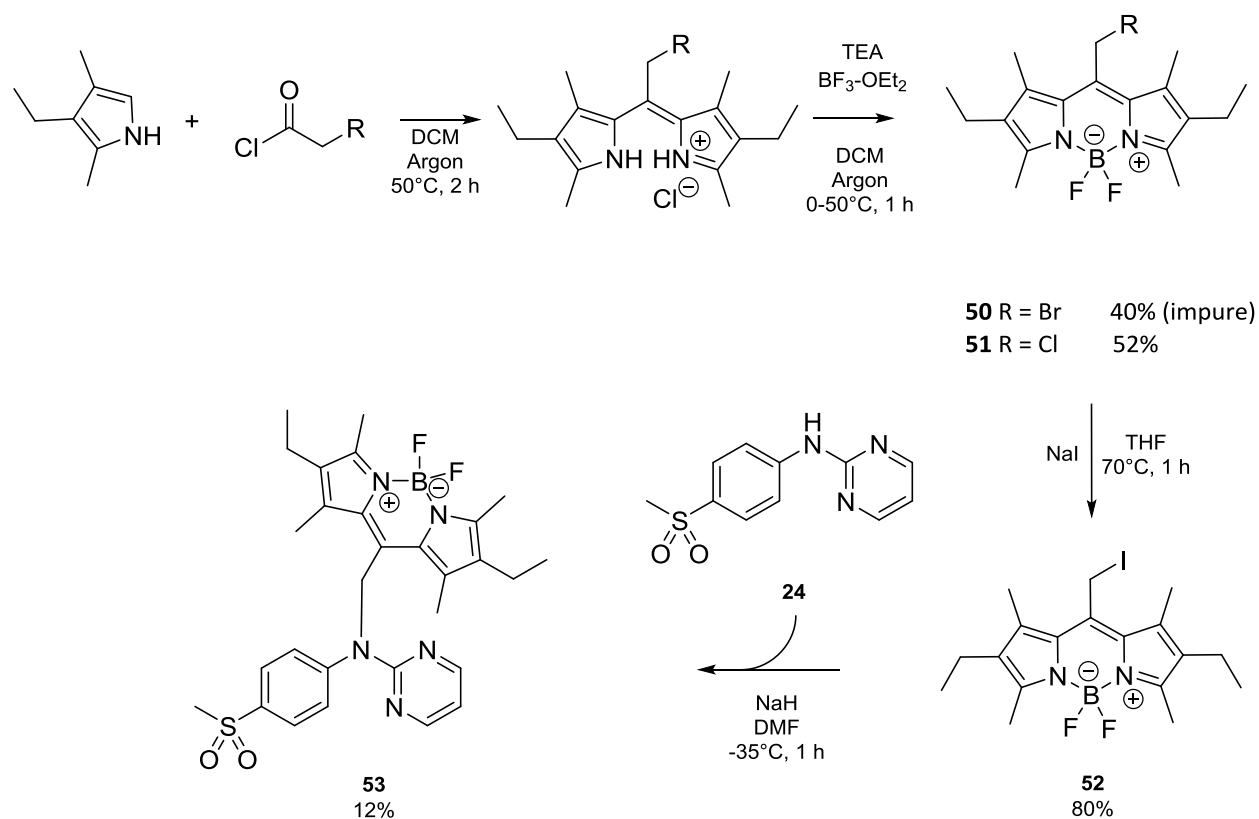


**Figure 51: Route of synthesis to cage the pharmacophoric scaffold 24 with the optimized BODIPY protecting group.** Synthesis of the BODIPY precursor **51** was adapted from literature <sup>173,174</sup>. Conversion to the 8-iodomethyl BODIPY precursor **52** was performed according to literature <sup>174</sup>.

Having found an sufficient way to cage the pharmacophoric scaffold **24** with the BODIPY protecting group, caging of CDK inhibitor **16** with the BODIPY protecting group was performed. Again, optimized reaction conditions identified using the scaffold were applied yielding the BODIPY-caged CDK inhibitor **54**. Considering a potential light sensitivity synthesis as well as purification was performed under light exclusion as much as possible.

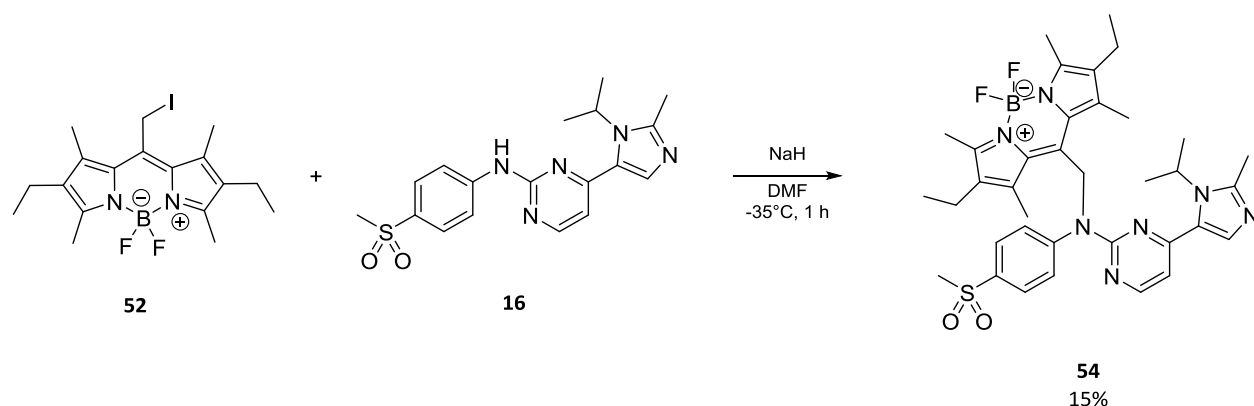


Figure 52: Synthesis of the BODIPY-caged inhibitor **54**.

The synthetic approach exploiting the accessibility of the 8-chloromethyl-BODIPY derivatives with a subsequent conversion to their 8-iodomethyl derivatives enables a direct attachment of the BODIPY protecting group to nucleophilic nitrogens *e.g.* NH moieties of biological active compounds, although the formation of dehalogenated byproducts during all steps of synthesis could not be prevented.

### 3.3.3 Photochemical characterization

In the first step of the photochemical characterization the UV/Vis absorption spectra of both BODIPY-caged scaffolds **49** and **53** have been evaluated in order to determine an ideal irradiation wavelength by identifying respective absorption maxima. This represents a crucial step for characterizing the utilized BODIPY protecting groups, since a high light absorption at the irradiation wavelength is mandatory for an efficient photoactivation.

The 2,6-unsubstituted BODIPY-caged scaffold **49** exhibited a broad unsymmetrical absorption band with a maximum around 520 nm (Figure 53). From 460 nm the light absorption increases slowly up to the maximum whereas the light absorption drops sharply above 520 nm. By the intension of achieving a bathochromic shift of the light absorption maximum, the second BODIPY-caged scaffold **53** was prepared where two ethyl groups were introduced at the 2,6-positions of the BODIPY core. The results showed that the absorption maximum shifted to 550 nm. In addition to this bathochromic shift the light absorption increased as well compared to the 2,6-unsubstituted BODIPY-caged scaffold **49**.

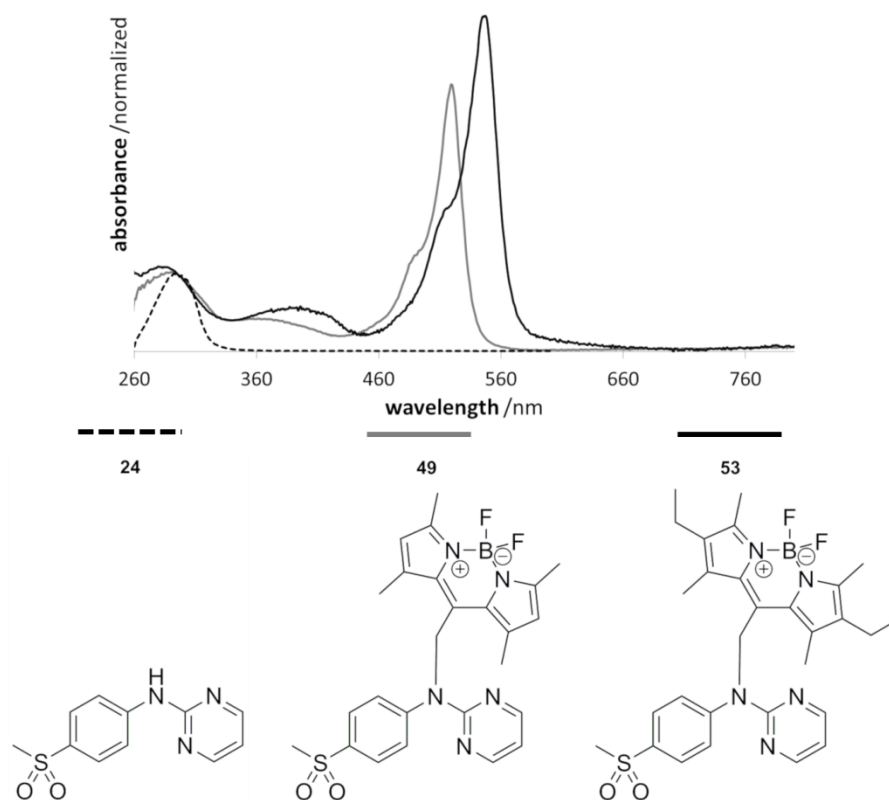


**Figure 53:** UV/Vis absorption spectra of the BODIPY-caged scaffolds **49** and **53**. UV/Vis absorption spectra of both BODIPY-caged scaffolds **49** (grey) and **52** (black) were recorded in DMSO and normalized to the UV/Vis absorption spectrum of pharmacophoric scaffold **24** (dashed).

To examine and compare the rate of the photoactivation of both BODIPY-caged scaffolds **49** and **53** an irradiation wavelength of 530 nm was chosen since both compounds exhibit a decent light absorption at 530 nm. However, the BODIPY-caged scaffold **53** showed a significantly higher light absorption at 530 nm compared to **49**. Importantly, the uncaged scaffold **24** exhibited no light absorption above 330 nm implying that an interference of **24** while photoactivation with light of 530 nm is not possible. Thus, a custom made LED lamp with an emission wavelength of 530 nm with a maximum power of 4.6 W was utilized for the irradiation experiments. Thereby, compound solutions in DMSO of both BODIPY-caged scaffolds were irradiated in a 96-well plate for up to 20 minutes (Figure 54). Samples were subsequently analyzed by HPLC and LC-MS in order to determine contents of both the caged and uncaged species. Irradiating the 2,6-unsubstituted BODIPY-caged scaffold **49** for 20 minutes resulted in a 40% photoactivation (Figure 54). Introduction of the ethyl moieties at the 2 and 6 position led to a significant increase of the photoactivation rate. After 20 minutes of irradiation the 2,6-diethyl-



substituted BODIPY-caged scaffold **53** was fully cleaved. This increase in the rate of photoactivation might be due to the higher light absorption at 530 nm of **53** compared to **49**.

Both BODIPY-caged scaffolds were prepared and photochemically characterized with the intension of not only finding an efficient way to chemically introduce the BODIPY protecting group to an inhibitor but also identifying a BODIPY protecting group with a fast photoactivation. By that reason the 2,6-diethyl-substituted BODIPY protecting group was further chosen for caging of the CDK inhibitor **16**.

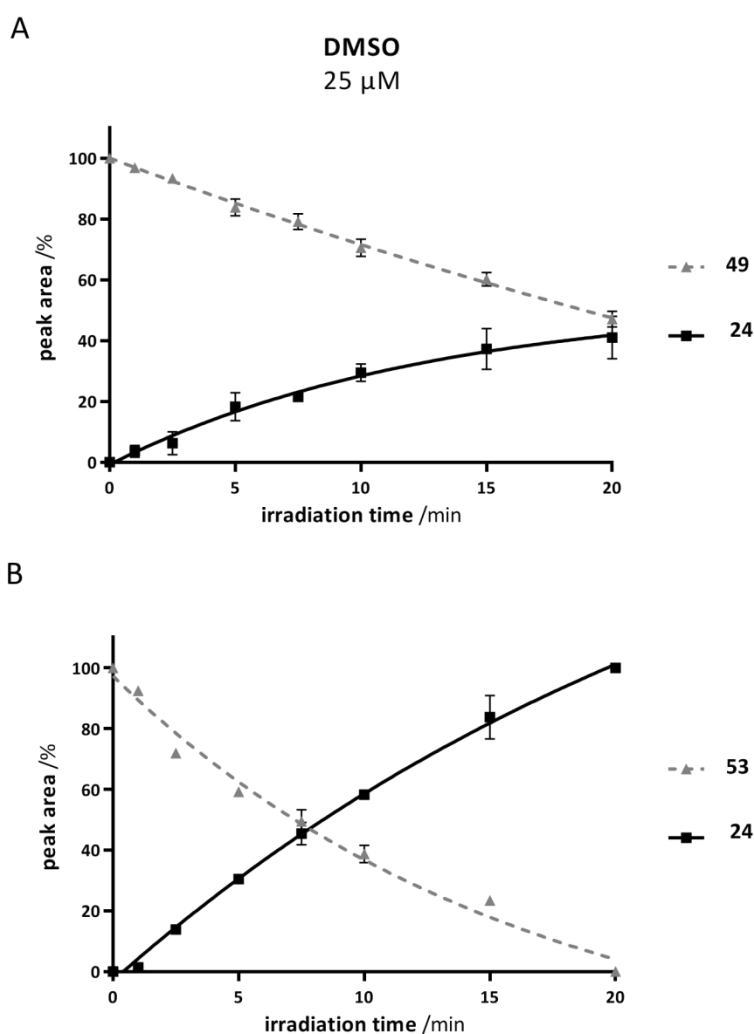


**Figure 54: Photoactivation of the BODIPY-caged scaffolds **49** (A) and **53** (B).** 100  $\mu$ L of each compound solution in DMSO (25  $\mu$ M) were irradiated in a well of a 96-well plate for the indicated time at 530 nm (4.6 W) and analyzed by HPLC (n = 2) and LC-MS. The amount of the caged compound (diamonds) is plotted against the released scaffold **24** (squares). Each value is a mean  $\pm$  SD of two independent experiments.

As shown in chapter 3.3.2, introduction of the 2,6-diethyl-substituted BODIPY protecting group to CDK inhibitor **16** worked applying the prior optimized  $S_N$  reaction conditions to yield the 2,6-diethyl-substituted BODIPY-caged inhibitor **54** (Figure 52). Having **54** in hand, its UV/Vis absorption spectrum was recorded. In agreement with data from the respective BODIPY-caged scaffold **53**, a strong absorption band with a maximum at 550 nm was observed (Figure 55). Since a LED lamp with an emission maximum of 530 nm was available, the rate of photoactivation was examined at an irradiation wavelength of 530 nm although the light absorption at 550 nm would be significantly higher. With the aim of determining utility for future biological application the irradiation experiments were again performed in a 96-well plate at a concentration of 25  $\mu$ M. Unfortunately, due to a poor water solubility of **54** the rate of photoactivation could not be determined using PBS buffer as a solvent despite adding up to 30% of DMSO. The applied concentration of 25  $\mu$ M for the photoactivation experiments could not be decreased due to the limit of quantification of the HPLC analysis. However, all photoactivation experiments were performed as close to *in vitro* conditions as possible. As an important result, 80% of the BODIPY-caged inhibitor **54** were activated after 10 minutes of irradiation (Figure 56). Furthermore, a full photoactivation was achieved after 15 minutes of irradiation at 530 nm.

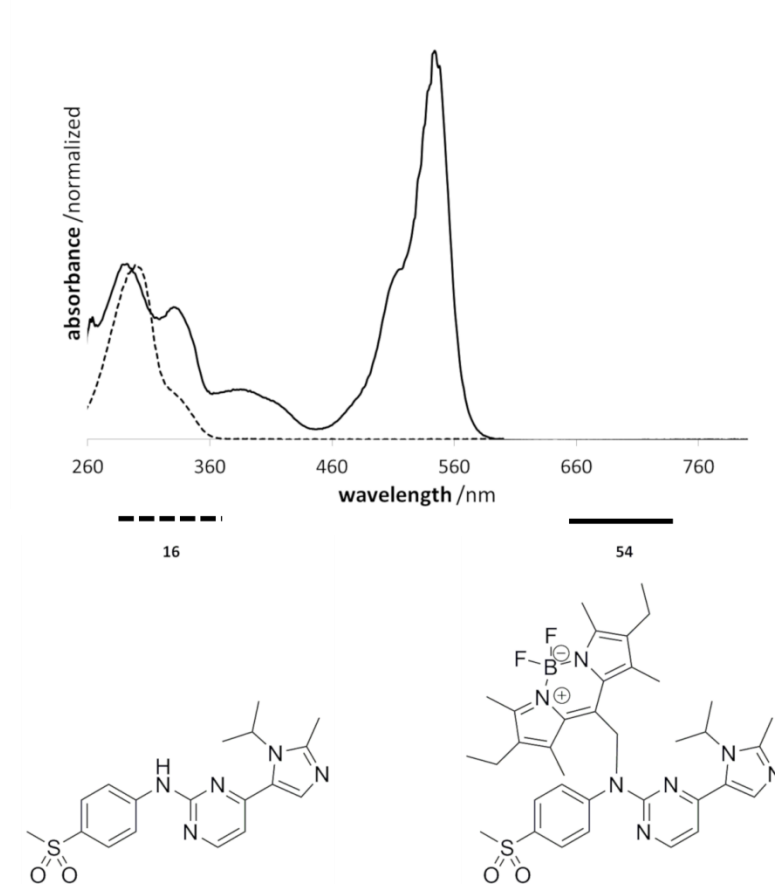


**Figure 55: UV/Vis absorption spectrum of the BODIPY-caged CDK inhibitor 54.** The UV/Vis absorption spectrum of the BODIPY-caged CDK inhibitor **54** (black) was recorded in DMSO and normalized to the UV/Vis absorption spectrum of the uncaged CDK inhibitor **16** (dashed).

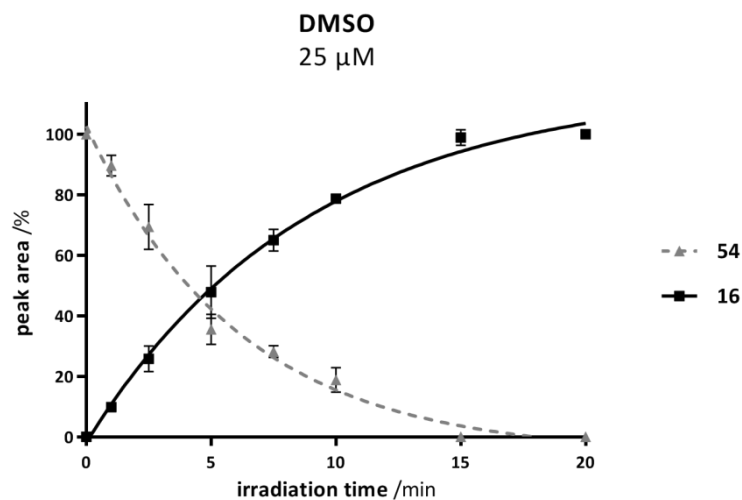


**Figure 56: Photoactivation of the BODIPY-caged CDK inhibitor 54.** 100  $\mu$ L of the compound solution in DMSO (25  $\mu$ M) were irradiated in a well of a 96-well plate for the indicated time at 530 nm (4.6 W) and analyzed by HPLC ( $n = 2$ ) and LC-MS. The amount of the caged compound (diamonds) is plotted against the released CDK inhibitor **16** (squares). Each value is a mean  $\pm$  SD of two independent experiments.

### 3.3.4 Biological evaluation

Having determined the photoactivation rate of the BODIPY-caged prodrug **54**, the question whether this rate is sufficient to be useful for biological applications had to be answered next. An irradiation inducing the photoactivation of a photoactivatable prodrug should not affect cell viability. In order to investigate the cell's maximum tolerable light dose of the respective wavelength, so-called light titration experiments were performed utilizing the Panc89 cell line which was used for the photoactivatable CDK inhibitor project. Therefore, Panc89 cells were irradiated at 530 nm (4.6 W) for different durations up to a maximum of 30 minutes with the same LED lamp used for the photochemical characterization. The number of living cells is subsequently detected using a resazurin assay. The cell growth is determined in relation to the number of living cells at the day of treatment in order to distinguish between a cytostatic (> 0% cell growth) and cytotoxic effect (< 0% cell growth). Interestingly the cell growth increased significantly by irradiation up to 5 minutes to 150% cell growth compared to the DMSO control (Figure 57). Not until 15 minutes of irradiation the cell growth starts to be impaired significantly. Importantly, even after 30 minutes of irradiation no cytotoxic effect was observed, although the cell growth was diminished to 0%.

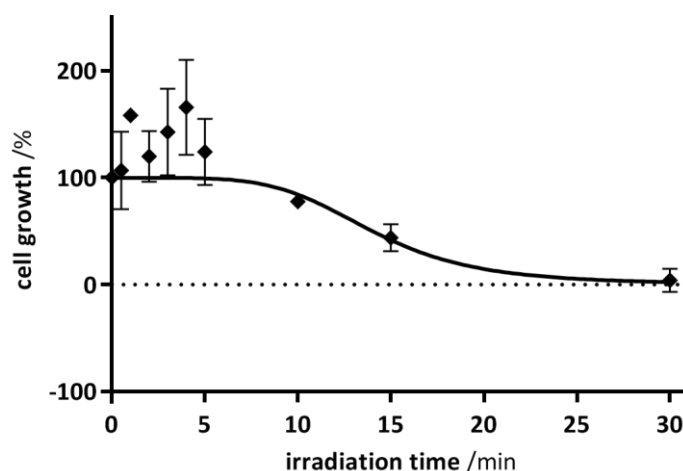


**Figure 57: Light titration experiment with Panc89 cells.** Panc89 cells were treated with light of a wavelength of 530 nm (4.6 W) using the same LED lamp used for the photochemical characterization of **54**. After two days the cell growth was determined using a resazurin assay in relation to the number of living cells at the day of treatment. Data represents mean  $\pm$  SEM from three independent experiments performed in a quadruplicate.

Concerning the results from synthesis, photochemical characterization and biological evaluation in this project, utility of the 2,6-diethyl-substituted BODIPY protecting group for biological applications is considered to be given. Although 15 minutes of irradiation are required for an entire photoactivation of the BODIPY-caged prodrug **54** under experimental conditions, a compromise of 10 minutes of irradiation *in vitro* was chosen in order to minimize cell damage by light, but restore the biological activity at the same time. The planned biological evaluation of **54** with and without irradiation will shed light to this hypothesis. In the view of the UV spectrum of the BODIPY-caged prodrug **54**, a considerably faster photoactivation might be enabled by adapting the irradiation wavelength to its absorption maximum of 550 nm. Regarding studies from the groups of Weinstain and Symanzski a carbamate linker implemented between the BODIPY protecting group and the inhibitor might be beneficial to the rate of photoactivation as well, although 15 minutes of irradiation are acceptable in the terms of a biological application.<sup>52,170</sup> Yet the issue of poor water solubility of **54** remains. Due to the introduction of the ethyl groups to the BODIPY core at the 2,6-positions, the water solubility further decreased. However, the issue of poor water solubility can be solved by introduction of hydrophilic moieties *e.g.* sulfonate groups to the BODIPY protecting group, enhancing the water solubility dramatically, whereas absorption and emission maxima do not change significantly.<sup>51,167,175</sup> In conclusion the visible light absorbing BODIPY protecting group exhibits unique qualities regarding the utility as a PPG for biological applications, especially since readily substitution of the ring systems enables custom-tailored BODIPY protecting groups for specific applications.

### 3.4 Activation by Cherenkov radiation

In order to overcome the issue of a limited light penetration of UV light into biological tissues, another strategy next to the implementation of a visible light absorbing PPG was approached. If the required irradiation is not able to reach deeper tissue sites it might be an option to induce the irradiation in place. Since the most commonly utilized DMNB protecting group is cleaved upon irradiation with near UV light, induction of UV light has to be achieved. Interestingly, Cherenkov radiation, induced by fast moving particles such as electrons or positrons *e.g.* emitted during beta decay of certain radionuclides, exhibits an emission maximum in the near UV range. Thus, the hypothesis whether *e.g.* a beta emitter is able to activate a DMNB caged prodrug by induction of Cherenkov radiation emerged. Besides beta emitting radionuclides, external beam radiation commonly used for radiation tumor therapy in clinic is able to induce Cherenkov radiation as well.<sup>56</sup> Thereby, charged particles such as electrons are vastly accelerated by a linear particle accelerator. If the charged particles' speed exceeds a certain threshold within a medium such as waters, Cherenkov radiation is induced. Although the induction of Cherenkov radiation is subject to charged particles the effect might as well be observed by the use of high energy photon radiation due to Compton scattering. Thereby, a photon is scattered by a charged particle such as an electron resulting in a decrease in energy of the photon accompanied by an energy transfer to the recoiling electron.<sup>176</sup> The energy rich recoiling electron might subsequently induce Cherenkov radiation. Linear particle accelerators might be capable of activating a DMNB caged prodrug due to induction of Cherenkov radiation in solution by high energy charged particles such as electrons or potentially high energy photons. Thus, a collaboration with the clinic for nuclear medicine as well as the clinic for radiation therapy at the university hospital (UKSH) in Kiel has been established with the intention of addressing both hypotheses.

### 3.4.1 Activation utilizing beta emitting radionuclides

First, the capability of Fluorine-18 ( $^{18}\text{F}$ ) to activate the DMNB caged prodrug **23** was investigated.  $^{18}\text{F}$  was chosen due to its everyday use for positron-emission tomography (PET) in the clinic as well as its short half-life of 110 min. Its decay mode is characterized by mainly positron emission with a maximum decay energy of 0.63 MeV, which is just above the threshold for induction of Cherenkov radiation in water (0.26 MeV).<sup>177,178</sup> Thus, the readily cleavable DMNB caged prodrug **23** was incubated with  $^{18}\text{F}$  from two different radioactive sources and contents of both the caged and uncaged species were quantified by HPLC analysis after different times of incubation. Noteworthy, the HPLC was placed behind appropriate shielding and blocked for 1-2 days due to its radioactive contamination. Furthermore, incubation was performed in an amber glass HPLC vial in the autosampler of the HPLC in order to avoid opening the radioactive incubation vessel during the experiment. The first experiments were performed using pure  $^{18}\text{F}$ . To exclude a possible migration of  $^{18}\text{F}$  into the glass of the incubation vial, following experiments were performed with  $^{18}\text{F}$ Fluorodeoxyglucose ( $^{18}\text{F}$ FDG), which is commonly used for tumor imaging by PET. Since **23** exhibited a poor aqueous solubility, addition of an organic solvent such as DMSO or methanol as a solubilizer was inevitable, although the induction of Cherenkov radiation is almost exclusively investigated in pure water. Notably, the threshold condition for the induction for Cherenkov radiation as well as its intensity is strongly dependent on the refractive index of the medium rendering the solvent a relevant parameter.<sup>57</sup> With the intension of identifying an activation upon incubation with a radioactive source, we designed five screening experiments. Thereby, the source of radioactivity, the amount of radioactivity, the solvent, the total volume as well as the inhibitor concentration were altered. All of these variables were considered as relevant for induction of Cherenkov radiation.

Importantly, no activation was observed incubating **23** with the beta emitter  $^{18}\text{F}$  for up to 24 h at any applied condition (Table 4). In order to exclude false negative results, samples were irradiated with UV light after incubation to demonstrate that a photoactivation of **23** is possible under the applied conditions. However, the intensity of the Cherenkov radiation is strongly dependent on the decay energy of the utilized radionuclide.<sup>177</sup>  $^{18}\text{F}$ 's decay energy of 0.63 MeV is just above the threshold condition for induction of Cherenkov radiation in water and thus might be insufficient to induce an activation of **23**.

Table 4: Results from activation experiments using  $^{18}\text{F}$  as the radioactive source.

#	radioactive source	radioactivity /Mbj	solvent	total volume /ml	compound concentration / $\mu\text{M}$	result
1	$^{18}\text{F}$	20	10% DMSO in water	1	50	no activation
2	$^{18}\text{F}$	200	10% DMSO in water	1	50	no activation
3	$^{18}\text{F}$	150	water	1	50	no activation
	positive control	samples 1-3 irradiated with UV light after incubation				activation
4	$^{18}\text{FDG}$	107	50% MeOH in water	0.4	125	no activation
5	$^{18}\text{FDG}$	120	50% MeOH in water	0.4	125	no activation
	positive control	samples 4-5 irradiated with UV light after incubation				activation



To examine the hypothesis of an insufficient decay energy,  $^{18}\text{F}$  was replaced by Gallium-68 ( $^{68}\text{Ga}$ ) as the beta emitter. Again, decay of  $^{68}\text{Ga}$  is characterized by 88% positron emission but with a significantly higher maximum decay energy of 1.9 MeV.<sup>178</sup> Because of its short half-life of 68 min,  $^{68}\text{Ga}$  had to be prepared in house using a gallium-68 generator. Thereby  $^{68}\text{Ga}$  is enriched by decay of its mother nuclide Germanium-68 and eluted from the generator by the use of hydrochloric acid (HCl). Since the acid  $^{68}\text{Ga}$  solution is highly radioactive, experiments had to be designed as simple as possible in order to minimize potential radiation exposure. Therefore, in a first approach, a solution of the DMNB caged prodrug was directly incubated with the acid  $^{68}\text{Ga}$  solution. To exclude that the low pH present in the samples results in an activation of the prodrug, a negative control with non-radioactive  $^{69}\text{Ga}$  in 1 M HCl was prepared and concurrently quantified. Interestingly, incubation with  $^{68}\text{Ga}$  in 1 M HCl results in a 26% activation of **23** within the first 2 hours whereas the negative control showed full stability at the acid conditions (Figure 58). After 2 hours of incubation the effect terminates leaving a stable solution.

**Table 5: Results from activation experiments using  $^{68}\text{Ga}$  as the radioactive source.**

#	radioactive source	radioactivity /Mbq	solvent	total volume /ml	compound concentration / $\mu\text{M}$	result
6	$^{68}\text{Ga}$	900	20% DMSO in 1 M HCl	1.25	50	26% activation
	$^{69}\text{Ga}$	-	20% DMSO in 1 M HCl	1.25	50	no activation
7	$^{68}\text{Ga}$	900	20% DMSO in buffer	1.25	50	<b>to be performed</b>

The obtained results remain to be reproduced using a solvent with a neutral pH. Therefore, an efficient way to neutralize the radioactive  $^{68}\text{Ga}$  solution in HCl has to be identified. Significant dilution of the radioactive  $^{68}\text{Ga}$  solution should be avoided in order to minimize the loss of radioactivity. Furthermore the increase in ionic strength should be kept as small as possible. Since neutralization has to be performed behind radioactive shielding using robotic arms, the use of Eppendorf pipettes is precluded. However, the proof of activation upon incubation with  $^{68}\text{Ga}$  in a neutral solvent is planned to be performed.

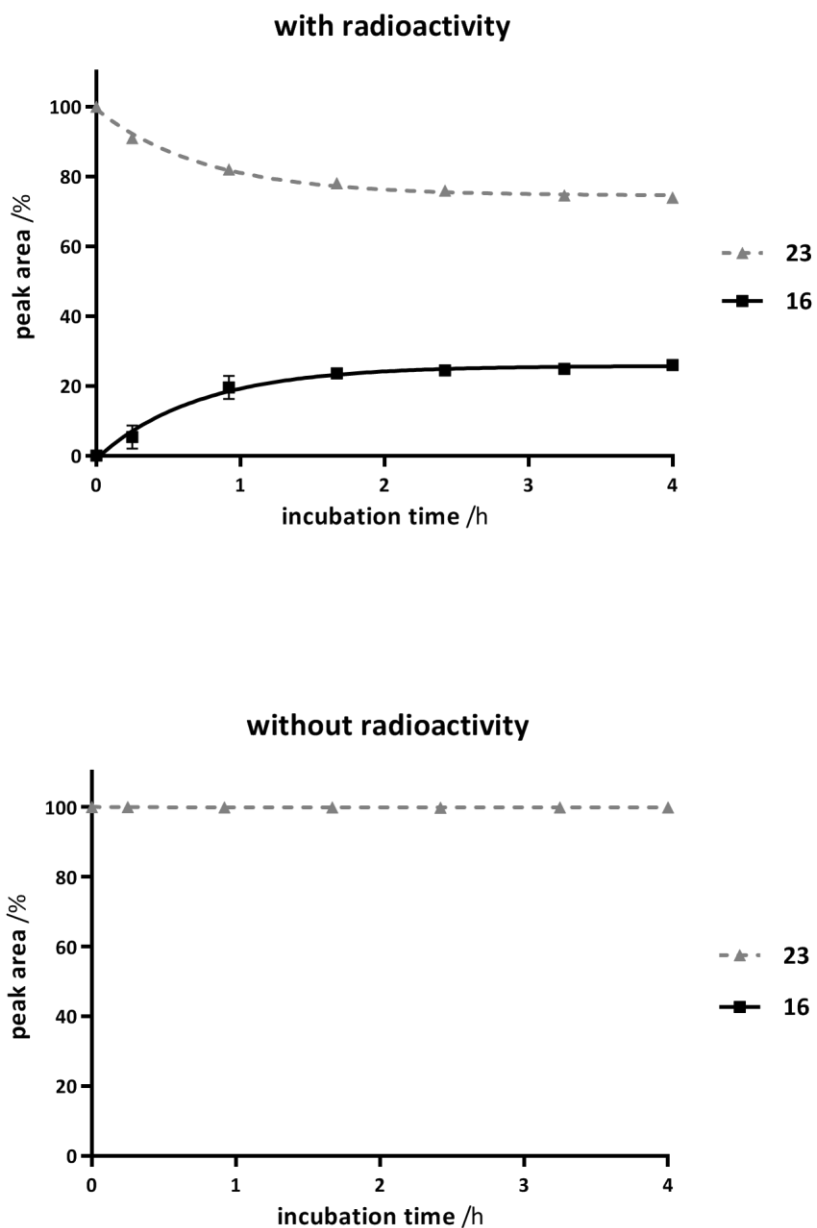


**Figure 58: Activation of DMNB caged prodrug **23** upon incubation with the beta emitter  $^{68}\text{Ga}$  in 1 M HCl.** Top: 1.25 ml compound solution of **23** (50  $\mu\text{M}$ , 20% DMSO in 1 M HCl) with 900 Mbq  $^{68}\text{Ga}$  were prepared in an amber glass HPLC vial and incubated for 4 hours in the autosampler of a HPLC. After the indicated time points peak areas of both the caged (**23**) and uncaged (**16**) species were determined using HPLC analysis. Bottom: a compound solution of **23** (50  $\mu\text{M}$ , 20% DMSO in 1 M HCl) with non-radioactive  $^{69}\text{Ga}$  was prepared in an amber glass HPLC vial and analogously incubated in the same HPLC autosampler as a negative control. Peak areas were determined after the indicated time points by HPLC analysis. Each value is a mean  $\pm$  SD of three independent experiments.

### 3.4.2 Activation utilizing external radiation beams

Having seen evidence for uncaging of **23** by incubation with a beta emitter, the utility of external radiation beams from a linear particle accelerator usually used for radiation therapy in clinic were investigated in a second approach. In a first experiment, a 1 ml compound solution of the DMNB caged prodrug **23** in methanol was exposed to a beam of 6 MeV photons in a translucent HPLC vial. A maximum energy dose of 10 gray was applied. Peak area determination of both the caged and uncaged species by HPLC analysis determined that under these conditions no activation occurred compared to the negative control. Although due to Compton scattering, high energy photons cause energy rich electrons in solution, a subsequent sufficient induction of Cherenkov radiation in methanol might not have occurred (Table 6). Therefore, the second experiment was performed utilizing high energy electron radiation. A 1.5 ml compound solution of **23** in water with 25% DMSO was brought into an 6 MeV electron beam of the linear particle accelerator and a maximum radiation dose of 3 Gy was applied. The addition of DMSO was inevitable to avoid compound precipitation, although the role of organic solvents in the induction of Cherenkov radiation is unclear. Contents were subsequently determined using HPLC analysis before and after the irradiation. In addition a negative control was conducted. Again, no activation was observed under these condition. Since the intensity of Cherenkov radiation is strongly dependent on the energy of the charged particles, a third experiment was performed using electrons with a significantly higher energy of 18 MeV. Importantly, the total volume was increased to 4 ml as well in order to enhance the distance the electrons have to cover within the sample solution. However, an activation of **23** did not occur. As usual, photoactivation of all three samples upon UV irradiation was proven afterwards as a positive control.

Results from the experiments utilizing the radiation beam of a linear particle accelerator imply that the Cherenkov radiation induced under the chosen conditions is not sufficient to cleave the PPG from the caged prodrug **23**. This fact could be due to several reasons. The intensity of Cherenkov radiation induced by particle beams might be generally too low to induce bond cleavage. Particularly, since radiation exposure is no longer than a couple of seconds in order to reach the maximum radiation dose. Furthermore, as emphasized above, the impact of organic solvents such as DMSO on the induction of Cherenkov radiation is unclear. However, the total volume of the irradiated medium is considered to be a critical parameter. In order to address the issue of a critical distance charged particles have to cover, the use of a water tank around the sample vial might be highly beneficial to the induction of Cherenkov radiation.<sup>179</sup> Translucent HPLC vials containing the compound solutions, fixed in the middle of the tank would thereby be completely surrounded by water. This experimental setup would not only allow a significant enhancement of the interaction between the high energy particles and the solvent but also allow the use of solely water as the medium in which the Cherenkov radiation should be induced.

**Table 6: Results from activation experiments using external particle beams from a linear particle accelerator.**

#	radiation	energy /MeV	maximum dose /Gy	solvent	volume /ml	compound concentration /μM	result
1	Photons	6	10	MeOH	1	50	no activation
2	Electrons	6	3	25% DMSO in water	1.5	50	no activation
3	Electrons	18	3	25% DMSO in water	4	50	no activation
	positive control			samples 1-3 irradiated with UV light			activation
4	Electrons	18	3	sample recessed in water tank		50	<b>to be performed</b>

## 4 Conclusion

---

The unique qualities of the caging concept have been utilized for a variety of applications for decades. Surprisingly, only a few photoactivatable prodrugs in biological settings have been described yet despite the fact that the caging technique allows targeting of two major issues: severe side effects and acquired resistances. Both issues are commonly linked with novel potent drugs. Since implementation of the caging concept is limited to only a selected group of drug classes so far, the main focus of the present thesis was its extension to further drug classes. Since potent drugs with strong side effects may benefit particularly from the caging technique, a small-molecule microtubule-targeting agent (smMTA) as well as a CDK inhibitor have been chosen. Hence, the present thesis comprised the development of both a photoactivatable smMTA and CDK inhibitor by the following of a specifically evolved workflow.

## 4.1 Photoactivatable small-molecule microtubule-targeting agent

This project included the successful design, synthesis, photochemical characterization and biological evaluation of a photoactivatable smMTA. Identified as a potent inhibitor of microtubule polymerization, smMTA **17** represented an attractive lead for the development of an anti-brain tumor drug.<sup>104</sup> Due to its well understood photochemistry as well as its rapid and clean photocleavage upon irradiation with UV light, the 4,5-dimethoxy-2-nitrobenzyl protecting group (DMNB) was the PPG of choice.<sup>28</sup> Stability towards UV irradiation of **17** was proven at the very start of this project in order to meet this indispensable requirement. Since molecular modeling studies were unsuitable to reveal **17**'s pharmacophore, the decision where to attach the PPG was based on data from earlier structure-activity relationship studies.<sup>104</sup> Thereupon, the terminal phenolic group was selected for caging due its relevance for biological activity as well as its chemical accessibility. The smMTA **17** was subsequently synthesized following a characterized 4-step synthesis route and consequently caged to obtain its DMNB caged prodrug **20** in decent yields.<sup>104</sup> From this point, due to its light sensitivity, light exposure had to held to a minimum, rendering the purification particularly elaborate. Subsequent photochemical characterization demonstrated a quantitative, fast and clean activation upon UV irradiation.

An extensive biological evaluation followed to assess the utility of the DMNB caged prodrug for biological applications. Several biological assays have been successfully adapted for the purpose of mainly addressing two objectives: biological inactivity of the caged prodrug as well as its recovery of biological activity upon light irradiation. First of all, attachment of the DMNB protecting group to the terminal phenolic group clearly diminished biological activity. Examining tubulin polymerization, cell viability, microtubule-interference and induction of apoptosis, only marginal residual activity of the caged prodrug could be determined. Importantly, biological activity in cell viability assays was reduced by factor 55 using U251 cells respectively factor 185 working with primary tumor cells, RN1. Secondly, the photoactivation *in vitro* using UV light worked perfectly. Even a to 30 s reduced irradiation time, working with the primary cancer cells RN1 led to an almost complete restoration of biological activity. Hence, providing a notable proof of concept *in vitro*.

In conclusion, the DMNB caged prodrug **20** represents the first photoactivatable smMTA with a high utility for biological applications to the best of my knowledge. Specifically, **20** could serve as an attractive tool compound for studying of microtubule dynamics or binding kinetics of smMTAs. Importantly, the required irradiation dose of UV light does not affect cell viability of the primary brain tumor cells RN1, enabling an exciting option for novel therapeutic approaches regarding brain tumors. A valuable starting point for the development of an advanced photoactivatable smMTA for the treatment of brain tumors was therefore characterized. A targeted irradiation would allow high local drug concentrations in cancer-afflicted tissues while reducing systemic side effects.

Although, for future applications several barriers have to be broken down. Penetration of the blood-brain-barrier is indispensable for anti-brain tumor drugs rendering small-molecule MTAs particularly attractive. Addition of a PPG necessarily increases the molecular weight of a smMTA potentially decreasing the penetration ability of a photoactivatable prodrug. However, pharmacokinetic properties such as solubility and the ability to penetrate membranes such as the blood-brain-barrier of photoactivatable prodrugs can be governed by specific substitution of the PPG. For instance, the water solubility of the DMNB protecting group can be significantly improved by the introduction of a carboxylic acid substituents.<sup>180,181</sup> Importantly, the ability of a photoactivatable smMTA to cross the blood-brain-barrier has to be assessed prior a potential medicinal application.

Furthermore, due to the limited penetration depth of UV light, surgery is mandatory for a targeted irradiation of brain tumors with UV light. Even an advanced visible-light absorbing PPG such as BODIPY or two-photon uncaging might not overcome this restriction, since the irradiation has to penetrate the skull. However, utilization of Cherenkov radiation induced by high energy particle beams of linear particle accelerators could be highly beneficial although the question whether its intensity is enough to activate the prodrug in sufficient quantities remains to be answered.

## 4.2 Photoactivatable CDK inhibitor

This project comprised the successful application of the caging technique to CDK inhibitor **16**. It included the design, synthesis, photochemical characterization and biological evaluation of a DMNB caged CDK inhibitor.

Having proven stability towards UV irradiation, molecular modelling studies were performed to reveal the binding mode of **16** to its target kinase, CDK2. By forming a critical H-bond towards the hinge region of the kinase, its free amino function was identified as crucial for ligand affinity and biological activity. Hence, caging aimed for that specific amino function. Again, dummy experiments were implemented utilizing the pharmacophoric scaffold **24** prior approaching the caging of the actual inhibitor. As an important insight in both projects, the implementation of dummy experiments, utilizing only the relevant substructures or pharmacophore respectively, turned out to be highly useful in order to save time and valuable drug material. Working with the pharmacophoric scaffold **24** an efficient synthetic strategy to attach a PPG to the amino function of the *N*-phenylpyrimidine-2-amine scaffold in terms of nucleophilic substitution reaction was identified using sodium hydride at -30°C. These optimized reaction conditions were not only successfully applied for the actual CDK inhibitor **16** but for both the scaffold project as well as the BODIPY project. Subsequent photochemical characterization highlighted a rapid and clean photoactivation upon UV irradiation of the DMNB caged prodrug **23**. Since the project aimed to develop photoactivatable prodrugs for biological applications, photoexperiments were designed as close to biological assay conditions as possible. This strategy turned out particularly helpful regarding the evaluation of the required irradiation dose for *in vitro* photoactivation, although true biological conditions could not be simulated due to limits of quantification as well as poor water solubility of the caged prodrug.

Seeing the exceptional fast photoactivation of **23** under experimental conditions, the question whether that prompt photoactivation is generally valid for amino caged *N*-phenylpyrimidine-2-amine scaffolds arose. Hence, the hypothesis was addressed by investigating the photoactivation of differently substituted DMNB caged *N*-phenylpyrimidine-2-amine scaffolds. Specifically, the electron-donating and -withdrawing effects of para-substituents to the caged amino function on the rate of photoactivation were assessed. Importantly, electron-donating substituents significantly reduced the rate of photoactivation. In contrast, electron-withdrawing substituents did not further increase the rate of photoactivation compared to the unsubstituted DMNB caged *N*-phenylpyrimidine-2-amine scaffold. This result is of major interest since the *N*-phenylpyrimidine-2-amine scaffold is part of the hinge binding



motifs of a variety of CDK and other kinase inhibitors.<sup>78,149–151</sup> Thus, designing further photoactivatable CDK or kinase inhibitors exhibiting the *N*-phenylpyrimidine-2-amine scaffold, strong electron-donating substituents should be minded in terms of a fast photoactivation.

Having studied the rate of photoactivation under experimental conditions, the demonstration of *in vitro* photoactivation upon UV irradiation represented one central role of the biological evaluation. Additionally, residual biological activity of the DMNB caged prodrug **23** was to be assessed. Firstly, the ability of **23** to inhibit the kinase activity of CDK2 was determined. Compared to inhibitor **16**, the inhibitory efficacy decreased by more than factor 1000 rendering the DMNB caged prodrug **23** inactive in CDK2 kinase assays. Secondly, cell proliferation assays using Panc89 cells were performed. The DMNB caged prodrug **23** exhibited a significantly higher EC<sub>50</sub> compared to the uncaged inhibitor **16**, although a considerably lower factor in difference of  $\approx 24$  was achieved. Off-target effects might contribute to residual cytotoxic activity in particular, since CDK2 kinase activity was not inhibited. However, the caged prodrug did not affect cell proliferation up to high micromolar concentrations ( $\approx 17.3 \mu\text{M}$ ), which still would allow a decent therapeutic window, since potent kinase inhibitors such as **16** are applied at considerably lower concentrations (EC<sub>50</sub> = 0.70  $\mu\text{M}$ ).

To finalize the proof of concept, *in vitro* photoactivation upon irradiation with UV light worked perfectly in both kinase and cell proliferation assays. Upon 2 minutes of UV irradiation at a considerably low power of 37.5 mW the biological activity of the caged prodrug **23** was restored completely. Furthermore, the used Panc89 cell tolerated the applied irradiation dose well. Hence, to the best of my knowledge the first photoactivatable CDK inhibitor is presented. The biological activity thus CDK inhibition can be activated upon irradiation with a high spatiotemporal control, making the DMNB caged prodrug **23** an attractive tool compound to study biological processes like CDK signal transduction within a cell or with regard to binding kinetics.

Despite this notable proof of concept *in vitro*, the water solubility of the caged prodrug has to be significantly increased regarding a medicinal application. The utilization of a hydrophilic PPG represents a promising approach.<sup>180,181</sup> However, the little penetration depth of UV light into biological tissues restricts studies utilizing the DMNB caged prodrug **23** to thin cell layers or superficial tissues. Considering **23** as a tool compound to study biological processes *in vitro*, this penetration depth might be sufficient, whereas a medical application appears difficult. In order to overcome this limitation, two promising strategies were approached. Firstly, the utilization of a visible-light absorbing PPG was obvious. The BODIPY group was chosen due to its stability in various media, sharp absorption peaks and low *in vitro* toxicity.<sup>52</sup> Furthermore, readily substitution of the ring systems enables custom-tailored BODIPY

protecting groups.<sup>51,167,175</sup> This is particularly interesting in terms of water solubility. Although BODIPY derivatives are widely used as laser dyes<sup>48,49</sup>, photosensitizers<sup>50</sup> and fluorescent tags<sup>51</sup>, its utility as a PPG for biological applications remained unclear. Hence, caging of inhibitor **16** with a BODIPY PPG was aimed for with the intention of studying its photoactivation upon irradiation with visible light. As an important result, a universal strategy of synthesis was characterized exploiting chemical accessibility of the 8-chloro-substituted BODIPY derivatives with a subsequent conversion to their 8-iodo-substituted derivatives by a Finkelstein reaction. These 8-iodo-substituted BODIPY derivatives can serve as valuable precursors in order to attach the BODIPY PPG to various nucleophilic nitrogen such as amine functions of kinase inhibitors. Following photochemical characterization utilizing moderately tissue penetrating green light proved its utility for biological applications. An almost complete photoactivation upon irradiation was achieved within a time of irradiation which only slightly impaired cell proliferation of Panc89 cells. Having proven utility, the proof of concept utilizing the BODIPY PPG *in vitro* is part of present projects in our work group. The preparation of a water soluble BODIPY group, the investigation of the mechanism of photorelease and assessment of a possible cellular toxicity of the cleaved protecting group will represent further milestones within this project.

In a second approach to overcome the limited penetration depth of UV light, the possibility to activate a DMNB caged prodrug by the use of Cherenkov radiation induced by either a beta radiation emitting radionuclide or external particle beams from linear particle accelerators was investigated. Incubating the DMNB caged prodrug **23** with the positron emitting radionuclide <sup>18</sup>F did not lead to a cleavage of the PPG considerably due to <sup>18</sup>F's decay energy which happens to be just above the threshold condition for induction of Cherenkov radiation. Hence, <sup>68</sup>Ga was chosen as the positron emitting radionuclide for further experiments because of its significantly higher decay energy. In fact, incubation with <sup>68</sup>Ga as the beta radiation emitter in 1 M HCl resulted in a 26% activation of the DMNB caged prodrug **23**. This experiment represents an important proof of concept. However, the ability of beta radiation emitting radionuclides to activate a DMNB caged compound remains to be proven at a neutral pH value in order to validate the observed effect. Furthermore, cleavage of the PPG was assessed using external beam radiation from a linear particle accelerator. Therefore, compound solutions of the DMNB caged prodrug **23** with a maximum total volume of 4 ml were placed in the particle beam of a linear particle accelerator. Both photon as well as electron radiation could not cleave the PPG from the DMNB caged prodrug **23**. However, the critical total volume of the compound solutions might not have been sufficient since the particles from the particle beam might need to travel a certain distance within the solvent to efficiently induce Cherenkov radiation. The installation of a water tank surrounding the probes might be a

promising approach to induce Cherenkov radiation within the water tank and to subsequently activate the prodrug.

In summary, the utilization of Cherenkov radiation would offer unparalleled opportunities regarding light delivery into difficult accessible treatment sites, since the required UV irradiation would be generated deep in place. An activation by a beta emitting radionuclide was firstly demonstrated by the use of  $^{68}\text{Ga}$ . To further validate and study the observed effect remains for current projects within our workgroup.

In conclusion, both a photoactivatable small-molecule MTA as well as a photoactivatable CDK inhibitor with high utility *in vitro* were developed. Since the DMNB group was chosen as the PPG, both prodrugs are highly valuable as tool compounds to study biological processes *in vitro* due to a precise spatiotemporal control of their biological activity upon irradiation with UV light. Furthermore, the basis of two promising strategies to enhance their medicinal applicability was laid: installation of the novel visible-light absorbing BODIPY PPG as well as the utilization of Cherenkov radiation for photoactivation. Both strategies would increase the value of photoactivatable prodrugs tremendously. In particular, utilization of Cherenkov radiation in combination with clinically used tumor targeting vectors for delivery of radiation to specific tumor sites *in vivo* would enable a precise control of biological activity in nearly every spot within the human body and could lead to a novel therapeutic approach combining caged prodrugs with existing radiotherapeutic applications.

## 5 Experimental

---

### 5.1 Molecular modeling

Molecular modeling was performed on a DELL 8 core system. For visualization Maestro, version 10.4, Schrödinger, LLC, New York, NY, 2014 was used. Protein crystal structures were prepared prior to docking by the Protein Preparation Wizard<sup>135</sup> utilizing the following programs: Epik<sup>136</sup>, version 2.7, 2013; Impact, version 6.2, 2014; Prime<sup>137,138</sup>, version 3.4, 2014. Thus, the X-ray crystal structure refinement process included addition of hydrogen atoms, optimization of hydrogen bonds, and removal of atomic clashes. Default settings were used. Missing side chains and loops were filled in with Prime. Furthermore, selenomethionines were converted to methionines and water molecules were deleted.

Additionally, ligands were prepared in order to create energetically minimized 3D geometries and assign proper bond orders (MacroModel, version 10.3, 2014). Accessible tautomer and ionization states were calculated prior to screening (LigPrep, version 2.9, 2014). To generate bioactive conformers a conformational search method was used (ConfGen<sup>139</sup>, version 2.7, 2014). Receptor grid generation was performed by Glide<sup>140,141</sup>, version 6.2, 2014. For ligand docking and screening the Glide SP workflow was used. Energetically minimized ligand conformations were docked into the active site of the protein; possible binding poses were determined and subsequently ranked based on their calculated binding affinities.

Furthermore, caged ligands were investigated regarding their interactions within the ATP binding pocket. The structures were therefore superimposed with crystallized or modeled inhibitors by the flexible ligand alignment function. Afterwards, steric hindrance was determined by calculation of ligand-protein contacts. Ugly contacts with a contact cutoff ratio  $< 0.5$  were indicated by red dashed lines. The cutoff ratio was calculated by Maestro based on the following formula:  $C = D_{1,2} / (R_1 + R_2)$  where  $D_{1,2}$  is the distance between the two atomic centers and where  $R_1$  resp.  $R_2$  are the radii of the atomic centers.  $C$  increases monotonically for each contact type, that is  $C(\text{ugly}) < C(\text{bad}) < C(\text{good})$ .

## 5.2 Photoexperiments

### 5.2.1 Inhibitor stability upon irradiation

Compound **17** and **21** were dissolved in DMSO (1 mM). 5 mL were irradiated in a glass flask at 365 nm (LED source: 12x Nichia NCSU033B, Sahlmann Photochemical Solutions, 100%, 5.4 W) up to 20 min. Aliquots were diluted with HPLC grade methanol (1:1) and analyzed by HPLC.

Compound **16** and **26** were dissolved in DMSO (1 mM) resp. in PBS buffer with 10% DMSO (25  $\mu$ M). 100  $\mu$ L of each solution were irradiated in a well of a 96-well plate at 365 nm (LED source: 8x Nichia NCSU033B, Sahlmann Photochemical Solutions, 10%, 75 mW) up to 10 min. Content determination was performed by HPLC analysis.

Compound **16** was dissolved in PBS buffer with 20% DMSO (25  $\mu$ M). 100  $\mu$ L each were irradiated in a well of a 96-well plate at 530 nm (LED source: 8x Nichia NCSG219-V1, Sahlmann Photochemical Solutions, 100%, 4.6 W) up to 25 min. Content determination was performed by HPLC analysis.

### 5.2.2 UV/Vis absorptions spectra

Spectra were recorded on UV/Vis spectrophotometer Varian Cary® 50 Scan, Agilent Technologies. UV/Vis absorbance was measured in DMSO or PBS buffer with 10% DMSO. Concentration is either indicated or the compounds were dissolved and diluted until peak absorbance was in a range of 0.6 to 0.8. Absorbance was subsequently normalized to the uncaged compounds **16**, **17** and **24**.

### 5.2.3 Photoactivation

#### Photoactivatable small-molecule microtubule-targeting agent

Compound **20** was dissolved in DMSO (1 mM). 5 ml were irradiated in a glass flask at 365 nm (LED source: 12x Nichia NCSU033B, Sahlmann Photochemical Solutions, 100%, 5.4 W). After 0, 20, 40, 60, 90, 120, 180, 240, 300 and 600 seconds samples were taken, diluted with HPLC grade methanol (1:1) and analyzed by HPLC at a wavelength of 254 nm. Each sample was injected to HPLC twice. Additional to HPLC analysis LC-MS was used to confirm compound identity.

**Photoactivatable CDK inhibitor**

Compounds **23** and **25** were dissolved in DMSO (1 mM) resp. in PBS buffer with 10% DMSO (25  $\mu$ M). 100  $\mu$ L of each solution were irradiated in a well of a 96-well plate at 365 nm (LED source: 16x Nichia NCSU276A U365, Sahlmann Photochemical Solutions). The light intensity in mW is indicated for each experiment. After 0, 10, 20, 30, 45, 60, 90, 120 and 180 seconds samples were taken and analyzed by HPLC at a wavelength of 296 nm without further dilution. Each sample was injected to HPLC twice. Additional to HPLC analysis LC-MS was used to confirm compound identity.

**Scaffold project**

Compounds **25,35-45** were dissolved in DMSO (500  $\mu$ M) resp. in PBS buffer with 20% DMSO (500  $\mu$ M). 100  $\mu$ L of each solution were irradiated in a well of a 96-well plate at 365 nm (LED source: 16x Nichia NCSU276A U365, Sahlmann Photochemical Solutions) with 7.5 mW. After 0, 5, 10, 15, 20, 25, 30, 45, 60 and 120 seconds samples were taken and analyzed by HPLC at a wavelength of 296 nm without further dilution. Each sample was injected to HPLC twice.

**Visible-light absorbing PPG**

Compounds **49,53** and **54** were dissolved in DMSO (25  $\mu$ M). 100  $\mu$ L of each solution were irradiated in a well of a 96-well plate at 530 nm (LED source: 8x Nichia NCSG219-V1, Sahlmann Photochemical Solutions). The light intensity in mW is indicated for each experiment. After 0, 1, 2.5, 5, 7.5, 10, 15 and 20 minutes samples were taken and analyzed by HPLC at a wavelength of 296 nm without further dilution. Each sample was injected to HPLC twice. Additional to HPLC analysis LC-MS was used to confirm compound identity.

## 5.3 Chemical Synthesis and Characterization

### 5.3.1 Reagents and solvents

All reagents and solvents that have been applied in synthetic and analytic approaches were, if not specified otherwise, obtained from the commercial companies abcr GmbH (Karlsruhe, Germany), Sigma-Aldrich Chemie GmbH, Merck Group (Munich, Germany), Merck Millipore (Darmstadt, Germany), Acros Organics, Thermo Fisher Scientific (Geel, Belgium), and VWR International GmbH (Hannover, Germany). They were used without further purification.

### 5.3.2 TLC

Monitoring of reactions progress included thin-layer chromatography (TLC) utilizing silica gel polyester sheets (SIL G/UV254, 0.2 mm, Polygram®, Macherey-Nagel).

### 5.3.3 Flash Chromatography

Flash chromatography was performed using a LaFlash system, VWR International GmbH (Hannover Germany). Pre-packed silica gel columns (PuriFlash-30SIHP, 30  $\mu\text{m}$ , Interchim) and RP-18 modified silica gel columns (PuriFlash-15C18HP, 15  $\mu\text{m}$ , Interchim) were used for separation. Composition of the mobile phases are indicated with the appropriate synthetic procedures. Flow rates were adjusted to column sizes.

### 5.3.4 HPLC

High-performance liquid chromatography (HPLC) was performed with a Hewlett Packard 1050 Series (Agilent Technologies, Waldbronn, Germany) and served for monitoring of reaction progress, purity control and peak area determination of photochemical characterizations and stability experiments.

The column was either a Kinetex® C8, 5  $\mu\text{m}$  (150 · 4.6 mm, Phenomenex, Aschaffenburg, Germany) or a STAGROMA® C18, 5  $\mu\text{m}$  (125 · 4 mm, Stagroma AG, Reinach, Switzerland). The injection volume was 20  $\mu\text{L}$ . Depending of the compounds to separate, different gradients of acetonitrile and  $\text{KH}_2\text{PO}_4$  buffer (10 mM, pH 2.3) were used as the mobile phase with a fixed flow rate (1.5 ml · min<sup>-1</sup>). UV detection was achieved at 254 nm, 296 nm or 515 nm.

### 5.3.5 NMR

$^1\text{H}$  and  $^{13}\text{C}$  NMR spectra were recorded on a Bruker Avance III 300 instrument at a temperature of 298 K resp. 300 K with a multinuclear probe head using the manufacture's pulse program:  $^1\text{H}$  (300 MHz) and  $^{13}\text{C}$  (75 MHz). Spectra were referenced to the respective deuterated solvents signals of DMSO- $d_6$  ( $\delta$   $^1\text{H}$  NMR: 2.50 ppm,  $\delta$   $^{13}\text{C}$  NMR: 39.52 ppm) and  $\text{CDCl}_3$  ( $\delta$   $^1\text{H}$  NMR: 7.26 ppm,  $\delta$   $^{13}\text{C}$  NMR: 77.00 ppm) as an internal standard. H,H-COSY, HSQC, HMBC spectra were further consulted for compound identity. The following abbreviations have been used to classify the appropriate signals: b (broad), s (singlet), d (doublet), t (triplet), q (quartet), quint (quintet), m (unresolved multiplet).

NMR spectroscopy was performed by Dr. Ulrich Girreser and his NMR team.

### 5.3.6 LC-MS

Liquid chromatographic (LC) separation was performed with an Agilent 1100 HPLC system (Agilent Technologies, Waldbronn, Germany) over an Waters Xterra MS C8 (50 · 4.6 mm, 3.5  $\mu\text{m}$ ) column tempered at 20°C using a 0.1 % acetic acid in double distilled water/acetonitrile gradient for mobile phase (flow rate = 1 ml · min $^{-1}$ ).

Mass spectra were recorded on a Bruker Esquire ~LC ion trap mass spectrometer (Bruker Daltonics, Bremen, Germany) with electron spray ionization (ESI) in the positive ion mode (dry gas 6.5 l · min $^{-1}$ , nebulizer 25 psi, drying temperature 250 °C).

LC-MS analyses were performed by Dr. Ulrich Girreser and Sven Wichmann.

### 5.3.7 HRMS

High resolution mass spectra were recorded either on a Thermo Fisher Q Exactive Plus mass spectrometer (Hybrid Quadrupol Orbitrap) with electron spray ionization (ESI) in the positive ion mode, a Joel Accu (TOF 4G) with electron impact ionization (EI) or a Bifex III mass spectrometer (Fa. Bruker Daltonics) with matrix-assisted laser desorption/ionization (MALDI, applied matrix: 4-chloro- $\alpha$ -cyanocinnamic acid, wavelength ionization laser: 337 nm, acceleration voltage: 19 kV) and time of flight detector (TOF). The method used is indicated for each compound respectively.



### 5.3.8 X-ray Crystallography

X-ray ligand crystal structure analysis was performed by Dr. Dieter Schollmeyer at the Institute of Organic Chemistry, Johannes Gutenberg University (Mainz, Germany) on a Stoe IPDS 2T with Cu and Mo-X ray tubes and Oxford Cryostream.

### 5.3.9 Synthetic procedures

#### **General procedure for caging of *N*-phenylpyrimidin-2-amines with benzyl bromides (23, 25, 26, 35-42)**

Sodium hydride (1.2 equiv.) was dissolved in 5 ml of dry DMF under a nitrogen atmosphere. After cooling to 0°C, the respective *N*-phenylpyrimidin-2-amine (1.0 equiv.), dissolved in 3 ml of dry DMF, was added dropwise to the reaction. After 1 h the reaction was cooled to -35°C and the respective benzyl bromide (1.1 equiv.), dissolved in 3 ml of dry DMF, was added to the reaction dropwise. After stirring at -35°C for 1 h the reaction was quenched by slow addition of H<sub>2</sub>O. After 1 h the reaction was filtrated. The precipitate was purified by flash chromatography (stationary phase and eluent given for each compound, respectively) to afford the particular compound.

#### **General procedure for caging of *N*-phenylpyrimidin-2-amines with BODIPY protecting groups (49,53,54)**

Sodium hydride (1.2 equiv.) was dissolved in 5 ml of dry DMF under an argon atmosphere. After cooling to 0°C, the respective *N*-phenylpyrimidin-2-amine (1.0 equiv.), dissolved in 3 ml of dry DMF, was added dropwise to the reaction. After 1 h the reaction was cooled to -35°C and the respective BODIPY iodide or chloride (2.5 equiv.), dissolved in 10 ml of dry DMF, was added to the reaction dropwise. After stirring at -35°C for 1 h the reaction was quenched by addition of 2 drops H<sub>2</sub>O. The solvent was removed by reduced pressure. The raw product was purified by flash chromatography (stationary phase and eluent given for each compound, respectively) to afford the particular compound.

**4-(4-(2-Fluoropyridin-3-yl)phenyl)-*N*-(4-hydroxyphenyl)butanamide (17)**

alex-raj

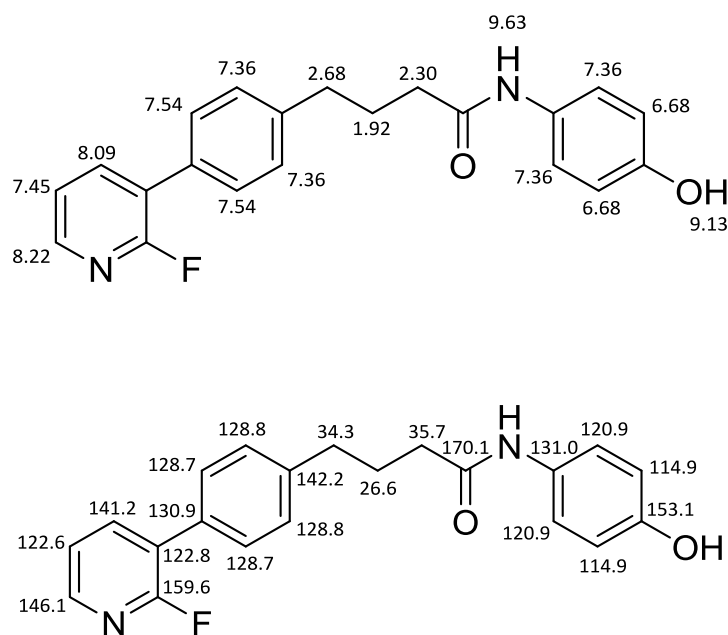
 $C_{21}H_{19}FN_2O_2$  ( $M_r$  350.14)

Synthesis was performed by Dr. Mohammed Abadleh.

4-(4-(2-Fluoropyridin-3-yl)phenyl)-*N*-(4-hydroxyphenyl)butanamide was synthesized according to literature<sup>104</sup> (99% HPLC purity).

**<sup>1</sup>H NMR** (300 MHz, DMSO- $d_6$ ):  $\delta$  = 1.92 (quint,  $^3J_{HH}$  = 7.5 Hz, 2H), 2.30 (t,  $^3J_{HH}$  = 7.4 Hz, 2H), 2.68 (t,  $^3J_{HH}$  = 7.5 Hz, 2H), 6.68 (d,  $^3J_{HH}$  = 8.9 Hz, 2H), 7.36 (m, 4H), 7.45 (m, 1H), 7.54 (dd,  $^4J_{HH}$  = 1.7 Hz,  $^3J_{HH}$  = 8.3 Hz, 2H), 8.09 (m, 1H), 8.22 (m, 1H), 9.13 (s, 1H), 9.63 (bs, 1H) ppm.

**<sup>13</sup>C NMR** (75 MHz, DMSO- $d_6$ ):  $\delta$  = 26.6, 34.3, 35.7, 114.9, 120.9, 122.6 (d,  $^4J_{CF}$  = 4.3 Hz), 122.8 (d,  $^2J_{CF}$  = 29.2 Hz), 128.7 (d,  $^4J_{CF}$  = 3.0 Hz), 128.8, 130.9 (d,  $^3J_{CF}$  = 5.1 Hz), 131.0, 141.2 (d,  $^3J_{CF}$  = 4.4 Hz), 142.2, 146.1 (d,  $^3J_{CF}$  = 14.9 Hz), 153.1, 159.6 (d,  $^1J_{CF}$  = 236.9 Hz), 170.1 ppm.

**HRMS** (EI):  $m/z$  = 350.14281  $M^+$  (calc.  $m/z$  = 350.14306)

***N*-4-((4,5-dimethoxy-2-nitrobenzyl)oxy)phenyl)-4-(4-(2-fluoropyridin-3-yl)phenyl)butanamide (20)**

alex-3.8

 $C_{30}H_{28}FN_3O_6$  ( $M_r$  545.20)

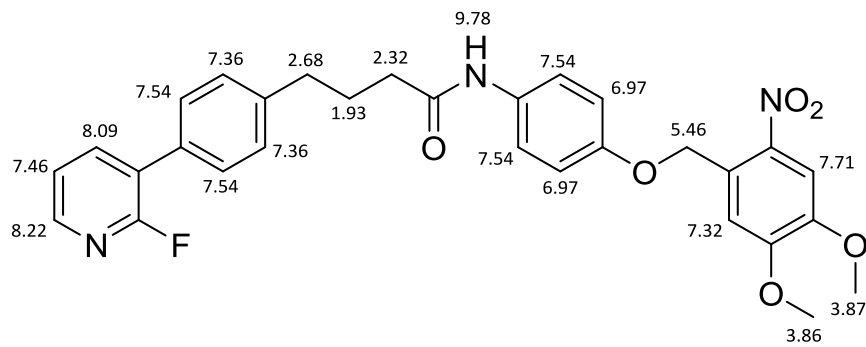
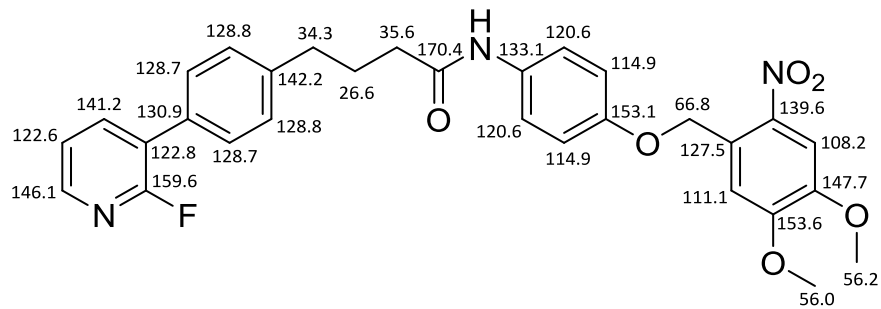
4-(4-(2-Fluoropyridin-3-yl)phenyl)-*N*-(4-hydroxyphenyl)butanamide **17** (100 mg, 0.29 mmol) and potassium carbonate (98 mg, 0.71 mmol) were dissolved in DMF (10 ml) and stirred at room temperature for 30 min, followed by drop-wise addition of 4,5-dimethoxy-2-nitrobenzyl bromide (86 mg, 0.31 mmol in DMF). The reaction mixture was stirred at RT for 12 h and demineralized water was added drop-wise until complete precipitation of the product. The solvent was removed by filtration and the product was purified by reverse phase flash silica gel chromatography with a gradient of methanol and water to yield *N*-4-((4,5-dimethoxy-2-nitrobenzyl)oxy)phenyl)-4-(4-(2-fluoropyridin-3-yl)phenyl)butanamide as a yellow solid (100% HPLC purity).

**Yield:** 93 mg (0.17 mmol, 60%)

**$^1H$  NMR** (300 MHz, DMSO- $d_6$ ):  $\delta$  = 1.93 (quint,  $^3J_{HH}$  = 7.4 Hz, 2H), 2.32 (t,  $^3J_{HH}$  = 7.4 Hz, 2H), 2.68 (t,  $^3J_{HH}$  = 7.5 Hz, 2H), 3.86 (s, 3H), 3.87 (s, 3H), 5.46 (s, 2H), 6.97 (d  $^3J_{HH}$  = 9.0 Hz, 2H), 7.32 (s, 1H), 7.36 (d,  $^3J_{HH}$  = 8.1 Hz, 2H), 7.46 (m, 1H), 7.54 (m, 4H), 7.71 (s, 1H), 8.09 (m, 1H), 8.22 (m, 1H), 9.78 (bs, 1H) ppm.

**$^{13}C$  NMR** (75 MHz, DMSO- $d_6$ ):  $\delta$  = 26.6, 34.3, 35.6, 56.0, 56.2, 66.8, 108.2, 111.1, 114.9, 120.6, 122.6 (d,  $^4J_{CF}$  = 4.3 Hz), 122.8 (d,  $^2J_{CF}$  = 28.0 Hz), 127.5, 128.7 (d,  $^4J_{CF}$  = 3.3 Hz), 128.8, 130.9 (d,  $^3J_{CF}$  = 5.0 Hz), 133.1, 139.6, 141.2 (d,  $^3J_{CF}$  = 4.4 Hz), 142.2, 146.1 (d,  $^3J_{CF}$  = 15.4 Hz), 147.7, 153.1, 153.6, 159.6 (d,  $^1J_{CF}$  = 237.1 Hz), 170.4 ppm.

**HRMS** (EI):  $m/z$  = 545.19486  $M^+$  (calc.  $m/z$  = 545.19621)



***N*-(4-(benzyloxy)phenyl)-4-(4-(2-fluoropyridin-3-yl)phenyl)butanamide (21)**

alex-3.18

C<sub>28</sub>H<sub>25</sub>FN<sub>2</sub>O<sub>2</sub> (M<sub>r</sub> 440.19)

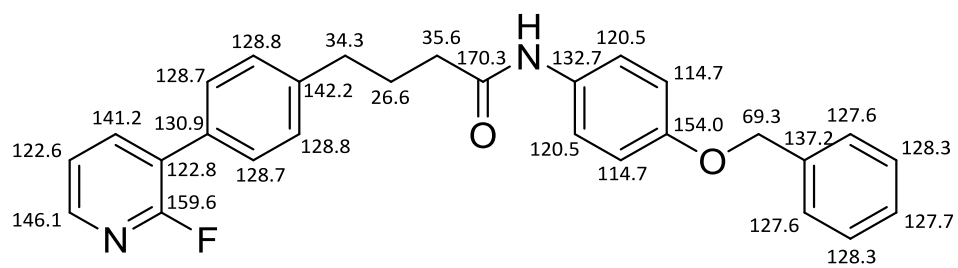
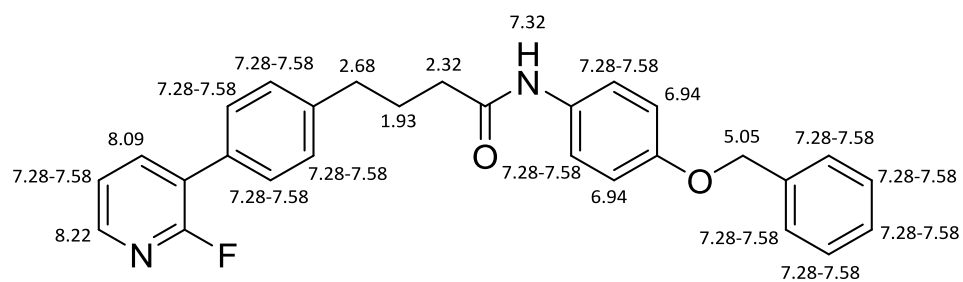
4-(4-(2-Fluoropyridin-3-yl)phenyl)-*N*-(4-hydroxyphenyl)butanamide **17** (100 mg, 0.285 mmol) and sodium carbonate (38 mg, 0.570 mmol) were dissolved in DMF (10 ml) and left stirring at room temperature. After 30 minutes benzyl bromide (63 mg, 0.371 mmol, 44  $\mu$ l in DMF) was added to the reaction dropwise. The reaction mixture was left stirring at room temperature. After 12 hours the reaction mixture was extracted with ethyl acetate three times. The combined ethyl acetate phases were dried over sodium sulfate and the solvent was removed under reduced pressure. The product was purified by flash chromatography with a gradient of ethyl acetate and petroleum ether to yield *N*-(4-(benzyloxy)phenyl)-4-(4-(2-fluoropyridin-3-yl)phenyl)butanamide as a light yellow solid (100% HPLC purity).

**Yield:** 69 mg (0.16 mmol, 55%)

**<sup>1</sup>H NMR** (300 MHz, DMSO-d<sub>6</sub>):  $\delta$  = 1.93 (quint, <sup>3</sup>J<sub>HH</sub> = 7.7 Hz, 2H), 2.32 (t, <sup>3</sup>J<sub>HH</sub> = 7.3 Hz, 2H), 2.68 (t, <sup>3</sup>J<sub>HH</sub> = 7.5 Hz, 2H), 5.05 (s, 2H), 6.94 (d, <sup>3</sup>J<sub>HH</sub> = 9.2 Hz, 2H), 7.28-7.58 (m, 12H), 8.09 (m, 1H), 8.22 (m, 1H), 7.32 (bs, 1H) ppm.

**<sup>13</sup>C NMR** (75 MHz, DMSO-d<sub>6</sub>):  $\delta$  = 26.6, 34.3, 35.6, 69.3, 114.7, 120.5, 122.6 (d, <sup>4</sup>J<sub>CF</sub> = 4.2 Hz), 122.8 (d, <sup>2</sup>J<sub>CF</sub> = 28.2 Hz), 127.6, 127.7, 128.3, 128.7 (d, <sup>4</sup>J<sub>CF</sub> = 2.9 Hz), 128.8, 130.9 (d, <sup>3</sup>J<sub>CF</sub> = 5.1 Hz), 132.7, 137.2, 141.2 (d, <sup>3</sup>J<sub>CF</sub> = 4.4 Hz), 142.2, 146.1 (d, <sup>3</sup>J<sub>CF</sub> = 14.9 Hz), 154.0, 159.6 (d, <sup>1</sup>J<sub>CF</sub> = 236.6 Hz), 170.3 ppm.

**HRMS** (EI):  $m/z$  = 440.18996 M<sup>+</sup> (calc.  $m/z$  = 440.19001)



**4-(1-Isopropyl-2-methyl-1H-imidazol-5-yl)-N-(4-(methylsulfonyl)phenyl)pyrimidin-2-amine (16)**

AZD5438

 $C_{18}H_{21}N_5O_2S$  ( $M_r$  371.46)

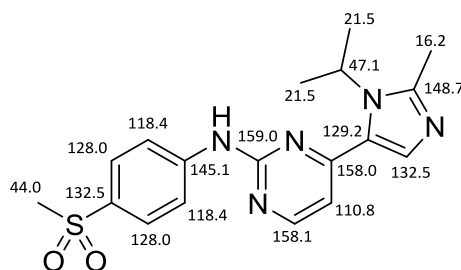
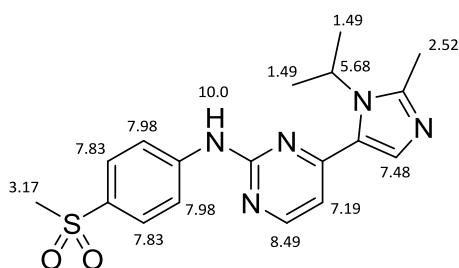
AZD5438 was obtained from Taizhou Crene Biotechnology Co., Ltd (China).

Before usage, the compound was purified and fully characterized. Purification was achieved by RP flash chromatography with a gradient of water and methanol to yield a white powder (100% HPLC purity).

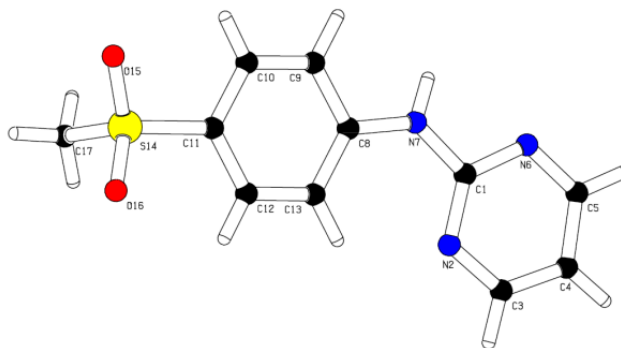
$^1H$  NMR (300 MHz, DMSO- $d_6$ ):  $\delta$  = 1.49 (d,  $^3J_{HH}$  = 7.1 Hz, 6H), 2.52 (s, 3H), 3.17 (s, 3H), 5.68 (sept,  $^3J_{HH}$  = 7.1 Hz, 1H), 7.19 (d,  $^3J_{HH}$  = 5.3 Hz, 1H), 7.48 (s, 1H), 7.83 (d,  $^3J_{HH}$  = 8.9 Hz, 2H), 7.98 (d,  $^3J_{HH}$  = 8.9 Hz, 2H), 8.49 (d,  $^3J_{HH}$  = 5.3 Hz, 1H), 10.0 (s, 1H) ppm.

$^{13}C$  NMR (75 MHz, DMSO- $d_6$ ):  $\delta$  = 16.2, 21.5, 44.0, 47.1, 110.8, 118.4, 128.0, 129.2, 132.5, 132.5, 145.1, 148.7, 158.0, 158.1, 159.0 ppm.

HRMS (ESI):  $m/z$  = 372.14873 [ $M+H$ ] $^+$  (calc.  $m/z$  = 372.14887)





***N*-(4-(methylsulfonyl)phenyl)pyrimidin-2-amine (24)**

Molecular structure determined by X-ray crystallography.

alex-1.2

$C_{11}H_{11}N_3O_2S$  ( $M_r$  249.06)

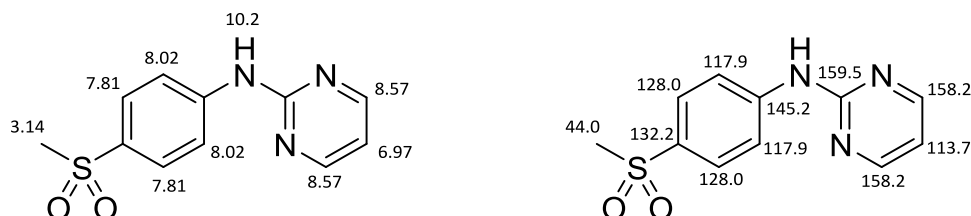
**24** was synthesized according to literature<sup>137</sup>. 2-Chloropyrimidine (2341 mg, 20.44 mmol) and 4-aminophenylmethylsulfonate (4200 mg, 24.53 mmol) were dissolved in 100 ml propan-2-ol. Four drops of conc. HCl were added and the reaction was left stirring at 85 °C for 24h. The solvent was removed under reduced pressure. The crude product was recrystallized from MeOH/H<sub>2</sub>O to yield *N*-(4-(methylsulfonyl)phenyl)pyrimidin-2-amine as bright yellow needles (100% HPLC purity).

**Yield:** 3100 mg (12.45 mmol, 61%).

**<sup>1</sup>H NMR** (300 MHz, DMSO-*d*<sub>6</sub>):  $\delta$  = 3.14 (s, 3H), 6.97 (t, <sup>3</sup>*J*<sub>HH</sub> = 4.8 Hz, 1H), 7.81(d, <sup>3</sup>*J*<sub>HH</sub> = 8.9 Hz, 2H), 8.02 (d, <sup>3</sup>*J*<sub>HH</sub> = 9.0 Hz, 2H), 8.57 (d, <sup>3</sup>*J*<sub>HH</sub> = 4.8 Hz, 2H), 10.2 (s, 1H) ppm.

**<sup>13</sup>C NMR** (75 MHz, DMSO-*d*<sub>6</sub>):  $\delta$  = 44.0, 113.7, 117.9, 128.0, 132.2, 145.2, 158.2, 159.5 ppm.

**HRMS** (ESI):  $m/z$  = 272.04619 [M+Na]<sup>+</sup>; 250.06434 [M+H]<sup>+</sup> (calc.  $m/z$  = 250.06447)



***N*-(4,5-dimethoxy-2-nitrobenzyl)-*N*-(4-(methylsulfonyl)phenyl)pyrimidin-2-amine (25)**

alex-1.3

 $C_{20}H_{20}N_4O_6S$  ( $M_r$  444.11)

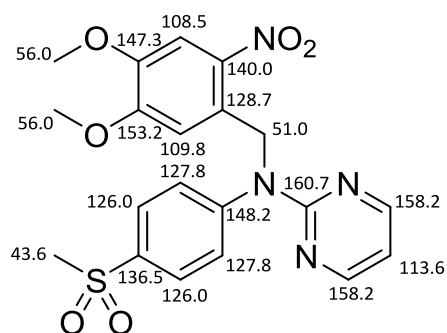
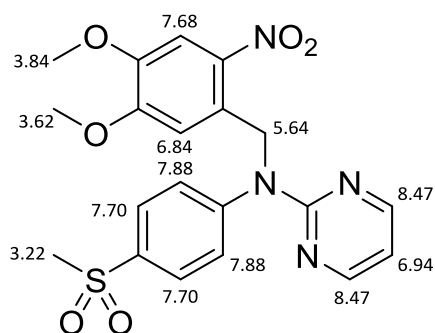
**25** was synthesized according to the general procedure for caging of *N*-phenylpyrimidin-2-amines with benzyl bromides from **24** (122 mg, 0.44 mmol) and 4,5-dimethoxy-2-nitrobenzylbromide (137 mg, 0.484 mmol). Purification was achieved by RP flash chromatography with a gradient of methanol and water to afford *N*-(4,5-dimethoxy-2-nitrobenzyl)-*N*-(4-(methylsulfonyl) phenyl)pyrimidin-2-amine as a bright yellow solid (98% HPLC purity).

**Yield:** 117 mg (0.26 mmol, 60%).

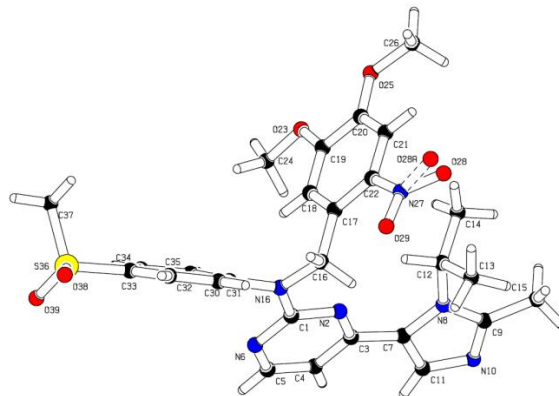
$^1\text{H NMR}$  (300 MHz,  $\text{DMSO-d}_6$ ):  $\delta$  = 3.22 (s, 3H), 3.62 (s, 3H), 3.84 (s, 3H), 5.64 (s, 2H), 6.84 (s, 1H), 6.94 (t,  $^3J_{\text{HH}} = 4.8$  Hz, 1H), 7.70 (m, 3H), 7.88 (d,  $^3J_{\text{HH}} = 8.8$  Hz, 2H), 8.47 (d,  $^3J_{\text{HH}} = 4.8$  Hz, 2H) ppm.

$^{13}\text{C NMR}$  (75 MHz,  $\text{DMSO-d}_6$ ):  $\delta$  = 43.6, 51.0, 56.0, 56.0, 108.5, 109.8, 133.6, 126.0, 127.8, 128.7, 136.5, 140.0, 147.3, 148.2, 153.2, 158.2, 160.7 ppm.

**HRMS** (ESI):  $m/z$  = 467.09947  $[\text{M}+\text{Na}]^+$  (calc.  $m/z$  = 467.09958); 445.11744  $[\text{M}+\text{H}]^+$  (calc.  $m/z$  = 445.11763)



***N*-(4,5-dimethoxy-2-nitrobenzyl)-4-(1-isopropyl-2-methyl-1H-imidazol-5-yl)-*N*-(4-(methylsulfonyl)phenyl)pyrimidin-2-amine (23)**



Molecular structure determined by X-ray crystallography.

alex-1.4

$C_{27}H_{30}N_6O_6S$  ( $M_r$  566.19)

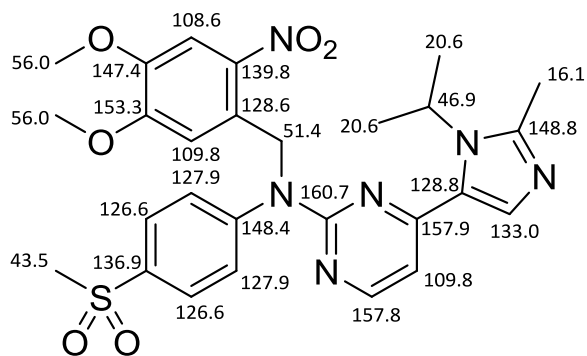
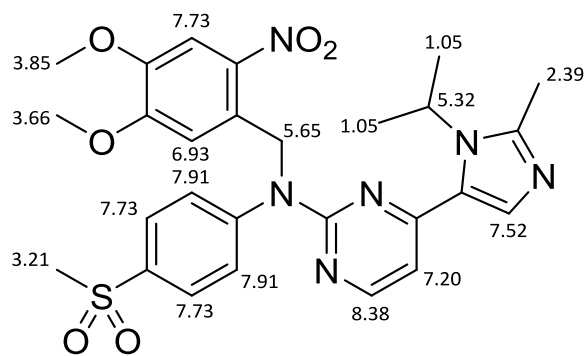
**23** was synthesized according to the general procedure for caging of *N*-phenylpyrimidin-2-amines with benzyl bromides from **16** (100 mg, 0.27 mmol) and 4,5-dimethoxy-2-nitrobenzylbromide (82 mg, 0.30 mmol). Purification was achieved by RP flash chromatography with a gradient of methanol and water to afford *N*-(4,5-dimethoxy-2-nitrobenzyl)-4-(1-isopropyl-2-methyl-1H-imidazol-5-yl)-*N*-(4-(methylsulfonyl)phenyl)pyrimidin-2-amine as a bright yellow solid (100% HPLC purity).

**Yield:** 84 mg (0.15 mmol, 50%).

**$^1H$  NMR** (300 MHz,  $DMSO-d_6$ ):  $\delta$  = 1.05 (d,  $^3J_{HH}$  = 7.1 Hz, 6H), 2.39 (s, 3H), 3.21 (s, 3H), 3.84 (s, 3H), 3.66 (s, 3H), 3.85 (s, 3H), 5.32 (sept,  $^3J_{HH}$  = 7.0 Hz, 1H), 5.65 (s, 2H), 6.93 (s, 1H), 7.20 (d,  $^3J_{HH}$  = 5.3 Hz, 1H), 7.52 (s, 1H), 7.73 (d,  $^3J_{HH}$  = 8.8 Hz, 2H), 7.73 (s, 1H), 7.91 (d,  $^3J_{HH}$  = 8.8 Hz, 2H), 8.38 (d,  $^3J_{HH}$  = 5.3 Hz, 1H) ppm.

**$^{13}C$  NMR** (75 MHz,  $DMSO-d_6$ ):  $\delta$  = 16.1, 20.6, 43.5, 46.9, 51.4, 56.0, 56.0, 108.6, 109.8, 109.8, 126.6, 127.9, 128.6, 128.8, 133.0, 136.9, 139.8, 148.4, 147.4, 148.8, 153.3, 157.8, 157.9, 160.7 ppm.

**HRMS** (ESI):  $m/z$  = 567.20204 [ $M+H$ ] $^+$  (calc.  $m/z$  = 567.20203)



**4,5-Dimethoxy-2-nitrobenzyl (tert-butoxycarbonyl)alaninate (22)**

alex-1.6

 $C_{17}H_{24}N_2O_8$  ( $M_r$  384.15)

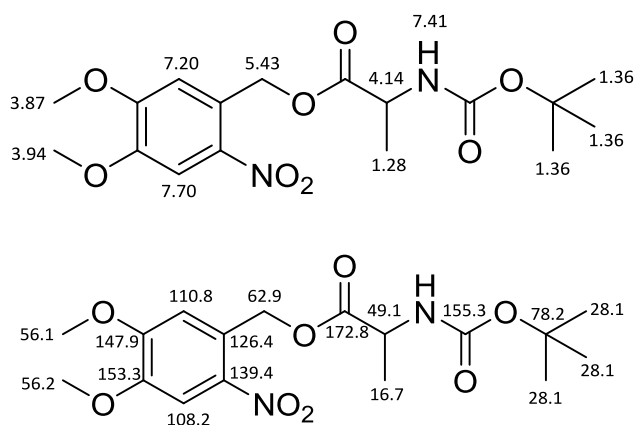
**22** was synthesized according to literature<sup>182</sup>. A solution of BOC protected L-alanine (**22a**) in toluene was treated with 4,5-dimethoxy-2-nitrobenzyl bromide in the presence of DBU and stirred at 80 °C for one hour. The crude product was filtered, washed with brine, dried over sodium carbonate and purified by flash silica gel chromatography to yield 4,5-dimethoxy-2-nitrobenzyl (tert-butoxycarbonyl)alaninate as a white solid (100% HPLC purity).

**Yield:** 3100 mg (12.45 mmol, 61%).

<sup>1</sup>H NMR (300 MHz, DMSO-*d*<sub>6</sub>):  $\delta$  = 1.28 (d, <sup>3</sup>*J*<sub>HH</sub> = 7.3 Hz, 3H), 1.36 (s, 9H), 3.87 (s, 3H), 3.94 (s, 3H), 4.14 (quint, <sup>3</sup>*J*<sub>HH</sub> = 7.2 Hz, 1H), 5.43 (s, 2H), 7.20 (s, 1H), 7.41 (d, <sup>3</sup>*J*<sub>HH</sub> = 7.2 Hz, 1H), 7.70 (s, 1H) ppm.

<sup>13</sup>C NMR (75 MHz, DMSO-*d*<sub>6</sub>):  $\delta$  = 16.7, 28.1, 49.1, 56.1, 56.2, 62.9, 78.2, 108.2, 110.8, 126.4, 139.4, 147.9, 153.3, 155.3, 172.8 ppm.

**HRMS** (EI):  $m/z$  = 384.15347  $M^+$  (calc.  $m/z$  = 384.15326)



***N*-benzyl-4-(1-isopropyl-2-methyl-1H-imidazol-5-yl)-*N*-(4-(methylsulfonyl)phenyl)pyrimidin-2-amine  
(26)**

alex-1.7

C<sub>25</sub>H<sub>27</sub>N<sub>5</sub>O<sub>2</sub>S (M<sub>r</sub> 461.19)

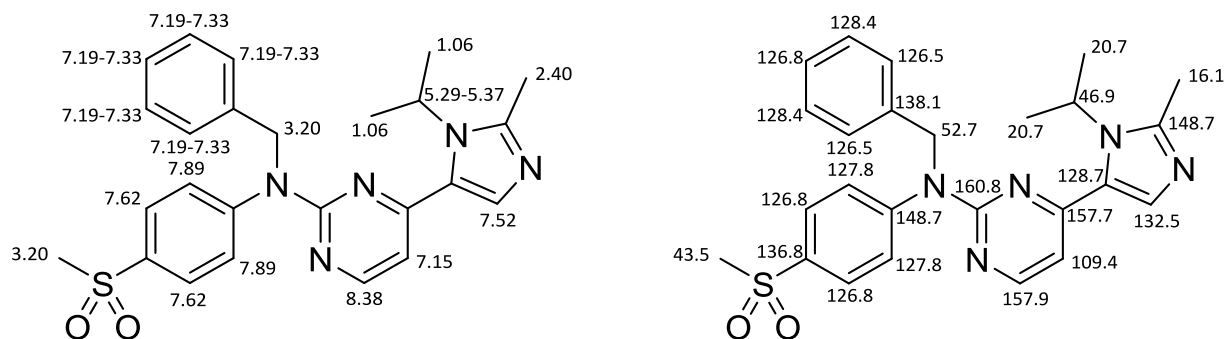
**26** was synthesized according to the general procedure for caging of *N*-phenylpyrimidin-2-amines with benzyl bromides from **16** (100 mg, 0.27 mmol) and benzyl bromide (51 mg, 0.30 mmol). Purification was achieved by RP flash chromatography with a gradient of methanol and water to afford *N*-benzyl-4-(1-isopropyl-2-methyl-1H-imidazol-5-yl)-*N*-(4-(methylsulfonyl)phenyl)pyrimidin-2-amine as a bright yellow solid (100% HPLC purity).

**Yield:** 81 mg (0.18 mmol, 65%).

<sup>1</sup>H NMR (300 MHz, DMSO-d<sub>6</sub>): δ = 1.06 (d, <sup>3</sup>J<sub>HH</sub> = 7.1 Hz, 6H), 2.40 (s, 3H), 3.20 (s, 3H), 5.29-5.37 (m, 1H), 5.37 (s, 2H), 7.15 (d, <sup>3</sup>J<sub>HH</sub> = 5.3 Hz, 1H), 7.19-7.33 (m, 5H), 7.52 (s, 1H), 7.62 (d, <sup>3</sup>J<sub>HH</sub> = 8.7 Hz, 2H), 7.89 (d, <sup>3</sup>J<sub>HH</sub> = 8.7 Hz, 2H), 8.38 (d, <sup>3</sup>J<sub>HH</sub> = 5.3 Hz, 1H) ppm.

<sup>13</sup>C NMR (75 MHz, DMSO-d<sub>6</sub>): δ = 16.1, 20.7, 43.5, 46.9, 52.7, 109.4, 126.5, 126.8, 126.8, 127.8, 128.4, 128.7, 132.5, 136.8, 138.1, 148.7, 148.7, 157.7, 157.9, 160.8 ppm.

**HRMS** (ESI): *m/z* = 462.19573[M+H]<sup>+</sup> (calc. *m/z* = 462.19582)



## ***N*-phenylpyrimidin-2-amine**

alex-1.1

C<sub>10</sub>H<sub>9</sub>N<sub>3</sub> (M<sub>r</sub> 171.20)

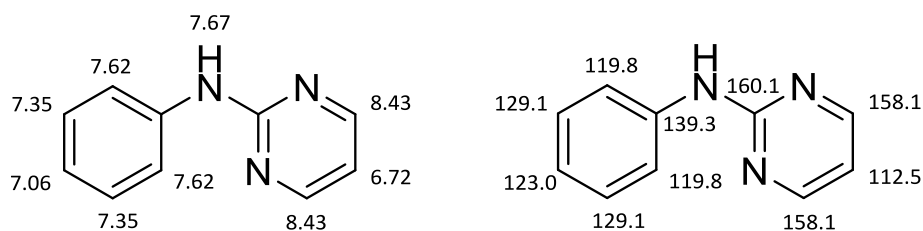
*N*-phenylpyrimidine-2-amine was synthesized according to literature<sup>183</sup>. The reaction was carried out in a microwave for synthesis. Bis(dibenzylideneacetone)palladium(0) (30 mg, 0,03 mmol), S-BINAP (40 mg, 0,06 mmol) and potassium *tert*-butoxide (505 mg, 4.5 mmol) were dissolved in 1.5 ml of anhyd. dioxane in a microwave vessel. The reaction was heated to 80°C and stirred for 10 min. After addition of 2-chloropyrimidine (370 mg, 3.22 mmol), aniline (300 mg, 3.22 mmol) and 3.5 ml of anhyd. dioxane the reaction was heated to 100°C. After stirring for 2 hours the reaction was filtrated. The filtrate was concentrated under reduced pressure. The residue was dissolved in 20 ml of ethyl acetate, washed with brine and dried over sodium sulfate. The solvent was removed under reduced pressure. The crude product was purified by flash chromatography with a gradient of ethyl acetate and petroleum ether to afford *N*-phenylpyrimidine-2-amine as a white solid (100% HPLC purity).

**Yield:** 320 mg (1.87 mmol, 58%).

**<sup>1</sup>H NMR** (300 MHz, DMSO-d<sub>6</sub>): δ = 6.72 (t, <sup>3</sup>J<sub>HH</sub> = 4.8 Hz, 1H), 7.06 (t, <sup>3</sup>J<sub>HH</sub> = 7.4 Hz, 1H), 7.35 (t, <sup>3</sup>J<sub>HH</sub> = 7.4 Hz, 2H), 7.62 (d, <sup>3</sup>J<sub>HH</sub> = 7.5 Hz, 2H), 7.67 (bs, 1H), 8.43 (d, <sup>3</sup>J<sub>HH</sub> = 4.9 Hz, 2H) ppm.

**<sup>13</sup>C NMR** (75 MHz, DMSO-d<sub>6</sub>): δ = 112.5, 119.8, 123.0, 129.1, 139.3, 158.1, 160.1 ppm.

**HRMS** (ESI): *m/z* = 172.08699 [M+H]<sup>+</sup> (calc. *m/z* = 172.08692)



***N*-(*p*-tolyl)pyrimidin-2-amine**

TD-001

 $C_{11}H_{11}N_3$  ( $M_r$  185.10)

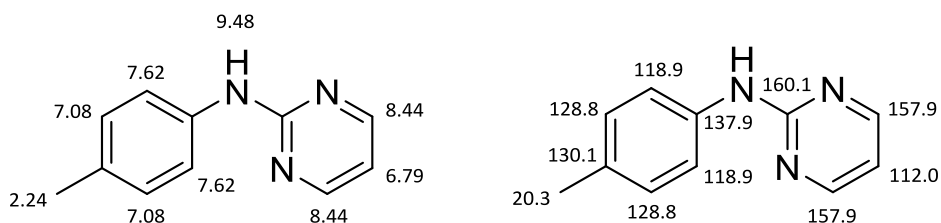
The synthesis of *N*-(*p*-tolyl)pyrimidin-2-amine was adapted from literature <sup>137</sup>. 2-Chloropyrimidine (1602 mg, 14.0 mmol) and *p*-toluidine (1000 mg, 9.3 mmol) were dissolved in 20 ml dioxane. 14 ml of acetic acid were added and the reaction was left stirring at 85 °C for 24h. The reaction was neutralized by addition of an aqueous solution of  $NaHCO_3$  and extracted with ethyl acetate three times. The organic phase was dried over  $Na_2SO_4$  and the solvent was removed under reduced pressure. The crude product was recrystallized from MeOH/ $H_2O$  to yield *N*-(*p*-tolyl)pyrimidin-2-amine as light yellow needles (100% HPLC purity).

**Yield:** 1463 mg (7.9 mmol, 85%)

<sup>1</sup>H NMR (300 MHz,  $CDCl_3$ ):  $\delta$  = 2.24 (s, 3H), 6.79 (t,  $^3J_{HH}$  = 4.8 Hz, 1H), 7.08 (d,  $^3J_{HH}$  = 8.6 Hz, 2H), 7.62 (d,  $^3J_{HH}$  = 8.6 Hz, 2H), 8.44 (d,  $^3J_{HH}$  = 4.8 Hz, 2H), 9.48 (s, 1H) ppm.

<sup>13</sup>C NMR (75 MHz,  $CDCl_3$ ):  $\delta$  = 20.3, 112.0, 118.9, 128.8, 130.1, 137.9, 157.9, 160.1 ppm.

**HRMS** (ESI):  $m/z$  = 186.10260 [ $M+H$ ]<sup>+</sup> (calc.  $m/z$  = 186.10257)





***N*-(4-bromophenyl)pyrimidin-2-amine**

TD-002

 $C_{10}H_8BrN_3$  ( $M_r$  250.00)

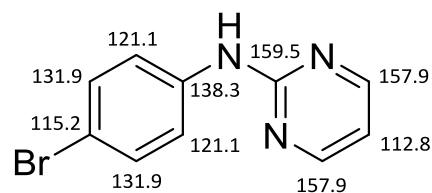
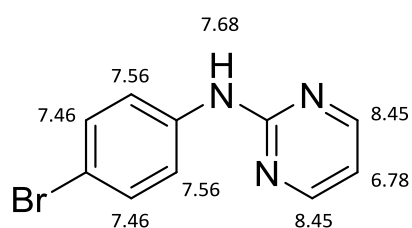
Synthesis of *N*-(4-bromophenyl)pyrimidin-2-amine was adapted from literature <sup>183</sup>. The reaction was carried out in a microwave for synthesis. Bis(dibenzylideneacetone)palladium(0) (12 mg, 0.013 mmol), Xantphos (15 mg, 0.025 mmol) and potassium *tert*-butoxide (200 mg, 1.78 mmol) were dissolved in 2 ml of anhyd. dioxane in a microwave vessel. The reaction was heated to 110°C and stirred for 20 min. After addition of 2-aminopyrimidine (169 mg, 1.78 mmol), 1,4-dibromobenzene (300 mg, 1.27 mmol) and 3 ml of anhyd. dioxane the reaction was heated to 140°C. After stirring for 2 hours the reaction was filtrated. The filtrate was concentrated under reduced pressure. The residue was dissolved in 20 ml of ethyl acetate, washed with brine and dried over sodium sulfate. The solvent was removed under reduced pressure. The crude product was purified by flash chromatography with a gradient of ethyl acetate and petroleum ether to afford *N*-(4-bromophenyl)pyrimidin-2-amine as a white solid (99% HPLC purity).

**Yield:** 119 mg (0.48 mmol, 37%)

<sup>1</sup>H NMR (300 MHz, CDCl<sub>3</sub>):  $\delta$  = 6.78 (t, <sup>3</sup> $J_{HH}$  = 4.8 Hz, 1H), 7.46 (d, <sup>3</sup> $J_{HH}$  = 9.0 Hz, 2H), 7.56 (d, <sup>3</sup> $J_{HH}$  = 9.0 Hz, 2H), 7.68 (bs, 1H), 8.45 (d, <sup>3</sup> $J_{HH}$  = 4.8 Hz, 2H) ppm.

<sup>13</sup>C NMR (75 MHz, CDCl<sub>3</sub>):  $\delta$  = 112.8, 115.2, 121.1, 131.9, 138.3, 157.9, 159.5 ppm.

**HRMS** (ESI):  $m/z$  = 249.99738 [M+H]<sup>+</sup> (calc.  $m/z$  <sup>79</sup>Br = 249.99744)



***N*-(4-nitrilphenyl)pyrimidin-2-amine**

TD-008

 $C_{11}H_8N_3$  ( $M_r$  196.08)

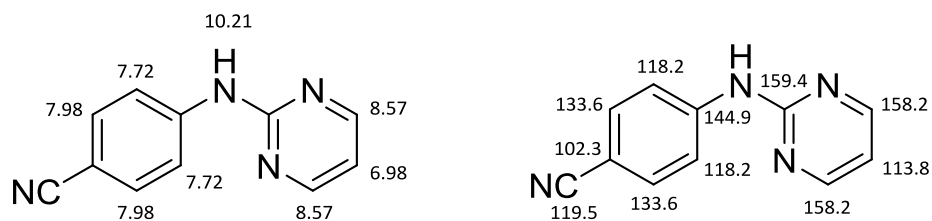
Synthesis of *N*-(4-nitrilphenyl)pyrimidin-2-amine was adapted from literature<sup>183</sup>. The reaction was carried out in a microwave for synthesis. Bis(dibenzylideneacetone)palladium(0) (15 mg, 0.017 mmol), Xantphos (19 mg, 0.033 mmol) and potassium *tert*-butoxide (259 mg, 2.31 mmol) were dissolved in 3 ml of anhyd. dioxane in a microwave vessel. The reaction was heated to 110°C and stirred for 20 min. After addition of 2-aminopyrimidine (188 mg, 1.98 mmol), 4-bromobenzonitrile (300 mg, 1.65 mmol) and 2 ml of anhyd. dioxane the reaction was heated to 130°C. After stirring for 2 hours the reaction was filtrated. The filtrate was concentrated under reduced pressure. The residue was dissolved in 20 ml of ethyl acetate, washed with brine and dried over sodium sulfate. The solvent was removed under reduced pressure. The crude product was purified by flash chromatography with a gradient of ethyl acetate and petroleum ether to afford *N*-(4-nitrilphenyl)pyrimidin-2-amine as a bright yellow solid (99% HPLC purity).

**Yield:** 113 mg (0.58 mmol, 35%)

**<sup>1</sup>H NMR** (300 MHz, DMSO- $d_6$ ):  $\delta$  = 6.98 (t,  $^3J_{HH}$  = 4.8 Hz, 1H), 7.72 (d,  $^3J_{HH}$  = 8.9 Hz, 2H), 7.98 (d,  $^3J_{HH}$  = 8.9 Hz, 2H), 8.57 (d,  $^3J_{HH}$  = 4.8 Hz, 2H), 10.21 (s, 1H) ppm.

**<sup>13</sup>C NMR** (75 MHz, DMSO- $d_6$ ):  $\delta$  = 102.3, 113.8, 118.2, 119.5, 133.0, 144.9, 158.2, 159.4 ppm.

**HRMS** (ESI):  $m/z$  = 197.08221 [ $M+H$ ]<sup>+</sup> (calc.  $m/z$  = 197.08217)



***N*-(4-(trifluoromethyl)phenyl)pyrimidin-2-amine**

SK-006

 $C_{11}H_8F_3N_3$  ( $M_r$  239.07)

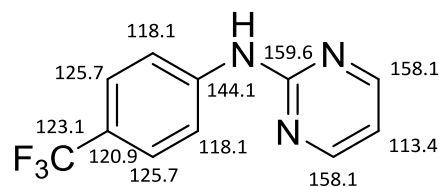
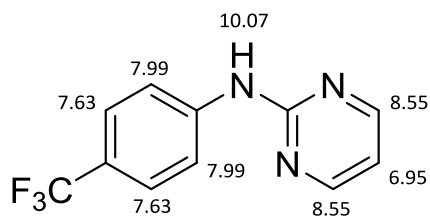
The synthesis of *N*-(4-(trifluoromethyl)phenyl)pyrimidin-2-amine was adapted from literature <sup>137</sup>. 2-Chloropyrimidine (1940 mg, 17.0 mmol) and 4-(trifluoromethyl)aniline (2100 mg, 13.0 mmol) were dissolved in 50 ml propan-2-ol. Three drops of conc. HCl were added and the reaction was left stirring at 85 °C for 24h. The solvent was removed under reduced pressure. The crude product was recrystallized from MeOH/H<sub>2</sub>O to yield *N*-(4-(trifluoromethyl)phenyl)pyrimidin-2-amine as light yellow needles (100% HPLC purity).

**Yield:** 3034 mg (12.7 mmol, 98%)

<sup>1</sup>H NMR (300 MHz, DMSO-*d*<sub>6</sub>): δ = 6.95 (t, <sup>3</sup>*J*<sub>HH</sub> = 4.8 Hz, 1H), 7.63 (d, <sup>3</sup>*J*<sub>HH</sub> = 8.7 Hz, 2H), 7.99 (d, <sup>3</sup>*J*<sub>HH</sub> = 8.6 Hz, 2H), 8.55 (d, <sup>3</sup>*J*<sub>HH</sub> = 4.8 Hz, 2H), 10.07 (s, 1H) ppm.

<sup>13</sup>C NMR (75 MHz, DMSO-*d*<sub>6</sub>): δ = 113.4, 118.1, 120.9, 123.1, 125.7, 144.1, 158.1, 159.6 ppm.

**HRMS (ESI):** *m/z* = 240.07422 [M+H]<sup>+</sup> (calc. *m/z* = 240.07431)



**Ethyl 4-(pyrimidin-2-ylamino)benzoate**

SK-007

 $C_{13}H_{13}N_3O_2$  ( $M_r$  243.11)

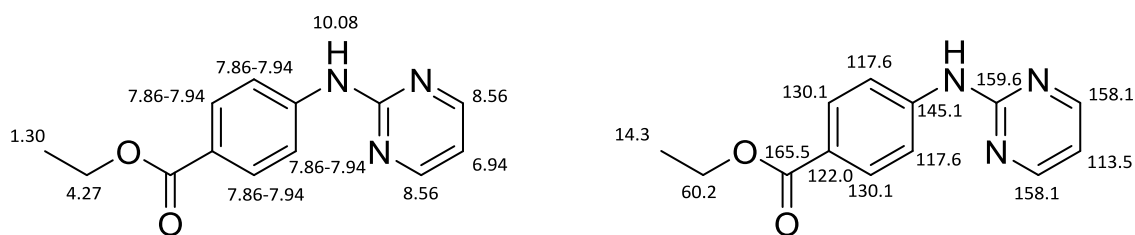
The synthesis of Ethyl 4-(pyrimidin-2-ylamino)benzoate was adapted from literature <sup>137</sup>. 2-Chloropyrimidine (1000 mg, 8.73 mmol) and ethyl 4-aminobenzoate (2164 mg, 13.1 mmol) were dissolved in 50 ml dioxane. Subsequent, 14 ml of acetic acid were added and the reaction was left stirring at 110 °C for 24h. The solvent was removed under reduced pressure. The crude product was recrystallized from MeOH/H<sub>2</sub>O to yield ethyl 4-(pyrimidin-2-ylamino)benzoate as a bright yellow solid (100% HPLC purity).

**Yield:** 1804 mg (7.42 mmol, 85%)

<sup>1</sup>H NMR (300 MHz, DMSO-d<sub>6</sub>):  $\delta$  = 1.30 (t, <sup>3</sup>J<sub>HH</sub> = 7.1 Hz, 3H), 4.27 (q, <sup>3</sup>J<sub>HH</sub> = 7.1 Hz, 2H), 6.94 (t, <sup>3</sup>J<sub>HH</sub> = 4.8 Hz, 1H), 7.86-7.94 (m, 4H), 8.56 (d, <sup>3</sup>J<sub>HH</sub> = 4.8 Hz, 2H), 10.08 (s, 1H) ppm.

<sup>13</sup>C NMR (75 MHz, DMSO-d<sub>6</sub>):  $\delta$  = 14.3, 60.2, 113.5, 117.6, 122.0, 130.1, 145.1, 158.1, 159.6, 165.5 ppm.

**HRMS (ESI):**  $m/z$  = 244.10812 [M+H]<sup>+</sup> (calc.  $m/z$  = 244.10805)



***N*-(4-methoxyphenyl)pyrimidin-2-amine**

alex-1.11

 $C_{11}H_{11}N_3O$  ( $M_r$  201.09)

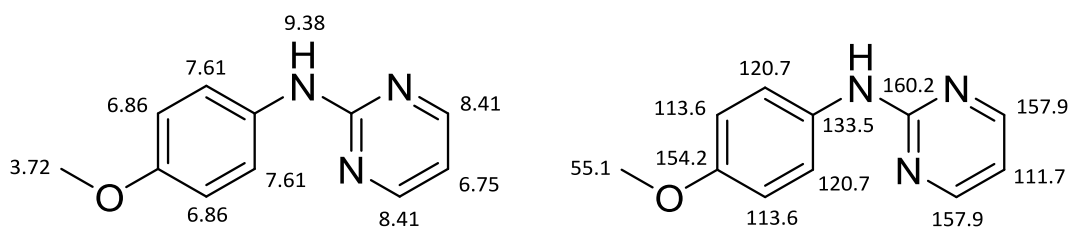
Synthesis of *N*-(4-methoxyphenyl)pyrimidin-2-amine was adapted from literature<sup>183</sup>. The reaction was carried out in a microwave for synthesis. Bis(dibenzylideneacetone)palladium(0) (16 mg, 0.018 mmol), *S*-BINAP (22 mg, 0.036 mmol) and potassium *tert*-butoxide (274 mg, 2.45 mmol) were dissolved in 1.5 ml of anhyd. dioxane in a microwave vessel. The reaction was heated to 80°C and stirred for 10 min. After addition of 2-chloropyrimidine (200 mg, 1.75 mmol), 4-methoxyaniline (258 mg, 2.10 mmol) and 3.5 ml of anhyd. dioxane the reaction was heated to 130°C. After stirring for 2 hours the reaction was filtrated. The filtrate was concentrated under reduced pressure. The residue was dissolved in 20 ml of ethyl acetate, washed with brine and dried over sodium sulfate. The solvent was removed under reduced pressure. The crude product was purified by flash chromatography with a gradient of ethyl acetate and petroleum ether to afford *N*-(4-methoxyphenyl)pyrimidin-2-amine as a white solid (99% HPLC purity).

**Yield:** 123 mg (0.62 mmol, 35%)

**<sup>1</sup>H NMR** (300 MHz, DMSO-*d*<sub>6</sub>):  $\delta$  = 3.72 (s, 3H), 6.75 (t,  $^3J_{HH}$  = 4.8 Hz, 1H), 6.86 (d,  $^3J_{HH}$  = 9.1 Hz, 2H), 7.61 (d,  $^3J_{HH}$  = 9.1 Hz, 2H), 8.41 (d,  $^3J_{HH}$  = 4.7 Hz, 2H), 9.38 (s, 1H) ppm.

**<sup>13</sup>C NMR** (75 MHz, DMSO-*d*<sub>6</sub>):  $\delta$  = 55.1, 111.7, 113.6, 120.7, 133.5, 154.2, 157.9, 160.2 ppm.

**HRMS** (ESI):  $m/z$  = 202.09766 [ $M+H$ ]<sup>+</sup> (calc.  $m/z$  = 202.09749)



***N*<sup>1</sup>,*N*<sup>1</sup>-dimethyl-*N*<sup>4</sup>-(pyrimidin-2-yl)benzene-1,4-diamine**

alex-1.10

C<sub>12</sub>H<sub>14</sub>N<sub>4</sub> (M<sub>r</sub> 114.12)

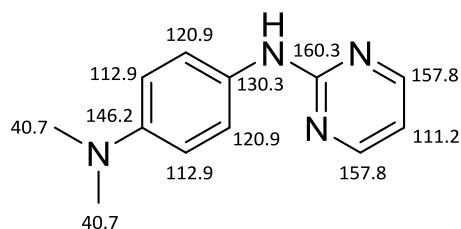
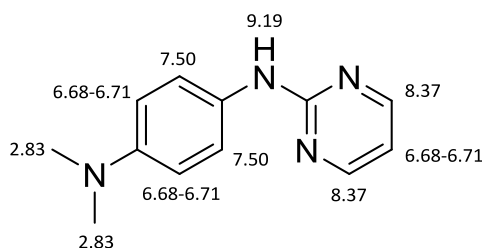
The synthesis of *N*<sup>1</sup>,*N*<sup>1</sup>-dimethyl-*N*<sup>4</sup>-(pyrimidin-2-yl)benzene-1,4-diamine was adapted from literature<sup>183</sup>. The reaction was carried out in a microwave for synthesis. Bis(dibenzylideneacetone)palladium(0) (24 mg, 0.026 mmol), S-BINAP (33 mg, 0.052 mmol) and potassium *tert*-butoxide (412 mg, 3.67 mmol) were dissolved in 1.5 ml of anhyd. dioxane in a microwave vessel. The reaction was heated to 80°C and stirred for 10 min. After addition of 2-chloropyrimidine (300 mg, 2.62 mmol), *N,N*-dimethylbenzene-1,4-diamine (428 mg, 3.14 mmol) and 3.5 ml of anhyd. dioxane the reaction was heated to 130°C. After stirring for 2 hours the reaction was filtrated. The filtrate was concentrated under reduced pressure. The residue was dissolved in 20 mL of ethyl acetate, washed with brine and dried over sodium sulfate. The solvent was removed under reduced pressure. The crude product was purified by flash chromatography with a gradient of ethyl acetate and petroleum ether to afford *N*<sup>1</sup>,*N*<sup>1</sup>-dimethyl-*N*<sup>4</sup>-(pyrimidin-2-yl)benzene-1,4-diamine as a yellow solid (96% HPLC purity).

**Yield:** 72 mg (0.63 mmol, 24%)

<sup>1</sup>H NMR (300 MHz, DMSO-*d*<sub>6</sub>): δ = 2.83 (s, 6H), 6.68-6.71 (m, 3H), 7.50 (d, <sup>3</sup>*J*<sub>HH</sub> = 9.1 Hz, 2H), 8.37 (d, <sup>3</sup>*J*<sub>HH</sub> = 4.8 Hz, 2H), 9.19 (s, 1H) ppm.

<sup>13</sup>C NMR (75 MHz, DMSO-*d*<sub>6</sub>): δ = 40.7, 111.2, 112.9, 120.9, 130.3, 146.2, 157.8, 160.3 ppm

**HRMS** (ESI): *m/z* = 215.12911 [M+H]<sup>+</sup> (calc. *m/z* = 215.12912)



***N*-(4,5-dimethoxy-2-nitrobenzyl)-*N*-phenylpyrimidin-2-amine (38)**

alex-1.0

 $C_{19}H_{18}N_4O_4$  ( $M_r$  366.14)

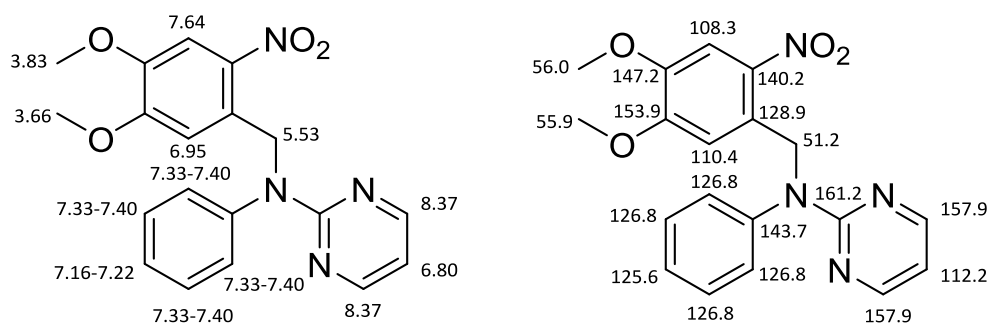
**38** was synthesized according to the general procedure for caging of *N*-phenylpyrimidin-2-amines with benzyl bromides from *N*-phenylpyrimidin-2-amine (200 mg, 1.16 mmol) and 4,5-dimethoxy-2-nitrobenzyl bromide (352 mg, 1.28 mmol). Purification was achieved by RP flash chromatography with a gradient of methanol and water to afford *N*-(4,5-dimethoxy-2-nitrobenzyl)-*N*-phenylpyrimidin-2-amine as a bright yellow solid (99% HPLC purity).

**Yield:** 170 mg (0.46 mmol, 40%).

$^1\text{H NMR}$  (300 MHz,  $\text{DMSO-d}_6$ ):  $\delta$  = 3.66 (s, 3H), 3.83 (s, 3H), 5.53 (s, 2H), 6.80 (t,  $^3J_{\text{HH}} = 4.7$  Hz, 1H), 6.95 (s, 1H), 7.16-7.22 (m, 1H), 7.33-7.40 (m, 4H), 7.64 (s, 1H), 8.97 (d,  $^3J_{\text{HH}} = 4.7$  Hz, 2H) ppm.

$^{13}\text{C NMR}$  (75 MHz,  $\text{DMSO-d}_6$ ):  $\delta$  = 51.2, 55.9, 56.0, 108.3, 110.4, 112.2, 125.6, 126.8, 128.9, 128.9, 140.2, 143.7, 147.2, 153.9, 157.9, 161.2 ppm.

**HRMS (ESI):**  $m/z = 367.13991$  [ $\text{M}+\text{H}$ ] $^+$  (calc.  $m/z = 367.1408$ )



***N*-(4,5-dimethoxy-2-nitrobenzyl)-*N*-(*p*-tolyl)pyrimidin-2-amine (37)**

TD-S-001

 $C_{20}H_{20}N_4O_4$  ( $M_r$  380.15)

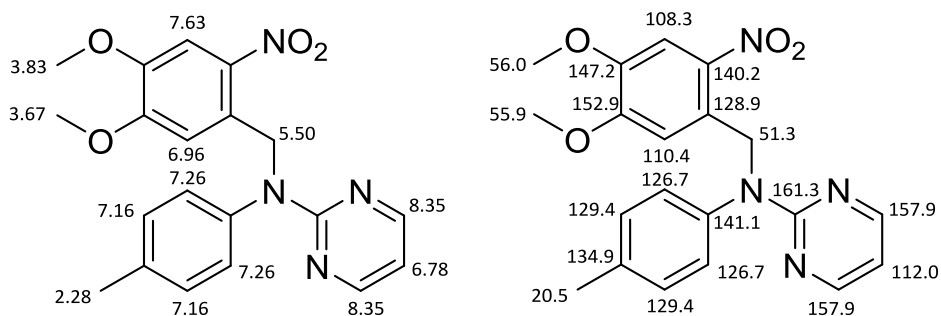
**37** was synthesized according to the general procedure for caging of *N*-phenylpyrimidin-2-amines with benzyl bromides from *N*-(*p*-tolyl)pyrimidin-2-amine (300 mg, 1.61 mmol) and 4,5-dimethoxy-2-nitrobenzyl bromide (537 mg, 1.94 mmol). Purification was achieved by flash chromatography with a gradient of ethyl acetate and petroleum ether to afford *N*-(4,5-dimethoxy-2-nitrobenzyl)-*N*-(*p*-tolyl)pyrimidin-2-amine as a bright yellow solid (99% HPLC purity).

**Yield:** 398 mg (1.05 mmol, 65%)

$^1\text{H NMR}$  (300 MHz, DMSO- $d_6$ ):  $\delta$  = 2.28 (s, 3H), 3.67 (s, 3H), 3.83 (s, 3H), 5.50 (s, 2H), 6.78 (t,  $^3J_{\text{HH}}$  = 4.8 Hz, 1H), 6.96 (s, 1H), 7.16 (d,  $^3J_{\text{HH}}$  = 8.1 Hz, 2H), 7.26 (d,  $^3J_{\text{HH}}$  = 8.4 Hz, 2H), 7.63 (s, 1H), 8.35 (d,  $^3J_{\text{HH}}$  = 4.7 Hz, 2H) ppm.

$^{13}\text{C NMR}$  (75 MHz, DMSO- $d_6$ ):  $\delta$  = 20.5, 51.3, 55.9, 26.0, 108.3, 110.4, 112.0, 126.7, 128.9, 129.4, 134.9, 140.2, 141.1, 147.2, 152.9, 157.9, 161.3 ppm.

**HRMS** (ESI):  $m/z$  = 381.15560  $[\text{M}+\text{H}]^+$  (calc.  $m/z$  = 381.15573)





***N*-(4-bromophenyl)-*N*-(4,5-dimethoxy-2-nitrobenzyl)pyrimidin-2-amine (39)**

TD-S-002

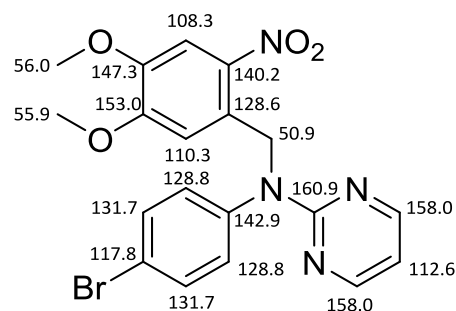
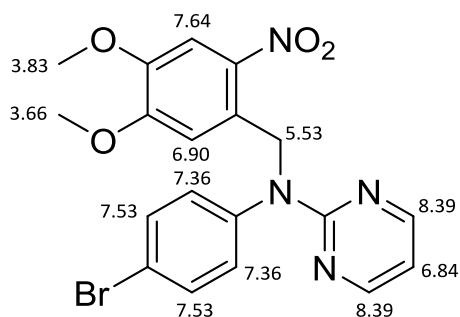
 $C_{19}H_{17}BrN_4O_4$  ( $M_r$  444.04)

**39** was synthesized according to the general procedure for caging of *N*-phenylpyrimidin-2-amines with benzyl bromides from *N*-(4-bromophenyl)pyrimidin-2-amine (95 mg, 0.38 mmol) and 4,5-dimethoxy-2-nitrobenzyl bromide (105 mg, 0.38 mmol). Purification was achieved by flash chromatography with a gradient of ethyl acetate and petroleum ether to afford *N*-(4,5-dimethoxy-2-nitrobenzyl)-*N*-(*p*-tolyl)pyrimidin-2-amine as a bright yellow solid (99% HPLC purity).

**Yield:** 89 mg (0.20 mmol, 53%)

**$^1H$  NMR** (300 MHz, DMSO- $d_6$ ):  $\delta$  = 3.66 (s, 3H), 3.83 (s, 3H), 5.53 (s, 2H), 6.84 (t,  $^3J_{HH}$  = 4.8 Hz, 1H), 6.90 (s, 1H), 7.36 (d,  $^3J_{HH}$  = 9.0 Hz, 2H), 7.53 (d,  $^3J_{HH}$  = 9.0 Hz, 2H), 7.64 (s, 1H), 8.39 (d,  $^3J_{HH}$  = 4.8 Hz, 2H) ppm.

**$^{13}C$  NMR** (75 MHz, DMSO- $d_6$ ):  $\delta$  = 50.9, 55.9, 56.0, 108.3, 110.3, 112.6, 117.8, 128.6, 128.8, 131.7, 140.2, 142.9, 147.3, 153.0, 158.0, 160.9 ppm.

**HRMS** (ESI):  $m/z$  = 445.05035 [ $M+H$ ] $^+$  (calc.  $m/z$   $^{79}Br$  = 445.05059)

***N*-(4,5-dimethoxy-2-nitrobenzyl)-*N*-(4-nitrilephenyl)pyrimidin-2-amine (42)**

TD-S-008

 $C_{20}H_{17}N_5O_4$  ( $M_r$  391.14)

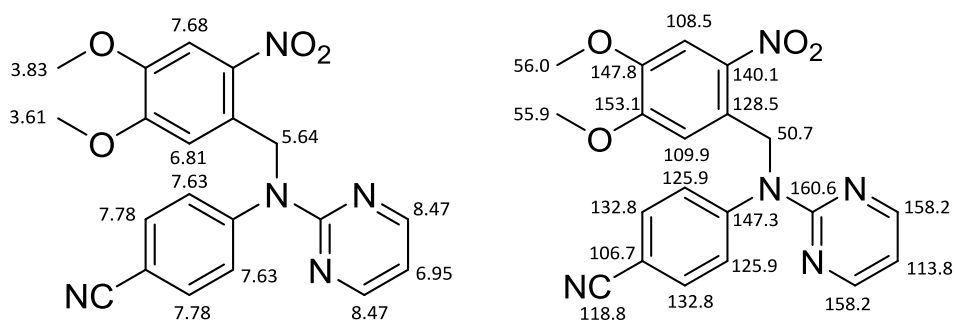
**42** was synthesized according to the general procedure for caging of *N*-phenylpyrimidin-2-amines with benzyl bromides from *N*-(4-nitrilephenyl)pyrimidin-2-amine (105 mg, 0.54 mmol) and 4,5-dimethoxy-2-nitrobenzyl bromide (148 mg, 0.54 mmol). Purification was achieved by flash chromatography with a gradient of ethyl acetate and petroleum ether to afford *N*-(4,5-dimethoxy-2-nitrobenzyl)-*N*-(4-nitrilephenyl)pyrimidin-2-amine as a bright yellow solid (95% HPLC purity).

**Yield:** 120 mg (0.33 mmol, 57%)

**$^1H$  NMR** (300 MHz, DMSO- $d_6$ ):  $\delta$  = 3.61 (s, 3H), 3.83 (s, 3H), 5.64 (s, 2H), 6.81 (s, 1H), 6.95 (t,  $^3J_{HH}$  = 4.8 Hz, 1H), 7.63 (d,  $^3J_{HH}$  = 8.7 Hz, 2H), 7.68 (s, 1H), 7.78 (d,  $^3J_{HH}$  = 8.7 Hz, 2H), 8.47 (d,  $^3J_{HH}$  = 4.8 Hz, 2H) ppm.

**$^{13}C$  NMR** (75 MHz, DMSO- $d_6$ ):  $\delta$  = 50.7, 55.9, 56.0, 106.7, 108.5, 109.9, 113.8, 118.8, 125.9, 128.5, 132.8, 140.1, 147.3, 147.8, 153.1, 158.2, 160.6 ppm.

**HRMS** (ESI):  $m/z$  = 392.13510 [ $M+H$ ] $^+$  (calc.  $m/z$  = 392.13533)



***N*-(4,5-dimethoxy-2-nitrobenzyl)-*N*-(4-(trifluoromethyl)phenyl)pyrimidin-2-amine (41)**

SK-C-006

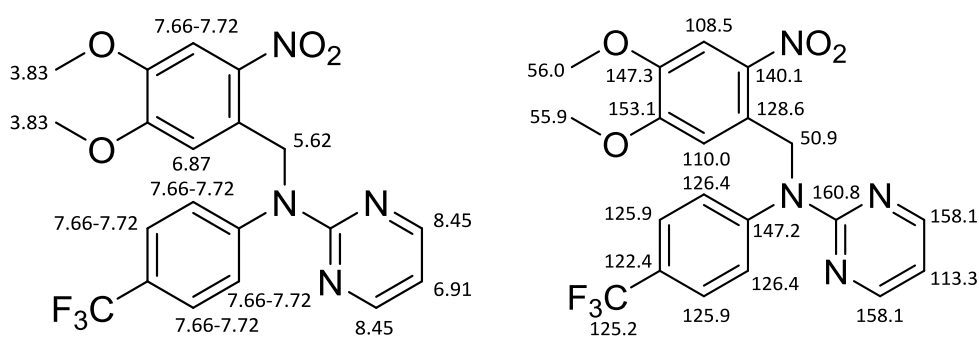
 $C_{20}H_{17}F_3N_4O_4$  (M<sub>r</sub> 434.12)

**41** was synthesized according to the general procedure for caging of *N*-phenylpyrimidin-2-amines with benzyl bromides from *N*-(4-(trifluoromethyl)phenyl)pyrimidin-2-amine (300 mg, 1.25 mmol) and 4,5-dimethoxy-2-nitrobenzyl bromide (416 mg, 1.51 mmol). Purification was achieved by flash chromatography with a gradient of ethyl acetate and petroleum ether to afford *N*-(4,5-dimethoxy-2-nitrobenzyl)-*N*-(4-(trifluoromethyl)phenyl)pyrimidin-2-amine as a bright yellow solid (97% HPLC purity).

**Yield:** 293 mg (0.68 mmol, 54%)

<sup>1</sup>H NMR (300 MHz, DMSO-d<sub>6</sub>): δ = 3.93 (s, 3H), 3.83 (s, 3H), 5.62 (s, 2H), 6.87 (s, 1H), 6.91 (t, <sup>3</sup>J<sub>HH</sub> = 4.8 Hz, 1H), 7.66-7.72 (m, 5H), 8.45 (d, <sup>3</sup>J<sub>HH</sub> = 4.8 Hz, 2H) ppm.

<sup>13</sup>C NMR (75 MHz, DMSO-d<sub>6</sub>): δ = 50.9, 55.9, 56.0, 108.5, 110.0, 113.3, 122.4, 125.2, 125.9, 126.4, 128.6, 140.1, 147.2, 147.3, 153.1, 158.1, 160.8 ppm.

**HRMS (ESI):** *m/z* = 435.12750 [M+H]<sup>+</sup> (calc. *m/z* = 435.12747)

**Ethyl 4-((4,5-dimethoxy-2-nitrobenzyl)(pyrimidin-2-yl)amino)benzoate (40)**

SK-C-007

 $C_{22}H_{22}N_4O_6$  ( $M_r$  438.15)

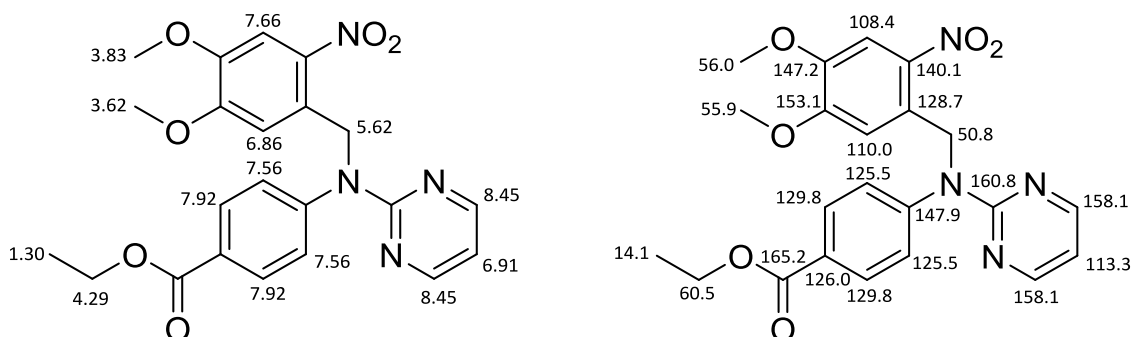
**40** was synthesized according to the general procedure for caging of *N*-phenylpyrimidin-2-amines with benzyl bromides from ethyl 4-(pyrimidin-2-ylamino)benzoate (100 mg, 0.41 mmol) and 4,5-dimethoxy-2-nitrobenzyl bromide (136 mg, 0.49 mmol). Purification was achieved by flash chromatography with a gradient of ethyl acetate and petroleum ether to afford ethyl 4-((4,5-dimethoxy-2-nitrobenzyl)(pyrimidin-2-yl)amino)benzoate as a brown yellow solid (94% HPLC purity).

**Yield:** 131 mg (0.30 mmol, 73%)

**$^1H$  NMR** (300 MHz, DMSO- $d_6$ ):  $\delta$  = 1.30 (t,  $^3J_{HH}$  = 7.1 Hz, 3H), 3.62 (s, 3H), 3.83 (s, 3H), 4.29 (q,  $^3J_{HH}$  = 7.1 Hz, 2H), 5.62 (s, 2H), 6.86 (s, 1H), 6.91 (t,  $^3J_{HH}$  = 4.8 Hz, 1H), 7.56 (d,  $^3J_{HH}$  = 8.7 Hz, 1H), 7.66 (s, 1H), 7.92 (d,  $^3J_{HH}$  = 8.7 Hz, 1H), 8.45 (d,  $^3J_{HH}$  = 4.8 Hz, 2H) ppm.

**$^{13}C$  NMR** (75 MHz, DMSO- $d_6$ ):  $\delta$  = 14.1, 50.8, 55.9, 56.0, 60.5, 108.4, 110.0, 113.3, 125.5, 126.0, 128.7, 129.8, 140.1, 147.2, 147.9, 153.1, 158.1, 160.8, 165.2 ppm.

**HRMS** (EI):  $m/z$  = 438.15296  $M^+$  (calc.  $m/z$  = 438.15393)



***N*-(4,5-dimethoxy-2-nitrobenzyl)-*N*-(4-methoxyphenyl)pyrimidin-2-amine (36)**

alex-1.12

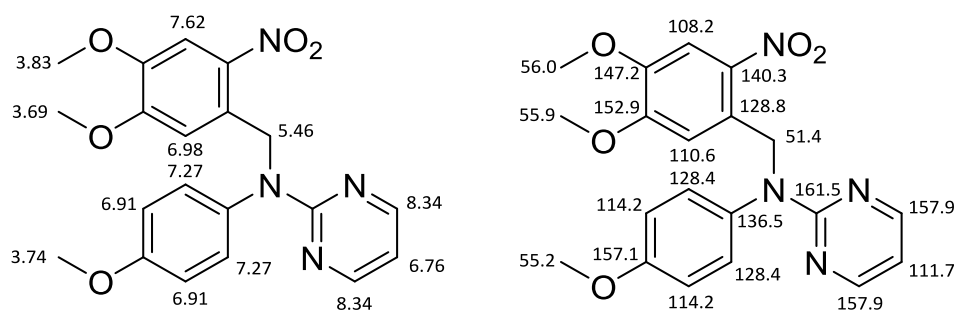
 $C_{20}H_{20}N_4O_5$  ( $M_r$  396.14)

**36** was synthesized according to the general procedure for caging of *N*-phenylpyrimidin-2-amines with benzyl bromides from *N*-(4-methoxyphenyl)pyrimidin-2-amine (90 mg, 0.44 mmol) and 4,5-dimethoxy-2-nitrobenzyl bromide (134 mg, 0.48 mmol). Purification was achieved by flash chromatography with a gradient of ethyl acetate and petroleum ether to afford *N*-(4,5-dimethoxy-2-nitrobenzyl)-*N*-(4-methoxyphenyl)pyrimidin-2-amine as a bright yellow solid (100% HPLC purity).

**Yield:** 107 mg (0.27 mmol, 62%)

**$^1H$  NMR** (300 MHz, DMSO- $d_6$ ):  $\delta$  = 3.69 (s, 3H), 3.74 (s, 3H), 3.83 (s, 3H), 5.46 (s, 2H), 6.76 (t,  $^3J_{HH}$  = 4.7 Hz, 1H), 6.91 (d,  $^3J_{HH}$  = 8.8 Hz, 1H), 6.98 (s, 1H), 7.27 (d,  $^3J_{HH}$  = 8.8 Hz, 1H), 7.62 (s, 1H), 8.34 (d,  $^3J_{HH}$  = 4.7 Hz, 2H) ppm.

**$^{13}C$  NMR** (75 MHz, DMSO- $d_6$ ):  $\delta$  = 51.4, 55.2, 55.9, 56.0, 108.2, 110.6, 111.7, 114.2, 128.4, 128.8, 136.5, 140.3, 147.2, 152.9, 157.1, 157.9, 161.5 ppm.

**HRMS** (ESI):  $m/z$  = 397.15062 [ $M+H$ ] $^+$  (calc.  $m/z$  = 397.15065)

***N*<sup>1</sup>-(4,5-dimethoxy-2-nitrobenzyl)-*N*<sup>4</sup>,*N*<sup>4</sup>-dimethyl-*N*<sup>1</sup>-(pyrimidin-2-yl)benzene-1,4-diamine (35)**

alex-1.13

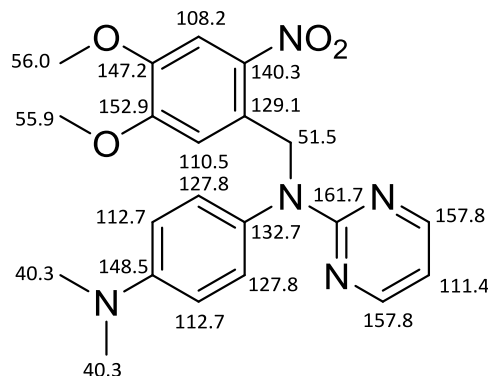
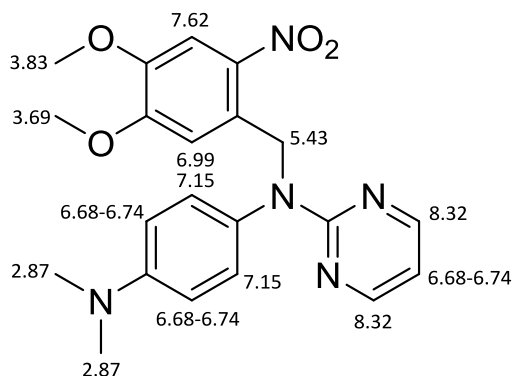
C<sub>21</sub>H<sub>23</sub>N<sub>5</sub>O<sub>4</sub> (M<sub>r</sub> 409.18)

**35** was synthesized according to the general procedure for caging of *N*-phenylpyrimidin-2-amines with benzyl bromides from *N*<sup>1</sup>,*N*<sup>1</sup>-dimethyl-*N*<sup>4</sup>-(pyrimidin-2-yl)benzene-1,4-diamine (80 mg, 0.38 mmol) and 4,5-dimethoxy-2-nitrobenzyl bromide (115 mg, 0.42 mmol). Purification was achieved by flash chromatography with a gradient of ethyl acetate and petroleum ether to afford *N*<sup>1</sup>-(4,5-dimethoxy-2-nitrobenzyl)-*N*<sup>4</sup>,*N*<sup>4</sup>-dimethyl-*N*<sup>1</sup>-(pyrimidin-2-yl)benzene-1,4-diamine as a yellow solid (95% HPLC purity).

**Yield:** 109 mg (0.27 mmol, 70%)

<sup>1</sup>H NMR (300 MHz, DMSO-*d*<sub>6</sub>): δ = 2.87 (s, 6H), 3.69 (s, 3H), 3.83 (s, 3H), 5.43 (s, 2H), 6.68-6.74 (m, 3H), 6.99 (s, 1H), 7.15 (d, <sup>3</sup>J<sub>HH</sub> = 8.8 Hz, 2H) 7.62 (s, 1H), 8.32 (d, <sup>3</sup>J<sub>HH</sub> = 4.7 Hz, 2H) ppm.

<sup>13</sup>C NMR (75 MHz, DMSO-*d*<sub>6</sub>): δ = 40.3, 51.5, 55.9, 56.0, 108.2, 110.5, 111.4, 112.7, 127.8, 129.1, 132.7, 140.3, 147.2, 148.5, 152.9, 157.8, 161.7 ppm

**HRMS (ESI):** *m/z* = 410.18214 [M+H]<sup>+</sup> (calc. *m/z* = 410.18228)

**8-Chloromethyl-4,4-difluoro-1,3,5,7-tetramethyl-4-bora-3a,4a-diaza-s-indacene (47)**

alex-1.29

 $C_{14}H_{16}BClF_2N_2$  ( $M_r$  296.55)

8-Chloromethyl-4,4-difluoro-1,3,5,7-tetramethyl-4-bora-3a,4a-diaza-s-indacene was synthesized according to literature<sup>171</sup>. Under an argon atmosphere chloroacetyl chloride (1098 mg, 9.7 mmol) was added dropwise to a solution of 2,4-dimethylpyrrole (1850 mg, 19.4 mmol) in 100 ml of anhyd. dichloromethane at room temperature with intense stirring. The reaction was heated to 50°C and left stirring for two hours. Subsequently, the mixture was cooled to 0°C and neutralized by addition of triethylamine (4922 mg, 48.6 mmol). After 15 min boron trifluoride etherate (9661 mg, 68.1 mmol) was added dropwise to the reaction. The reaction was heated to 50°C and left stirring for another hour. After full conversion the organic layer was washed with both a solution of hydrogen carbonate and water twice, dried over anhyd. sodium sulfate and concentrated under reduced pressure. The crude product was purified by flash chromatography with a gradient of dichloromethane and petroleum ether to afford 8-chloromethyl-4,4-difluoro-1,3,5,7-tetramethyl-4-bora-3a,4a-diaza-s-indacene as a dark orange solid with a green gloss (93% HPLC purity).

**Yield:** 450 mg (1.52 mmol, 16%). $^1H$  NMR (300 MHz,  $CDCl_3$ ):  $\delta$  = 2.53 (s, 12H), 4.77 (s, 2H), 6.09 (s, 2H) ppm. $^{13}C$  NMR (75 MHz,  $CDCl_3$ ):  $\delta$  = 14.8, 15.7, 37.3, 122.4, 131.5, 136.1, 141.3, 156.8 ppm.**HRMS** (EI):  $m/z$  = 296.10607  $M^+$  (calc.  $m/z$  = 296.10631)

**8-Chloromethyl-4,4-difluoro-1,3,5,7-tetramethyl-2,6-diethyl-4-bora-3a,4a-diaza-s-indacene (51)**

alex-1.21

 $C_{18}H_{24}BClF_2N_2$  ( $M_r$  352.17)

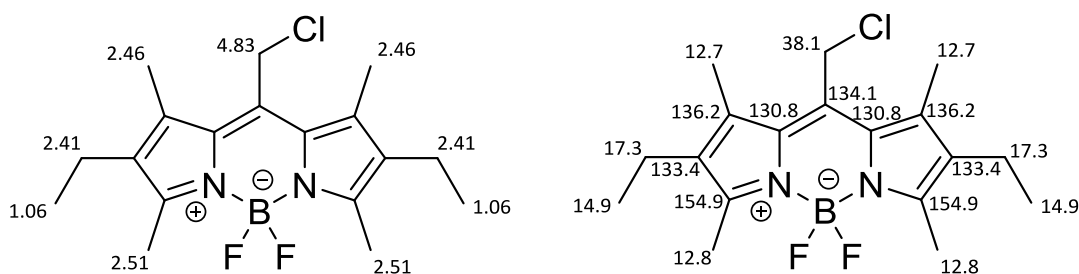
Synthesis was performed according to literature<sup>173</sup>. Under an argon atmosphere chloroacetyl chloride (834 mg, 7.4 mmol) was added dropwise to a solution of 3-ethyl-2,4-dimethylpyrrole (1820 mg, 14.8 mmol) in 100 ml of anhyd. dichloromethane at room temperature with intense stirring. The reaction was heated to 50°C and left stirring for two hours. Subsequently, the mixture was cooled to 0°C and neutralized by addition of triethylamine (3738 mg, 36.9 mmol). After 15 min boron trifluoride etherate (7337 mg, 51.7 mmol) was added dropwise to the reaction. The reaction was heated to 50°C and left stirring for another hour. After full conversion the organic layer was washed with both a solution of hydrogen carbonate and water twice, dried over anhyd. sodium sulfate and concentrated under reduced pressure. The crude product was purified by flash chromatography with a gradient of dichloromethane and petroleum ether to afford 8-chloromethyl-4,4-difluoro-1,3,5,7-tetramethyl-2,6-diethyl-4-bora-3a,4a-diaza-s-indacene as a dark orange solid with a green gloss (90% HPLC purity).

**Yield:** 1300 mg (3.7 mmol, 52%).

$^1H$  NMR (300 MHz,  $CDCl_3$ ):  $\delta$  = 1.06 (t,  $^3J_{HH}$  = 7.6 Hz, 6H), 2.41 (q,  $^3J_{HH}$  = 7.6 Hz, 4H), 2.46 (s, 6H), 2.51 (s, 6H), 4.83 (s, 2H) ppm.

$^{13}C$  NMR (75 MHz,  $CDCl_3$ ):  $\delta$  = 12.7, 12.8, 14.9, 17.3, 38.1, 130.8, 133.4, 134.1, 136.2, 154.9 ppm.

**HRMS** (EI):  $m/z$  = 352.16990  $M^+$  (calc.  $m/z$  = 352.16891)





**8-Iodomethyl-4,4-difluoro-1,3,5,7-tetramethyl-2,6-diethyl-4-bora-3a,4a-diaza-s-indacene (52)**

alex-1.34

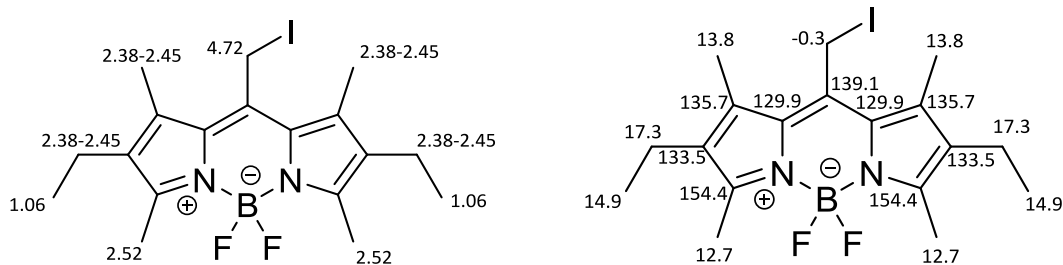
 $C_{18}H_{24}BF_2IN_2$  ( $M_r$  444.10)

Synthesis was performed according to literature <sup>174</sup>. Under an argon atmosphere 8-chloromethyl-4,4-difluoro-1,3,5,7-tetramethyl-2,6-diethyl-4-bora-3a,4a-diaza-s-indacene (500 mg, 1.4 mmol) and sodium iodide (425 mg, 2.8 mmol) were dissolved in 10 mL of anhyd. THF. The reaction was refluxed for one hour. After cooling, the solution was diluted with Et<sub>2</sub>O (20 ml), washed with water (20 ml) and the organic phase was dried (MgSO<sub>4</sub>), filtered and evaporated. The residue was purified by flash column chromatography (hexane/Et<sub>2</sub>O) to give the title compound as a dark purple solid (90% HPLC purity).

**Yield:** 498 mg (1.1 mmol, 80%).

<sup>1</sup>H NMR (300 MHz, CDCl<sub>3</sub>):  $\delta$  = 1.06 (t, <sup>3</sup>J<sub>HH</sub> = 7.6 Hz, 6H), 2.38-2.45 (m, 10H), 2.52 (s, 6H), 4.72 (s, 2H) ppm.

<sup>13</sup>C NMR (75 MHz, CDCl<sub>3</sub>):  $\delta$  = -0.3, 12.7, 13.8, 14.9, 17.3, 129.9, 133.5, 135.7, 139.1, 154.4 ppm.

**HRMS (EI):**  $m/z$  = 444.10421 M<sup>+</sup> (calc.  $m/z$  = 444.10453)

***N*-((4,4-difluoro-1,3,5,7-tetramethyl-4-bora-3a,4a-diaza-*s*-indacen-8-yl)methyl)-*N*-(4-(methylsulfonyl)phenyl)pyrimidin-2-amine (49)**

alex-1.26

C<sub>25</sub>H<sub>36</sub>BF<sub>2</sub>N<sub>5</sub>O<sub>2</sub>S (M<sub>r</sub> 509.19)

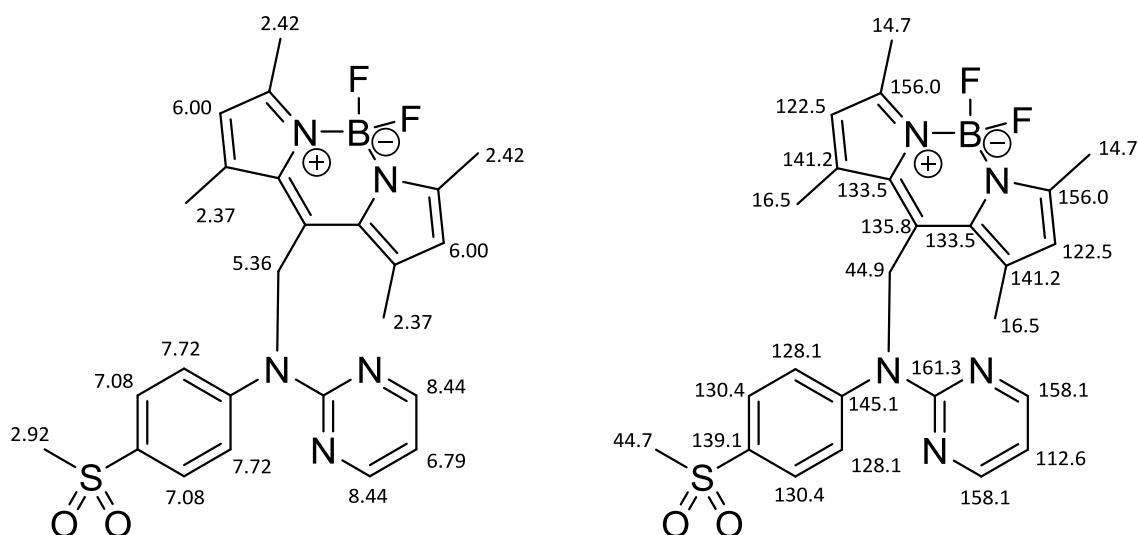
**49** was synthesized according to the general procedure for caging of *N*-phenylpyrimidin-2-amines with BODIPY protecting groups from **24** (50 mg, 0.20 mmol) and 8-chloromethyl-4,4-difluoro-1,3,5,7-tetramethyl-4-bora-3a,4a-diaza-*s*-indacene (150 mg, 0.50 mmol). Purification was achieved by flash chromatography on aluminum oxide with a gradient of ethyl acetate and petroleum ether, followed by RP flash chromatography with a gradient of acetonitrile and water to afford the title compound as a bright red solid (100% HPLC purity).

**Yield:** 5 mg (0.01 mmol, 3%).

<sup>1</sup>H NMR (300 MHz, DMSO-*d*<sub>6</sub>): δ = 2.37 (s, 6H), 2.42 (s, 6H), 2.92 (s, 3H), 5.36 (s, 2H), 6.00 (s, 2H), 6.79 (t, <sup>3</sup>J<sub>HH</sub> = 4.8 Hz, 1H), 7.08 (d, <sup>3</sup>J<sub>HH</sub> = 8.6 Hz, 2H), 7.72 (d, <sup>3</sup>J<sub>HH</sub> = 8.6 Hz, 2H), 8.44 (d, <sup>3</sup>J<sub>HH</sub> = 4.8 Hz, 2H) ppm.

<sup>13</sup>C NMR (75 MHz, DMSO- *d*<sub>6</sub>): δ = 14.7, 16.5, 44.7, 44.9, 112.6, 122.5, 128.1, 130.4, 133.5, 135.8, 139.1, 141.2, 145.1, 156.0, 158.1, 161.3 ppm.

**HRMS (MALDI):** m/z = 531.17999 [M+Na]<sup>+</sup> (calc. m/z = 531.17969)



***N*-((4,4-difluoro-1,3,5,7-tetramethyl-2,6-diethyl-4-bora-3a,4a-diaza-s-indacen-8-yl)methyl)-*N*-(4-(methylsulfonyl)phenyl)pyrimidin-2-amine (53)**

alex-1.30

C<sub>29</sub>H<sub>34</sub>BF<sub>2</sub>N<sub>5</sub>O<sub>2</sub>S (M<sub>r</sub> 565.26)

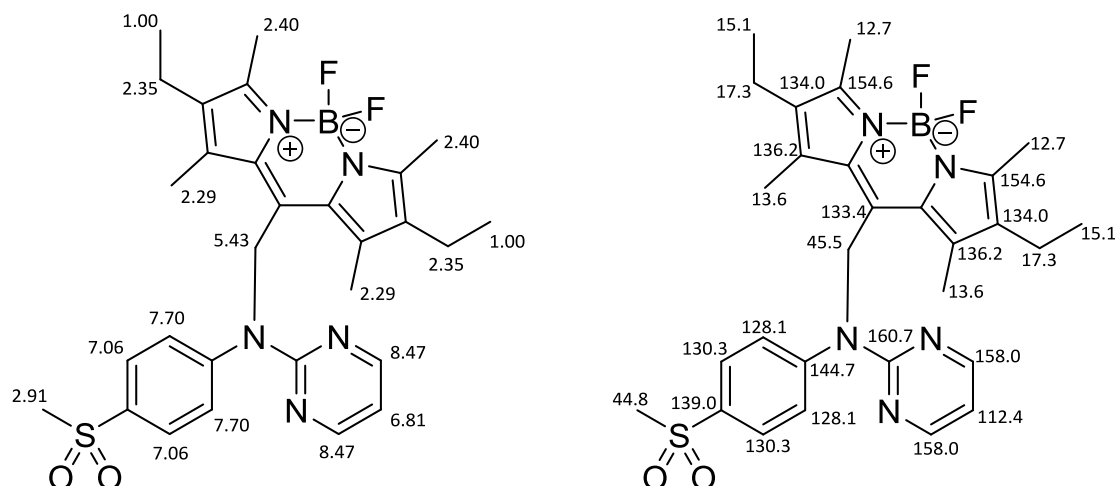
**53** was synthesized according to the general procedure for caging of *N*-phenylpyrimidin-2-amines with BODIPY protecting groups from **24** (80 mg, 0.32 mmol) and 8-iodomethyl-4,4-difluoro-1,3,5,7-tetramethyl-2,6-diethyl-4-bora-3a,4a-diaza-s-indacene (357 mg, 0.80 mmol). Purification was achieved by flash chromatography on aluminum oxide with a gradient of ethyl acetate and petroleum ether, followed by RP flash chromatography with a gradient of acetonitrile and water to afford the title compound as a bright red solid (100% HPLC purity).

**Yield:** 22 mg (0.04 mmol, 12%).

<sup>1</sup>H NMR (300 MHz, DMSO-d<sub>6</sub>): δ = 1.00 (t, <sup>3</sup>J<sub>HH</sub> = 7.5 Hz, 6H), 2.29 (s, 6H), 2.35 (q, <sup>3</sup>J<sub>HH</sub> = 7.5 Hz, 4H), 2.40 (s, 6H), 2.91 (s, 3H), 5.42 (s, 2H), 6.81 (t, <sup>3</sup>J<sub>HH</sub> = 4.9 Hz, 1H), 7.06 (d, <sup>3</sup>J<sub>HH</sub> = 8.6 Hz, 2H), 7.70 (d, <sup>3</sup>J<sub>HH</sub> = 8.6 Hz, 2H), 8.47 (d, <sup>3</sup>J<sub>HH</sub> = 4.9 Hz, 2H) ppm.

<sup>13</sup>C NMR (75 MHz, DMSO- d<sub>6</sub>): δ = 12.7, 13.6, 15.1, 17.3, 44.8, 45.5, 112.4, 128.1, 130.3, 133.4, 134.0, 136.2, 139.0, 144.7, 154.6, 158.0, 160.7 ppm.

**HRMS (ESI):** m/z = 566.26370 [M+H]<sup>+</sup> (calc. m/z = 566.26034)



***N*-((4,4-difluoro-1,3,5,7-tetramethyl-2,6-diethyl-4-bora-3a,4a-diaza-s-indacen-8-yl)methyl)-4-(1-isopropyl-2-methyl-1H-imidazol-5-yl)-*N*-(4-(methylsulfonyl)phenyl)pyrimidin-2-amine (54)**

alex-1.42

C<sub>36</sub>H<sub>44</sub>BF<sub>2</sub>N<sub>7</sub>O<sub>2</sub>S (M<sub>r</sub> 687.33)

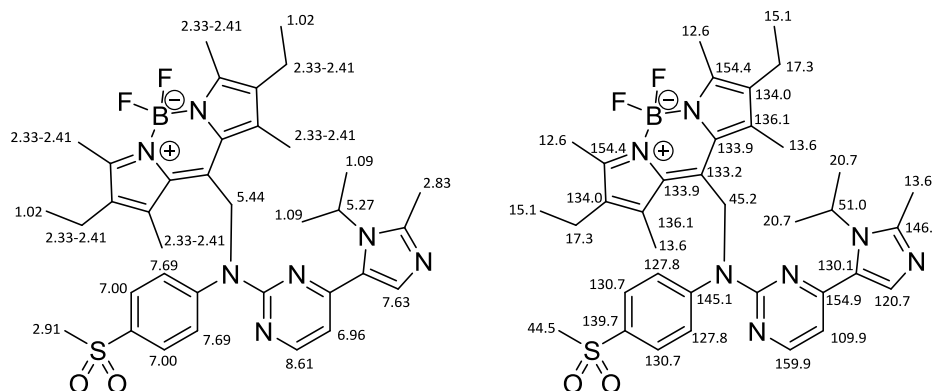
**54** was synthesized according to the general procedure for caging of *N*-phenylpyrimidin-2-amines with BODIPY protecting groups from **16** (150 mg, 0.40 mmol) and 8-iodomethyl-4,4-difluoro-1,3,5,7-tetramethyl-2,6-diethyl-4-bora-3a,4a-diaza-s-indacene (450 mg, 1.0 mmol). Purification was achieved by flash chromatography on silica with a gradient of methanol and dichloromethane, followed by RP flash chromatography with a gradient of acetonitrile and water to afford the title compound as a red solid (100% HPLC purity).

**Yield:** 41 mg (0.06 mmol, 15%).

<sup>1</sup>H NMR (300 MHz, DMSO-d<sub>6</sub>): δ = 1.02 (t, <sup>3</sup>J<sub>HH</sub> = 7.5 Hz, 6H), 1.09 (d, <sup>3</sup>J<sub>HH</sub> = 7.1 Hz, 6H), 2.33-2.41 (m, 16H), 2.83 (s, 3H), 2.91 (s, 3H), 5.27 (sept, <sup>3</sup>J<sub>HH</sub> = 7.1 Hz, 1H), 5.44 (s, 2H), 6.96 (d, <sup>3</sup>J<sub>HH</sub> = 5.2 Hz, 1 H), 7.00 (d, <sup>3</sup>J<sub>HH</sub> = 8.5 Hz, 2H), 7.63 (s, 1H), 7.69 (d, <sup>3</sup>J<sub>HH</sub> = 8.5 Hz, 2H), 8.61 (d, <sup>3</sup>J<sub>HH</sub> = 5.2 Hz, 1 H) ppm.

<sup>13</sup>C NMR (75 MHz, DMSO-d<sub>6</sub>): δ = 12.6, 13.6, 13.6, 15.1, 17.3, 20.7, 44.5, 45.2, 51.0, 109.9, 120.7, 127.8, 130.1, 130.7, 133.2, 133.9, 134.0, 136.1, 139.7, 145.1, 146.3, 154.4, 154.9, 159.9 ppm.

**HRMS** (EI): m/z = 687.33350 M<sup>+</sup> (calc. m/z = 687.33383)



## 5.4 Biological evaluation

### 5.4.1 Kinase assay

CDK2 Cyclin E1 assays were performed with the ADP-Glo™ Assay (Promega) according to the manufacturer's manual. Compounds **16** and **23** were dissolved in 100% DMSO and tested in a range of  $1 \cdot 10^{-5}$  to  $2 \cdot 10^{-10}$  M, in duplicate. Kinase, the respective compound, ATP and substrate were incubated for 1 h at 30°C under ambient light exclusion. For the photoactivation experiments the test plates were irradiated at 365 nm for 3 min (LED source: 16x Nichia NCSU276A U365, 5%, 37.5 mW, Sahlmann Photochemical Solutions). Final concentrations of reagents were 10 μM ATP, 0,1 μg/μl Histone H1 (substrate), 1% DMSO. Plate read out was performed with the FLUOstar Omega (BMG Labtech). Dose response curves and IC<sub>50</sub>-values were calculated with GraphPad Prism 7.03 using the Sigmoidal fitting (*log(inhibitor) vs. response – variable slope*).

Analysis was performed by Theo Rhodat.<sup>184</sup>

### 5.4.1 Tubulin polymerization assay

Compound **20** (0.5 mM in H<sub>2</sub>O) was UV irradiated for 5 min (365 nm, 1800 mW). Fluorescence-based tubulin polymerization assay was conducted in a final volume of 55 μL using the Tubulin Polymerization Assay kit (Cytoskeleton, CO, USA) as per manufacturer's instructions. Porcine brain tubulin was incubated with test compounds at 37°C and fluorescence was measured using Tecan M200 PRO+ microplate reader (excitation at 350 nm and emission at 420 nm).

### 5.4.2 Immunofluorescence imaging

Compound **20** (0.5 mM in DMEM) was irradiated with UV light (365 nm, 1800 mW, 5 min). U251 cells ( $3 \times 10^3$ ) were treated with vehicle or compounds for 24 h. Cells were fixed with ice-cold 100% methanol for 20 min at RT and blocked in 1% bovine serum albumin/PBS for 20 min. Cells were incubated with β-tubulin antibody (Abcam, #11308) and Alexa488-conjugated anti-mouse IgG (Life Technologies, #A-11029). Cell nuclei were counterstained using Prolong Gold mounting media with DAPI (4',6'-diamidino-2-phenylindole) and images were captured under an Olympus IX81 inverted fluorescence microscope and analyzed using AutoDEblur v 9.3 (AutoQuant Imaging).

### 5.4.3 Apoptosis assay

RN1 cells ( $2 \times 10^5$  cells/well) were treated with vehicle or test compounds and exposed to UV irradiation for 30s (365 nm, 1800 mW). The quantitative analysis of apoptotic cells after 48 h incubation was performed using the Muse™ Annexin V and Dead Cell Kit (MerckMillipore), as per manufacturer's instructions and analyzed using the Muse™ Cell Analyzer (MerckMillipore).

### 5.4.4 Cell culture

#### Photoactivatable small-molecule microtubule-targeting agent

U251 cell lines were obtained from the European Collection of Cell Cultures (ECACC, Salisbury, UK) through CellBank Australia and were cultured in DMEM medium supplemented with 10% FBS and Antibiotic-Antimycotic solution (both Life Technologies) at 37°C and 5% CO<sub>2</sub>. RN1 glioblastoma cell line was derived from glioblastoma specimen and maintained in KnockOut DMEM/F-12 basal medium supplemented with StemPro NSC SFM supplement, 2 mM GlutaMAX-ICTS, 20 ng/mL EGF, 10 ng/mL FGFβ and Antibiotic-Antimycotic solution (all Life Technologies). RN1 cells were grown as adherent cells on Matrigel-coated flasks. The protocols have been approved by the Human Ethics Committee of The University of Sydney (HREC 2013/131) and the Human Ethics Committee of the Royal Brisbane & Women's Hospital (RBWH 2004/161).

#### Photoactivatable CDK inhibitor

Panc89 (also known as T3M4) cell lines were kindly provided by Dr. Anna Trauzold from the Institute for Experimental Tumor Research, Faculty of Medicine, University of Kiel, Germany and were cultured in RPMI 1640 medium supplemented with 10% FBS and 1 mM pyruvate at 37°C and 5% CO<sub>2</sub>.

Cell culture was performed by Theo Rhodat.<sup>184</sup>

### 5.4.5 Cell viability assay

U251 ( $2 \times 10^3$  cells/well) and RN1 ( $4 \times 10^3$  cells/well) were seeded in 96-well plate in triplicate. On the following day, cells were treated with vehicle or test compounds (0.001 - 50  $\mu$ M) and exposed to UV irradiation (365 nm, 1800 mW, LED source: 8x Nichia NCSU033B, Sahlmann Photochemical Solutions) for 30 s (RN1 cells) or 60 s (U251 cells). After 72 h incubation, 10  $\mu$ L of the Cell-Titer Blue reagent (Promega) was added to the cell culture and incubated at 37°C for 4 h. Fluorescence was measured with Tecan M200 PRO+ microplate reader (excitation at 560 nm and emission at 590 nm).

### 5.4.6 Cell proliferation assay

The cells were grown in cell flasks until approximately 90% confluence and then seeded to give 1000 - 1500 cells in 100  $\mu$ L per well into 96-well CulturePlates™ (PerkinElmer, US). In addition to the test plates, one plate was prepared for reference measurement at day zero. All plates were incubated for 24 h at 37 °C in a humidified atmosphere with 5% CO<sub>2</sub>. Compounds **16**, **22**, **22a**, **23** and **26** were dissolved in 100% DMSO (v/v) and added to the test plates. The final DMSO concentration in the assay was 1% (v/v). Viability of the cells in the day zero control plates were determined on the same day without adding any compounds. For viability measurement the resazurin assay was used. The shift in the fluorescence signal was measured at the FLUOstar Omega (BMG Labtech). For the photoactivation experiments the test plates were irradiated at 365 nm for 3 min (LED source: 16x Nichia NCSU276A U365, 5%, 37.5 mW, Sahlmann Photochemical Solutions). Test plates were incubated for further 48 h and cell viability was defined as described above. Measured raw data was converted into percent of cell growth by using the high control (1% DMSO (v/v) without compound) and the day zero control. For dose-response studies, 11 different concentrations of compounds were tested in triplicates. EC<sub>50</sub> values were calculated using the log(inhibitor) - variable slope fit option of GraphPad Prism 5.

Analysis was performed by Theo Rhodat.<sup>184</sup>

### 5.4.7 Compound stability for biological evaluation

Compound **23** and **26** were dissolved in DMSO or PBS buffer with 20% DMSO (100  $\mu$ M resp. 50  $\mu$ M) and incubated in a clear glass HPLC vial either at a shelf in the lab (room temperature and ambient light) or inside the incubator of the cell culture (37°C, 5% CO<sub>2</sub> humidified atmosphere and dark) for 48 h. The samples were analyzed by HPLC after 0, 12, 24, 36 and 48 hours.



## 5.5 Cherenkov radiation experiments

All experiments were carried out in the clinic for nuclear medicine and radiopharmacy at the UKSH in Kiel.

### <sup>18</sup>F experiments

A stock solution (500  $\mu$ M) of compound **23** was prepared in DMSO. 100  $\mu$ L of the stock solution were transferred into a common amber glass HPLC vial (1.5 ml maximum volume). 900  $\mu$ L of <sup>18</sup>F in water respectively 900  $\mu$ L water for the negative control were added to the HPLC vial. Both samples were incubated in the autosampler of the HPLC at room temperature behind shielding. Samples were injected to HPLC alternating and analyzed. Time points and peak areas are indicated for each experiment.

### <sup>18</sup>Fluorodeoxyglucose experiments

A stock solution (250  $\mu$ M) of compound **23** was prepared in HPLC methanol. 200  $\mu$ L of the stock solution were transferred into a common amber glass HPLC vial (1.5 ml maximum volume). 200  $\mu$ L of <sup>18</sup>FDG in water respectively 200  $\mu$ L water for the negative control were added to the HPLC vial. Both samples were incubated in the autosampler of the HPLC at room temperature behind shielding. Samples were injected to HPLC alternating and analyzed. Time points and peak areas are indicated for each experiment.

### <sup>68</sup>Gallium experiments

A stock solution (250  $\mu$ M) of compound **23** was prepared in DMSO. 250  $\mu$ L of the stock solution were transferred into a common amber glass HPLC vial (1.5 ml maximum volume). 1000  $\mu$ L of <sup>68</sup>Ga in 1 M HCl, prepared with a Gallium-68 generator, respectively 1000  $\mu$ L of 100  $\mu$ M non-radioactive <sup>69</sup>Ga in 1 M HCl for the negative control were added to the HPLC vial behind shielding. The used radioactivity is indicated at each experiment. Both samples were incubated in the autosampler of the HPLC at room temperature behind shielding. Samples were injected to HPLC alternating and analyzed. Time points and peak areas are indicated for each experiment.

### Activation experiments using the linear particle accelerator

Compound solutions of **23** (50  $\mu\text{M}$ ) were prepared according to Table 6 in either a clear glass HPLC vial (Experiments 1 and 2) or in a 10 ml clear glass vessel (Experiment 3). The vessels or HPLC vials resp. were placed without a cap in the particle beam of the linear particle accelerator and irradiated with the resp. radiation, energy and maximum dose. Peak areas of both the caged and uncaged species were determined by HPLC analysis before and after irradiation. Additionally, both a negative and positive sample were measured. The positive samples were irradiated with UV light by a LED (5.4 W, 365 nm, 2 min) after irradiation using the linear particle accelerator.

#### 5.5.1 Reagents

Both  $^{18}\text{F}$  and  $^{18}\text{F}$ Fluorodeoxyglucose were obtained from the commercial company: f-con Eckert & Ziegler (Strahlen- und Medizintechnik AG, Berlin). They were used without further purification.  $^{68}\text{Ga}$  Gallium was generated in place at the UKSH Kiel in the department of nuclear medicine and radiopharmacy using a Gallium-68 generator.

#### 5.5.2 Linear Particle Accelerator

Activation experiments using a linear particle accelerator were performed using an electron linear accelerator type Artiste (Siemens Medical Systems).

#### 5.5.3 HPLC

Content determination of radioactive samples were performed using a Agilent 1100 HPLC with DAD detector and column heating placed behind shielding (Agilent Technologies, Waldbronn, Germany). The column was a Chromolit® SemiPrep RP18 (100 · 4.6 mm, Merck Millipore, Darmstadt, Germany). The injection volume was 20  $\mu\text{L}$ . A gradient of acetonitrile and water both with 0.1% (v/v) formic acid were used as the mobile phase with a fixed flow rate (1.5 ml · min<sup>-1</sup>). UV detection at 296 nm was used for content determination.

## 6 References

---

1. Fang, Z.; Grütter, C.; Rauh, D. Strategies for the Selective Regulation of Kinases with Allosteric Modulators: Exploiting Exclusive Structural Features. *ACS Chem. Biol.* **2013**, *8*, 58–70.
2. Levitzki, A. Tyrosine Kinase Inhibitors: Views of Selectivity, Sensitivity, and Clinical Performance. *Annu. Rev. Pharmacol. Toxicol.* **2013**, *53*, 161–185.
3. Velema, W. A.; Szymanski, W.; Feringa, B. L. Photopharmacology: Beyond proof of principle. *Journal of the American Chemical Society* **2014**, *136*, 2178–2191.
4. Ellis-Davies, G. Caged compounds: photorelease technology for control of cellular chemistry and physiology. *Nat. Methods* **2007**, *4*, 619–628.
5. Deiters, A. Principles and Applications of the Photochemical Control of Cellular Processes. *ChemBioChem* **2010**, *11*, 47–53.
6. Ferreira, R.; Nilsson, J. R.; Solano, C. *et al.* Design, Synthesis and Inhibitory Activity of Photoswitchable RET Kinase Inhibitors. *Scientific reports* **2015**, *5*, 9769.
7. Szymański, W.; Beierle, J. M.; Kistemaker, H. A. V. *et al.* Reversible Photocontrol of Biological Systems by the Incorporation of Molecular Photoswitches. *Chem. Rev.* **2013**, *113*, 6114–6178.
8. Brieke, C.; Rohrbach, F.; Gottschalk, A. *et al.* Light-controlled tools. *Angewandte Chemie (International ed. in English)* **2012**, *51*, 8446–8476.
9. Deisseroth, K. Optogenetics. *Nature methods* **2011**, *8*, 26–29.
10. Deisseroth, K.; Feng, G.; Majewska, A. K. *et al.* Next-Generation Optical Technologies for Illuminating Genetically Targeted Brain Circuits. *The Journal of neuroscience : the official journal of the Society for Neuroscience* **2006**, *26*, 10380.
11. Dolmans, D. E.J.G.J.; Fukumura, D.; Jain, R. K. Photodynamic therapy for cancer. *Nature Reviews Cancer* **2003**, *3*, 380–387.
12. Zhou, Z.; Song, J.; Nie, L. *et al.* Reactive oxygen species generating systems meeting challenges of photodynamic cancer therapy. *Chemical Society reviews* **2016**, *45*, 6597–6626.
13. Dougherty, T. J.; Gomer, C. J.; Henderson, B. W. *et al.* Photodynamic Therapy. *JNCI: Journal of the National Cancer Institute* **1998**, *90*, 889–905.

14. [http://www.ema.europa.eu/ema/index.jsp?curl=pages/medicines/human/medicines/004182/human\\_med\\_002190.jsp&mid=WCOb01ac058001d124](http://www.ema.europa.eu/ema/index.jsp?curl=pages/medicines/human/medicines/004182/human_med_002190.jsp&mid=WCOb01ac058001d124).
15. Bundesinstitut für Arzneimittel und Medizinprodukte. VASKULÄRE PHOTODYNAMISCHE THERAPIE (VASCULAR-TARGETED PHOTODYNAMIC THERAPY (VTP)) MIT TOOKAD® (padeliporfin): Leitfaden für den Arzt.
16. Bugaj, A. M. Vascular targeted photochemotherapy using padoporfin and padeliporfin as a method of the focal treatment of localised prostate cancer - clinician's insight. *World Journal of Methodology* **2016**, *6*, 65–76.
17. Slanina, T.; Shrestha, P.; Palao, E. *et al.* In Search of the Perfect Photocage: Structure-Reactivity Relationships in *meso*-Methyl BODIPY Photoremovable Protecting Groups. *Journal of the American Chemical Society* **2017**, *139*, 15168–15175.
18. Kaplan, J. H.; Forbush, B.; Hoffman, J. F. Rapid photolytic release of adenosine 5'-triphosphate from a protected analog: utilization by the Na:K pump of human red blood cell ghosts. *Biochemistry* **1978**, *17*, 1929–1935.
19. Milburn, T.; Matsubara, N.; Billington, A. P. *et al.* Synthesis, photochemistry, and biological activity of a caged photolabile acetylcholine receptor ligand. *Biochemistry* **1989**, *28*, 49–55.
20. Walker, J. W.; Reid, G. P.; McCray, J. A. *et al.* Photolabile 1-(2-nitrophenyl)ethyl phosphate esters of adenine nucleotide analogs. Synthesis and mechanism of photolysis. *Journal of the American Chemical Society* **1988**, *110*, 7170–7177.
21. Ando, H.; Furuta, T.; Tsien, R. Y. *et al.* Photo-mediated gene activation using caged RNA/DNA in zebrafish embryos. *Nature Genetics* **2001**, *28*, 317–325.
22. Walker, J. W.; Gilbert, S. H.; Drummond, R. M. *et al.* Signaling pathways underlying eosinophil cell motility revealed by using caged peptides. *Proceedings of the National Academy of Sciences* **1997**, *95*, 1568–1573.
23. Horbert, R.; Pinchuk, B.; Davies, P. *et al.* Photoactivatable Prodrugs of Antimelanoma Agent Vemurafenib. *ACS chemical biology* **2015**, *10*, 2099–2107.
24. Zindler, M.; Pinchuk, B.; Renn, C. *et al.* Design, Synthesis, and Characterization of a Photoactivatable Caged Prodrug of Imatinib. *ChemMedChem* **2015**, *10*, 1335–1338.
25. Horbert, R. Photoactivatable Kinase Inhibitors **2015**, Universität zu Kiel.
26. Holderfield, M.; Deuker, M. M.; McCormick, F. *et al.* Targeting RAF kinases for cancer therapy: BRAF-mutated melanoma and beyond. *Nature Reviews Cancer* **2014**, *14*, 455–467.
27. Das Thakur, M.; Salangsang, F.; Landman, A. S. *et al.* Modelling vemurafenib resistance in melanoma reveals a strategy to forestall drug resistance. *Nature* **2013**, *494*, 251–255.
28. Klán, P.; Šolomek, T.; Bochet, C. G. *et al.* Photoremovable Protecting Groups in Chemistry and Biology: Reaction Mechanisms and Efficacy. *Chem. Rev.* **2013**, *113*, 119–191.

29. Patchornik, A.; Amit, B.; Woodward, R. B. Photosensitive protecting groups. *Journal of the American Chemical Society* **1970**, *92*, 6333–6335.
30. Sheehan, J. C.; Wilson, R. M. Photolysis of Desyl Compounds. A New Photolytic Cyclization. *Journal of the American Chemical Society* **1964**, *86*, 5277–5281.
31. Schmidt, R.; Geissler, D.; Hagen, V. *et al.* Mechanism of Photocleavage of (Coumarin-4-yl)methyl Esters. *The Journal of Physical Chemistry A* **2007**, *111*, 5768–5774.
32. Šolomek, T.; Wirz, J.; Klán, P. Searching for Improved Photoreleasing Abilities of Organic Molecules. *Accounts of chemical research* **2015**, *48*, 3064–3072.
33. Šebej, P.; Wintner, J.; Müller, P. *et al.* Fluorescein Analogues as Photoremovable Protecting Groups Absorbing at ~520 nm. *The Journal of Organic Chemistry* **2013**, *78*, 1833–1843.
34. Štacko, P.; Šebej, P.; Veetil, A. T. *et al.* Carbon–Carbon Bond Cleavage in Fluorescent Pyronin Analogues Induced by Yellow Light. *Organic Letters* **2012**, *14*, 4918–4921.
35. Zayat, L.; Noval, M. G.; Campi, J. *et al.* A new inorganic photolabile protecting group for highly efficient visible light GABA uncaging. *ChemBioChem* **2007**, *8*, 2035–2038.
36. Olson, J. P.; Banghart, M. R.; Sabatini, B. L. *et al.* Spectral Evolution of a Photochemical Protecting Group for Orthogonal Two-Color Uncaging with Visible Light. *Journal of the American Chemical Society* **2013**, *135*, 15948–15954.
37. Solomek, T.; Mercier, S.; Bally, T. *et al.* Photolysis of ortho-nitrobenzylic derivatives: The importance of the leaving group. *Photochem. Photobiol. Sci.* **2012**, *11*, 548–555.
38. Phan, T. G.; Bullen, A. Practical intravital two-photon microscopy for immunological research: faster, brighter, deeper. *Immunology and cell biology* **2010**, *88*, 438–444.
39. Sternberg, E. D.; Dolphin, D.; Brückner, C. Porphyrin-based photosensitizers for use in photodynamic therapy. *Tetrahedron* **1998**, *54*, 4151–4202.
40. Goswami, P. P.; Syed, A.; Beck, C. L. *et al.* BODIPY-derived photoremovable protecting groups unmasked with green light. *Journal of the American Chemical Society* **2015**, *137*, 3783–3786.
41. Pehrson, J. R. Thymine dimer formation as a probe of the path of DNA in and between nucleosomes in intact chromatin. *Proceedings of the National Academy of Sciences* **1989**, *86*, 9149–9153.
42. Pinchuk, B. Characterization of photoactivatable Prodrugs of Kinase Inhibitors **2017**, Universität zu Kiel.
43. Dommaschk, M., Herges R. Design of Photoswitchable Contrast Agents for Magnetic Resonance Imaging **2016**. Dissertation, Universität zu Kiel.

44. Mallidi, S.; Anbil, S.; Bulin, A.-L. *et al.* Beyond the Barriers of Light Penetration: Strategies, Perspectives and Possibilities for Photodynamic Therapy. *Theranostics* **2016**, *6*, 2458–2487.
45. Fain, R.; Barbosa, F.; Cardenas, J. *et al.* Photonic Needles for Light Delivery in Deep Tissue-like Media. *Scientific reports* **2017**, *7*, 5627.
46. Bort, G.; Gallavardin, T.; Ogden, D. *et al.* From one-photon to two-photon probes: "caged" compounds, actuators, and photoswitches. *Angewandte Chemie (International ed. in English)* **2013**, *52*, 4526–4537.
47. Xie, R.; Yi, Y.; He, Y. *et al.* A simple BODIPY–imidazole-based probe for the colorimetric and fluorescent sensing of Cu(II) and Hg(II). *Tetrahedron* **2013**, *69*, 8541–8546.
48. Thorat, K. G.; Kamble, P.; Mallah, R. *et al.* Congeners of Pyrromethene-567 Dye: Perspectives from Synthesis, Photophysics, Photostability, Laser, and TD-DFT Theory. *The Journal of Organic Chemistry* **2015**, *80*, 6152–6164.
49. Krumova, K.; Cosa, G. Bodipy dyes with tunable redox potentials and functional groups for further tethering: Preparation, electrochemical, and spectroscopic characterization. *Journal of the American Chemical Society* **2010**, *132*, 17560–17569.
50. Durantini, A. M.; Greene, L. E.; Lincoln, R. *et al.* Reactive Oxygen Species Mediated Activation of a Dormant Singlet Oxygen Photosensitizer: From Autocatalytic Singlet Oxygen Amplification to Chemically Controlled Photodynamic Therapy. *Journal of the American Chemical Society* **2016**, *138*, 1215–1225.
51. Loudet, A.; Burgess, K. BODIPY dyes and their derivatives: Syntheses and spectroscopic properties. *Chemical reviews* **2007**, *107*, 4891–4932.
52. Sitkowska, K.; Feringa, B. L.; Szymański, W. Green-Light-Sensitive BODIPY Photoprotecting Groups for Amines. *The Journal of Organic Chemistry* **2018**, *83*, 1819–1827.
53. Schoder, S.; Kord Daoroun Kalai, S.; Reissig, H.-U. Novel Alkoxy-Substituted Dipyrins and Near-IR BODIPY Dyes: Preparation and Photophysical Properties. *Chemistry (Weinheim an der Bergstrasse, Germany)* **2017**, *23*, 12527–12533.
54. Volkert, W. A.; Hoffman, T. J. Therapeutic Radiopharmaceuticals. *Chem. Rev.* **1999**, *99*, 2269–2292.
55. <http://www.nuclear-power.net/nuclear-power/reactor-physics/atomic-nuclear-physics/fundamental-particles/beta-particle/cherenkov-radiation/>.
56. Axelsson, J.; Davis, S. C.; Gladstone, D. J. *et al.* Čerenkov emission induced by external beam radiation stimulates molecular fluorescence. *Medical physics* **2011**, *38*, 4127–4132.
57. Tanha, K.; Pashazadeh, A. M.; Pogue, B. W. Review of biomedical Čerenkov luminescence imaging applications. *Biomedical optics express* **2015**, *6*, 3053–3065.

58. Eldrick, R. H.; Parker, R. P. The Use of Cherenkov Radiation in the Measurement of  $\beta$ -Emitting Radionuclides. *International Journal of Applied Radiation and Isotopes* **1968**, *19*, 264–271.
59. Seguinot, J.; Ypsilantis, T. Photo-ionization and Cherenkov ring imaging. *Nuclear Instruments and Methods* **1977**, *142*, 377–391.
60. Čerenkov, P. A. Visible Radiation Produced by Electrons Moving in a Medium with Velocities Exceeding that of Light. *Phys. Rev.* **1937**, *52*, 378–379.
61. Bernlohr, K. Simulation of Imaging Atmospheric Cherenkov Telescopes with CORSIKA and sim\_telarray. *Astroparticle Physics* **2008**, *30*, 149–158.
62. Yang, Y.; Mu, J.; Xing, B. Photoactivated drug delivery and bioimaging. *WIREs Nanomed Nanobiotechnol* **2017**, *9*, e1408.
63. Spinelli, A. E.; Ferdeghini, M.; Cavedon, C. *et al.* First human Cerenkovgraphy. *Journal of Biomedical Optics* **2013**, *18*, 20202.
64. Takiue, M.; Natake, T.; Fujii, H. *et al.* Accuracy of Cerenkov measurements using a liquid scintillation spectrometer. *Applied Radiation and Isotopes* **1996**, *47*, 123–126.
65. Fujii, H.; Takiue, M. Radioassay of dual-labeled samples by sequential Cherenkov counting and liquid scintillation efficiency tracing technique. *Nuclear Instruments and Methods in Physics Research Section A: Accelerators, Spectrometers, Detectors and Associated Equipment* **1988**, *273*, 377–380.
66. Hastie, C. J.; McLauchlan, H. J.; Cohen, P. Assay of protein kinases using radiolabeled ATP: A protocol. *Nature Protocols* **2006**, *1*, 968-971.
67. Ran, C.; Zhang, Z.; Hooker, J. *et al.* In vivo photoactivation without "light": Use of Cherenkov radiation to overcome the penetration limit of light. *Molecular imaging and biology : MIB : the official publication of the Academy of Molecular Imaging* **2012**, *14*, 156–162.
68. Mayani, D. D. Proton therapy for cancer treatment. *Journal of Oncology Pharmacy Practice* **2010**, *17*, 186–190.
69. Schwartz, P. A.; Murray, B. W. Protein kinase biochemistry and drug discovery. *Bioorg. Chem.* **2011**, *39*, 192–210.
70. Müller, S.; Chaikuad, A.; Gray, N. S. *et al.* The ins and outs of selective kinase inhibitor development. *Nature chemical biology* **2015**, *11*, 818–821.
71. Fabbro, D. 25 years of small molecular weight kinase inhibitors: potentials and limitations. *Mol. Pharmacol.* **2015**, *87*, 766–775.
72. Roskoski, R. Classification of small molecule protein kinase inhibitors based upon the structures of their drug-enzyme complexes. *Pharmacological research* **2016**, *103*, 26–48.

73. Fischer, P. M. Approved and Experimental Small-Molecule Oncology Kinase Inhibitor Drugs: A Mid-2016 Overview. *Medicinal research reviews* **2016**, *37*, 314–367.
74. Dar, A. C.; Shokat, K. M. The Evolution of Protein Kinase Inhibitors from Antagonists to Agonists of Cellular Signaling. *Annu. Rev. Biochem.* **2011**, *80*, 769–795.
75. Roskoski, R. FDA-approved protein kinase inhibitors: <http://www.brimr.org/PKI/PKIs.htm>.
76. Imai, K.; Takaoka, A. Comparing antibody and small-molecule therapies for cancer. *Nature Reviews Cancer* **2006**, *6*, 714–727.
77. Manning, G.; Whyte, D. B.; Martinez, R. *et al.* The protein kinase complement of the human genome. *Science* **2002**, *298*, 1912–1934.
78. Wu, P.; Nielsen, T. E.; Clausen, M. H. FDA-approved small-molecule kinase inhibitors. *Trends Pharmacol. Sci.* **2015**, *36*, 422–439.
79. Malumbres, M. Cyclin-dependent kinases. *Genome Biol* **2014**, *15*, 122.
80. Asghar, U.; Witkiewicz, A. K.; Turner, N. C. *et al.* The history and future of targeting cyclin-dependent kinases in cancer therapy. *Nature reviews. Drug discovery* **2015**, *14*, 130–146.
81. Cicens, J.; Valius, M. The CDK inhibitors in cancer research and therapy. *Journal of cancer research and clinical oncology* **2011**, *137*, 1409–1418.
82. Raghavan, P.; Tumati, V.; Yu, L. *et al.* AZD5438, an Inhibitor of Cdk1, 2, and 9, Enhances the Radiosensitivity of Non-Small Cell Lung Carcinoma Cells. *International journal of radiation oncology, biology, physics* **2012**, *84*, e507–e514.
83. Guha, M. Cyclin-dependent kinase inhibitors move into Phase III. *Nature Reviews Drug Discovery* **2012**, *11*, 892–894.
84. Beaver, J. A.; Amiri-Kordestani, L.; Charlab, R. *et al.* FDA Approval: Palbociclib for the Treatment of Postmenopausal Patients with Estrogen Receptor–Positive, HER2-Negative Metastatic Breast Cancer. *Clinical Cancer Research* **2015**, *21*, 4760–4766.
85. <https://www.fda.gov/Drugs/InformationOnDrugs/ApprovedDrugs/ucm546438.htm>.
86. <https://www.fda.gov/Drugs/InformationOnDrugs/ApprovedDrugs/ucm578081.htm>.
87. [http://www.ema.europa.eu/ema/index.jsp?curl=pages/medicines/human/medicines/003853/human\\_med\\_002034.jsp&mid=WC0b01ac058001d124](http://www.ema.europa.eu/ema/index.jsp?curl=pages/medicines/human/medicines/003853/human_med_002034.jsp&mid=WC0b01ac058001d124).
88. [http://www.ema.europa.eu/ema/index.jsp?curl=pages/medicines/human/medicines/004213/human\\_med\\_002149.jsp&mid=WC0b01ac058001d124](http://www.ema.europa.eu/ema/index.jsp?curl=pages/medicines/human/medicines/004213/human_med_002149.jsp&mid=WC0b01ac058001d124).



89. Byth, K. F.; Thomas, A.; Hughes, G. *et al.* AZD5438, a potent oral inhibitor of cyclin-dependent kinases 1, 2, and 9, leads to pharmacodynamic changes and potent antitumor effects in human tumor xenografts. *Molecular cancer therapeutics* **2009**, *8*, 1856–1866.
90. Camidge, D. R.; Smethurst, D.; Growcott, J. *et al.* A first-in-man phase I tolerability and pharmacokinetic study of the cyclin-dependent kinase-inhibitor AZD5438 in healthy male volunteers. *Cancer Chemotherapy and Pharmacology* **2007**, *60*, 391–398.
91. Kavallaris, M. Microtubules and resistance to tubulin-binding agents. *Nature Reviews Cancer* **2010**, *10*, 194–204.
92. Rusan, N. M.; Fagerstrom, C. J.; Yvon, A.-M. C. *et al.* Cell Cycle-Dependent Changes in Microtubule Dynamics in Living Cells Expressing Green Fluorescent Protein- $\alpha$  Tubulin. *Molecular Biology of the Cell* **2001**, *12*, 971–980.
93. Verhey, K. J.; Gaertig, J. The Tubulin Code. *Cell Cycle* **2007**, *6*, 2152–2160.
94. Lodish, H.; Berk, A.; Zipursky, S. L. *Molecular Cell Biology. 4th edition: Section 19.5, Microtubule Dynamics and Motor Proteins during Mitosis*, 2000.
95. Komlodi-Pasztor, E.; Sackett, D.; Wilkerson, J. *et al.* Mitosis is not a key target of microtubule agents in patient tumors. *Nature Reviews Clinical Oncology* **2011**, *8*, 244–250.
96. Jordan, M. A.; Wilson, L. Microtubules as a target for anticancer drugs. *Nature Reviews Cancer* **2004**, *4*, 253–265.
97. Dumontet, C.; Jordan, M. A. Microtubule-binding agents: A dynamic field of cancer therapeutics. *Nature reviews. Drug discovery* **2010**, *9*, 790–803.
98. Weaver, B. A. How Taxol/paclitaxel kills cancer cells. *Molecular Biology of the Cell* **2014**, *25*, 2677–2681.
99. Moudi, M.; Go, R.; Yien, C. Y. S. *et al.* Vinca Alkaloids. *International Journal of Preventive Medicine* **2013**, *4*, 1231–1235.
100. Nogales, E.; Grayer Wolf, S.; Khan, I. A. *et al.* Structure of tubulin at 6.5 Å and location of the taxol-binding site. *Nature* **1995**, *375*, 424–427.
101. Döbber, A.; Phoa, A. F.; Abbassi, R. H. *et al.* Development and Biological Evaluation of a Photoactivatable Small Molecule Microtubule-Targeting Agent. *ACS medicinal chemistry letters* **2017**, *8*, 395–400.
102. Markman, M. Antineoplastic agents in the management of ovarian cancer: Current status and emerging therapeutic strategies. *Trends Pharmacol. Sci.* **2008**, *29*, 515–519.
103. Stathopoulos, G. P.; Antoniou, D.; Dimitroulis, J. *et al.* Liposomal cisplatin combined with paclitaxel versus cisplatin and paclitaxel in non-small-cell lung cancer: A randomized phase III multicenter trial. *Annals of Oncology* **2010**, *21*, 2227–2232.

104. Phoa, A. F.; Browne, S.; Gurgis, F. M.S. *et al.* Pharmacology of novel small-molecule tubulin inhibitors in glioblastoma cells with enhanced EGFR signalling. *Biochemical Pharmacology* **2015**, *98*, 587–601.
105. Saville, M. W.; Lietzau, J.; Pluda, J. M. *et al.* Treatment of HIV-associated Kaposi's sarcoma with paclitaxel. *The Lancet* **1995**, *346*, 26–28.
106. Perez, E. A. Paclitaxel in breast cancer. *The Oncologist* **1998**, *3*, 373–389.
107. Banks, W. A. Characteristics of compounds that cross the blood-brain barrier. *BMC Neurology* **2009**, *9*, S3.
108. Liu, Y.; Ran, R.; Chen, J. *et al.* Paclitaxel loaded liposomes decorated with a multifunctional tandem peptide for glioma targeting. *Biomaterials* **2014**, *35*, 4835–4847.
109. Kang, T.; Gao, X.; Hu, Q. *et al.* iNGR-modified PEG-PLGA nanoparticles that recognize tumor vasculature and penetrate gliomas. *Biomaterials* **2014**, *35*, 4319–4332.
110. Prabhu, S.; Harris, F.; Lea, R. *et al.* Small-molecule clinical trial candidates for the treatment of glioma. *Drug Discovery Today* **2014**, *19*, 1298–1308.
111. Gurgis, F. M.S.; Åkerfeldt, M. C.; Heng, B. *et al.* Cytotoxic activity of the MK2 inhibitor CMPD1 in glioblastoma cells is independent of MK2. *Cell Death Discovery* **2015**, *1*, 15028.
112. Fojo, A. T.; Menefee, M. Microtubule Targeting Agents: Basic Mechanisms of Multidrug Resistance (MDR). *Seminars in Oncology* **2005**, *32*, 3–8.
113. Siau, C.; Xiao, W.; Bennett, G. J. Paclitaxel- and vincristine-evoked painful peripheral neuropathies: Loss of epidermal innervation and activation of Langerhans cells. *Experimental Neurology* **2006**, *201*, 507–514.
114. Davis, R. E.; Schlumpf, B. E.; Klinger, P. D. Comparative neurotoxicity of tubulin-binding drugs: Inhibition of goldfish optic nerve regeneration. *Toxicology and Applied Pharmacology* **1985**, *80*, 308–315.
115. Zhang, J.; Yang, P. L.; Gray, N. S. Targeting cancer with small molecule kinase inhibitors. *Nature Reviews Cancer* **2009**, *9*, 28–39.
116. Gorre, M. E.; Mohammed, M.; Ellwood, K. *et al.* Clinical Resistance to STI-571 Cancer Therapy Caused by BCR-ABL Gene Mutation or Amplification. *Science* **2001**, *293*, 876–880.
117. Davies, H.; Bignell, G. R.; Cox, C. *et al.* Mutations of the BRAF gene in human cancer. *Nature* **2002**, *417*, 949–954.
118. Lovly, C. M.; Shaw, A. T. Molecular Pathways: Resistance to Kinase Inhibitors and Implications for Therapeutic Strategies. *Clinical cancer research : an official journal of the American Association for Cancer Research* **2014**, *20*, 2249–2256.
119. Hartmann, J. T.; Haap, M.; Kopp, H.-G. *et al.* Tyrosine Kinase Inhibitors – A Review on Pharmacology, Metabolism and Side Effects. *Current Drug Metabolism* **2009**, *10*, 470–481.

120. Sodergren, S. C.; White, A.; Efficace, F. *et al.* Systematic review of the side effects associated with tyrosine kinase inhibitors used in the treatment of gastrointestinal stromal tumours on behalf of the EORTC Quality of Life Group. *Critical Reviews in Oncology / Hematology*, **91**, 35–46.
121. Goeldner, M.; Givens, R. *Dynamic studies in biology: Phototriggers, photoswitches and caged biomolecules*; Wiley-VCH: Weinheim, 2005.
122. Ellis-Davies, G. C. R.; Matsuzaki, M.; Paukert, M. *et al.* 4-Carboxymethoxy-5,7-Dinitroindoliny-Glu: An Improved Caged Glutamate for Expeditious Ultraviolet and Two-Photon Photolysis in Brain Slices. *The Journal of neuroscience : the official journal of the Society for Neuroscience* **2007**, *27*, 6601–6604.
123. Kantevari, S.; Matsuzaki, M.; Kanemoto, Y. *et al.* Two-color, two-photon uncaging of glutamate and GABA. *Nat. Methods* **2009**, *7*, 123–125.
124. Mbatia, H. W.; Burdette, S. C. Photochemical Tools for Studying Metal Ion Signaling and Homeostasis. *Biochemistry* **2012**, *51*, 7212–7224.
125. Specht, A.; Bolze, F.; Omran, Z. *et al.* Photochemical tools to study dynamic biological processes. *HFSP Journal* **2009**, *3*, 255–264.
126. Corrie, J. E.T.; Furuta, T.; Givens, R. *et al.* *Photoremovable Protecting Groups Used for the Caging of Biomolecules*; Wiley Online Books, 2005.
127. Grewer, C.; Jäger, J.; Carpenter, B. K. *et al.* A New Photolabile Precursor of Glycine with Improved Properties: A Tool for Chemical Kinetic Investigations of the Glycine Receptor. *Biochemistry* **2000**, *39*, 2063–2070.
128. Mitra, A.; Mishra, L.; Li, S. Technologies for deriving primary tumor cells for use in personalized cancer therapy. *Trends Biotechnol.* **2013**, *31*, 347–354.
129. Castell, J. V.; Gómez-Lechón, M. J. Liver Cell Culture Techniques. In *Hepatocyte Transplantation: Methods and Protocols*; Dhawan, A., Hughes, R. D., Eds.; Humana Press: Totowa, NJ, 2009; pp 35–46.
130. Chopra, D. P.; Yeh, K.-y.; Brockman, R. W. Isolation and Characterization of Epithelial Cell Types from the Normal Rat Colon. *Cancer Research* **1981**, *41*, 168–175.
131. McCallum, H. M.; Lowther, G. W. Long-term culture of primary breast cancer in defined medium. *Breast Cancer Research and Treatment* **1996**, *39*, 247–259.
132. Dairkee, S. H.; Deng, G.; Stampfer, M. R. *et al.* Selective Cell Culture of Primary Breast Carcinoma. *Cancer Research* **1995**, *55*, 2516–2519.
133. She, S.; Bian, S.; Huo, R. *et al.* Degradable Organically-Derivatized Polyoxometalate with Enhanced Activity against Glioblastoma Cell Line. *Scientific reports* **2016**, *6*, 33529.

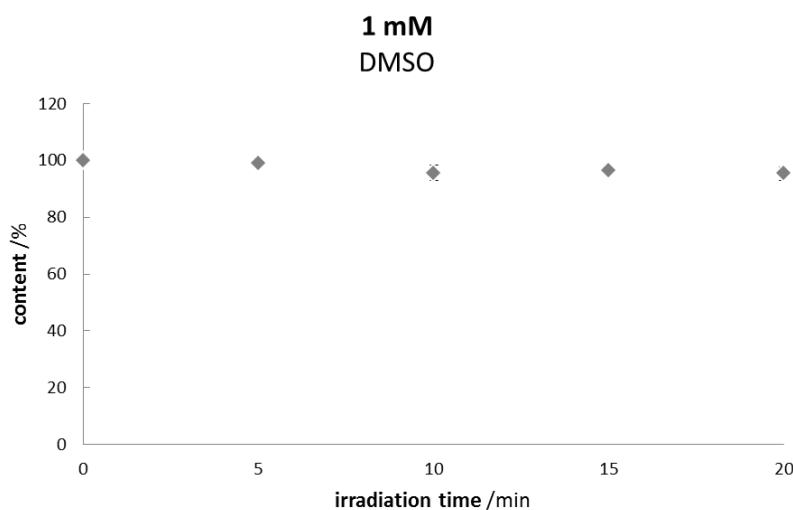
134. Motaln, H.; Koren, A.; Gruden, K. *et al.* Heterogeneous glioblastoma cell cross-talk promotes phenotype alterations and enhanced drug resistance. *Oncotarget* **2015**, *6*, 40998–401017.
135. Gan, P. P.; McCarroll, J. A.; Po'uha, S. T. *et al.* Microtubule Dynamics, Mitotic Arrest, and Apoptosis: Drug-Induced Differential Effects of  $\beta$ III-Tubulin. *Molecular cancer therapeutics* **2010**, *9*, 1339–1348.
136. Vermes, I.; Haanen, C.; Steffens-Nakken, H. *et al.* A novel assay for apoptosis Flow cytometric detection of phosphatidylserine expression on early apoptotic cells using fluorescein labelled Annexin V. *Journal of Immunological Methods* **1995**, *184*, 39–51.
137. Lv, Y.; Li, M.; Cao, S. *et al.* Discovery of anilinopyrimidine-based naphthamide derivatives as potent VEGFR-2 inhibitors. *Med. Chem. Commun.* **2015**, *6*, 1375–1380.
138. Lusic, H.; Deiters, A. A New Photocaging Group for Aromatic N -Heterocycles. *Synthesis* **2006**, *2006*, 2147–2150.
139. Morckel, A. R.; Lusic, H.; Farzana, L. *et al.* A photoactivatable small-molecule inhibitor for light-controlled spatiotemporal regulation of Rho kinase in live embryos. *J. Cell Sci.* **2012**, *125*, 437-442.
140. Subramaniam, D.; Periyasamy, G.; Ponnurangam, S. *et al.* CDK-4 Inhibitor P276 Sensitizes Pancreatic Cancer Cells to Gemcitabine-Induced Apoptosis. *Molecular cancer therapeutics* **2012**, *11*, 1598–1608.
141. Ge, Y.; Lei, W.; Ma, Y. *et al.* Synergistic antitumor effects of CDK inhibitor SNS-032 and an oncolytic adenovirus co-expressing TRAIL and Smac in pancreatic cancer. *Molecular Medicine Reports* **2017**, *15*, 3521–3528.
142. Al-Aynati, M. M.; Radulovich, N.; Ho, J. *et al.* Overexpression of G1-S Cyclins and Cyclin-Dependent Kinases during Multistage Human Pancreatic Duct Cell Carcinogenesis. *Clinical Cancer Research* **2004**, *10*, 6598–6605.
143. Kammari, L.; Šolomek, T.; Ngoy, B. P. *et al.* Orthogonal Photocleavage of a Monochromophoric Linker. *Journal of the American Chemical Society* **2010**, *132*, 11431–11433.
144. Pelliccioli, A. P.; Wirz, J. Photoremovable protecting groups: reaction mechanisms and applications. *Photochem. Photobiol. Sci.* **2002**, *1*, 441–458.
145. Il'ichev, Y. V. Rearrangements of 2-Nitrobenzyl Compounds. 2. Substituent Effects on the Reactions of the Quinonoid Intermediates. *The Journal of Physical Chemistry A* **2003**, *107*, 10159–10170.
146. Sonawane, Y. A.; Taylor, M. A.; Napoleon, J. V. *et al.* Cyclin Dependent Kinase 9 Inhibitors for Cancer Therapy. *Journal of Medicinal Chemistry* **2016**, *59*, 8667–8684.
147. Wang, S.; Meades, C.; Wood, G. *et al.* 2-Anilino-4-(thiazol-5-yl)pyrimidine CDK Inhibitors: Synthesis, SAR Analysis, X-ray Crystallography, and Biological Activity. *Journal of Medicinal Chemistry* **2004**, *47*, 1662–1675.

148. Shao, H.; Shi, S.; Foley, D. W. *et al.* Synthesis, structure–activity relationship and biological evaluation of 2,4,5-trisubstituted pyrimidine CDK inhibitors as potential anti-tumour agents. *European Journal of Medicinal Chemistry* **2013**, *70*, 447–455.
149. Yosaatmadja, Y.; Silva, S.; Dickson, J. M. *et al.* Binding mode of the breakthrough inhibitor AZD9291 to epidermal growth factor receptor revealed. *Journal of Structural Biology* **2015**, *192*, 539–544.
150. Villaseñor, A.; Kondru, R.; Ho, H. *et al.* Structural Insights for Design of Potent Spleen Tyrosine Kinase Inhibitors from Crystallographic Analysis of Three Inhibitor Complexes. *Chemical Biology & Drug Design* **2009**, *73*, 466–470.
151. Huang, W.-S.; Liu, S.; Zou, D. *et al.* Discovery of Brigatinib (AP26113), a Phosphine Oxide-Containing, Potent, Orally Active Inhibitor of Anaplastic Lymphoma Kinase. *Journal of Medicinal Chemistry* **2016**, *59*, 4948–4964.
152. Hammett, L. P. The Effect of Structure upon the Reactions of Organic Compounds. Benzene Derivatives. *Journal of the American Chemical Society* **1937**, *59*, 96–103.
153. Taft, R. W. Linear Free Energy Relationships from Rates of Esterification and Hydrolysis of Aliphatic and Ortho-substituted Benzoate Esters. *Journal of the American Chemical Society* **1952**, *74*, 2729–2732.
154. Frey, J.; Curchod, B. F. E.; Scopelliti, R. *et al.* Structure-property relationships based on Hammett constants in cyclometalated iridium(III) complexes: Their application to the design of a fluorine-free FIrPic-like emitter. *Dalton transactions (Cambridge, England : 2003)* **2014**, *43*, 5667–5679.
155. Hansch, C.; Leo, A.; Taft, R. W. A survey of Hammett substituent constants and resonance and field parameters. *Chem. Rev.* **1991**, *91*, 165–195.
156. Cong, M.; Fan, Y.; Raimundo, J.-M. *et al.* Pd(dba)<sub>2</sub> vs Pd<sub>2</sub>(dba)<sub>3</sub>: An in-Depth Comparison of Catalytic Reactivity and Mechanism via Mixed-Ligand Promoted C–N and C–S Coupling Reactions. *Organic Letters* **2014**, *16*, 4074–4077.
157. Schulte II, J. P.; Tweedie, S. R. Palladium-Catalyzed Couplings of Heteroaryl Amines with Aryl Halides Using Sodium Phenolate as the Stoichiometric Base. *Synlett* **2007**, *2007*, 2331–2336.
158. Shaw, J. W.; Grayson, D. H.; Rozas, I. Cleavage of 2-(Arylamino)-4,6-dimethoxypyrimidines To Yield Arylguanidines. *Eur. J. Org. Chem.* **2014**, *2014*, 3565–3569.
159. Tundel, R. E.; Anderson, K. W.; Buchwald, S. L. Expedited Palladium-Catalyzed Amination of Aryl Nonaflates through the Use of Microwave-Irradiation and Soluble Organic Amine Bases. *The Journal of Organic Chemistry* **2006**, *71*, 430–433.
160. Hippler, M. Photochemical Kinetics: Reaction Orders and Analogies with Molecular Beam Scattering and Cavity Ring-Down Experiments. *Journal of Chemical Education* **2003**, *80*, 1074.
161. Hippler, M. Does a Photochemical Reaction Have a Kinetic Order? (the author replies). *Journal of Chemical Education* **2005**, *82*, 37–38.

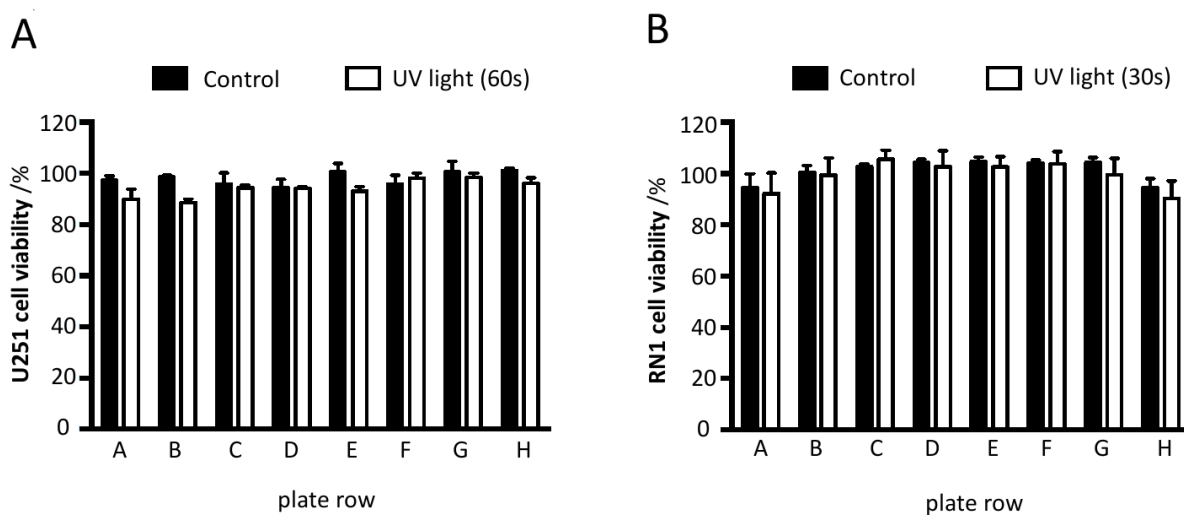
162. Logan, S. R. Does a Photochemical Reaction Have a Reaction Order? *Journal of Chemical Education* **1997**, *74*, 1303.
163. Toby, S. The Relationship between Stoichiometry and Kinetics. *Journal of Chemical Education* **2000**, *77*, 188.
164. Toby, S.; Tobias, I. What Is the Overall Stoichiometry of a Complex Reaction? *Journal of Chemical Education* **2003**, *80*, 520.
165. Shaw, H.; Toby, S. Light absorption in photochemistry. *Journal of Chemical Education* **1966**, *43*, 408.
166. Kolemen, S.; Cakmak, Y.; Erten-Ela, S. *et al.* Solid-State Dye-Sensitized Solar Cells Using Red and Near-IR Absorbing Bodipy Sensitizers. *Organic Letters* **2010**, *12*, 3812–3815.
167. Treibs, A.; Kreuzer, F.-H. Difluorboryl-Komplexe von Di- und Tripyrrylmethenen. *Justus Liebigs Ann. Chem.* **1968**, *718*, 208–223.
168. Kawatani, M.; Kamiya, M.; Takahashi, H. *et al.* Factors affecting the uncaging efficiency of 500 nm light-activatable BODIPY caging group. *Bioorganic & medicinal chemistry letters* **2018**, *28*, 1–5.
169. Bumagina, N. A.; Antina, E. V.; Berezin, M. B. *et al.* Influence of structural and solvation factors on the spectral-fluorescent properties of alkyl-substituted BODIPYs in solutions. *Spectrochimica acta. Part A, Molecular and biomolecular spectroscopy* **2017**, *173*, 228–234.
170. Rubinstein, N.; Liu, P.; Miller, E. W. *et al.* meso-Methylhydroxy BODIPY: A scaffold for photo-labile protecting groups. *Chemical communications (Cambridge, England)* **2015**, *51*, 6369–6372.
171. Wu, Y.; Peng, X.; Guo, B. *et al.* Boron dipyrromethene fluorophore based fluorescence sensor for the selective imaging of Zn(II) in living cells. *Organic & biomolecular chemistry* **2005**, *3*, 1387–1392.
172. Guo, B.; Peng, X.; Cui, A. *et al.* Synthesis and spectral properties of new boron dipyrromethene dyes. *Dyes and Pigments* **2007**, *73*, 206–210.
173. Amat-Guerri, F.; Liras, M.; Luisa Carrascoso, M. *et al.* Methacrylate-tethered Analogs of the Laser Dye PM567—Synthesis, Copolymerization with Methyl Methacrylate and Photostability of the Copolymers. *Photochem Photobiol* **2003**, *77*, 577–584.
174. Kálai, T.; Hideg, K. Synthesis of new, BODIPY-based sensors and labels. *Tetrahedron* **2006**, *62*, 10352–10360.
175. Mayur, S.; Kannappan, T.; Mou-Ling, S. *et al.* Pyrromethene–BF<sub>2</sub> complexes as laser dyes:1. *Heteroatom Chem.* **1990**, *1*, 389–399.
176. Compton, A. H. A Quantum Theory of the Scattering of X-rays by Light Elements. *Phys. Rev.* **1923**, *21*, 483–502.
177. Belcher, E. H. The luminescence of irradiated transparent media and the Cherenkov effect. *Journal of Biomedical Optics* **2015**, *20*, 36011.

178. Conti, M.; Eriksson, L. Physics of pure and non-pure positron emitters for PET: A review and a discussion. *EJNMMI physics* **2016**, *3*, 8.
179. Yoon, S. W.; Tsvankin, V.; Shrock, Z. *et al.* Enhancing Radiation Therapy Through Cherenkov Light-Activated Phototherapy. *International journal of radiation oncology, biology, physics* **2018**, *100*, 794–801.
180. Bliman, D.; Nilsson, J. R.; Kettunen, P. *et al.* A Caged Ret Kinase Inhibitor and its Effect on Motoneuron Development in Zebrafish Embryos. *Scientific reports* **2015**, *5*, 13109.
181. Ni, J.; Auston, D. A.; Freilich, D. A. *et al.* Photochemical Gating of Intracellular Ca<sup>2+</sup> Release Channels. *Journal of the American Chemical Society* **2007**, *129*, 5316–5317.
182. Aoshima, H.; Tanaka, D.; Kamimura, A. Synthesis of Photolabile Caged Amino Acids for Measuring Amino Acid Transporters. *Bioscience, Biotechnology, and Biochemistry* **1992**, *56*, 1086–1089.
183. Hao, X.; Yuan, J.; Yu, G.-A. *et al.* Air-stable and highly efficient indenyl-derived phosphine ligand: Application to Buchwald–Hartwig amination reactions. *Journal of Organometallic Chemistry* **2012**, *706-707*, 99–105.
184. Rhodat, T. *Current Work* **2018**.

## 7 Appendix

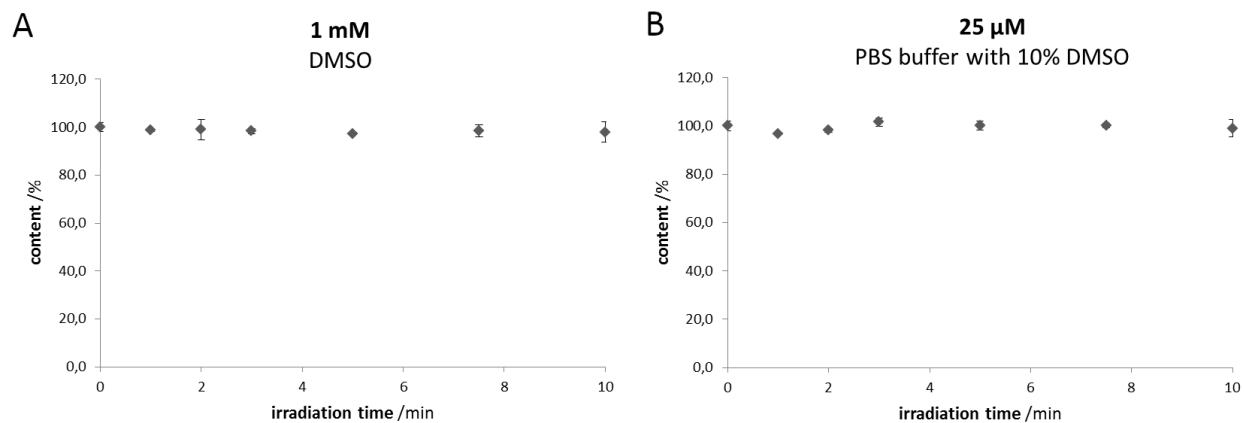


**Supplementary Figure 1: Stability of analogue 21 upon irradiation with UV light.** The compound solution was irradiated at 365 nm (5.4 W) and subsequently analyzed by HPLC. Each value is a mean  $\pm$  SD of two independent experiments.

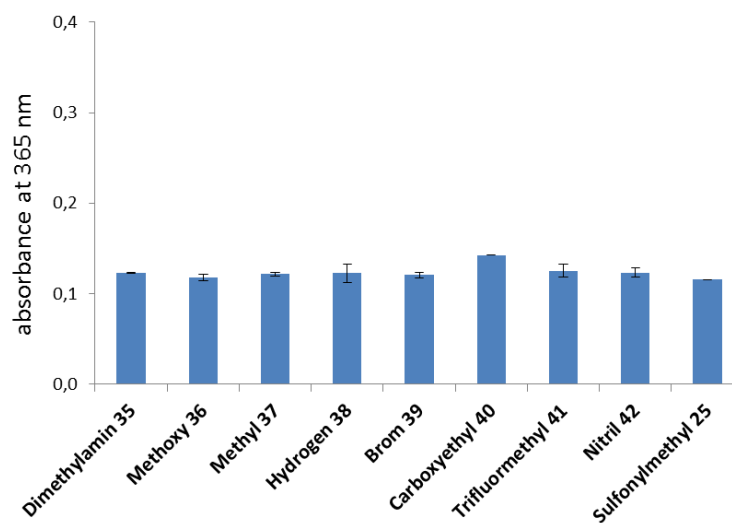


**Supplementary Figure 2: Cell viability of (A) U251 and (B) RN1 glioblastoma cells upon irradiation with UV light.** U251 cells were irradiated with 60 s of UV light (365 nm, 1.8 W). RN1 cells were irradiated for 30 s (365 nm, 1.8 W). Cell viability was assessed after 48 h of incubation respectively 72 h for RN1 cells.





**Supplementary Figure 3: Stability of benzyl caged analogue 26 upon irradiation with UV light.** The compound solutions A) 1 mM in DMSO and B) 25 μM in PBS buffer with 10% DMSO were irradiated in a well of a 96-well plate at 365 nm (75 mW) and subsequently analyzed by HPLC. Each value is a mean ± SD of two independent experiments.



**Supplementary Figure 4: Light absorbance of scaffolds 25,35-42 at a wavelength of 365 nm.** A light absorbance spectra of each compound solution (DMSO, 25 μM) was measured. The absorbance of 365 nm of each scaffold was plotted. Each value is a mean ± SD of two independent experiments.

## List of Abbreviations

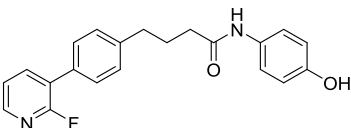
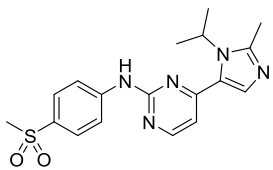
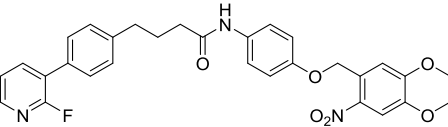
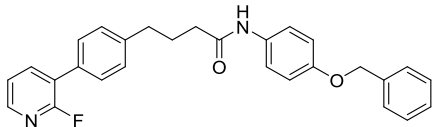
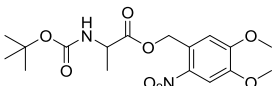
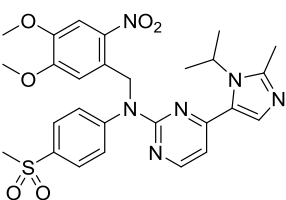
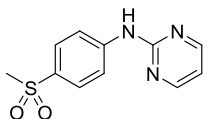
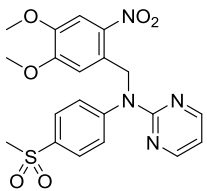
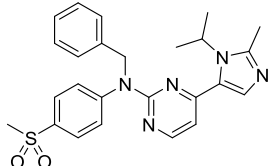
°C	degrees Celsius
μ	micro
2D / 3D	two-dimensional / three-dimensional
AlCl <sub>3</sub>	aluminium chloride
ATP	adenosine triphosphate
β	beta
b (NMR)	broad
BF <sub>3</sub> -OEt <sub>2</sub>	boron trifluoride etherate
boc	tert-butyloxycarbonyl
BODIPY	meso-methyl boron-dipyrromethene analogues
Br	bromo
C2	carbon number 2
C8	carbon number 8
CDK	cyclin-dependent kinase
CF <sub>3</sub>	trifluoromethyl
CH <sub>3</sub>	methyl
C-lobe	C-terminal lobe
cm	centimeter
CN	nitrile
CO <sub>2</sub>	carbon dioxide
COOEt	carboxyethyl ester
COSY (NMR)	correlation spectroscopy
CR	Cherenkov radiation
d (NMR)	doublet
DCM	dichloromethane
DEAC	diethylaminocoumarin analogues
DIPEA	diisopropylethylamine
DMEM	Dulbecco's modified Eagle's medium
DMF	dimethylformamide
DMNB	4,5-dimethoxy-2-nitrobenzyl
DMSO	dimethyl sulfoxide
EC <sub>50</sub>	half maximal effective concentration

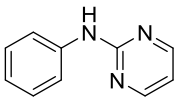
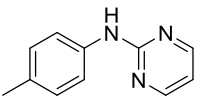
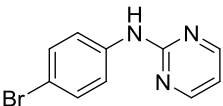
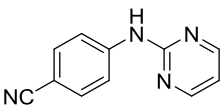
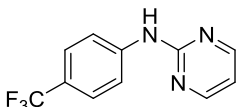
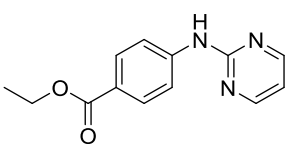
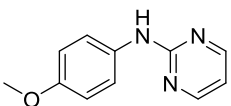
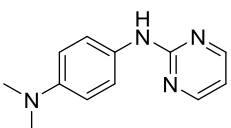
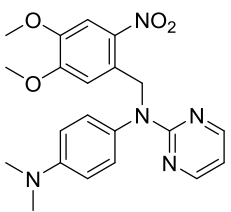
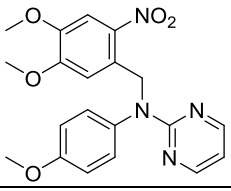
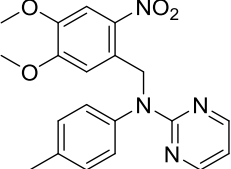
<i>e.g.</i>	<i>exempli grātiā</i> (lat. for example)
EI	electron impact
EMA	European Medicine Agency
equiv.	equivalents
ESI	electrospray ionization
EtOH	ethanol
<sup>18</sup> F	18-Fluorine
FBS	fetal bovine serum
FDA	Food and Drug Administration
FDG	fluorodesoxyglucose
g	gram
<sup>68</sup> Ga	Gallium-68
Gy	gray
h	hour(s)
H	hydrogen
HCl	hydrochloric acid
Hg	Mercury
HMBC (NMR)	heteronuclear multiple-bond correlation spectroscopy
H <sub>2</sub> O	water
HPLC	high-performance liquid chromatography
HRMS	high-resolution mass spectrometry
HSQC (NMR)	heteronuclear single-quantum correlation spectroscopy
Hz	hertz
IC <sub>50</sub>	half maximal inhibitory concentration
INN	international nonproprietary name
<i>i</i> -PrOH	isopropyl alcohol
<i>J</i> (NMR)	coupling constant
K	Kelvin
K <sub>2</sub> CO <sub>3</sub>	potassium carbonate
KH <sub>2</sub> PO <sub>4</sub>	potassium dihydrogen phosphate
KO- <i>t</i> -butyl	potassium- <i>tert</i> -butoxide
L	liter
LC-MS	liquid chromatography–mass spectrometry
LED	light-emitting diode

LEU	leucine
LG	leaving group
m	meter
m	milli
M	molar
m (NMR)	unresolved multiplet
MALDI	matrix-assisted laser desorption/ionization
MBq	mega becquerel
MeV	mega electronvolt
m/z	mass-to-charge ratio
MeOH	methanol
MHz	megahertz
min	minute(s)
mol	mole
$M_r$	relative molecular mass
MS	mass spectrometry
MTA	microtubule-targeting agent
n	nano
$N_2$	nitrogen
n/a	not applicable
$Na_2CO_3$	sodium carbonate
NaH	sodium hydride
NaI	sodium iodide
$N(CH_3)_2$	dimethylamine
NB	o-nitrobenzyl
N-lobe	N-terminal lobe
nm	nanometer
NMR	nuclear magnetic resonance spectroscopy
$OCH_3$	methoxy
PBS	phosphate-buffered saline
pdb	protein data bank (RCSB)
$Pd_2(dba)_3$	Tris(dibenzylideneacetone)dipalladium(0)
$Pd(PPh_3)_4$	Tetrakis(triphenylphosphine)palladium(0)
PDT	photodynamic therapy

PET	positron emission tomography
PPG	photoremovable protection group
ppm	parts per million
PS	phosphatidylserine
psi	pounds per square inch
PyBOP	(Benzotriazol-1-yloxy)tripyrrolidinophosphonium hexafluorophosphate
R	residue
resp.	respectively
ROS	reactive oxygen species
RP	reversed phase
rt	room temperature
s	second(s)
s (NMR)	singlet
S-BINAP	(S)-(-)-(1,1'-Binaphthalene-2,2'-diyl)bis(diphenylphosphine)
SD	standard deviation
SEM	standard error of the mean
smKI	small-molecule kinase inhibitor
smMTA	small-molecule microtubule-targeting agent
SN	nucleophilic substitution
SO <sub>2</sub> CH <sub>3</sub>	sulfonylmethyl
t (NMR)	triplet
TEA	triethylamine
TLC	thin-layer chromatography
TOF	time of flight
UKSH	university hospital Schleswig-Holstein
UV	ultraviolet
V	volt
v/v	volume fraction
vis	visible
vs.	versus
W	watt
Xantphos	4,5-bis(diphenylphosphino)-9,9-dimethylxanthene
Zn	Zinc

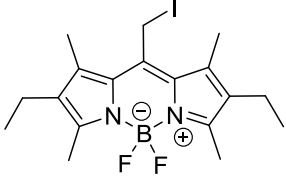
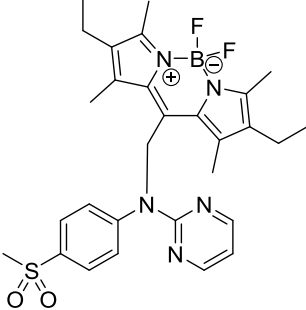
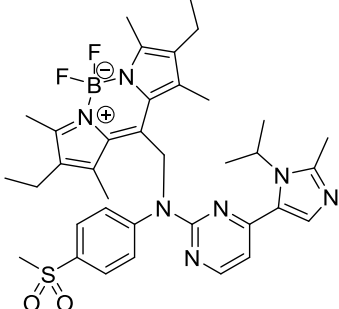
## Table of Compounds

#	lab code	formula	nomenclature	Page (prep.)
16	alex-raj		4-(4-(2-Fluoropyridin-3-yl)phenyl)-N-(4-hydroxyphenyl)butanamide	101
17	AZD5438		4-(1-Isopropyl-2-methyl-1H-imidazol-5-yl)-N-(4-(methylsulfonyl)phenyl)pyrimidin-2-amine	106
20	alex-3.8		N-(4-((4,5-dimethoxy-2-nitrobenzyl)oxy)phenyl)-4-(4-(2-fluoropyridin-3-yl)phenyl)butanamide	102
21	alex-3.18		N-(4-(benzyloxy)phenyl)-4-(4-(2-fluoropyridin-3-yl)phenyl)butanamide	104
22	alex-1.6		4,5-Dimethoxy-2-nitrobenzyl(tert-butoxycarbonyl)alaninate	111
23	alex-1.4		N-(4,5-dimethoxy-2-nitrobenzyl)-4-(1-isopropyl-2-methyl-1H-imidazol-5-yl)-N-(4-(methylsulfonyl)phenyl)pyrimidin-2-amine	109
24	alex-1.2		N-(4-(methylsulfonyl)phenyl)pyrimidin-2-amine	107
25	alex-1.3		N-(4,5-dimethoxy-2-nitrobenzyl)-N-(4-(methylsulfonyl)phenyl)pyrimidin-2-amine	108
26	alex-1.7		N-benzyl-4-(1-isopropyl-2-methyl-1H-imidazol-5-yl)-N-(4-(methylsulfonyl)phenyl)pyrimidin-2-amine	112

without	alex-1.1		<i>N</i> -phenylpyrimidin-2-amine	113
without	TD-001		<i>N</i> -( <i>p</i> -tolyl)pyrimidin-2-amine	114
without	TD-002		<i>N</i> -(4-bromophenyl)pyrimidin-2-amine	115
without	TD-008		<i>N</i> -(4-nitrophenyl)pyrimidin-2-amine	116
without	SK-006		<i>N</i> -(4-(trifluoromethyl)phenyl)pyrimidin-2-amine	117
without	SK-007		Ethyl 4-(pyrimidin-2-ylamino)benzoate	118
without	alex-1.11		<i>N</i> -(4-methoxyphenyl)pyrimidin-2-amine	119
without	alex-1.10		<i>N</i> 1, <i>N</i> 1-dimethyl- <i>N</i> 4-(pyrimidin-2-yl)benzene-1,4-diamine	120
35	alex-1.13		<i>N</i> 1, <i>N</i> 1-dimethyl- <i>N</i> 1-(4,5-dimethoxy-2-nitrobenzyl)- <i>N</i> 1-(pyrimidin-2-yl)benzene-1,4-diamine	128
36	alex-1.12		<i>N</i> -(4,5-dimethoxy-2-nitrobenzyl)- <i>N</i> -(4-methoxyphenyl)pyrimidin-2-amine	127
37	TD-S-001		<i>N</i> -(4,5-dimethoxy-2-nitrobenzyl)- <i>N</i> -( <i>p</i> -tolyl)pyrimidin-2-amine	122

38	alex-1.0		<i>N</i> -(4,5-dimethoxy-2-nitrobenzyl)- <i>N</i> -phenylpyrimidin-2-amine	121
39	TD-S-002		<i>N</i> -(4-bromophenyl)- <i>N</i> -(4,5-dimethoxy-2-nitrobenzyl)pyrimidin-2-amine	123
40	SK-C-007		Ethyl 4-((4,5-dimethoxy-2-nitrobenzyl)(pyrimidin-2-yl)amino)benzoate	126
41	SK-C-006		<i>N</i> -(4,5-dimethoxy-2-nitrobenzyl)- <i>N</i> -(4-(trifluoromethyl)phenyl)pyrimidin-2-amine	125
42	TD-S-008		<i>N</i> -(4,5-dimethoxy-2-nitrobenzyl)- <i>N</i> -(4-nitrilephenyl)pyrimidin-2-amine	124
47	alex-1.29		8-Chloromethyl-4,4-difluoro-1,3,5,7-tetramethyl-4-bora-3a,4a-diaza-s-indacene	129
49	alex-1.26		<i>N</i> -((4,4-difluoro-1,3,5,7-tetramethyl-4-bora-3a,4a-diaza-s-indacen-8-yl)methyl)- <i>N</i> -(4-(methylsulfonyl)phenyl)pyrimidin-2-amine	132
51	alex-1.21		8-Chloromethyl-4,4-difluoro-1,3,5,7-tetramethyl-2,6-diethyl-4-bora-3a,4a-diaza-s-indacene	130



52	alex-1.34		8-Iodomethyl-4,4-difluoro-1,3,5,7-tetramethyl-2,6-diethyl-4-bora-3a,4a-diaza-s-indacene	131
53	alex-1.30		<i>N</i> -((4,4-difluoro-1,3,5,7-tetramethyl-2,6-diethyl-4-bora-3a,4a-diaza-s-indacen-8-yl)methyl)- <i>N</i> -(4-(methylsulfonyl)phenyl)pyrimidin-2-amine	133
54	alex-1.42		<i>N</i> -((4,4-difluoro-1,3,5,7-tetramethyl-2,6-diethyl-4-bora-3a,4a-diaza-s-indacen-8-yl)methyl)-4-(1-isopropyl-2-methyl-1H-imidazol-5-yl)- <i>N</i> -(4-(methylsulfonyl)phenyl)pyrimidin-2-amine	134

# Curriculum Vitae

## Persönliche Daten

---

Name	Alexander Döbber
Geburtsdatum	09. Februar 1989
Geburtsort	Ibbenbüren
Staatsangehörigkeit	Deutsch

## Ausbildung und Studium

---

08/1999 - 07/2008	Goethe-Gymnasium Ibbenbüren
07/2008	Allgemeine Hochschulreife
08/2008 - 03/2009	Zivildienst, Klinikum-Ibbenbüren
04/2009 - 05/2013	Studium der Pharmazie, Christian-Albrechts-Universität zu Kiel
07/2013 - 12/2013	Pharmaziepraktikum, School of medical science, University of Sydney
01/2014 - 07/2014	Pharmaziepraktikum, Sophienhof-Apotheke, Kiel
08/2014	Approbation als Apotheker

## Beruflicher Werdegang

---

2005 - 2010	Aushilfe/Werkstudent Wiewelhove GmbH, Ibbenbüren
2011 - 2013	Wissenschaftliche Hilfskraft Pharmazeutisches Institut, Kiel
2014 - 2018	Wissenschaftlicher Mitarbeiter und Doktorand Pharmazeutisches Institut, Kiel
2017	Fachapotheker für pharmazeutische Analytik



## Erklärung

Die vorliegende Arbeit wurde unter Anleitung von Herr Prof. Dr. Christian Peifer im Fachbereich Pharmazeutische und Medizinische Chemie des Pharmazeutischen Instituts der Christian-Albrechts-Universität zu Kiel im Zeitraum von September 2014 bis Juni 2018 angefertigt.

Hiermit erkläre ich, Alexander Döbber, dass der Inhalt und die Form dieser Abhandlung, abgesehen von der Beratung durch meinen Betreuer, selbständig von mir erarbeitet und zusammengestellt wurde. Es wurden keine weiteren Quellen als angegeben herangezogen. Die Arbeit hat an keiner Stelle im Rahmen eines Prüfungsverfahrens vorgelegen und ist unter Einhaltung der Regeln guter wissenschaftlicher Praxis der Deutschen Forschungsgemeinschaft entstanden.

Kiel, Juni 2018

Alexander Döbber

Teile dieser Arbeit wurden bereits an folgender Stelle veröffentlicht:

Döbber, Alexander; Phoa, Athena F.; Abbassi, Ramzi H.; Stringer, Brett W.; Day, Bryan W.; Johns, Terrance G.; Abadleh, Mohammed; Peifer, Christian; Munoz, Lenka:

Development and Biological Evaluation of a Photoactivatable Small Molecule Microtubule-Targeting Agent, ACS medicinal chemistry letters, **2017**, 8, 395-400.

## Danksagung

An erster Stelle gilt größter Dank meinem Doktorvater Prof. Dr. Christian Peifer. Das entgegengebrachte Vertrauen und die ständige Diskussionsbereitschaft, auch abseits des Promotionsthemas, haben die Promotion zu einer großartigen Zeit gemacht. Besonders das hervorragende persönliche Verhältnis bleibt als nicht selbstverständlich hervorzuheben. Auch legendäre Weintastings werden in Erinnerung bleiben.

Besonderer Dank gilt außerdem Prof. Dr. Maaz Zuhayra für die super Betreuung in der Klinik bei der ich unglaublich viel Neues gelernt habe. Deine große Lust auf Wissenschaft und Beharrlichkeit, gerade dann wenn vieles nicht geklappt hat, machen die Kooperation besonders wertvoll. Vielen Dank auch für viele interessante Kaffee-Diskussionen.

Darüber hinaus möchte ich Prof. Dr. Lenka Munoz für die tolle Zeit in Sydney, sowohl während meines praktischen Jahrs, als auch während meiner Promotion danken. Gerade während des PJs habe ich viele wichtige Dinge gelernt, die mir während meiner Promotion eine große Hilfe waren. Die Zeit in Sydney hat mich, mein Studium und die Promotion wesentlich geprägt. Dabei natürlich auch vielen Dank an Athena, Tomas&Thomas, Stephen, Fadi und Ramsey für die großartige Zeit in Sydney.

König Theo Pfeffi dem Ersten danke ich für die fruchtbare Zusammenarbeit in mehreren Projekten und ganz neue musikalische Erfahrungen im Büro. Vielen Dank an Stefan für die Unterstützung als Hiwi und die unzähligen HPLC-Vials die ich dank dir nicht spülen musste. Besonderer Dank gilt Dorian für die Aufnahme ins 2.Liga-Büro, als es im Partybüro zu wild wurde, und diversen chemischen und surftechnischen Input während meiner gesamten Promotion. Dabei danke ich auch unseren anderen Chemikern Lydia, Björn und Miri für die Hilfe bei so vielen chemischen Fragen und letzterer vor allem für die Abgabe unzähliger Masseproben. Vielen Dank an Theo, Linda und Melanie für die unterhaltsame Semesterbetreuung. Ohne euch wären die vielen studentischen Missgeschicke nur halb so lustig gewesen.

Neben dem gesamten aktuellen Arbeitskreis gilt großer Dank natürlich den ehemaligen Doktoranden Rebecca, Boris, Jakob und Eugen die mich große Zeit meiner Promotion begleitet haben und von denen ich alles das zu Beginn der Promotion lernen durfte was das Studium einem nicht beibringt.

Ein besonderer Dank gilt Martin für die stetige Hilfsbereitschaft im und ums Labor und die ein oder andere nach Feierabend gemessene NMR-Probe. Vielen Dank an Sven Wichmann für die kompetente Hilfe bei diversen HPLC-Problemchen. Kalle Bock danke ich nicht nur für die zügigen Reparaturen

jeglicher Geräte, sondern auch für das zur Verfügung stellen von Werkstatt und Werkzeug für verschiedenste Heimwerkerprojekte. Vielen Dank an Dr. Ulrich Girreser für die kompetente Beratung bei zahlreichen analytischen Fragestellungen. Dr. Dieter Schollmeyer danke ich für die Aufnahme der Kristallstrukturen.

Ein außergewöhnlicher Dank gilt Folknand für seine unvergleichbare, andersdenkende Art. Danke, dass du sowohl meine Studien- als auch Promotionszeit in jeder Hinsicht bereichert hast, für Diskussionen die ich nie gedacht hätte diskutieren zu müssen, Gitarre, Beachvolleyball und ganz vieles anderes! Dabei danke ich natürlich auch Stephan, Basti, Dirk, Inga, Tanja, Eileen und allen Kommilitonen für die großartige Studienzeit. Großen Dank auch an alle meine (Beach-)Volleyball-, Kite- und sonstigen Freunde, dafür dass ihr nichts mit Pharmazie zu tun habt und so einen perfekten Ausgleich geschaffen habt. Danke euch allen für die unglaublich geile Zeit in Kiel!

Das Beste kommt bekanntlich zum Schluss. Allergrößten Dank an meine Eltern, meine drei Schwestern und meine wunderbare Freundin Maren. Danke für eure uneingeschränkte Unterstützung, Rat in jeder Lebenslage und dass ich mich auf euch immer verlassen kann. Mit einem so liebevollen Zuhause wie ihr es schafft, ist alles so viel einfacher. Danke!